Large Fully Nonlinear Solitary and Solitary-like Internal Waves in the Ocean

by

Marek Stastna

A thesis
presented to the University of Waterloo
in fulfilment of the
thesis requirement for the degree of
Doctor of Philosophy
in
Applied Mathematics

Waterloo, Ontario, Canada, 2001

The University of Waterloo requires the signatures of all persons using or photocopying this thesis. Please sign below, and give address and date.

Abstract

In this thesis we study fully nonlinear internal waves in a stratified ocean. These waves are isolated disturbances that do not change form as they propagate horizontally along the waveguide of the density stratified ocean. After surveying semi-analytical asymptotic theories for small, finite amplitude waves we present a variational technique for calculating large, fully nonlinear internal solitary waves which are exact solutions of the Euler equations governing an inviscid fluid. This technique is subsequently used to discuss the effect of horizontal background currents on solitary wave properties. Particular attention is paid to upper bounds on the solitary wave amplitude. Next we discuss one way the variational algorithm can be used to compute solitary-like waves which are past breaking, and the properties of such solitary wave-like objects. Finally we consider the interaction of an initially solitary wave with a viscous boundary layer. We show that for cases in which vorticity is produced in the boundary layer upstream of the wave, for example due to an appropriately chosen background current, this interaction can lead to the instability of the solitary wave and can result in significant transport of sediment out of the bottom boundary layer into the main water column.

Acknowledgements

Looking back at graduate school it strikes me that it lasts an awful long time. This means, of course, that there are many people to thank for a great many things, so as briefly as possible, my thanks go out to: To Kevin Lamb, my supervisor, for trying to teach me to be careful and patient (and for introducing me to Sibelius no. 5 on one of my many visits to the Lamb house). To Sean and Graeme Lamb for all the pillow fights. To Mary Lamb for the homebrew. To Pino Tenti, Marita Chidichimo and Siv Sivaloganathan for showing me that there is a variety of ways one can stay honest and still remain in academics. To 'mama a tata' for the many free vacations in the Rockies and other ways of showing they know the scoop. To my sister Kazi for the great mail from around the world. To my in-laws, for all the weekend hikes, cookouts and other loud family activities. To Shaloub Razak for a lifetime's worth of g-funk in just five years. To Sean Boudron for delivering both ze good news and ze bad news. To Todd Parsons for all the caffeine and bike repairs. To Fahad Razak for letting me keep that Doctor CD for so long. To all the rest of my friends whom space constraints keep me from placing in their just spots. To the staff of the Fields Institute, especially Pauline Grant, without whom I would have never had the chance to work there. To Helen, Ann and Nancy in the AM office for all the times they opened my office when I locked myself out and all the times they helped me navigate the seas of bureaucracy. To baby Martinique, keep bouncing my girl, you'll be crawling before I finish the corrections to this thesis. To Myra most of all: we managed to get married, have a child and write two theses. At the same time, we've travelled half the world and had some mighty nice suppers out on the deck watching the skyscrapers light up as the wine disappeared. For this balancing act as for so many other things you have my deepest admiration.

Contents

List of Figures

Chapter 1

Introduction and Historical Background

"There is one thing in the world more wicked than the desire to command, and that is the will to obey."

William Kingdon Clifford

In this thesis we will study large internal solitary waves (henceforth ISWs) propagating horizontally in a coastal ocean, their theoretical description and numerical modeling. While these waves have appeared quite often in the oceanographic and applied mathematics literature in the past twenty years, it seems prudent to define certain terms for the reader. More complete introductions can be found in standard text books, for example the book by Gill ([21]) on ocean dynamics, the book by Johnson on water waves (surface waves) ([28]), or the book by Whitham ([66]) on nonlinear waves.

Solitary waves are isolated, nonlinear disturbances that propagate along a wave-guide without changing shape. An example of a solitary wave is given in figure 1.1.

Let us consider a right-handed system of Cartesian coordinate axes with the origin at the bottom of the ocean. We take the z axis to be pointing up towards the surface, and the x axis to

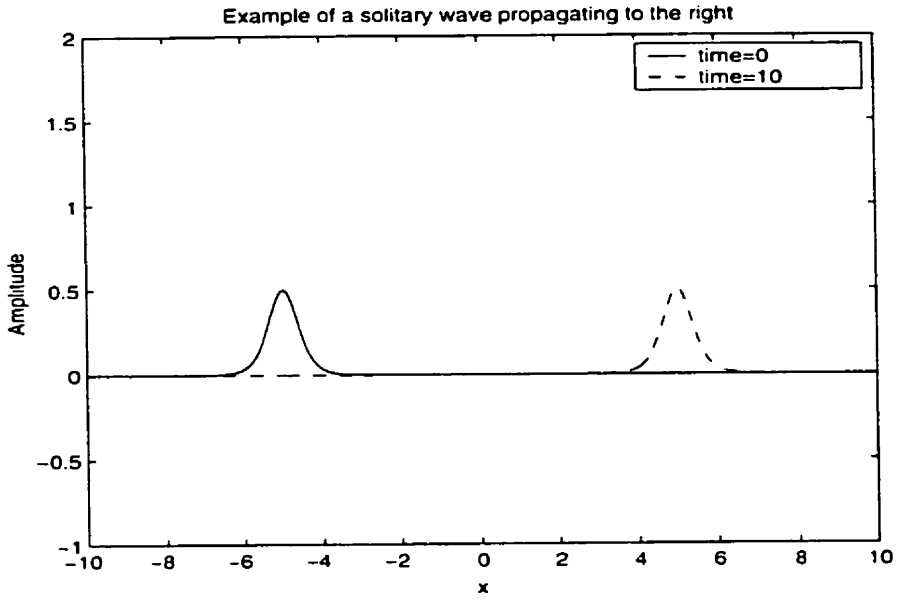

Figure 1.1: Example of a solitary wave propagating to the right with unit speed

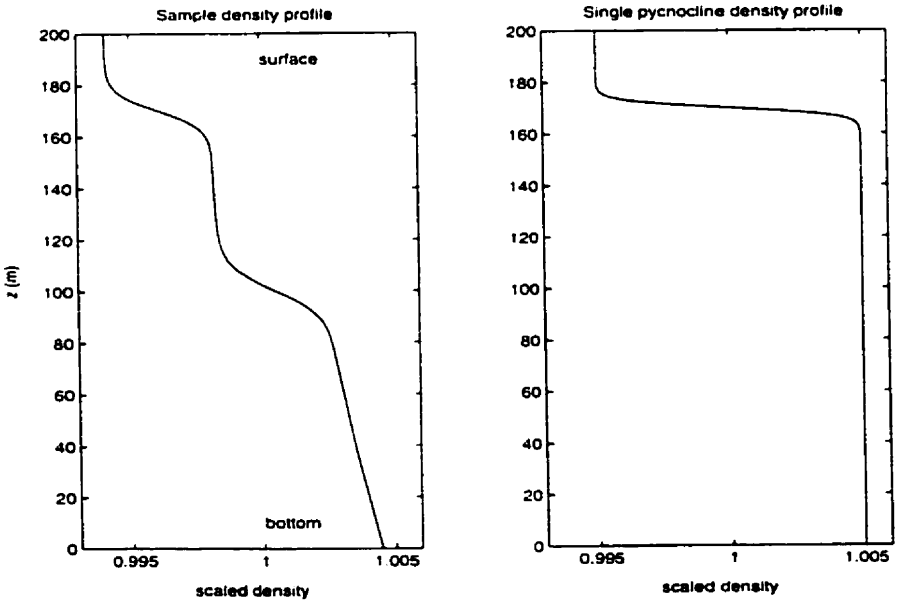

Figure 1.2: Two examples of a $\bar{\rho}(z)$. (a) General, (b) single pycnocline

run along a flat bottom. Throughout this thesis we will neglect the effect of the Earth's rotation, and hence consider an inertial frame of reference. This is a valid approximation because the phenomena of interest occur on time scales much smaller than those needed for the effects of the Earth's rotation to become apparent. The density of sea water is a function of temperature and salinity. Throughout this thesis we will consider the density only and ignore the exact variation of salinity and temperature. Given a hypothetical, still ocean, the density (denoted by $\bar{\rho}$, and henceforth caled the background density profile or background stratification) will be a function of depth $(H - z)$ only (i.e. $\bar{\rho} = \bar{\rho}(z)$), and the pressure will be given by the hydrostatic equation

$$\frac{dP}{dz} = -\bar{\rho}(z)g$$

where g is the acceleration due to gravity. In the field, it is often observed that the density profile has one or more regions of rapid change called pycnoclines, separated by regions that have nearly constant density (well-mixed regions). A simple example is provided by a single pycnocline. See figure 1.2 for an example of a general and single pycnocline stratification. A useful further idealization assumes the pycnocline to be infinitely thin, in other words as the interface between two fluids of different, but constant, densities (think of a layer of oil on water). We can then consider waves propagating horizontally along this interface, and call such waves vertically trapped internal waves. The analogy with surface waves then becomes obvious. However, the density changes in the ocean interior are much smaller than at the water-air interface. This means that the restoring forces are weaker and hence for the same energy, internal wave amplitudes are much larger than surface wave amplitudes. It is often assumed that the ocean has a rigid lid, thereby eliminating the complications of a free boundary at the surface, as well as the fast moving surface waves (see [29] for more details). We will make this approximation throughout this thesis.

For a general $\bar{\rho}(z)$ the situation is further complicated by internal waves that propagate in directions other than the horizontal (see the books by Kundu [29] or Gill [21] for an introduction to such waves). In this thesis we will concern ourselves only with horizontally propagating (vertically trapped) waves.

The equations for an incompressible fluid under the Boussinesq approximation read

$$\begin{aligned} \rho_0 \left(\frac{\partial \vec{u}}{\partial t} + \vec{u} \cdot \vec{\nabla} \vec{u} \right) &= -\vec{\nabla} P - \rho g \hat{k} + \vec{F}_b + \mu \nabla^2 \vec{u} \\ \vec{\nabla} \cdot \vec{u} &= 0 \\ \frac{\partial \rho}{\partial t} + \vec{u} \cdot \vec{\nabla} \rho &= \kappa \nabla^2 \rho. \end{aligned} \tag{1.1}$$

where u is the fluid velocity, ρ_0 is the constant density of the reference state, ρ is the density perturbation to the reference state, P is the dynamic pressure (the hydrostatic part corresponding to the reference stratification has been subtracted off), μ is the dynamic viscosity (or alternatively the eddy viscosity for a simple turbulence model) of the fluid. For a simple turbulence model κ is the eddy diffusivity of the density. For laminar flow $\kappa = 0$ and density is conserved. We should note that the Boussinesq approximation amounts to three approximations. The first sets ρ constant in all terms of the momentum equations except for the buoyancy term. The second approximates the conservation of mass equation by $\vec{\nabla} \cdot \vec{u} = 0$, while the third reduces the energy equation to a form that looks like the original consevation of mass equation (hence the energy equation is often referred to as the density equation). A thorough discussion can be found in the text by Kundu ([29]). The vector $\vec{F}_b$ includes any body forces we wish to include (something that is useful for certain numerical simulations). If we divide through by ρ_0 the Laplacian term would involve the kinematic viscosity

$$\nu = \frac{\mu}{\rho_0}.$$

For internal motions the perturbations to the background density profile $\bar{\rho}(z)$ are small and hence it makes sense to define

$$\rho = \bar{\rho}(z) + \rho'. \tag{1.2}$$

We introduce the buoyancy frequency $N(z)$ via

$$N^2(z) = -\frac{g}{\rho_0} \frac{d\bar{\rho}}{dz}. \tag{1.3}$$

It is easy to show that a fluid parcel at a given height z displaced vertically oscillates about its equilibrium height with the frequency $N(z)$ (see [21]). The governing equations can be written as

$$\rho_0\left(\frac{\partial \vec{u}}{\partial t} + \vec{u}\cdot\vec{\nabla}\vec{u}\right) = -\vec{\nabla}P - \rho' g + \vec{F}_b + \mu\nabla^2\vec{u}$$

$$\vec{\nabla}\cdot\vec{u} = 0$$

$$\frac{\partial \rho'}{\partial t} + \vec{u}\cdot\vec{\nabla}\rho' - \frac{N^2(z)\rho_0}{g}w = \kappa\nabla^2\rho'. \tag{1.4}$$

(1.5)

In situations where the viscosity and diffusivity are not important to the phenomenon in question we simply drop all the terms which include μ and κ. The governing equations are then referred to as the Euler equations.

We will discuss 2D phenomena only. With the axes defined as above, we consider all field variables to be functions of x, z and t only. Furthermore, we take $v = 0$ (no velocity in the y direction). We can then introduce a stream-function $\Psi(x, z, t)$ so that

$$(u, w) = \left(\frac{\partial \Psi}{\partial z}, -\frac{\partial \Psi}{\partial x}\right). \tag{1.6}$$

The governing equations can now be rewritten in a form that is more convenient for theoretical analysis (This is discussed in detail in the next chapter).

1.0.1 Some Historical Background

In what is now a standard part of the applied mathematics folklore, solitary waves were discovered by John Scott Russell in 1834 as he rode along the Edinburgh-Glasgow shipping canal. These were solitary waves on the free surface of the water. After some initial interest (and controversy) by the great minds of 19th century physics (Airy, Rayleigh, Boussinesq, etc.) solitary waves were largely relegated to the periphery of applied mathematics until 1965 (see the review of Miles [46] for more complete historical notes, as well as other interesting information on solitary waves). That year solitary waves returned to prominence via the amazing discovery of Zabusky and Kruskal

([68]) that numerical solutions of the KdV equation contained finite amplitude solitary waves that interacted with one another without losing their form (as particles do). Furthermore, a general initial condition broke up into a number of these particle-like 'solitons'. The KdV equation was derived by Korteweg and deVries in 1895 to describe surface waves propagating in one direction. The same authors discussed a family of periodic solutions to this equation (called cnoidal waves) which yield solitary wave solutions in the limit of infinite period. In retrospect it should be noted that it was Russell himself who first showed that a fairly general initial disturbance in a long, shallow tank breaks up into a rank-ordered (largest waves propagate fastest) train of solitary waves. Since the KdV equation is an asymptotic model of such an experimental situation, in some sense the property discovered by Zabusky and Kruskal was anticipated by Russel.

Further work on solitary waves was stimulated by the astonishing work of Gardner *et al.* ([17], [18]) which showed that the initial value problem for the nonlinear KdV equation could be solved exactly using analytical methods on linear equations. This technique, called the inverse scattering method (or sometimes inverse scattering transform), has since produced a hefty volume of mathematical literature and has been applied to a wide variety of model equations (of which the KdV equation is just one example). See the books by Drazin and Johnson [16] or Ablowitz and Segur ([1]) for more on this topic.

From a mathematical point of view solitary waves were interesting because certain special nonlinear equations possessed solitary waves as solutions. These equations could be analyzed using the inverse scattering method and had a host of interesting mathematical properties (see the early collection [39] for an approachable introduction).

The study of internal waves has a long history of its own ([19]). In his book, Gill ([21]) includes an entry from Benjamin Franklin's journal regarding the motion at the interface between oil and water. Franklin noted that the motion at the interface is quite pronounced even though the motion at the free surface is nearly negligible. Gill's book contains many other interesting historical notes regarding waves in stratified fluids. The connection between vertically trapped internal waves and solitary waves was established through the work of Benney ([7]) and Benjamin ([4])in 1966. Benney showed that small, finite amplitude, vertically trapped waves in a shallow

ocean were governed by the KdV equation (which has solitary wave solutions), while Benjamin used a variational technique to derive a solitary wave solution without explicitly deriving the KdV equation. We will quote extensively from a version of Benney's analysis in the following chapter. Benney's theory is an example of so called weakly nonlinear theories (henceforth WNL). These theories have a very extensive, and active, literature with applications to internal waves reviewed by Grimshaw in ([22]).

The mathematical work on the KdV and related equations took some time to make its way into the field of oceanography. In what is now a standard review ([50]) Ostrovsky and Stepanyants state that while oceanographers often observed solitary waves in the interior of the ocean, it was not until the language of solitons and inverse scattering became widely known that a means to discuss such observations became available. Some of the observations were quite spectacular (for example those of Osborn and Burch in the Andaman sea [49]) and during the 1980s photos from space (which can be found on the Internet) served to stimulate even more interest. Ostrovsky and Stepanyants also note that it was advances in remote sensing and oceanographic measurement techniques that made reliable observations of internal solitary waves possible, a useful reminder in the present theoretical work.

The advent of cheap computation in the 1990s opened up new avenues for investigation of ISWs. In 1991 Turkington *et al.* published a technique for computing fully nonlinear ISWs for a given stratification ([64]). This work presented a departure from WNL theory in the sense that the ISWs computed were exact solutions of the Euler equations. A version of Turkington *et al.*'s algorithm, along with more discussion of the related literature will be presented in the next chapter. The algorithm derived there will subsequently be used throughout the remainder of this work. Lamb and various co-workers have used Turkington's method as well as various other computational techniques to study many aspects of ISWs ([38], [31], [37], [32], [35]).

A large part of this thesis was motivated by the observations of Bogucki, Dickey and Redekopp off the California coast ([8], henceforth referred to as BDR). These observations showed a correlation between the passage of a packet of ISWs of elevation and an increase in resuspended sediment at 8 m above the ocean bottom. The paper also made a variety of predictions about how the

ISWs interacted with the bottom boundary layer and how they were generated. Subsequently, Bogucki and Redekopp ([10]) published numerical simulations outlining a possible scenario for ISW induced sediment resuspension. These simulations did not use fully nonlinear ISWs (and in fact were not presented in a clear manner). Redekopp ([11]) subsequently presented observational evidence of ISW induced resuspension at a number of sites in the Atlantic. The problem of sediment resuspension (and transport into the main water column) is very broad and we will aim to examine several different aspects of its relation to fully nonlinear ISWs in this thesis.

More generally, interest in ISWs and their life cycle continues today. There are well known regions of the world oceans where the generation, propagation and dissipation of ISWs are observed and measured (Ostrovsky and Stepanyants provide a map and a great deal of information is available on the Internet). Similarly there are several standard theoretical scenarios for ISW generation (see [22] and [31]) and many (usually based on WNL) models for ISW structure (see [22]). ISW dissipation remains largely unresolved (though [22] does discuss some simple models).

1.0.2 Plan of Thesis

In this thesis we wish to examine three broad topics in the study of fully nonlinear ISWs. First we investigate how the presence of a background current affects fully nonlinear ISW properties (maximum amplitude, propagation speed, etc.). Second we introduce one method for computing ISWs past breaking, and subsequently use this method to discuss ISWs with trapped cores. Third, we discuss the interaction of ISWs with a viscous bottom boundary layer (henceforth BL). As a particular application we examine the relevance of ISW passage to sediment resuspension into the water column.

Before each of these three topics is discussed in its own chapter a chapter of mathematical and numerical tools is provided.

Each of the chapters presenting results ends with a discussion of how the results in this work relate to the relevant literature as well as to future research directions for the particular topic.

For readers interested in specific topics the thesis need not be read in a sequential manner. The chapter on ISW-BL interaction can be read on its own with the reader flipping back to the

Tools chapter and Steady Waves chapter when necessary. Similarly, a reader less interested in numerical simulations can read the Tools and Steady Waves chapters and skim the remaining chapters according to their interest. The ISWs with Trapped Cores chapter depends to some degree on both the Tools and Steady Waves chapters, but is wholly independent of the ISW-BL Interaction chapter.

Chapter 2

Fundamental Tools

The phenomenology of ISWs is very complicated. This is the case primarily due to the complexity of the underlying physical situation of a variable temperature and salinity (and hence density) ocean which is constantly in motion on a variety of length scales, and in physical and thermal contact with the similarly active atmosphere. In this chapter we develop the various tools (or rational simplifications) used in this thesis to investigate the behaviour of steady ISWs (steady in an appropriate frame of reference). We will consider 2-D situations only. We begin by discussing the theory of weakly nonlinear waves (henceforth WNL) which extends the linear theory of infinitesimal waves to the case of finite, but small, amplitude waves. We quote results that derive the well known Korteweg de-Vries (KdV) equation for the horizontal structure of the wave. This equation demonstrates the possibility of a balance between nonlinearity and dispersion (both finite amplitude effects), and indeed we write down the solitary wave solution (the proof that such a balance is possible).

Following the section on WNL, and following the work of Turkington *et al.* ([64]), we derive a nonlinear elliptic eigenvalue problem for fully nonlinear ISWs. This eigenvalue problem is found to be amenable to a variational formulation, which in turn provides an efficient means for numerically calculating ISWs for a given background density and current. This algorithm allows us to compare and contrast the predictions WNL makes with large, fully nonlinear waves

(computed by the algorithm). It has been found that for a large class of background density profiles WNL does not successfully predict the structure of large ISWs ([34]). An alternative theory to WNL for discussing large waves is given by the conjugate flow theory, which is discussed in the fourth section. Unlike WNL this theory is exact, hence not restricted to small amplitudes, however it assumes the flow is uni-directional and hence leaves out all mention of dispersion.

In the final section of the chapter we discuss the numerical model, as developed by Lamb ([31]) and modified by the author, used in all subsequent work for simulations that evolve in time.

2.1 Weakly Non-Linear Theory

We quickly summarize the results of WNL for ISWs in shallow water, as developed by Lamb and Yan ([38]) and extended by Lamb ([34]). Let ϵ and μ be two small, dimensionless parameters measuring the wave amplitude and the aspect ratio (the ratio of typical vertical to horizontal length scales) of the waves, respectively. Define b, sometimes referred to as the buoyancy, as

$$b = \frac{g}{\rho_0}\rho. \tag{2.1}$$

Next introduce an asymptotic expansion in the two small parameters

$$\begin{aligned} \psi &= \psi^0 + \epsilon\psi^{1,0} + \mu\psi^{0,1} + \cdots \\ b &= b^0 + \epsilon b^{1,0} + \mu b^{0,1} + \cdots \end{aligned} \tag{2.2}$$

This assumption linearizes the governing equations at all orders. The fluid occupies the infinite strip bounded by $z = 0$ and $z = 1$. We seek separable solutions at each order, and find that at leading order

$$\psi^0 = B(x,t)c_{lw}\phi(z). \tag{2.3}$$

where $B(x,t)$ is the horizontal structure function. $\phi(z)$, the vertical structure function, and c_{lw}, the linear, longwave speed are given by the eigenvalue problem

$$\begin{aligned} \mathcal{L}\phi \equiv \phi_{zz} + \left(\frac{N^2(z)}{(c_{lw}-U)^2} + \frac{U''}{c_{lw}-U}\right)\phi &= 0 \\ \phi(0) &= 0 \\ \phi(1) &= 0. \end{aligned} \tag{2.4}$$

$\mathcal{L}$ is a linear differential operator defined by the above. The above is commonly known as the Taylor-Goldstein equation (strictly speaking, the Taylor-Goldstein equation in the longwave limit). For the case of no background current, and physically relevant $N(z)$ (e.g. stratifications with continuous $N(z)$, multiple layer stratifications) the above eigen-value problem has an infinite set

of discrete eigenvalues c_n which decrease as the mode number n increases ([67]). The corresponding eigen-functions are labeled ϕ_n. The mode of an eigenfunction is defined as the number of zeros of the function strictly between $z = 0$ and $z = 1$ plus 1. In other words the eigenfunction that never crosses zero between the two boundaries is called the mode 1 solution and has the largest propagation speed. We will focus solely on mode 1 waves and hence drop the subscript on c_n and ϕ_n. When a nonzero background current is included the requirement that $c_{lw} - U > 0$ will preclude the formation of critical layers (see [44] for a discussion of critical layers in this context). As an aside, note that it is not possible to demand that all modes satisfy $c_n - U > 0$, and thus a nonzero background current will restrict the number of higher modes we can consider, though this will not be relevant in the following. To leading order b^0 is given by

$$\frac{b^0}{N^2} = E(z)B(x,t), \tag{2.5}$$

where

$$E(z) = \frac{c_{lw}}{c_{lw} - U}\phi. \tag{2.6}$$

Extensions to higher order can be found in ([38], [34]).

To first order in both small parameters, the evolution equation for the wave amplitude is given by

$$B_t = -c_{lw}B_x + \epsilon 2r_{10}c_{lw}BB_x + \mu r_{01}B_{xxx}. \tag{2.7}$$

By dropping the first-order nonlinear and dispersive terms in this equation, we see that the eigenvalue c_{lw} is indeed the linear, longwave propagation speed. The physical parameters r_{10} and r_{01} are given by

$$r_{10} = \frac{-3\int_0^1 (c_{lw} - U)^2 E'^3 dz}{4c_{lw}\int_0^1 (c_{lw} - U)E'^2 dz}. \tag{2.8}$$

and

$$r_{01} = \frac{-\int_0^1 (c_{lw} - U)^2 E^2 dz}{2\int_0^1 (c_{lw} - U) E'^2 dz}. \tag{2.9}$$

Note that since $c_{lw} - U > 0$, $r_{01} < 0$ while r_{10} can have either sign. With $\mu = \epsilon$ equation (2.7) is the KdV equation and can be converted to standard form by switching to a reference frame moving with the wave speed. It can be shown that (2.7) has solitary wave solutions (see for example, [32]) of the form

$$B(x,t) = -b_0 \mathrm{sech}^2(\theta) \tag{2.10}$$

where

$$\theta = \frac{x - Vt}{\lambda}. \tag{2.11}$$

Waves are depressions if $b_0 > 0$ and elevations if $b_0 < 0$. The wavelength λ, and the nonlinear propagation speed are related via

$$b_0 \lambda^2 = -6 \frac{r_{01}}{c_{lw} r_{10}} \tag{2.12}$$

and

$$V = (1 + \frac{2}{3} r_{10} b_0) c_{lw}. \tag{2.13}$$

In a frame moving with the wave the waves are symmetric about the z axis, with the largest disturbance occurring at the wave center ($\theta = 0$). Note that since $r_{01} < 0$ and $\lambda^2 > 0$ waves are waves of depression if $r_{10} > 0$ and waves of elevation if $r_{10} < 0$. With no background current the theory yields waves of depression (elevation) if the majority of the change in density occurs in the top (bottom) half of the water column. However, since varying $U(z)$ varies r_{10}, including possibly its sign, a background current may have an effect on this simple relationship. Note also that $b_0 r_{10} > 0$, implying that solitary waves with larger amplitude propagate faster and are narrower. In particular this means that all finite amplitude waves propagate faster than the linear long wave speed (often labeled c_{lw} in the following as c will be used for the ISW propagation speed).

Waves break if, in a frame moving with the wave, a streamline is vertical, or in other words if

the z component of the gradient of the streamfunction is zero. In this frame, to leading order we have

$$\psi^T(\theta) = -Vz + \psi^b(z) + c_{lw}B(\theta)\phi(z)$$

where ψ^b is the streamfunction of the background flow. As mentioned above, the largest disturbances occur when $\theta = 0$ and hence to find the smallest wave amplitude at which breaking occurs (henceforth b_0^b) we consider vertical profiles at $x = 0$ only. With the solitary wave solution (2.10) the condition for breaking reads

$$U(z) - b_0 c_{lw}\phi_z = V. \tag{2.14}$$

To facilitate the solution for b_0^b, define the height at which the maximum of horizontal velocity occurs, z^*, as

$$\max(U(z) + u(0,z)) = U(z^*) + u(0,z^*). \tag{2.15}$$

Then

$$b_0^b = \frac{U(z^*) - c_{lw}}{c_{lw}(\phi_z(z^*) + \frac{2}{3}r_{10})}. \tag{2.16}$$

This means that first-order WNL predicts that waves will break for all stratifications and background currents. We shall see that this true only for some cases.

The approach discussed above can be extended to higher order as in ([34]). Higher order extensions are more accurate.

2.2 Fully Nonlinear ISWs

WNL is a very useful conceptual tool, however being an aymptotic theory it cannot be expected to give valid results for very large waves. The shortcomings of first order theory were mentioned in the previous section. Some of these can be fixed by higher-order theories (see [22] and references therein). Nevertheless, it is desirable to have a method for calculating solitary wave solutions of the full Euler equations for any given stratification $N^2(z)$ and background current $U(z)$. These exact solutions could then be compared to WNL to test the validity of the asymptotic theory.

We closely follow the work of Turkington *et al.* (henceforth TEW) ([64]) and its extension by Wang (henceforth Wang) ([65]) The formulation of TEW was for ISWs without a background current. Wang's extension allowed a steady, horizontal current's geometric shape to be specified, but not its top to bottom velocity difference (this somewhat bizarre result will be discussed below once we have derived an eigenvalue problem governing ISWs). The algorithm outlined below allows one to specify both the geometric shape and the top to bottom velocity difference of the current. As before, we let $U(z)$ denote the steady horizontal current. We define σ^T and σ to represent the total and wave induced vorticity, respectively. i.e.

$$\begin{aligned} \sigma^T &= U'(z) + \nabla^2\psi, \\ \sigma &= \nabla^2\psi. \end{aligned} \tag{2.17}$$

J is the Jacobian, defined as the bilinear differential operator with action

$$J(a,b) = a_x b_z - a_z b_x. \tag{2.18}$$

This allows us to write the governing equations as,

$$\rho_t + J(\rho, \psi^T) = 0, \tag{2.19}$$

$$\sigma_t + J(\sigma^T, \psi^T) + \rho_x g = 0, \tag{2.20}$$

where the first is the continuity equation and the second is the vorticity equation, which results from a cross-differentiation of the momentum equations. Note that the total streamfunction is given by

$$\begin{aligned} \psi^T &= \psi^b + \psi, \\ \psi^b &= \int U(z)dz, \end{aligned}$$

and that the above set of equations requires $U(z)$ to be steady. We switch to a frame of reference moving with the ISW. The continuity equation now reads

$$J(\rho, \psi + \psi^b - cz) = 0. \tag{2.21}$$

Next write

$$\rho(x, z) = \bar{\rho}(z - \eta(x, z)) \tag{2.22}$$

where η is the isopycnal displacement. This transformation states that the density along an isopycnal remains constant and implicitly defines the isopycnal displacement $\eta(x, z)$. A diagram of the situation is given in figure 2.1. We require that

$$\lim_{x \to \pm\infty} \eta(x, z) = 0 \tag{2.23}$$

as well as the vanishing of all derivatives of η as $x \longrightarrow \pm\infty$. Notice this implies that ψ and all its derivatives vanish as $x \longrightarrow \pm\infty$ as well. The definition of the isopycnal displacement $\eta(x, z)$ (2.22) lets us write

$$\bar{\rho}'(z - \eta)J(z - \eta, \psi + \psi^b - cz) = 0 \tag{2.24}$$

and provided that $\bar{\rho}'(z - \eta)$ is not zero on an interval

$$\psi + \psi^b - cz = F(z - \eta) \tag{2.25}$$

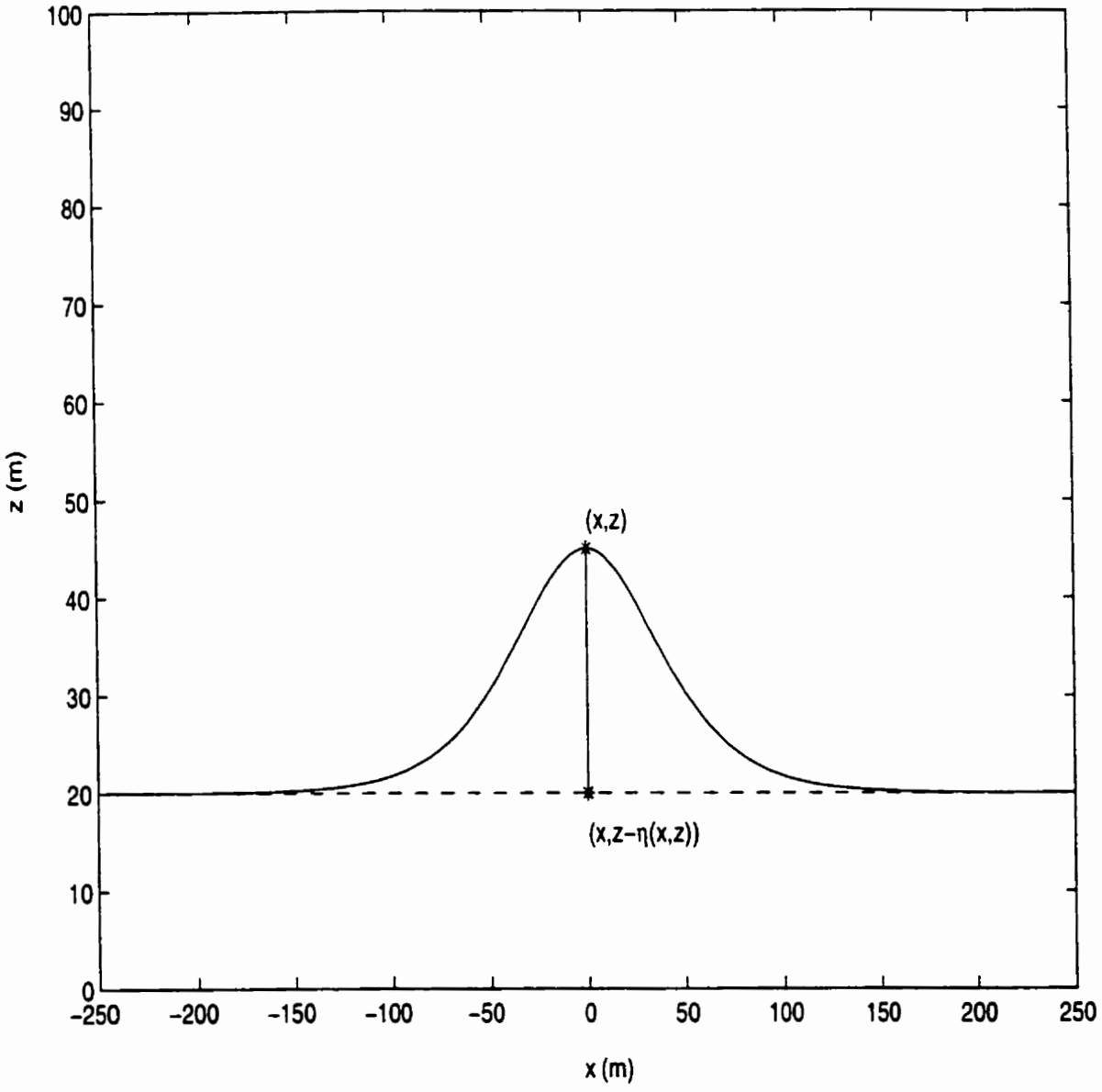

Figure 2.1: Definition diagram for $\eta(x, z)$, the isopycnal displacement

for some function F. Using the vanishing of η and all its derivatives for large x we find

$$F(z) = \psi^b(z) - cz \tag{2.26}$$

and hence

$$\psi = \psi^b(z - \eta) - \psi^b(z) + c\eta. \tag{2.27}$$

This means that once η is known all other field quantities are simple to calculate. Next write the vorticity equation in a frame moving with the wave as

$$J(\sigma^T, \psi^T - cz) + J(\rho, gz) = 0. \tag{2.28}$$

A series of algebraic manipulations leads to the equation

$$J\Big([U(z - \eta) - c]\sigma^T - g\eta\bar{\rho}'(z - \eta), z - \eta\Big) = 0 \tag{2.29}$$

or

$$G(z - \eta) = [U(z - \eta) - c]\sigma^T - g\eta\bar{\rho}'(z - \eta), \tag{2.30}$$

for some function $G(z - \eta)$. From the vanishing of η, ψ and their derivatives as $x \longrightarrow \pm\infty$ we find that

$$G(z) = -U'(z)\Big(U(z - \eta) - c\Big). \tag{2.31}$$

Using (2.30) and (2.31) along with the definition of σ^T, we get an equation for η. Some simplification shows that η satisfies the nonlinear, elliptic eigenvalue problem

$$\nabla^2\eta = -\frac{U'(z - \eta)}{U(z - \eta) - c}[1 - (\eta_x^2 + (1 - \eta_z)^2)] + \frac{g\bar{\rho}'(z - \eta)}{(U(z - \eta) - c)^2}\eta \tag{2.32}$$

where c is the unknown wave propagation speed and $U(z)$ is the known background current. The

boundary conditions are

$$\begin{aligned} \eta(x,0) &= 0 \\ \eta(x,H) &= 0 \end{aligned} \tag{2.33}$$

where H is the fluid depth, and

$$\lim_{x \to \pm\infty} \eta(x,z) = 0. \tag{2.34}$$

This boundary value problem was derived by Wang ([65]).

If we define $\hat{U}$ by

$$U(z) = c\hat{U}(z) \tag{2.35}$$

and λ according to

$$\lambda = \frac{gH}{c^2} \tag{2.36}$$

we can rewrite (2.32) as

$$-\gamma^2\nabla^2\eta - \hat{U}'(z-\eta)\gamma\beta = -\frac{\lambda}{H}\hat{\rho}'(z-\eta)\eta \tag{2.37}$$

$$\gamma = \hat{U}(z-\eta) - 1 \tag{2.38}$$

$$\beta = \eta_x^2 + (1-\eta_z)^2 \tag{2.39}$$

$$\tag{2.40}$$

a form amenable to a variational formulation. Indeed by defining

$$E(\eta) = \int\int_D \frac{(\hat{U}(z-\eta)-1)^2}{2}[\eta_x^2 + (1-\eta_z)^2]dxdz \tag{2.41}$$

$$Q(\eta) = \int\int_D \frac{(\hat{U}(z-\eta)-1)^2}{2}dxdz \tag{2.42}$$

and

$$F(\eta) = \int\int_D f(z,\eta)dxdz \tag{2.43}$$

where

$$f(z,\eta) = \int_0^\eta [\bar{\rho}(z-\eta) - \bar{\rho}(z-\xi)]d\xi, \tag{2.44}$$

we find that the eigenvalue problem (2.37) corresponds to the Euler-Lagrange equation for the constrained minimization problem

$$\text{minimize} \quad E(\eta) + Q(\eta) \qquad \text{subject to} \quad F(\eta) = A \tag{2.45}$$

where A is a constant specifying the size of the wave. Note that D is the domain on which we calculate the waves (the infinite strip in theory, a truncated strip in practice). For the case of no background current $E(\eta)$ and $F(\eta)$ can be identified with the kinetic energy and a potential energy for the wave, respectively. It can be shown that $HgF(\eta)$ is the available potential energy (henceforth APE) with or without a background current. The APE is the change in potential energy if the density field on an infinite strip is sorted adiabatically to be horizontally uniform (originally defined by Lorenz [42], a more recent reference being [13]).

To apply a generalized version of the algorithm from TEW we rewrite the problem as

$$-\nabla^2\eta = \lambda\frac{S(z,\eta)}{(\hat{U}(z-\eta)-1)^2} + R(z,U,\eta) \tag{2.46}$$

where

$$S(z,\eta) = -\frac{\bar{\rho}'(z-\eta)\eta}{H(\hat{U}(z-\eta)-1)^2}, \tag{2.47}$$

and

$$R(z,U,\eta) = \frac{\hat{U}'(z-\eta)}{\hat{U}(z-\eta)-1}[1-(\eta_z^2+(1-\eta_z)^2)]. \tag{2.48}$$

The generalized algorithm for getting the $(k+1)$th iteration assuming that the kth is known, then reads: Solve the linear elliptic problem,

$$-\nabla^2 v^k = \lambda^k S(z,\eta^k) + R(z,\eta^k) \tag{2.49}$$

with Dirichlet boundary conditions. All instances of $\hat{U}$ in (2.48 and 2.47) are replaced by $\hat{U}^k$,

which is defined as

$$\hat{U}^k = \frac{U}{c^k}. \tag{2.50}$$

c^k is defined from λ^k according to (2.36). Then define

$$\lambda^{k+1} = \lambda^k \max\left[0, \frac{A - F(\eta^k) + \int_D \int S(\eta^k)\eta^k dx dz}{\int_D \int S(\eta^k) v^k dx dz}\right] \tag{2.51}$$

and finally set

$$\eta^{k+1} = \frac{\lambda^{k+1}}{\lambda^k} v^k. \tag{2.52}$$

As the algorithm is quite complicated it seems prudent to highlight several points. First, the iteration over $\hat{U}^k$, which allows us to fix the magnitude of the background current, is new (TEW do not include a background current, and Wang does not fix the magnitude of the background current). In the work of Wang ([65]) the magnitude of the background current is allowed to change in order to, in the opinion of the present author, facilitate formal convergence proofs of the algorithm. Second, the step (2.51) is equivalent to the Kuhn-Tucker conditions of optimization theory (these can be thought of as an analogue of the method of steepest descent). It was derived in a more complicated form by TEW without the Boussinesq approximation. In this case it is actually possible to have $\lambda^{k+1} = 0$ since the expression for η^{k+1} has several terms. For the present case we have not found any cases where $\lambda^{k+1} = 0$. We should note that both the work of TEW and Wang on the convergence of the algorithm uses a notation that precludes a simple interpretation of the various steps of the algorithm.

In practice the method is simple to implement as each iteration requires the solution of a linear Helmholtz problem with Dirichlet boundary conditions. Note that since we fix A in (2.45) we do not specify the wave amplitude a *priori*. It should be noted that while the above algorithm is a simple generalization of the algorithm in TEW to the case of a wave superimposed on a background current, the convergence proofs as written in TEW or Wang do not apply to the above. The results were tested by computing a candidate solitary wave using the above method, then using this wave as an initial condition in a time stepping model of the full Euler equations to make sure that the numerical implementation of the algorithm was correct.

2.3 Conjugate Flows

The behaviour of ISWs as the value of A in (2.45) is increased can be classified under two different scenarios. The first is the one predicted by first-order WNL and has been discussed in that section. Briefly, as A increases the waves grow thinner and taller until they break (horizontal velocity equals wave propagation speed somewhere in the wave). In the second scenario, as A increases from 0, the ISWs initially grow thinner and taller, but after a certain point begin to broaden out and their amplitude tends to a limiting value. For large enough values of A the waves are flat in the middle. As an aside, note that higher order WNL which takes into account a cubic nonlinearity (and leads to the mKdV equation) predicts waves with a flat middle region ([22]). Indeed if we consider a frame moving with the wave and fix the origin to lie at the mid-point of the upstream transition region of a rightward traveling wave, then as we let $A \longrightarrow \infty$ the long, flat-centered wave tends to a dissipation-less bore, or a smooth, monotonic transition between two regions of flow in the horizontal direction only. The type of scenario encountered depends on the choice of the background stratification.

The algorithm of the previous section allows us to compute flat-centered waves, however we could ask (ignoring the shape of the transition region) if it is possible, given the background density and velocity profile in the upstream region, to compute the density and velocity profiles in the downstream region. The downstream region is referred to as conjugate to the upstream flow, or just the conjugate flow. The concept was introduced by Benjamin ([4]). In particular we would expect the computation of the conjugate flow to have a simpler form than the algorithm of the previous section since the flow is one-dimensional.

The problem with no background flow has been discussed in detail by Lamb and Wan ([37]) and the governing equation with a background flow is quoted in ([36]). In ([37]) the role of the Boussinesq approximation is discussed. We make the Boussinesq approximation in all subsequent calculations. Consider a frame moving with the wave (at the presently unknown wave speed c). The background upstream state is then given by

$$(u, w, \rho, p) = (U(z) - c, 0, \bar{\rho}(z), \bar{p}(z)) \tag{2.53}$$

and the downstream state by

$$(u, w, \rho, p) = (U_p(z) - c, 0, \bar{\rho}_p(z), \bar{p}_p(z)). \tag{2.54}$$

Next, define $\eta(z)$ to be a given isopycnal's displacement from its upstream height. In other words the upstream height of an isopycnal passing through z in the conjugate flow is given by $z - \eta$.

We assume that all streamlines connect to plus and minus infinity. This immediately yields, from the definition of η, that

$$\bar{\rho}_p(z) = \bar{\rho}(z - \eta). \tag{2.55}$$

If we consider two streamlines passing through z and $z + \Delta z$, respectively, conservation of volume between the two streamlines yields

$$\Delta z(U_p(z) - c) = (U(z - \eta) - c)[\Delta z - (\eta(z + \Delta z) - \eta(z))]. \tag{2.56}$$

We can solve this relation for $U_p(z)$ and hence in the continuous limit $\Delta z \longrightarrow 0$ get

$$U_p(z) = U(z - \eta)[1 - \eta_z] + c\eta_z. \tag{2.57}$$

For the case of no background current the above simplifies to

$$U_p(z) = c\eta_z. \tag{2.58}$$

Since the flow is steady and inviscid we can apply Bernoulli's Theorem along a streamline. This yields

$$\begin{aligned} \frac{1}{2}\rho_0(U(z - \eta) - c)^2 + \bar{p}(z - \eta) + \bar{\rho}(z - \eta)g(z - \eta) \quad &= \\ \frac{1}{2}\rho_0(U_p(z) - c)^2 + \bar{p}_p(z) + \bar{\rho}_p(z)gz. & \end{aligned}$$

However noting that

$$(U_p(z) - c)^2 = (U(z - \eta) - c)^2(1 - \eta_z)^2. \tag{2.59}$$

we can eliminate the term involving the unknown function U_p in favour of a term involving the known function $U(z)$. What is more, since we have assumed no vertical motion, both upstream and downstream states are in hydrostatic equilibrium. Hence on using (2.55), we get

$$\frac{d\bar{p}_p}{dz} = -g\bar{\rho}(z - \eta) \tag{2.60}$$

downstream. This means that if we differentiate (2.59) with respect to z we can hope to get an expression involving only c, η and the upstream density and velocity, both of which are known. Some simple, though tedious, algebraic manipulation yields

$$\eta_{zz} + \frac{(2 - \eta_z)\eta_z U'(z - \eta)}{c - U(z - \eta)} + \frac{N^2(z - \eta)}{(c - U(z - \eta))^2}\eta = 0. \tag{2.61}$$

The above can be obtained from equation (2.32) by assuming that η has no x dependence. In the above we employ the standard definition of the buoyancy frequency,

$$N^2(z) = g\frac{d\bar{\rho}(z)}{dz}.$$

This means that

$$N^2(z - \eta) = -g\bar{\rho}'(z - \eta).$$

Since we consider a flat bottom and a rigid lid we must impose the following boundary conditions

$$\begin{aligned} \eta(0) &= 0, \\ \eta(H) &= 0. \end{aligned} \tag{2.62}$$

The eigenvalue problem (2.61) can be easily solved by a shooting method. $\eta(0)$ is fixed to equal 0. $\eta_z(0)$ is chosen and c is varied to ensure $\eta(H) = 0$. In general each choice of $\eta_z(0)$

will yield at least one mode-1 solution. Note however that the eigenvalue problem is nonlinear, hence may yield more than one solution for a given choice of $\eta_z(0)$. What is more, unlike a linear eigenvalue problem, varying $\eta_z(0)$ may change the solution (as opposed to merely scaling it like in the linear case). The correct choice of $\eta_z(0)$ is determined by an auxiliary condition which reflects the conservation of total horizontal momentum flux, i.e.

$$\int_0^H (\tilde{p}(z) + \rho_0(U(z) - c)^2)dz = \int_0^H (\tilde{p}_p(z) + \rho_0(U_p(z) - c)^2)dz. \tag{2.63}$$

With some manipulation the auxiliary condition can be simplified to read

$$\int_0^H \rho_0(c - U(z - \eta(z)))^2\eta_z^3 dz = 0. \tag{2.64}$$

A conjugate flow is thus a solution of (2.61) subject to the boundary conditions (2.62) and with $\eta_z(0)$ chosen to satisfy (2.64). Finally we must make sure that the assumption of all streamlines extending to plus and minus infinity is not violated. A streamline found at z downstream of the wave is found at $z - \eta(z)$ upstream of the wave. We thus require $z - \eta(z)$ to be an increasing function of z. This means that

$$\eta_z(z) < 1 \tag{2.65}$$

for valid conjugate flows.

2.3.1 Two-layer flow with constant vorticity

Following the work of Lamb ([36]) on three layer fluids with piece-wise constant currents we aim to use the simple case of a two-layer stratification with a linear background current (constant vorticity) to derive some qualitative results regarding conjugate flows.

Consider a two-layer fluid with densities, ρ_2 and ρ_1 for the upper (lighter) and lower (heavier) layer as shown in figure 2.2. Without loss of generality we assume the wavefront is rightward propagating. Let the total water depth be given by H and far upstream set the lower layer thickness to equal H_1. This means that the upper layer has an upstream thickness $H - H_1$, which we label H_2. Further assume that in a frame moving with the disturbance (with velocity c) far upstream there is a background current given by

$$U(z) = \xi z - c \tag{2.66}$$

where ξ is a shear strength parameter. The problem we wish to solve is to determine the non-zero downstream lower layer thickness which we label $H_1 + \eta$ and the associated disturbance propagation speed c and downstream velocity $u'(z)$.

We begin by noting that within each layer the density is constant and hence vorticity (or u_z for parallel flow) is conserved. This means

$$u'(z) = U_i + \xi z - c \tag{2.67}$$

where $i = 1, 2$ depending on which layer we are considering. Next impose conservation of volume flux in each layer, i.e.

$$\begin{aligned} \int_{H_1}^{H} (\xi z - c)\, dz &= \int_{H_1+\eta}^{H} (U_2 + \xi z - c)\, dz \\ \int_{0}^{H_1} (\xi z - c)\, dz &= \int_{0}^{H_1+\eta} (U_1 + \xi z - c) \end{aligned} \tag{2.68}$$

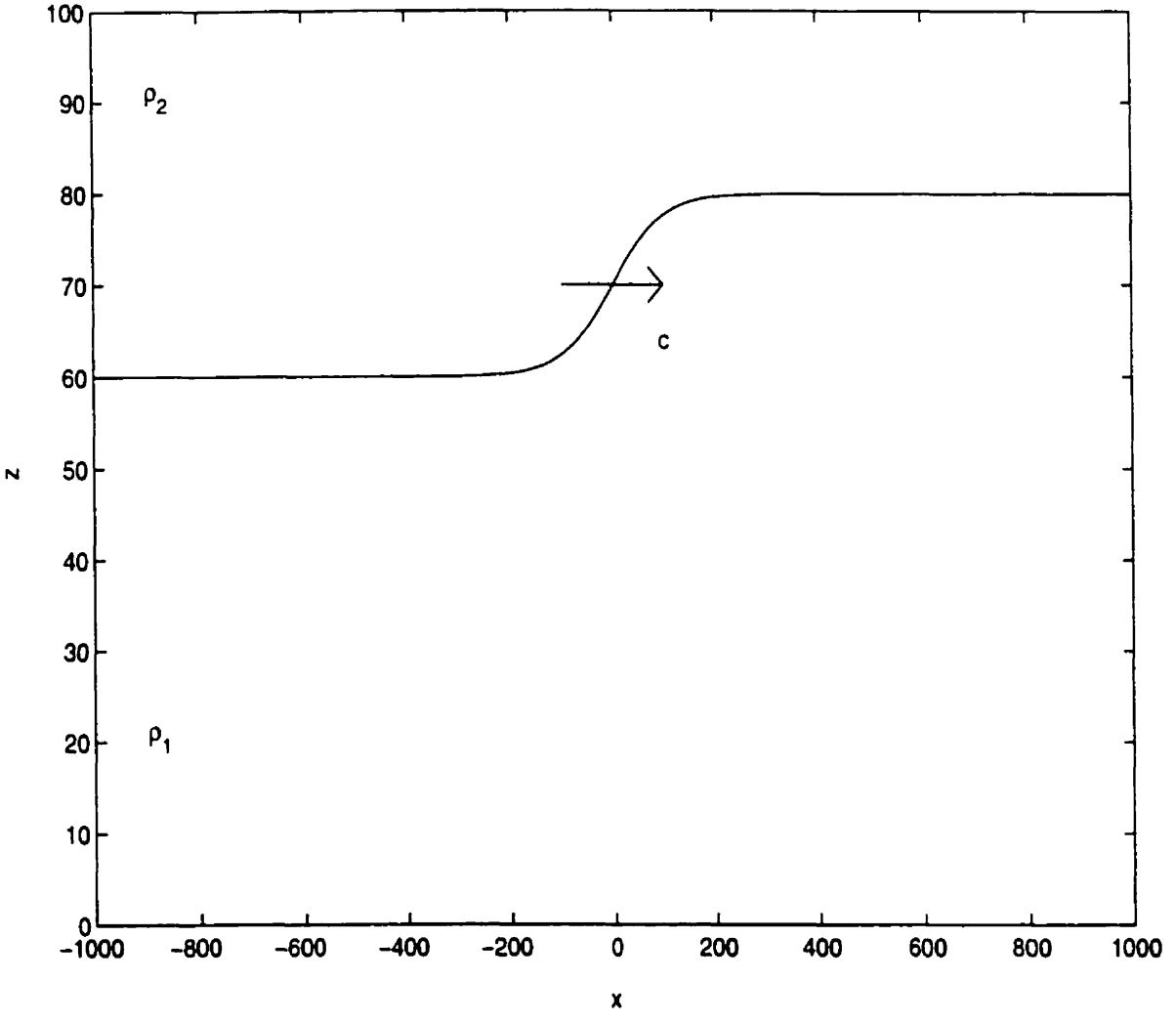

Figure 2.2: Definition sketch for conjugate flow in a two-layer fluid.

These equations readily yield expressions for U_1 and U_2:

$$U_1 = -\frac{c\eta - \frac{\xi}{2}\eta(2H_1 + \eta)}{H_1 + \eta} \tag{2.69}$$

$$U_2 = \frac{c\eta - \frac{\xi}{2}\eta(2H_1 + \eta)}{H - H_1 - \eta} \tag{2.70}$$

Next we wish to utilize Bernoulli's Theorem along two different streamlines to derive two expressions for $p'(0)$. Equating these two expressions will give us one of two equations for η and c needed to get a closed system of equations. First consider the streamline along the surface. Upstream we set the surface pressure to equal zero, but downstream of the disturbance there may be a change in pressure which we will label p_H. Bernoulli's theorem under the Boussinesq approximation with the reference density labeled ρ_0 then yields

$$\frac{1}{2}\rho_0(\xi H - c)^2 + \rho_2 g H = \frac{1}{2}\rho_0 (U_2 + \xi H - c)^2 + p_H + \rho_2 g H. \tag{2.71}$$

This can be solved for p_H to read

$$p_H = -\frac{1}{2}\rho_0 U_2 (U_2 + 2(\xi H - c)). \tag{2.72}$$

In order to apply Bernoulli's theorem along the streamline which follows the bottom we need to write down the hydrostatic pressure distribution upstream ($\bar{p}(z)$) and downstream ($p'(z)$). The upstream distribution has a simpler form due to the simpler expression for the layer thicknesses:

$$\bar{p}(z) = \begin{cases} \rho_2 g(H - z) & H_1 < z < H \\ \rho_1 g(H_1 - z) + \rho_2 g(H - H_1) & 0 < z < H_1 \end{cases}, \tag{2.73}$$

$$p'(z) = p_H + \begin{cases} \rho_2 g(H - z) & H_1 + \eta < z < H \\ \rho_1 g(H_1 + \eta - z) + \rho_2 g(H - H_1 - \eta) & 0 < z < H_1 \end{cases} \tag{2.74}$$

Thus at the bottom ($z = 0$) we have

$$\begin{aligned} p^s(0) &= p_H + \rho_1 g\,(H_1 + \eta) + \rho_2 g\,(H - H_1 - \eta) \\ \bar{p}(0) &= \rho_1 g H_1 + \rho_2 g\,(H - H_1) \end{aligned}$$

or if we define the density difference via

$$\Delta\rho = \rho_1 - \rho_2 \tag{2.75}$$

the simpler

$$\begin{aligned} p^s(0) &= p_H + \rho_2 g H + \Delta\rho g(H_1 + \eta) \\ \bar{p}(0) &= \rho_2 g H + \Delta\rho g H_1 \end{aligned} \tag{2.76}$$

With these definitions we can write down Bernoulli's Theorem along the bottom

$$\frac{1}{2}\rho_0(-c)^2 + \rho_2 g H + \Delta\rho g H_1 = \frac{1}{2}\rho_0(U_1 - c)^2 + p_H + \rho_2 g H + \Delta\rho g(H_1 + \eta). \tag{2.77}$$

Upon substituting for p_H and simplifying this yields the single equation

$$0 = \frac{1}{2}\rho_0\,(U_1(U_1 - 2c) - U_2(U_2 - 2c) - 2U_2\xi H) + \Delta\rho g\eta. \tag{2.78}$$

Note that both U_1 and U_2 are known from (2.69, 2.70) as functions of η and c. To get a second equation and close the system we must consider the conservation of momentum flux

$$\int_0^H (\rho_0 u^2 + p)\,dz = \text{constant}. \tag{2.79}$$

Upstream we get

$$M_{up} = \int_0^H \left[\rho_0\,(\xi z - c)^2 + \bar{p}(z)\right] dz \tag{2.80}$$

$$= \rho_0 \left(\frac{\xi}{3} H^3 - \xi c H^2 + c^2 H \right) + \frac{1}{2} \rho_1 g H_1^2 + \frac{1}{2} \rho_1 g (H^2 - H_1^2)$$

where the latter results from significant algebraic simplification. Downstream the expressions are even messier:

$$\begin{aligned} M_{down} &= \int_0^{H_1+\eta} \left[\rho_0 (U_1 + \xi z - c)^2 + p^s(z) \right] dz \\ &\quad + \int_{H_1+\eta}^{H} \left[\rho_0 (U_1 + \xi z - c)^2 + p^s(z) \right] dz \\ &= \frac{1}{2} \rho_1 g (H_1 + \eta)^2 + \frac{1}{2} \rho_1 g (H^2 - (H_1 + \eta)^2) + p_H H \\ &\quad + \rho_0 Q \end{aligned} \tag{2.81}$$

where

$$\begin{aligned} Q &= (U_1 - c)^2 (H_1 + \eta) + (U_2 - c)^2 (H - H_1 - \eta) + \\ &\quad \xi \left[(U_1 - c)(H_1 + \eta)^2 + (U_2 - c)(H^2 - (H_1 + \eta)^2) \right] + \\ &\quad \frac{\xi^2}{3} \left[(H_1 + \eta)^3 + (H^3 - (H_1 + \eta)^3) \right]. \end{aligned} \tag{2.82}$$

The second algebraic equation results from equating the expressions for the upstream and downstream momentum flux, i.e.

$$M_{up} = M_{down}. \tag{2.83}$$

2.3.2 Numerical Solution

We have not found it possible to solve (2.78) and (2.83) for η and c analytically (for piece-wise constant currents Lamb [36] was able to find an analytical solution). However it is easy to solve the two nonlinear algebraic equations numerically by Newton's method. First we can rewrite (2.78) and (2.83) in the form

$$\begin{pmatrix} F_1(\eta, c) \\ F_2(\eta, c) \end{pmatrix} = \begin{pmatrix} 0 \\ 0 \end{pmatrix}. \tag{2.84}$$

Next we choose an initial guess (η^0, c^0) and update according to the rule

$$\begin{pmatrix} \eta^{k+1} \\ c^{k+1} \end{pmatrix} = -(\mathbf{J}(\eta^k, c^k))^{-1} \begin{pmatrix} F_1(\eta^k, c^k) \\ F_2(\eta^k, c^k) \end{pmatrix} \tag{2.85}$$

where $\mathbf{J}$ is the Jacobian matrix.

In practice $\mathbf{J}$ is evaluated numerically (with adaptive refinement if the algorithm breaks down). The analytical solution given by Lamb [36] for the case of no background current is used as an initial guess. Next ξ is increased or decreased, Newton's method used to get an approximate solution at this value of ξ, and the process is repeated until the solution for the desired value of ξ is reached. The algorithm is easy to implement, very fast to execute, and provides a quick and easy way to get a qualitative idea of how the presence of a background current affects limiting ISW amplitudes. As an example consider $H = 100$ m and the stratification given by

$$\rho(z) = 1 - 0.01 \tanh\left(\frac{z - z_0}{d}\right).$$

As d gets smaller this stratification approaches the two layer limit.

In figures 2.3 and 2.4 we present numerical results for conjugate flow amplitude and propagation speed using the continuous and two-layer equations for two values of z_0. The results are presented as functions of the constant background vorticity

$$\xi = U'(z).$$

as given by equation (2.66). It can be seen that the two-layer technique is quantitatively accurate when the pycnocline has $\frac{d}{H} = 0.005$, not as accurate when $\frac{d}{H} = 0.05$, and qualitatively accurate in general. The isopycnal displacement and propagation speed decrease as ξ grows more negative for all stratifications shown in the figures. This variation of conjugate flow amplitude and propagation speed with background current will be discussed in more detail in the following chapter.

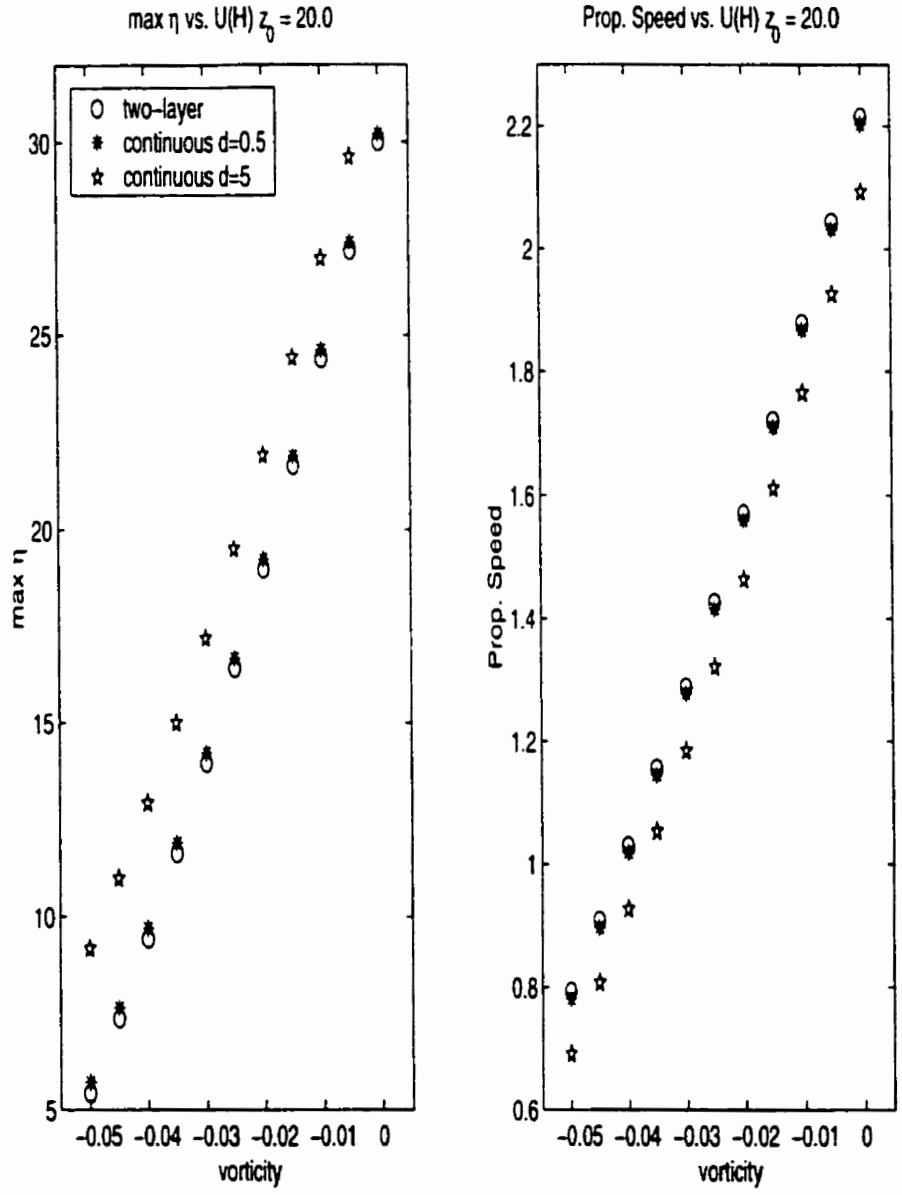

Figure 2.3: Conjugate flow maximum isopycnal displacement (left panel) and propagation speed (right panel) as a function of the constant background vorticity ξ for linear background velocity profile. $H = 100$. two-layer with interface at $z_0 = 20.0$ (circle), continuous hyperbolic tangent density profile with $(z_0, d) = (20.0, 0.5)$ (star), $(z_0, d) = (20.0, 5.0)$ (pentagram).

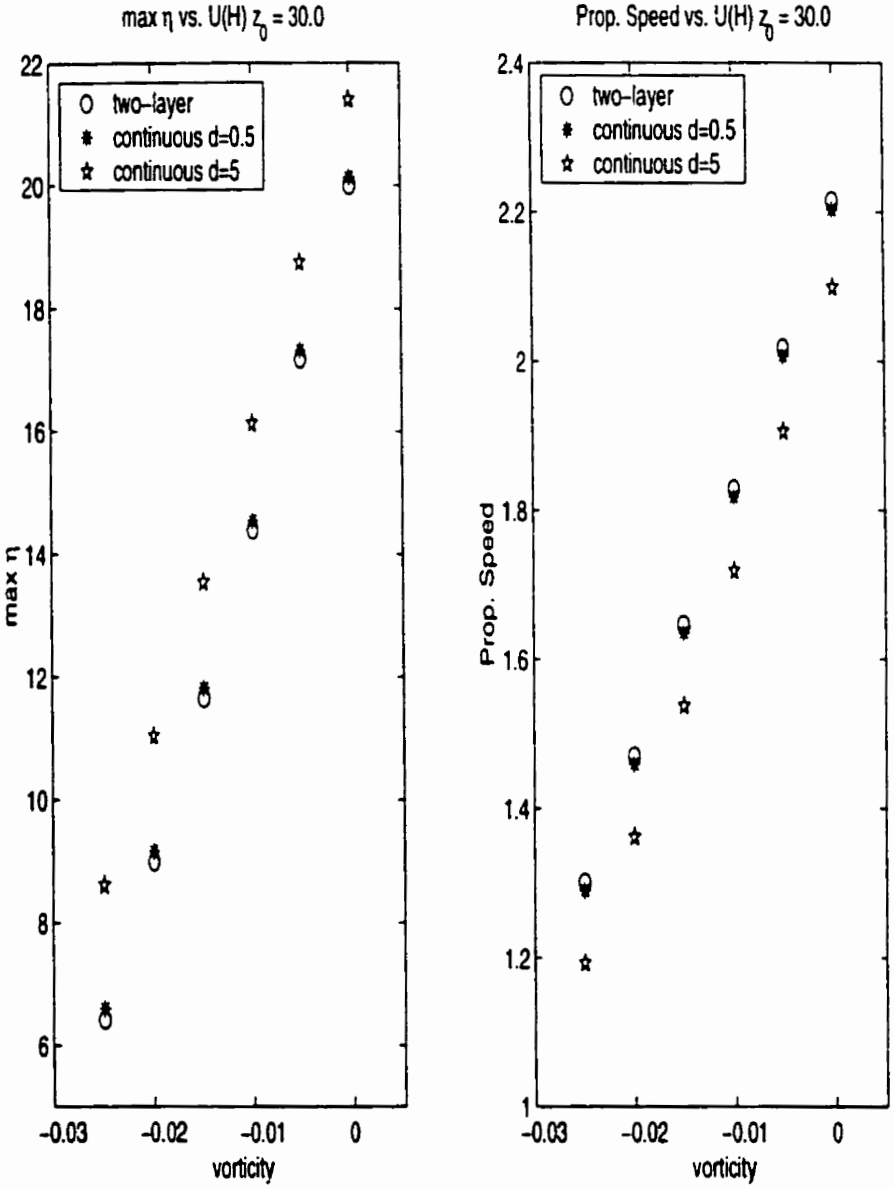

Figure 2.4: Conjugate flow maximum isopycnal displacement (left panel) and propagation speed (right panel) as a function of the constant background vorticity ξ for linear background velocity profile. two-layer with interface at $z_0 = 30.0$ (circle), continuous hyperbolic tangent density profile with $(z_0, d) = (30.0, 0.5)$ (star). $(z_0, d) = (30.0, 5.0)$ (pentagram).

2.4 Numerical Model

In this section we briefly discuss the numerical model used for all time-dependent simulations in this thesis. The model was developed by Lamb and is discussed in several of his articles ([30], [31], [33]). We follow the presentation in ([31]). In its original form the model solves the Euler equations (i.e. equations (1.1) with $\mu = 0$ and $\kappa = 0$) on a domain bounded by the topography at $z = h(x) < H$ and the rigid lid at $z = H$, where H is the total depth. The model is based on a second-order projection method.

The time stepping proceeds in the following manner: First ρ is updated via

$$\frac{\rho^{n+1} - \rho^n}{dt} = -(\vec{u} \cdot \vec{\nabla}\rho)^{n+\frac{1}{2}}. \tag{2.86}$$

Next the vector $\vec{V}$ is computed according to

$$\vec{V} = -(\vec{u} \cdot \vec{\nabla}\vec{u})^{n+\frac{1}{2}} - \frac{\rho^{n+1} + \rho^n}{2} g\hat{k}. \tag{2.87}$$

Finally the velocity field $\vec{u}$ and the pressure gradient $\vec{\nabla}P$ are updated via

$$\frac{\vec{u}^{n+1} - \vec{u}^n}{dt} = \mathcal{P}(\vec{V}), \tag{2.88}$$

$$\vec{\nabla}P^{n+\frac{1}{2}} = (I - \mathcal{P})(\vec{V}) \tag{2.89}$$

where I is the identity operator and $\mathcal{P}$ is the projection operator of a vector onto its divergence free part.

The time step is variable. It is restricted by calculating the Courant-Friedrichs-Lewy condition, which states that a fluid particle cannot travel the length of a grid cell in one time step, and then applying a safety factor smaller than 1. Quantities at the $n + \frac{1}{2}$ time step are calculated by an upwind extrapolation (see [31] and references therein for details of the method used).

The computational grid allows the specification of bottom topography. The governing equations are transformed to terrain following coordinates, and hence are solved in a slightly more complicated form than (1.1). The transformation allows grid refinement for regions of interest

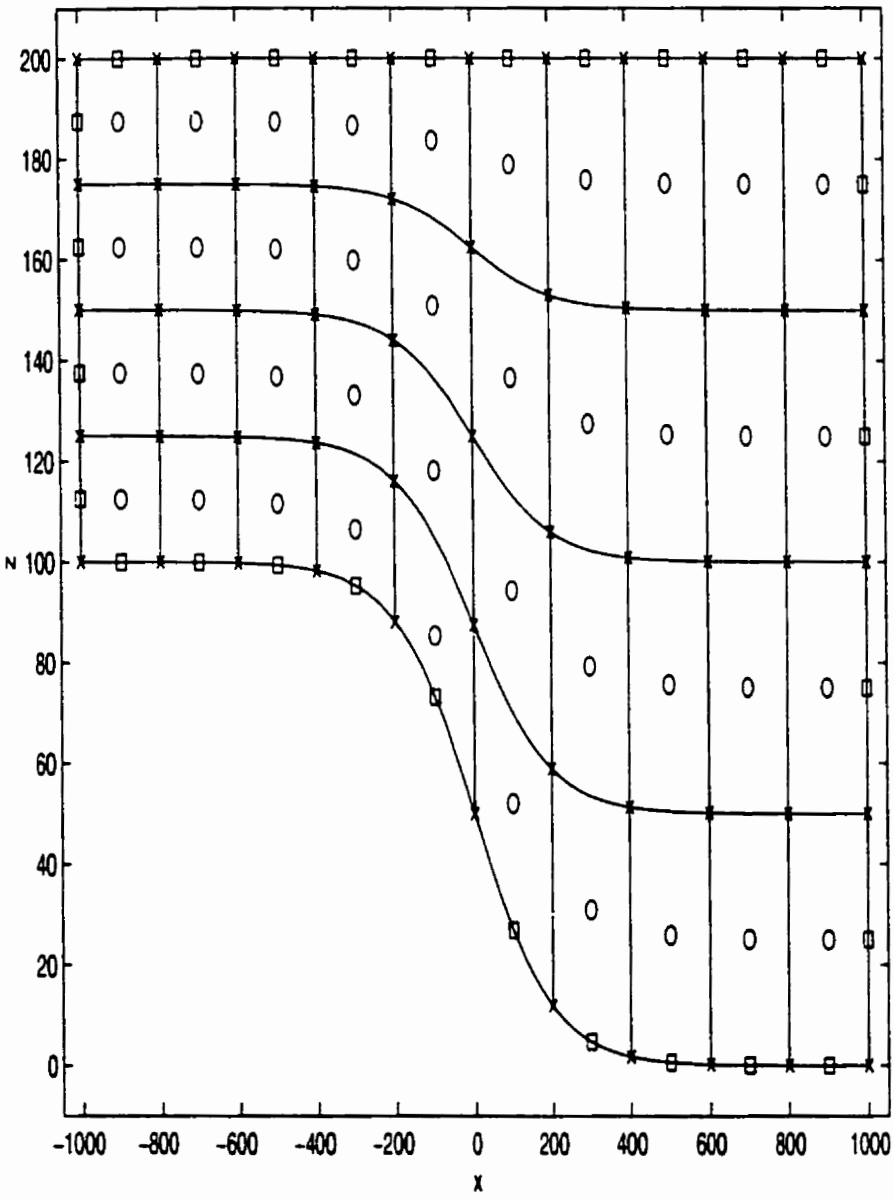

Figure 2.5: Schematic of the computational grid showing the interior (circles) and boundary (squares) vector grid points as well as the scalar grid points (crosses).

(for example near the bottom). The values of $\vec{u}$, ρ, and $\vec{\nabla} P$ are given at the cell centers for all interior points, and at the midpoints of cell edges for boundary points. A sample grid (taken from Lamb's paper on tidal simulations [31]) is shown in figure 2.5.

The extension of the numerical method to include diffusion and no-slip bottom boundary conditions was done in part by Lamb and in part by the present author. In its present state, the model allows for variable eddy viscosities and diffusivities, but this option was not utilized in this thesis.

Chapter 3

Steady Wave Results

In the previous chapter we derived a number of tools with which we can discuss large ISWs for a given background density and horizontal current. In this chapter we present results pertaining to steady waves as well as some of the consequences steady wave results can have on the evolution of an initial disturbance.

It is now reasonably well known that WNL does not accurately describe the spatial structure of large waves. We briefly quote from work on this topic by the present author ([59]). Lamb has carried out a higher order study for simpler stratifications ([34]).

We consider the observations of BDR in water 60.0 m deep. The observed density profile consists of a nearly unstratified upper layer 40.0 m thick overlying a linearly stratified layer 20.0 m thick. We follow the work of BDR and model this situation by the density profile

$$\begin{aligned} \rho_0\bar{\rho}(z) &= 1024.735 + C(\ln(\cosh(z-20)) - z) \\ C &= 0.0093. \end{aligned} \tag{3.1}$$

$\bar{\rho}$ is plotted in figure 3.1 along with the buoyancy frequency using $\rho_0 = 1024.8$ kg m^3.

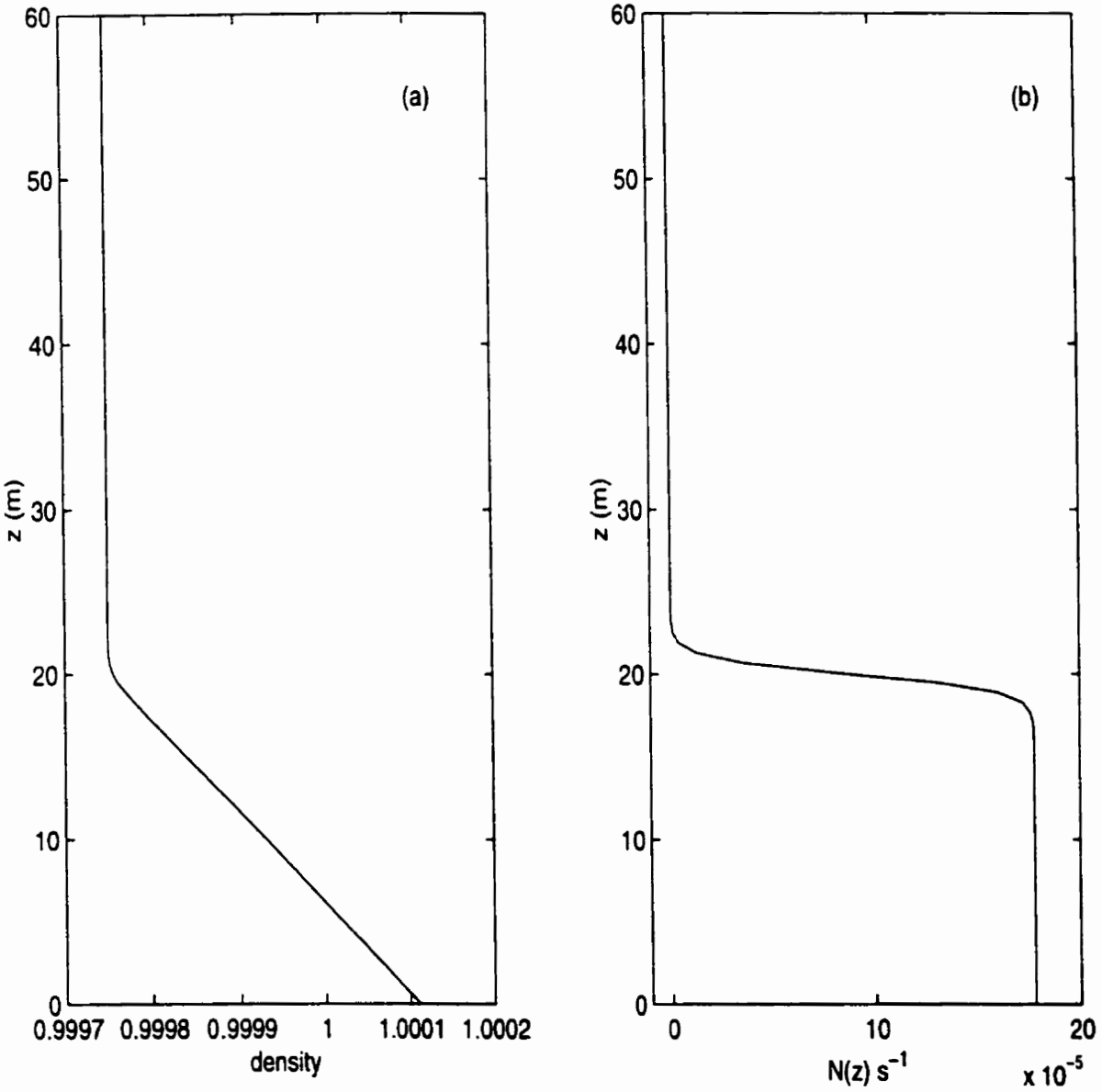

Figure 3.1: Density profiles. (a) Density for BDR density, (b) Buoyancy frequency $N(z)$ for BDR density.

We considered a background current of the form

$$U(z) = 0.1s(\frac{z}{H} - \frac{1}{2}), \tag{3.2}$$

where s specifies the direction of the background current at the surface. We will not go into the details of the study (the interested reader can read [59]). In figures 3.2, and 3.3 we present comparisons between the fully nonlinear and WNL vertical profiles at the wave crest of the isopycnal displacement η and horizontal velocity u, respectively. It is clear from the figures that the WNL fit deteriorates with increasing wave amplitude and hence if a method to calculate fully nonlinear ISWs is available it should be used to study large waves.

The main results section of this chapter focuses on a commonly used family of stratifications (the hyperbolic tangent family) and the effects varying the stratification properties and background current have on various wave properties. Particular attention is paid to large waves and the bounds on wave amplitude.

The next section discusses a few time dependent consequences that can be predicted using the computationally cheaper steady results. As well, one instance of an ISW that cannot be calculated by either WNL, or the variational ISW calculating algorithm, is presented.

The final section summarizes the major findings of the chapter and discusses them in terms of the relevant literature.

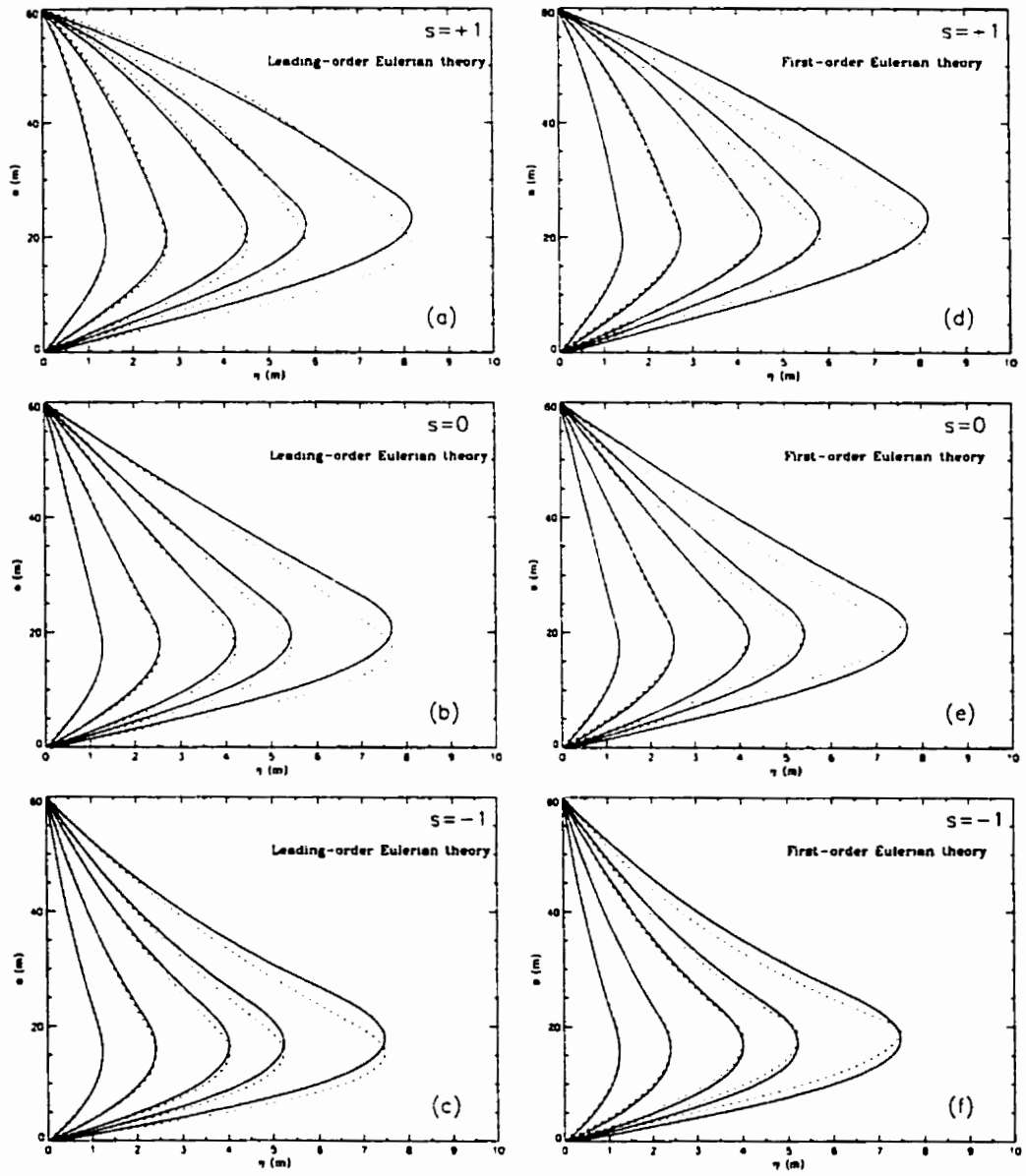

Figure 3.2: Comparison of WNL and fully nonlinear waves for the BDR density profile. Eulerian Theory: η profiles. Fully nonlinear - solid, WNL - dotted. Various s.

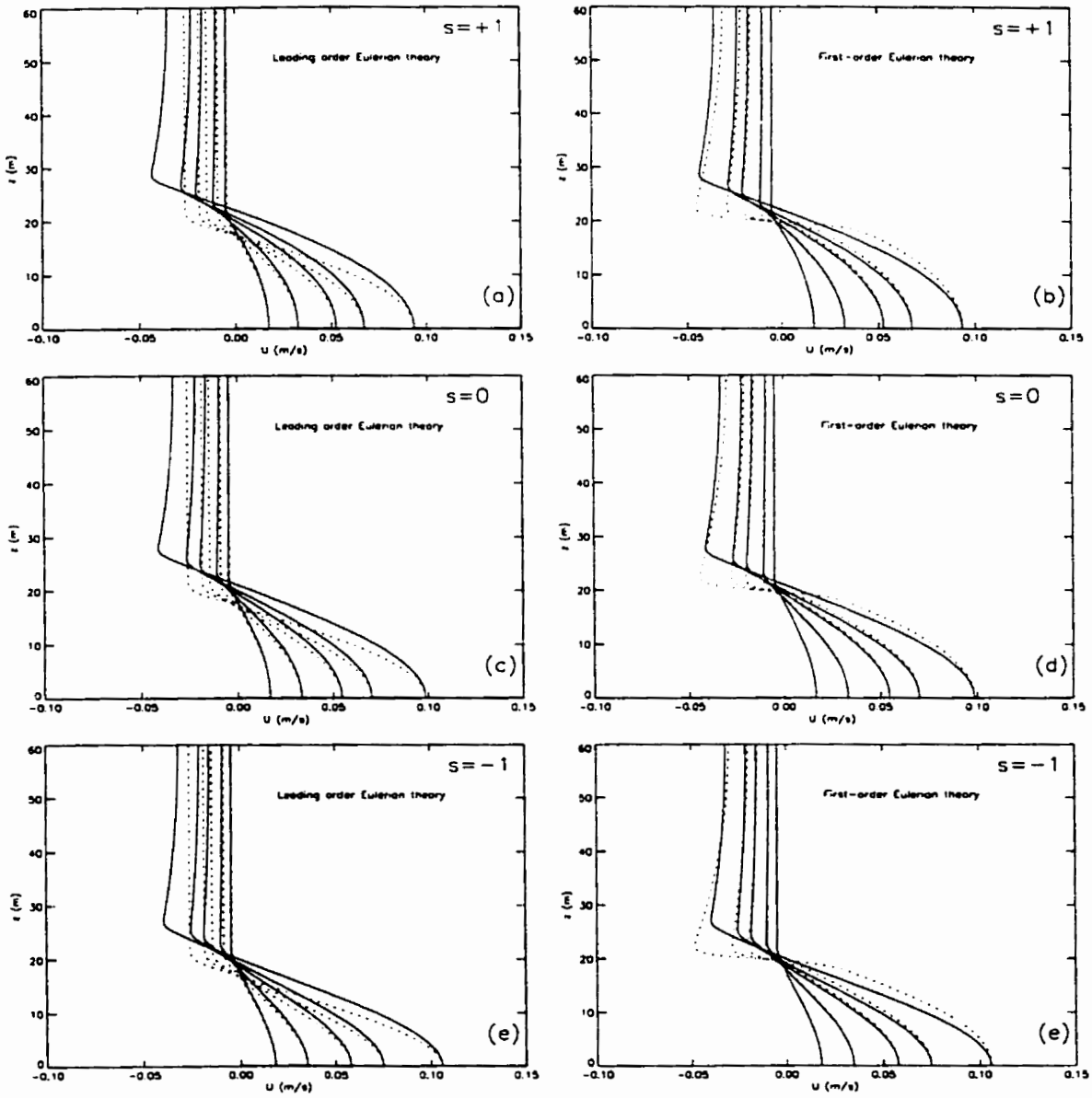

Figure 3.3: Comparison of WNL and fully nonlinear waves for the BDR density profile. Eulerian Theory: horizontal velocity profiles. Fully nonlinear - solid, WNL - dotted. Various s.

3.1 Solitary Waves with Open Streamlines

In the introduction to this chapter we have shown results, using a stratification observed in the field, indicating that WNL does not provide an accurate description of large ISWs. In this section we examine fully nonlinear ISWs for a class of simpler model stratifications with the aim of taking into account the role of a background current. In particular we wish to focus on large ISWs well past the region described successfully by WNL.

3.1.1 Sample Run

To motivate our investigation consider the following numerical simulations of the unsteady Euler equations. The simulations are performed on a computational domain that is 4000 m wide and 100 m deep with a grid spacing of 2 by 1 m in the horizontal and vertical, respectively. We consider an ambient stratification given by

$$\bar{\rho}(z) = 1.0 - 0.01 \tanh\left(\frac{z - 20.0}{5.0}\right) \tag{3.3}$$

and a background current given by

$$U(z) = 3.0\frac{z}{H} \tag{3.4}$$

with $H = 100$ m. The initial density profile is given by

$$\rho(x, z, 0) = \bar{\rho}(z - \eta_i) \tag{3.5}$$

with η_i given by

$$\eta_i = -15.0 \sin(\pi\frac{z}{H}) \left(\tanh(\frac{x - 150}{10}) - \tanh(\frac{x + 150}{10})\right). \tag{3.6}$$

The initial density contours, along with the contours after 600 seconds are presented in figure 3.4 for the case of no background current, and in figure 3.5 using the background current (3.4).

It is clear from these figures that the initially step-like density disturbance breaks up into two

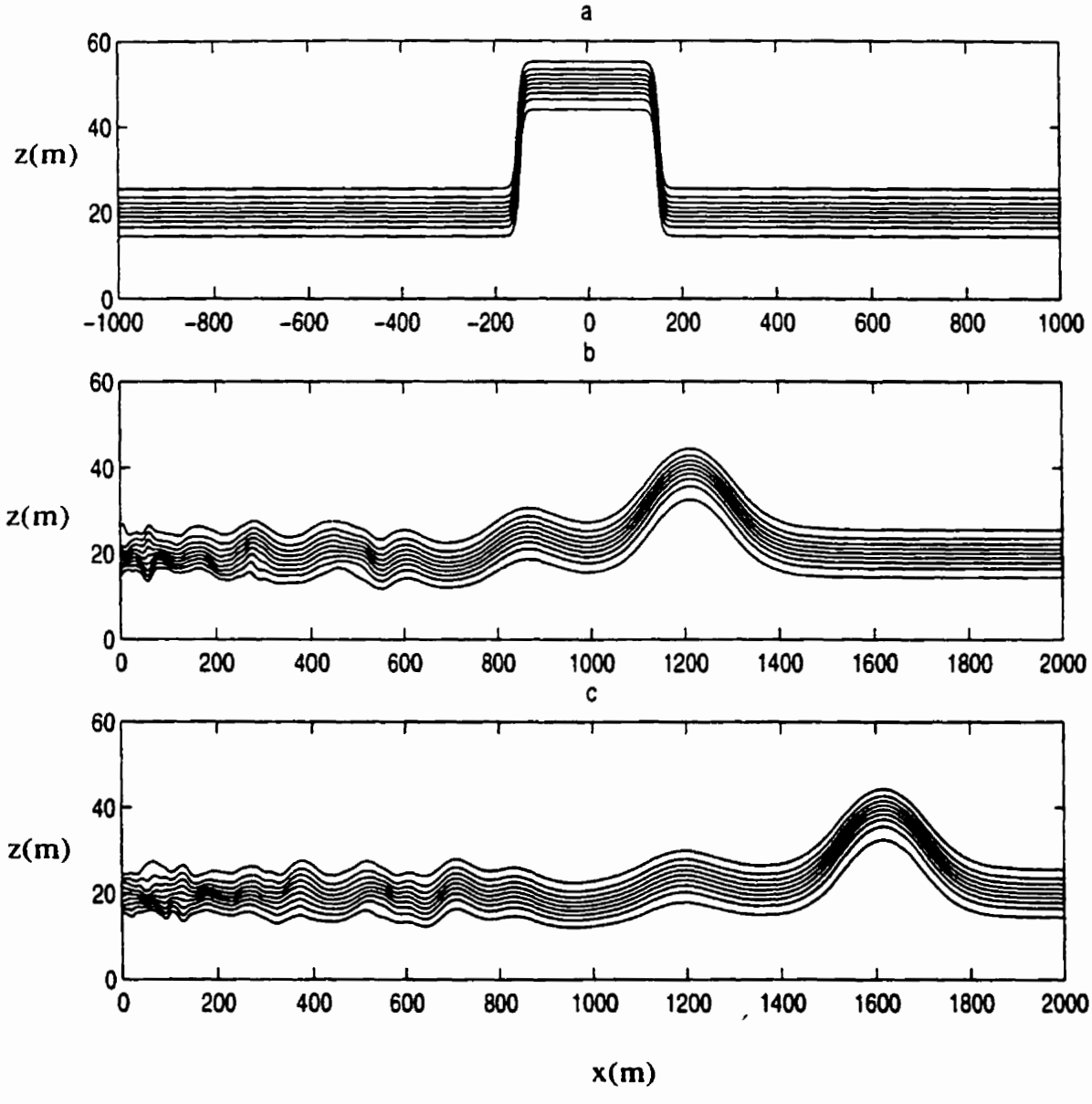

Figure 3.4: Density profiles for sample run with no background current. a) $t = 0$s b) rightward propagating disturbance $t = 600s$ c) rightward propagating disturbance $t = 1000s$. Only bottom 60.0 m of the water column is shown.

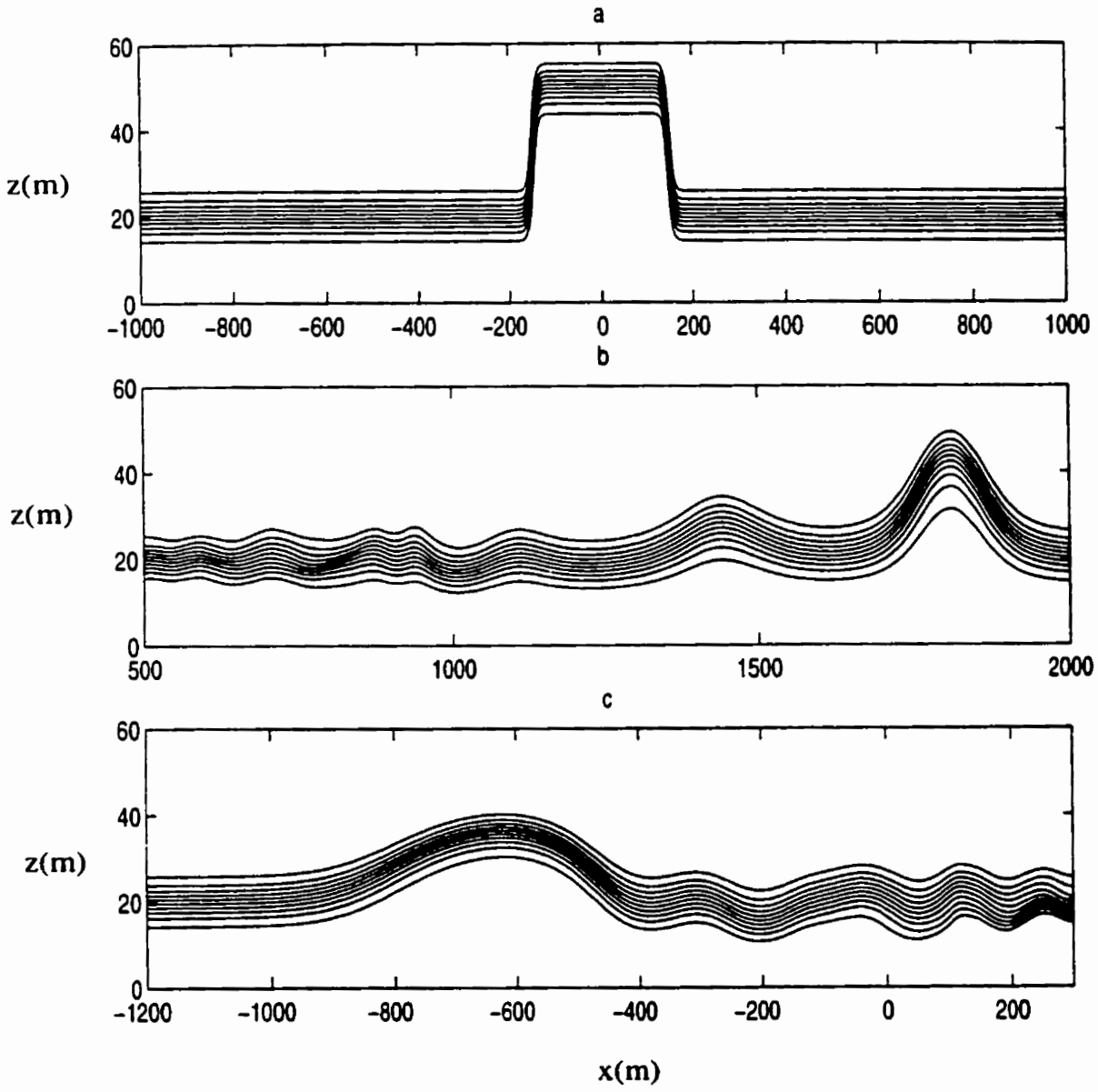

Figure 3.5: Density profiles for sample run with background current. a) $t = 0$s. Only bottom 60.0 m of the water column is shown. b) rightward propagating disturbance $t = 600s$ c) leftward propagating disturbance $t = 600s$

sets of rank-ordered wave trains and some small dispersive waves. However, due to the presence of the background current the rightward and leftward traveling disturbances are not symmetric. It can be seen from figure 3.5 that the leading rightward propagating wave is taller and narrower than the leading leftward propagating wave. Hence, while the evolution with no background current (figure 3.4) is symmetric about $x = 0$, the evolution with a non-constant background current is not. Also from figure 3.5 we can see that all waves are advected rightward. This is due to the fact that the vertically averaged background current is non-zero.

We will return to these sample simulations in the following section.

3.1.2 Methodology

Keeping in mind the qualitative results of figure 3.5 we now examine the effect of a background current on steady ISWs. We use both WNL and fully nonlinear waves, though the former is only used for qualitative ideas (given the results mentioned in the introductory section anything more would be inadvisable).

We consider stratifications of the form

$$\bar{\rho}(z) = 1.0 - 0.01 \tanh\left(\frac{z - z_0}{d}\right). \tag{3.7}$$

The stratification (3.3) is an example of this class of stratification. In the above, z_0 specifies the center while d specifies the thickness of the pycnocline. When there is no background current stratifications with $z_0 > 0.5$ have ISWs of depression, while those with $z_0 < 0.5$ have ISWs of elevation. By varying the parameters we can change the nature of the upper bound on the ISW amplitude. One type of stratification exhibits significant stratification right down to the ocean bottom (or up to the surface) and a second type exhibits a mixed layer adjacent to both the bottom and surface of the ocean. H, the total depth, is set to equal 100 m for all cases considered. We will consider $d = 5.0$ m (thin pycnoclines) and three values for z_0, 10.0, 20.0 and 30.0 m (though results will be presented in dimensionless form, as discussed below). We focus on rightward propagating waves (the exception is in time-stepping runs where both left and

right propagating waves result from the same initial condition). While we will generally consider waves of elevation, under the Boussinesq approximation the results can easily be generalized to situations involving waves of depression providing one transforms the density and background velocity profiles appropriately (more on this later).

Recall that the variational algorithm used to calculate ISWs fixes A, the available potential energy, and not the wave amplitude (maximum isopycnal displacement) or the wave propagation speed. The two types of stratification mentioned above correspond to two different scenarios of ISW behaviour as A is increased from 0. For stratifications with a mixed layer adjacent to the bottom and top boundaries, waves initially become thinner and taller (as predicted by WNL), but when the maximum isopycnal displacement reaches a certain point the waves stop growing in size and begin to broaden out, eventually becoming flat in the middle. For broad enough waves the velocity in the flat, middle part of the wave is horizontal and corresponds to a conjugate flow of the original stratification and background current. As discussed in the previous chapter, conjugate flows are governed by a nonlinear ODE eigenvalue problem and hence are computationally cheaper to calculate than fully nonlinear ISWs. See ([37]) and ([36]) for detailed discussions of conjugate flows. With no background current, wave broadening is generally observed when the mid-point of the pycnocline approaches the mid-depth. As we will show below (and as shown in [36]), including a background current changes this criterion. Note, in certain cases (generally when the pycnocline is well away from the mid-depth) the variational algorithm will fail to compute waves past a certain, generally large amplitude. These large waves are found to have Richardson numbers close to, or even below, 0.25 and hence we believe the variational algorithm fails to converge due to shear instability of any larger waves.

In summary, the wave amplitude is bounded above by one of three possible scenarios. First, the waves may reach the point at which the streamlines are vertical in a frame moving with the wave (i.e. $u_{total} = U(z) + u_{wave-induced} = c$) somewhere in the water column and the waves break. Second, the variational algorithm used to compute the waves may fail to converge to a solution due to shear instability. Third, the waves broaden out and tend to the conjugate flow solution. The size of the largest, non-breaking wave computable will always be identified by its

maximum isopycnal displacement, which will in turn be labeled η_b. Quasi-steady, solitary-like waves past breaking will be the subject of the following chapter. Note that the question of what is the maximum wave amplitude to actually appear in the ocean is a much more difficult question, and will not be pursued in the present work.

We will present the results in non-dimensional form. Towards this we define

$$\begin{aligned}(x, z, d, z_0) &= (\tilde{x}, \tilde{z}, \tilde{d}, \tilde{z}_0)H \\ g' &= g\frac{\max\tilde{\rho} - \min\tilde{\rho}}{\rho_0} \\ c_H &= \sqrt{g'H} \\ (c, U, u, w) &= (\tilde{c}, \tilde{U}, \tilde{u}, \tilde{w})c_H \end{aligned} \tag{3.8}$$

where $\tilde{Q}$ denotes a dimensionless quantity corresponding to a dimensional quantity Q, for all quantities.

We will mostly focus on linear background currents with a maximum velocity at the surface and zero slip velocity at the bottom, (in dimensionless form)

$$\tilde{U}(\tilde{z}) = \xi\tilde{z} \tag{3.9}$$

where ξ is given by

$$\xi = \max(\tilde{U}') \tag{3.10}$$

and specifies the maximum vorticity due to the background current. We will also consider shear layer currents given by (in dimensionless form)

$$\tilde{U}(\tilde{z}) = \xi\tilde{d}_j\left(1 + \tanh\left(\frac{\tilde{z} - \tilde{z}_j}{\tilde{d}_j}\right)\right) \tag{3.11}$$

The parameter $\tilde{z}_j$ specifies the center of the shear layer, while $\tilde{d}_j$ specifies its thickness. Notice that for both (3.9) and (3.11) $\tilde{U}(\tilde{z}) \geq 0$ for all $\tilde{z}$ whenever $\xi \geq 0$.

We will compare currents for fixed values of ξ. This means we will be comparing currents

whose absolute maxima may not match. We will refer to the maximum (minimum when the background current is negative) dimensional current as U^{par}, and will henceforth drop the tildes.

3.1.3 WNL Results

Let us now consider some results from WNL.

In figure 3.6 we plot the dimensionless linear longwave propagation speed c_{lw} (upper panel) and the scaled, dimensionless linear longwave propagation speed c^* (lower panel) versus ξ for the linear background current profile. The scaled, dimensionless propagation speed is defined via

$$c^* = \frac{c_{lw} - U(z_0)}{c_H}. \tag{3.12}$$

This scaling removes some of the linear trend of the c_{lw} vs ξ curves visible in the upper panel of figure 3.6. Also note from the upper panel that for all three values of z_0, c increases with ξ.

From figure 3.6 we can see that there is an upper bound on ξ for which we can compute WNL results. This bound is given by the value at which $U(H)$ and c_{lw} are equal (critical layer forms). From figure 3.6 one can see that the maximum value of ξ for which waves can be found increases as z_0 increases. This increase continues until $z_0 = 0.5$. When $z_0 = 0.5$ first-order WNL predicts no mode one ISWs. When $z_0 > 0.5$ we get ISWs of depression, which correspond (under the Boussinesq approximation) to the waves of elevation produced by a stratification with z_0 reflected about $z = 0.5$. ξ is bounded below due to the change in c_{lw} caused by the depth averaged current. At some point advection by the depth averaged background current will cause c_{lw} to become negative, and again a critical layer to form (i.e. critical layer forms when $c_{lw} = 0$). However, it is impossible to predict where this will occur *a priori*. Since finite amplitude waves have a larger c_{lw} this bound is also dependent on wave amplitude. In practice the variational algorithm fails to converge due to shear instability before the critical layer is reached in all cases tried.

In figures 3.7 and 3.8 we plot λ (a measure of wave width given by 2.12) and the first order WNL coefficients (the dispersive coefficient r_{01} and the nonlinear coefficient r_{10}), respectively, vs ξ. For the calculation of λ we take $b_0 = 1.0$. Both r_{10} and r_{01} are scaled by their counterparts

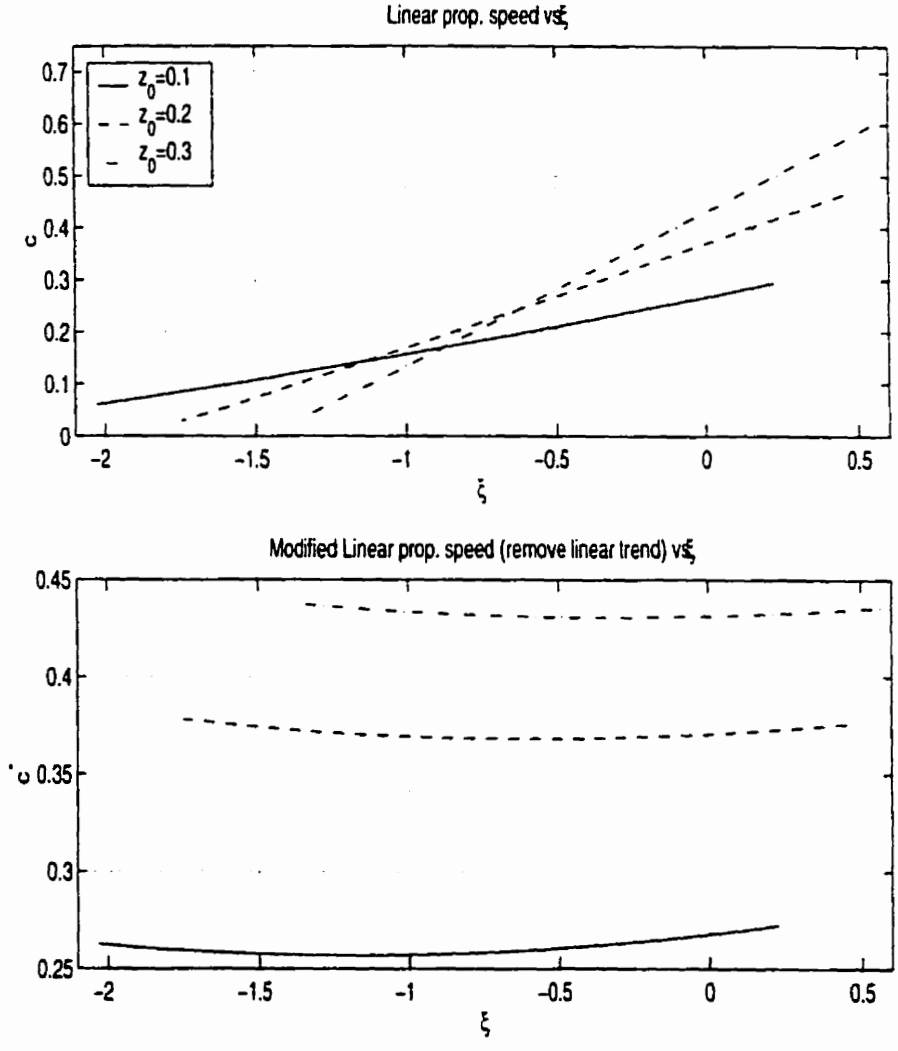

Figure 3.6: Linear longwave propagation speeds vs ξ. a) dimensionless c_{lw} b) scaled, dimensionless c_{lw}.

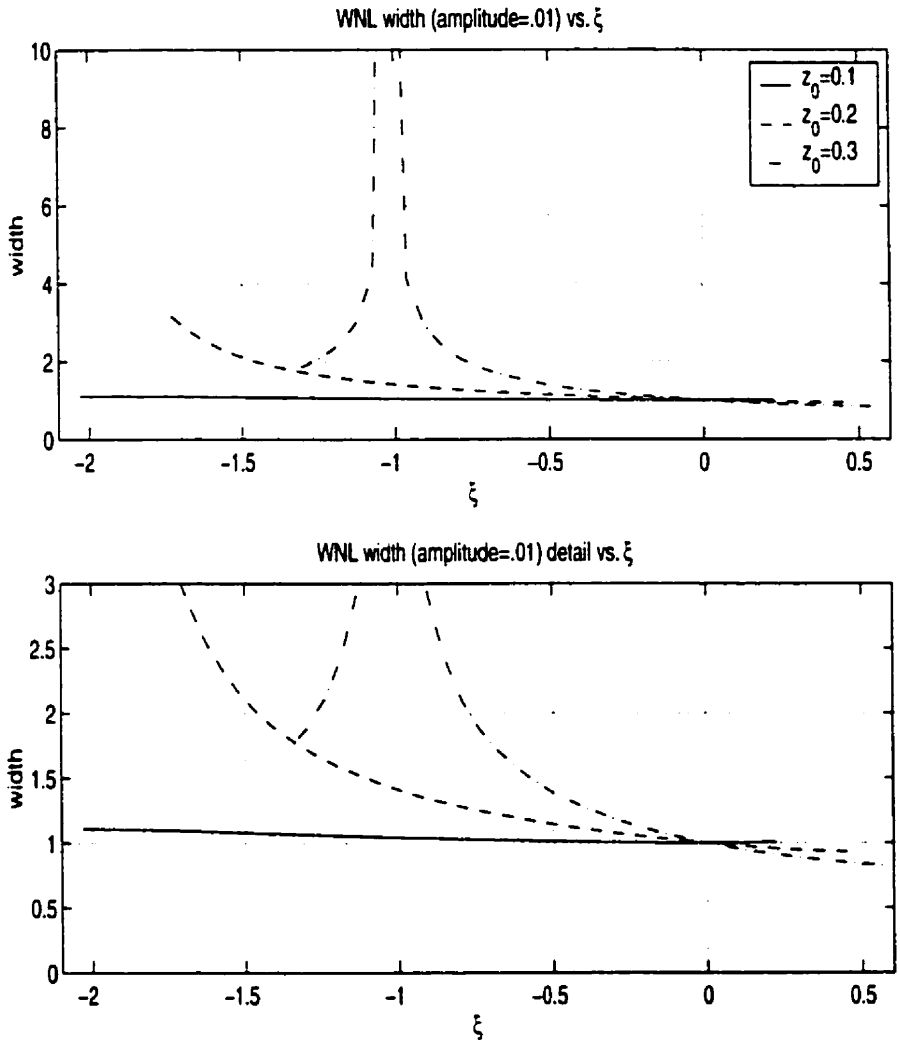

Figure 3.7: WNL width for waves with amplitude set to 1 vs ξ. Lower panel is a detail of the upper panel.

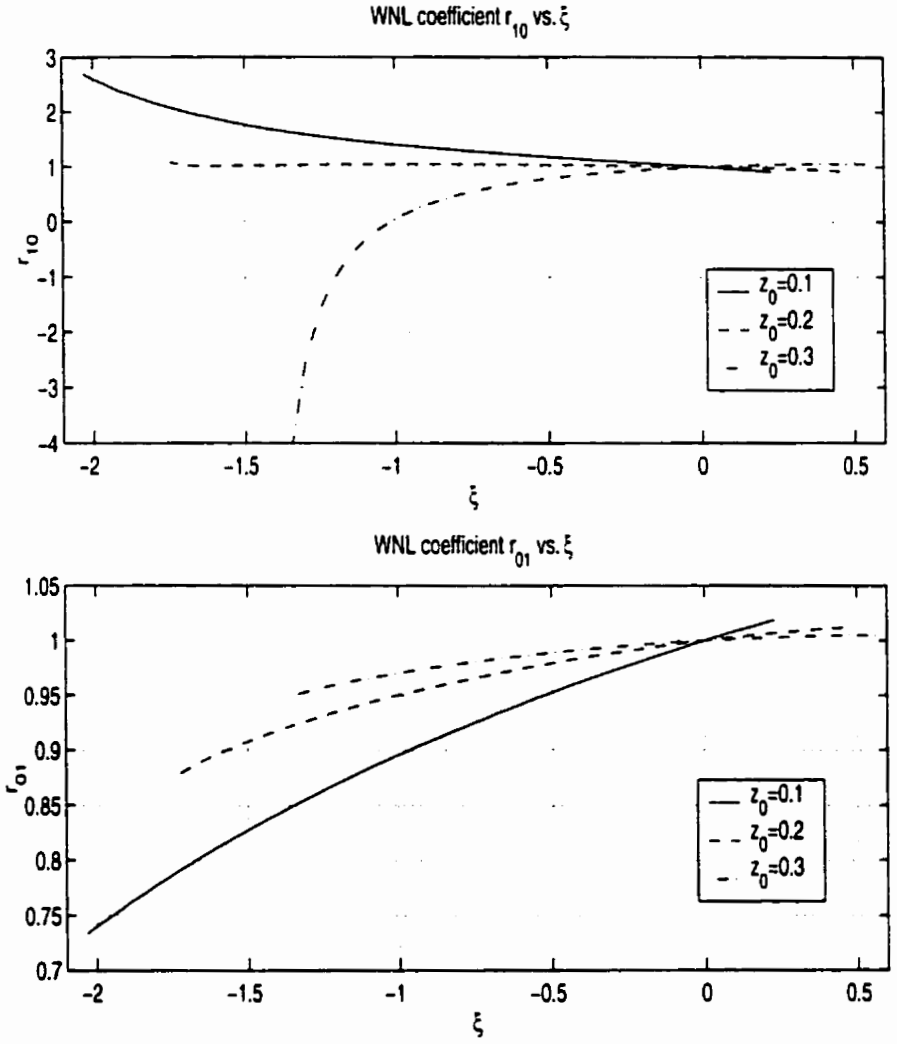

Figure 3.8: WNL parameters vs ξ. Upper panel - nonlinear coefficient r_{10}, Lower panel - dispersive coefficient r_{01}

found when $\xi = 0$ (see Table 3.1.1 for the values at $\xi = 0.0$).

z_0	d	r_{10}	r_{01}
0.1	0.05	-0.055	-241.0
0.2	0.05	-0.027	-504.3
0.3	0.05	-0.014	-738.6

Table 3.3.1 z_0, d, r_{10} and r_{01} for the case of no background current. These values are used to nondimensionalize the first-order coefficients r_{10} and r_{01}.

From figure 3.7 we can see that the width of the waves increases as ξ grows more negative. For the case $z_0 = 0.1$ this variation is small. For $z_0 = 0.2$ we find the wave width more than triples for the most negative value of ξ given. The case $z_0 = 0.3$ is even more extreme with the predicted width appearing to grow unbounded near $\xi = -1.0$ ($U^{par} = -4.0$ in dimensional form). Indeed from (2.12) and figure 3.8 we can see that $r_{10} = 0$ near $\xi = -1.0$ ($U^{par} = -4.0$ in dimensional form) and this gives a singularity in the formula for width. Notice that this means that WNL predicts waves with opposite polarity for the regimes $\xi < -1.0$ and $\xi > -1.0$ for the case $z_0 = 0.3$. In the region around $\xi = -1.0$ where r_{10} is nearly zero the weakly nonlinear theory presented in this thesis breaks down and must be augmented by adding higher order terms (for example a quadratic nonlinearity as in the mKdV equation could be added ([22])). We will return to the reversal of polarity for fully nonlinear ISWs later.

3.1.4 Fully nonlinear results: Bounds of wave amplitude

We now consider fully nonlinear ISWs as calculated by the variational technique discussed in the previous chapter. We wish to investigate several points. First of all we would like to know what the upper bound on isopycnal displacement is for various values of ξ and z_0 (i.e. how η_b changes). This means we also need to determine the nature of the upper bound (conjugate flow, shear instability or wave breaking). Second we would like to investigate the change in the maximum horizontal velocity, propagation speed, and wave half-width as ξ changes. For both of these issues we also investigate the role the geometric shape of the background current plays. Finally we

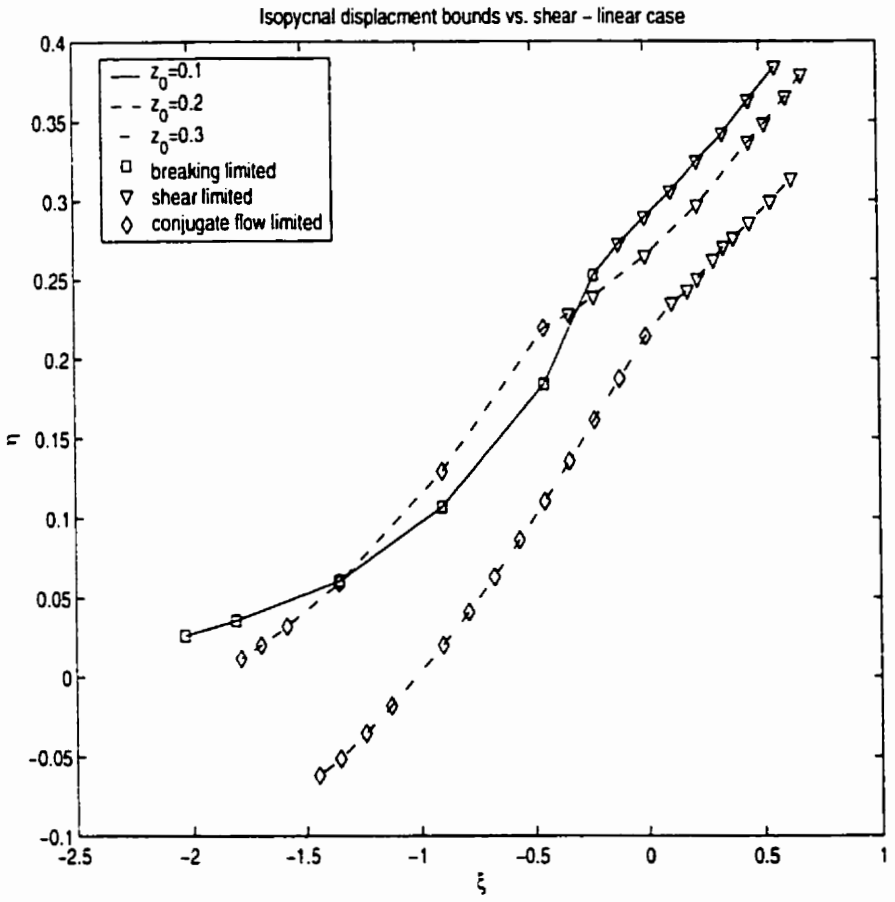

Figure 3.9: Bounds on isopycnal displacements as functions of ξ for linear background currents. All three cases of z_0 are shown

would like to investigate the actual vertical profiles of isopycnal displacement, horizontal velocity and Richardson number at the center of the wave (i.e. the wave crest). The horizontal profiles of the wave induced velocity at the surface will also be discussed.

We begin by showing, in figure 3.9, the upper bounds on isopycnal displacement as it varies with ξ for the linear background velocity profile (3.9). All three values of z_0 used are shown. In this figure, as in all future figures involving the upper bound on isopycnal displacement, we follow the convention that triangles denote upper bound by shear instability, diamonds indicate upper bound by conjugate flow, and squares indicate upper bound by wave breaking. From figure 3.9 we

can note that the $z_0 = 0.1$ case has the largest computable waves when ξ is positive and slightly negative. For positive values of ξ the three cases for differing z_0 behave in a similar manner. All three curves of η_b vs ξ are bounds by shear instability and increase with increasing ξ. The maximum value of ξ used for each of the three values of z_0 is determined by the formation of a critical layer. Since ISWs have a propagation speed that grows with amplitude, and is bounded below by the linear long-wave speed, this value of ξ is larger than that for WNL. In other words for a certain range of ξ values we will only be able to compute ISWs larger than a certain amplitude. Examples of this phenomenon will be presented below.

For negative values of ξ the $z_0 = 0.3$ case is bounded above by the conjugate flow amplitude. The $z_0 = 0.2$ is bounded above by the conjugate flow amplitude when $\xi < -0.5$ and is otherwise bounded above by shear instability. In general it can be said that the $z_0 = 0.2$ and 0.3 curves behave in a similar manner while the $z_0 = 0.1$ curve behaves quite differently. This is due to the fact that only the $z_0 = 0.1$ case exhibits wave breaking and hence does not have a conjugate flow. The amplitude of the conjugate flow that bounds the $z_0 = 0.2$ and 0.3 cases when $\xi < 0$ decreases as ξ becomes more negative. For the $z_0 = 0.3$ case the conjugate flow amplitude becomes negative, and hence ISWs reverse polarity (become waves of depression in this case). The point at which the reversal of polarity occurs corresponds to the point at which r_{10} changes sign. This means that reversal of polarity is successfully predicted by WNL. The possible values of ξ are bounded below by the point at which advection by the background current causes the wave propagation speed to become negative, and hence a critical layer to form. In practice we found that the variational algorithm failed to converge, du to shear instability, before a critical layer formed. Finally notice that for $z_0 = 0.1$ and $\xi < 0$ the curve is rather more concave up than the corresponding curves for the $z_0 = 0.2$ and 0.3 cases. Again this can be attributed to the qualitatively different nature of the upper bound on the wave amplitude.

Next we consider the three cases in detail on their own. In figure 3.10 we show results for the $z_0 = 0.3$ case. The reversal of polarity is now clearly visible, as is the region (small in this case) where there is a minimum amplitude for waves that can be calculated due to critical layer formation. Also included in the figure are actual values for the conjugate flow amplitude for

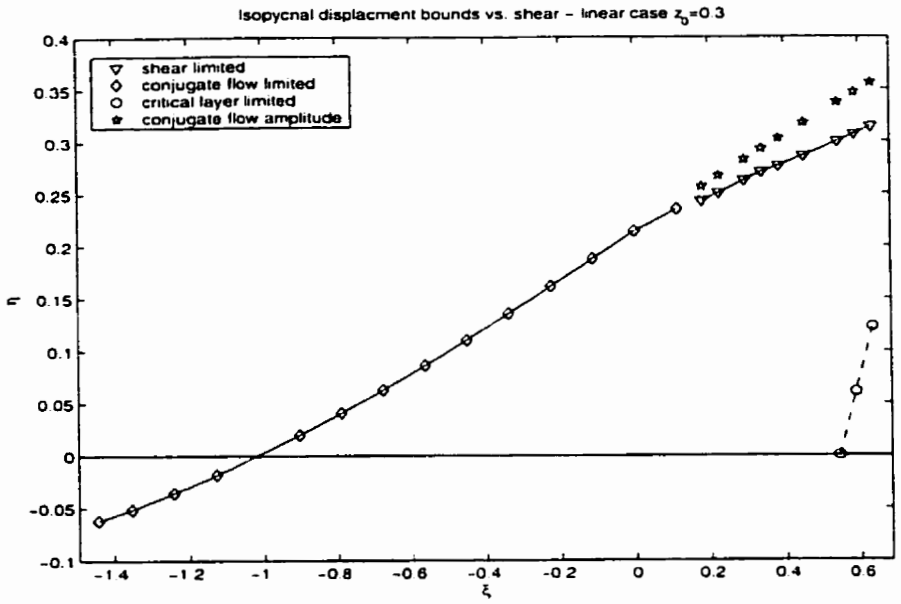

Figure 3.10: Bounds on isopycnal displacements as functions of ξ for linear background currents. $z_0 = 0.3$

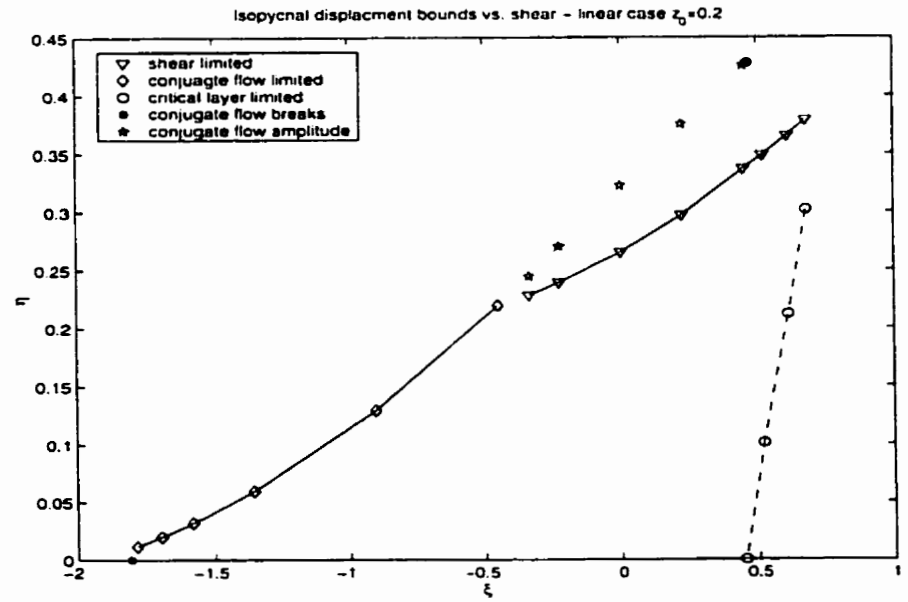

Figure 3.11: Bounds on isopycnal displacements as functions of ξ for linear background currents. $z_0 = 0.2$

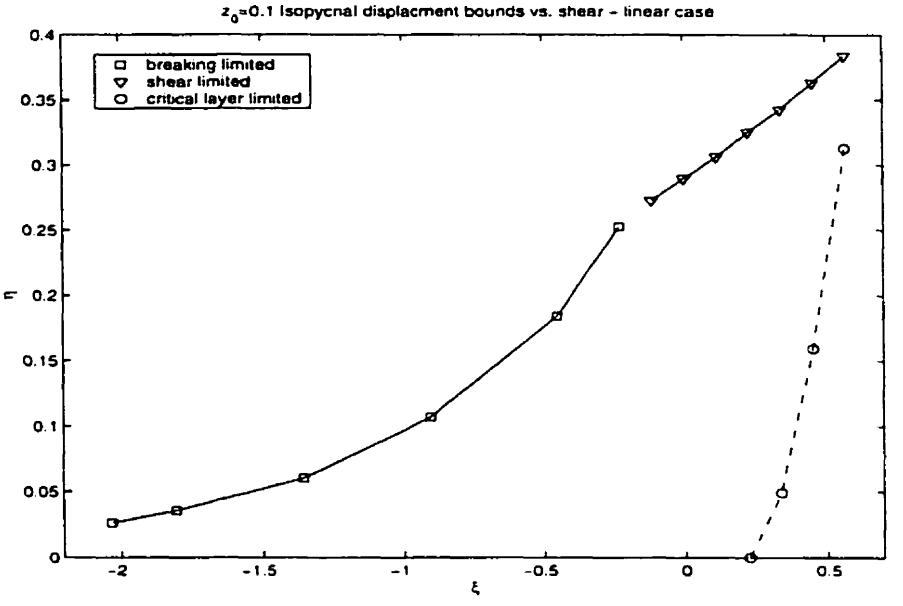

Figure 3.12: Bounds on isopycnal displacements as functions of ξ for linear background currents. $z_0 = 0.1$

cases in which shear instability prevents the calculation of ISWs right up to the conjugate flow amplitude. In practical terms, the shear instability exhibits itself in the variational algorithm's failure to converge.

Figure 3.11 (for $z_0 = 0.2$) is similar in most respects to figure 3.10. The two key points of difference being the larger region where a minimum wave amplitude due to critical layer formation exists and the fact that no reversal of polarity occurs. Instead it was found that for very negative values of ξ the computed conjugate flow was breaking. However the conjugate flow amplitude for the smallest non-breaking case was about 0.01.

Figure 3.12 shows the $z_0 = 0.1$ case. Again we see a clear region where a minimum wave amplitude due to critical layer formation exists. We can also note that much more negative values of ξ yield non-breaking waves for this case compared to $z_0 = 0.2$ or 0.3. This is due to the larger values of c for the $z_0 = 0.1$ stratification. No non-breaking conjugate flows were found for any values of ξ.

Next we turn to the issue of the geometric shape of the background current. At the outset of

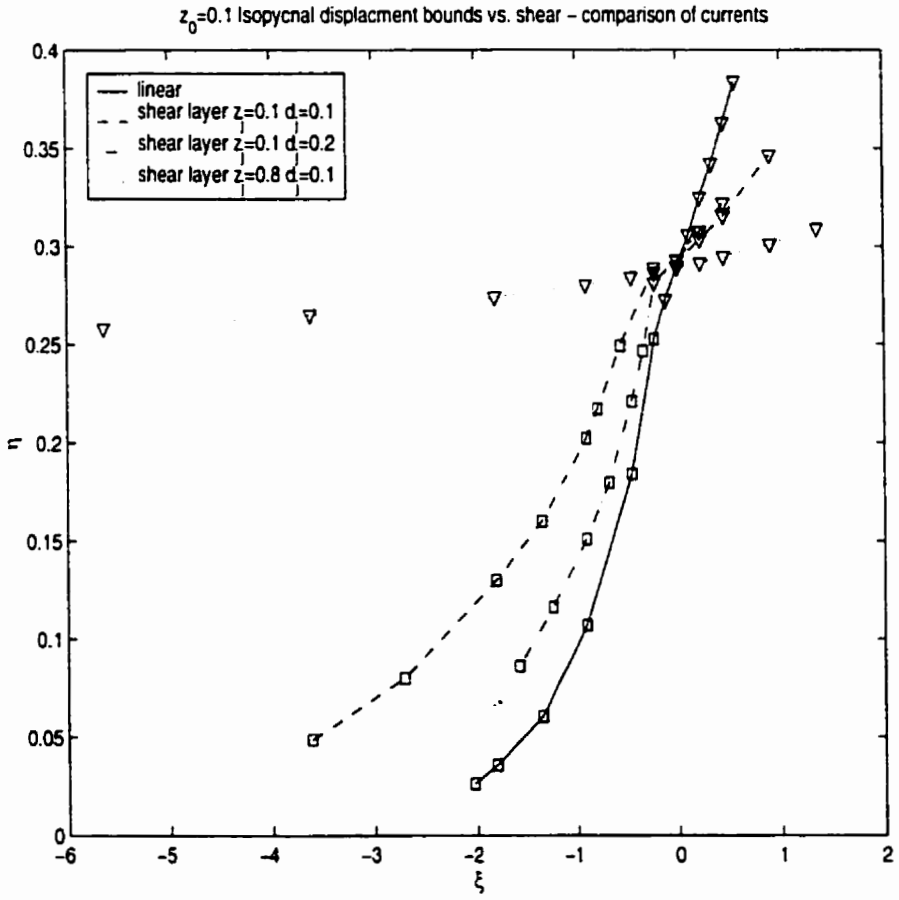

Figure 3.13: Bounds on isopycnal displacements as functions of ξ comparing linear background currents with various shear layer currents. $z_0 = 0.1$

the discussion it should be pointed out that there is no possibility of being exhaustive (something we can strive for with linear background currents). We can merely seek to gain an idea of how background currents that are geometrically more complex than linear currents change the results. Toward this end we consider three shear layer currents of the form (3.11) for the $z_0 = 0.1$ stratification. Two are centered at the center of the pycnocline ($z_j = 0.1$) and have thicknesses given by $d_j = 0.1$ and 0.2. The other is centered well away from the pycnocline (at $z_j = 0.8$) and has a thickness given by $d_j = 0.1$. The currents are chosen to allow us to make some statements about the importance of shear in, and away from, the pycnocline.

In figure 3.13 we show the isopycnal displacement bounds versus ξ for the linear current and the three shear layer currents. The most immediately obvious difference is between the shear layer centered well away from the pycnocline and all the other cases. The shear layer centered away from the pycnocline is bounded for all ξ by shear instability and η_b is only weakly dependent on ξ. Furthermore, the range of values for ξ is bounded above and below by points where the variational algorithm fails to converge (as opposed to critical layer formation). The shear layers centered at the center of the pycnocline are qualitatively similar to the linear case. Namely, positive values of ξ have an upper bound due to shear instability, while negative values of ξ are bounded above by wave breaking. For all the curves the breaking amplitude becomes smaller as ξ grows more negative. Note however that both shear layer cases centered at $z_j = 0.1$ have a range of ξ values bounded by points where the variational algorithm fails to converge. The $d_j = 0.2$ case has a smaller range of possible ξ values. A partial explanation for this is that for a fixed value of ξ the $d_j = 0.2$ case will have double the U^{par} of the $d_j = 0.1$ case. In other respects however, the $d_j = 0.2$ case is closer to the linear case when compared to the $d_j = 0.1$ case (i.e. thicker shear layers behave more like linear currents).

In figures 3.14, 3.15, 3.16 we show the η_b versus ξ curves for the three shear layer profiles in detail.

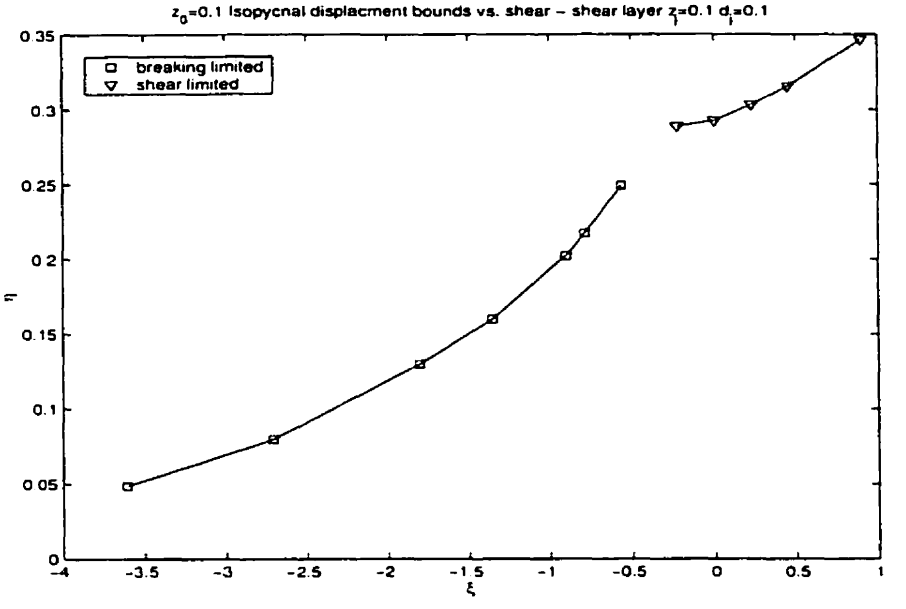

Figure 3.14: Bounds on isopycnal displacements as functions of ξ for $z_0 = 0.1$. Shear layer current $z_j = 0.1$ $d_j = 0.1$.

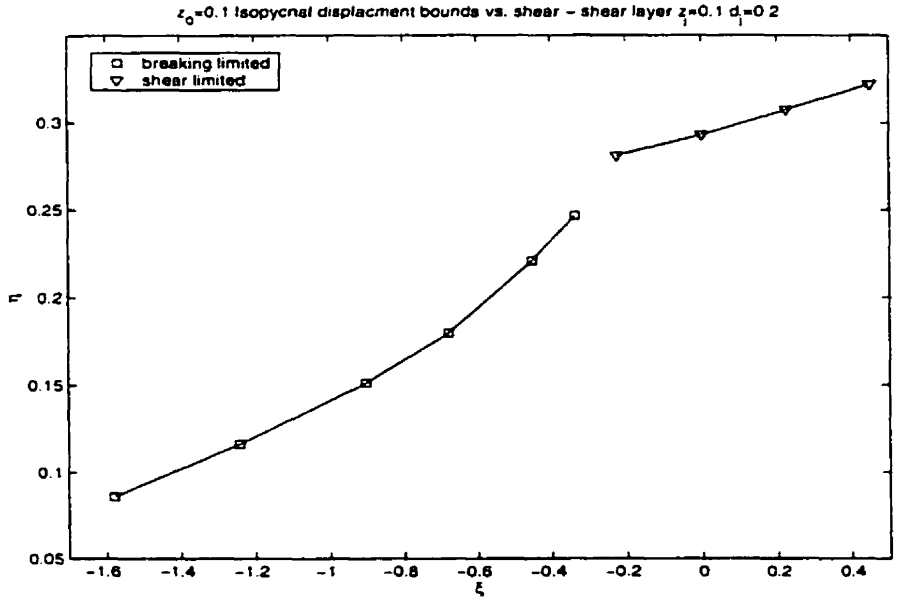

Figure 3.15: Bounds on isopycnal displacements as functions of ξ for $z_0 = 0.1$. Shear layer current $z_j = 0.1$ $d_j = 0.2$.

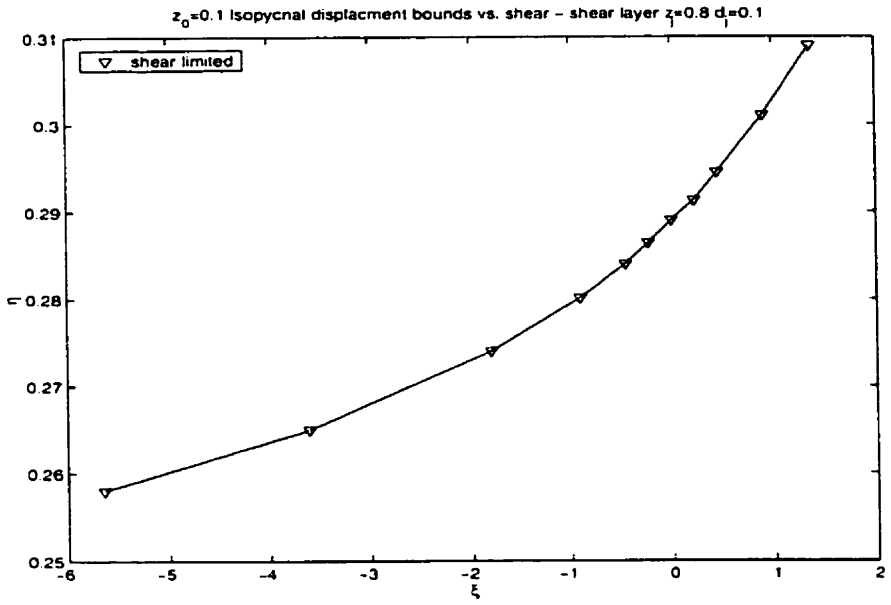

Figure 3.16: Bounds on isopycnal displacements as functions of ξ for $z_0 = 0.1$. Shear layer current $z_j = 0.8$ $d_j = 0.1$.

3.1.5 Fully nonlinear results: changes with wave amplitude

Next we'd like to get some perspective on what happens to the waves for a given background current as the wave amplitude (maximum isopycnal displacement, η_{max}) changes. The number of possible figures that can be shown can be quite overwhelming. For this reason we will focus on three quantities, namely the maximum horizontal velocity (henceforth referred to as u_{max}), the wave propagation speed (c) and the wave half-width. The first two are chosen to emphasize the difference between cases with and without wave breaking (recall that when wave breaking occurs $u = c$ somewhere in the water column). The depth averaged background current will, in general, modify both c and u_{max} by advecting the entire wave. To account for this problem (and because we expect the background current in the pycnocline to be more important than the background current outside of it) we plot $c - U(z_0)$ and $u_{max} - U(z_0)$. This, of course, will not affect whether wave breaking occurs, or shift its location. The curves will be referred to as the u_{max} and c versus η_{max} curves.

The point of showing how the wave half-width changes with wave amplitude, η_{max}, is obvious.

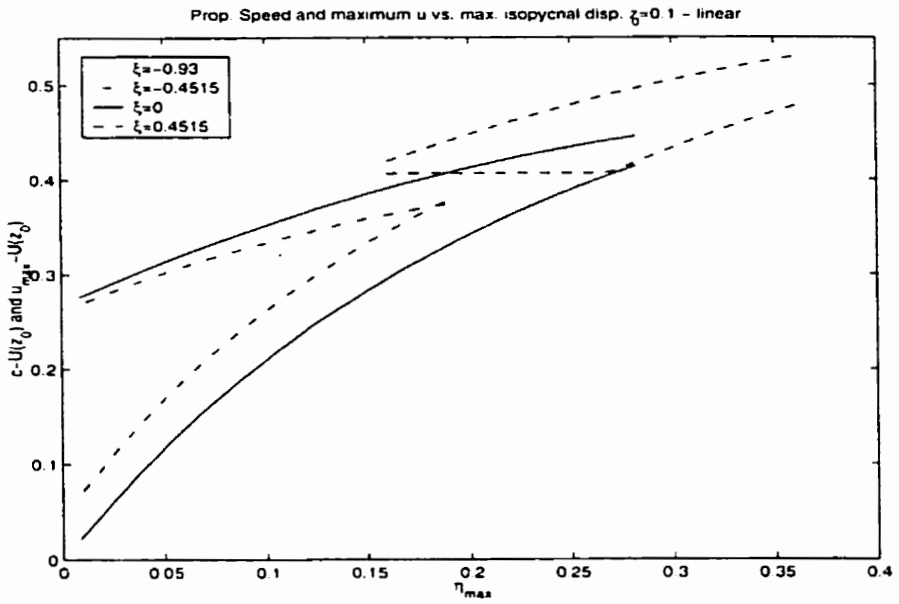

Figure 3.17: Maximum horizontal velocity and wave propagation speed as functions of the maximum isopycnal displacement. $z_0 = 0.1$, linear current $\xi = 0.4515, 0, -0.4515, -0.93$

Recall, however, that there is no unique way to define the half-wave width. We choose to do so in the following manner: first find the height at which the isopycnal displacement is maximum, second consider the density through this point as a function of x, third find the half-width of this function. Other possible choices include using the wave induced surface or bottom current. Both would give results qualitatively similar to those found below. Since the $z_0 = 0.3$ and $z_0 = 0.2$ cases were found to be qualitatively similar we show plots only for the $z_0 = 0.1$ and $z_0 = 0.2$ cases.

In figure 3.17 we show the u_{max} and c versus η_{max} curves for linear background current for four different values of ξ. For non-breaking waves $u_{max} < c$, with the difference decreasing with increasing η_{max}. It can be seen from the figure that for the two negative values of ξ the u_{max} and c curves cross indicating wave breaking. Note that strictly speaking we should stop the curves at the exact point where they cross and wave breaking sets in. We choose to continue the curves slightly past breaking to draw attention to the fact that the curves cross (and to hint at the fact that the variational algorithm may be used to discuss waves past breaking, as is done in the next chapter). For $\xi \geq 0$ we find that the curves do not cross, indicating, in this case,

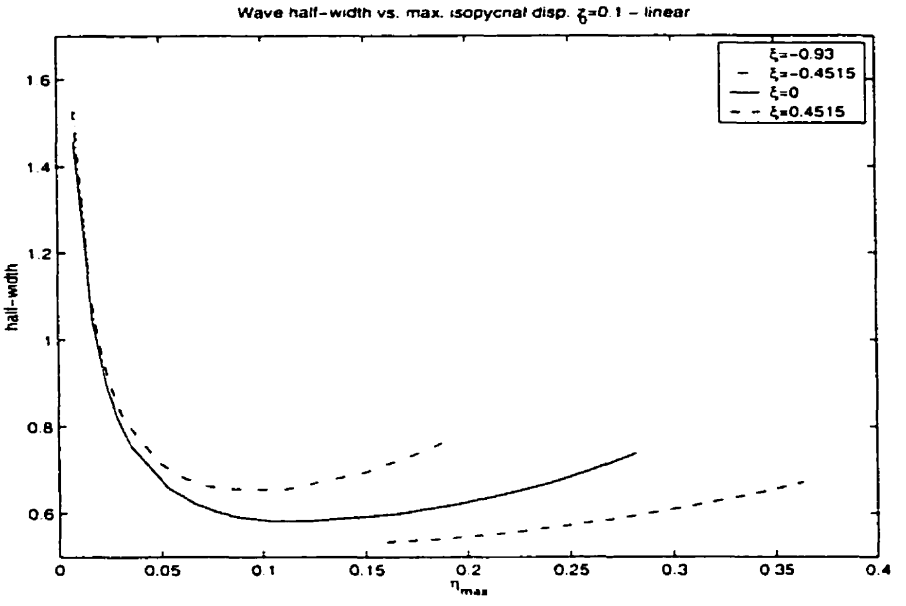

Figure 3.18: Wave half-width as a function of the maximum isopycnal displacement. $z_0 = 0.1$, linear current $\xi = 0.4515, 0, -0.4515, -0.93$

an upper bound due to shear instability. Note that for rightward propagating waves, in general, waves of elevation have the largest positive wave-induced currents near the bottom and the largest negative wave-induced currents near the surface. Furthermore the positive wave-induced currents tend to have a larger magnitude than the negative wave-induced currents. In practice this means that for non-negative background currents it is possible to have u_{max} occur outside the wave (i.e. due to the background current). This is exactly what happens for smaller waves (i.e. the u_{max} curve has a flat section and a corner) for $\xi = 0.4515$. Also note that the flat part of the u_{max} curve nearly intersects the c curve. The point where this occurs is the point at which the ISWs reach their minimum amplitude due to critical layer formation. The variational algorithm breaks down before this point is reached. For this reason we are never able to calculate the minimum amplitude exactly (though through carefully repeating the computations with different values of the available potential energy we can get rather close). To get the minimum amplitude we use the standard third order spline interpolation-extrapolation algorithm in the Matlab package.

In figure 3.18 we show the half-width versus maximum isopycnal displacement curves for linear

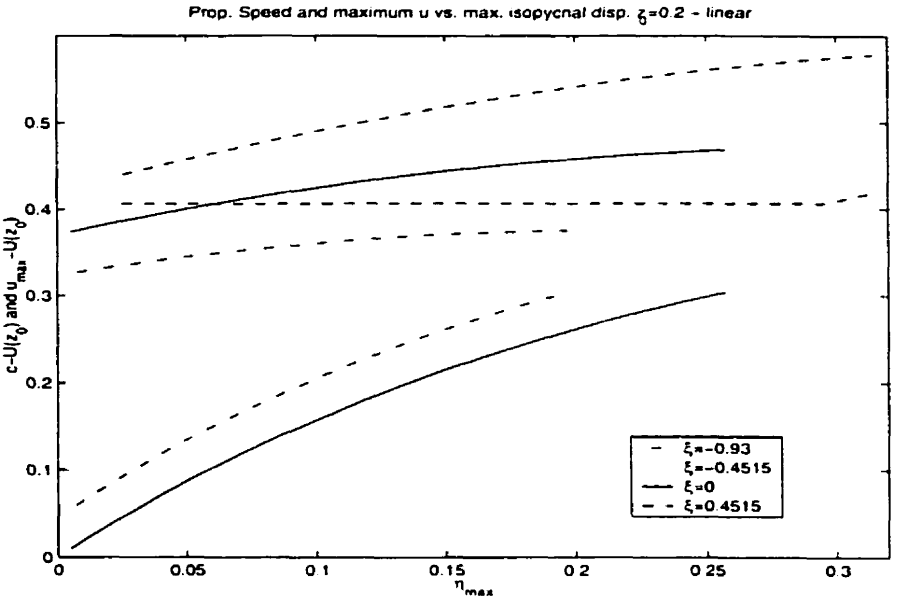

Figure 3.19: Maximum horizontal velocity and wave propagation speed as functions of the maximum isopycnal displacement. $z_0 = 0.2$, linear current $\xi = 0.4515,\ 0,\ -0.4515\ ,-0.93$

background currents with the same four values of ξ as in figure 3.17. It can be seen from figure 3.18 that in general the wave half-width is rather large for small waves, then decreases rapidly until a minimum is reached. The minimum is followed by a gradual increase. The more negative values of ξ yield larger wave half-widths. Also note that since there is a lower bound on the wave amplitude for the $\xi = 0.4515$ case no region of half-width decrease appears on the graph.

The above results can be compared and contrasted with the corresponding results for the $z_0 = 0.2$ case found in figures 3.19 and 3.20, for the u_{max} and c versus η_{max} curves, and the half-width versus η_{max} curves, respectively. From figure 3.20 we can note that the $z_0 = 0.2$ case has waves that are a great deal wider for all values of ξ when compared with the $z_0 = 0.1$ case. For the negative values of ξ where the maximum isopycnal displacement is bounded above by the conjugate flow amplitude this is very easy to understand: As waves near the conjugate flow amplitude increasing A can no longer be accomplished by increasing wave amplitude, hence the waves begin to broaden, eventually becoming flat in the middle (see the article by Lamb and Wan [37] for more details). From figure 3.19 we can see that since no wave breaking occurs for the

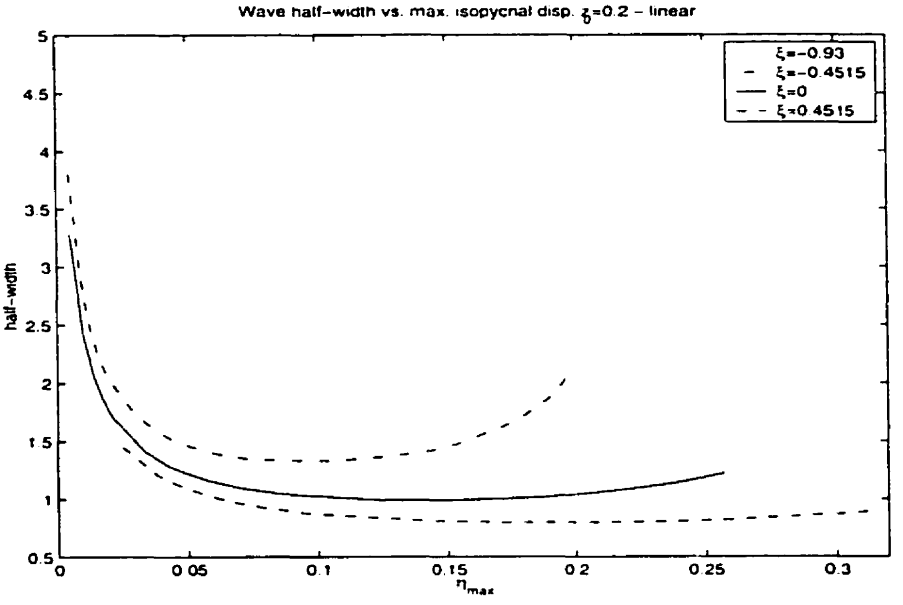

Figure 3.20: Wave half-width as a function of the maximum isopycnal displacement. $z_0 = 0.2$, linear current $\xi = 0.4515, 0, -0.4515, -0.93$

$z_0 = 0.2$ case, the u_{max} curves remain below the c curves for all values of ξ. Also notice that for $\xi = 0.4515$ u_{max} occurs outside the wave for all but the largest waves (i.e. nearly the entire u_{max} versus η_{max} curve is flat).

Next we return to the effect of shear layer currents versus the effect of linear currents. We choose $\xi = \pm 0.22575$. This value of ξ has no minimum wave amplitude for any of the cases considered and hence allows a comparison over the full range of wave amplitudes. As before we consider linear background currents as well as three different shear layer profiles: two centered at the center of the pycnocline (i.e. $z_j = 0.1$ and 0.2 for the cases $z_0 = 0.1$ and 0.2, respectively) and one centered well away from the pycnocline (i.e. $z_j = 0.8$). One of the shear layers centered at the pycnocline is chosen to be twice as broad as the other (i.e. $d_j = 0.1$ and 0.2). The shear layer outside of the pycnocline is chosen to have the same width as the narrower of the two shear layers centered at the center of the pycnocline (i.e. $d_j = 0.1$).

In figures 3.21 and 3.23 we show the u_{max} and c versus η_{max} curves for the various background currents with $\xi = -0.22575$ and 0.22575, respectively. The corresponding curves for half-width

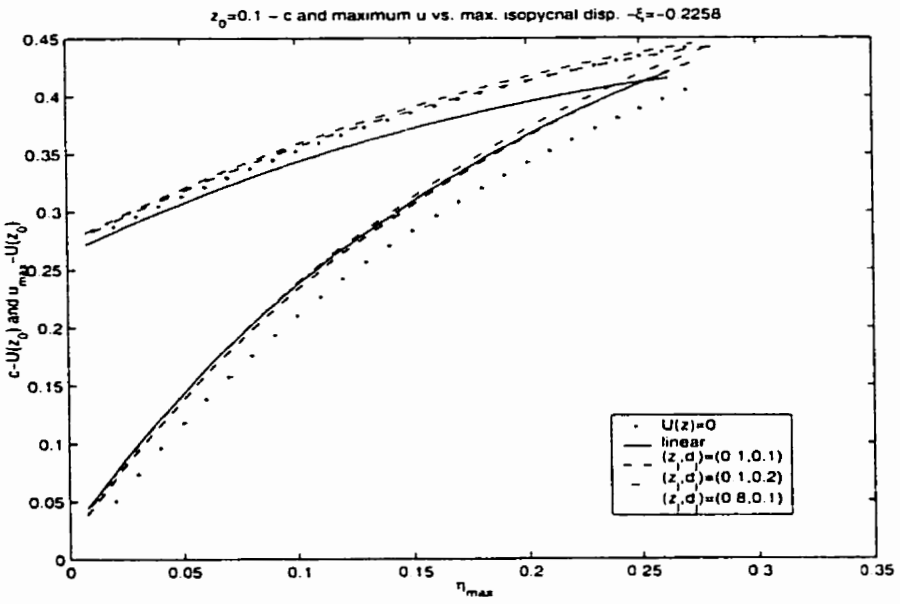

Figure 3.21: Maximum horizontal velocity and wave propagation speed as functions of the maximum isopycnal displacement. $z_0 = 0.1$, linear and shear layer currents $\xi = +0.22575$

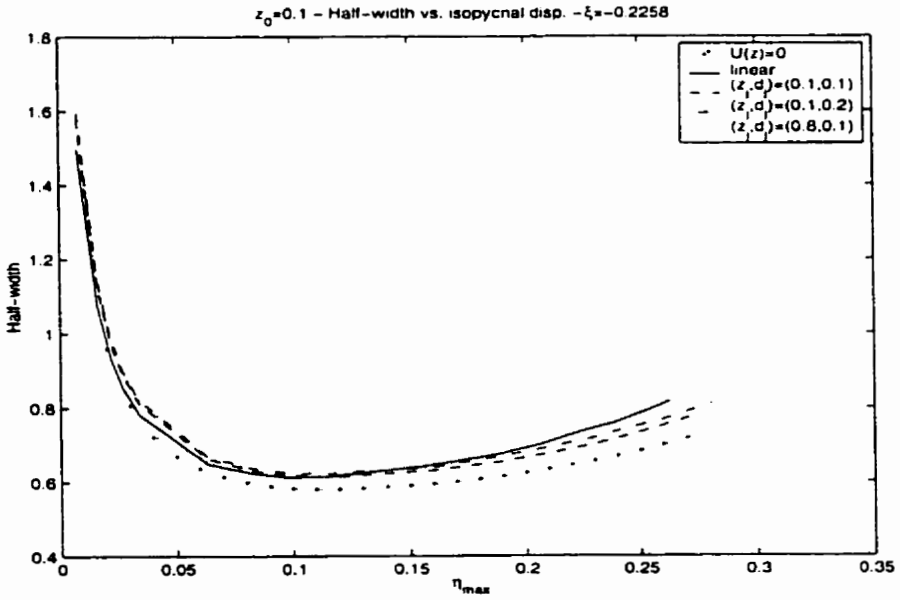

Figure 3.22: Wave half-width as a function of the maximum isopycnal displacement. $z_0 = 0.1$, linear and shear layer currents $\xi = -0.22575$

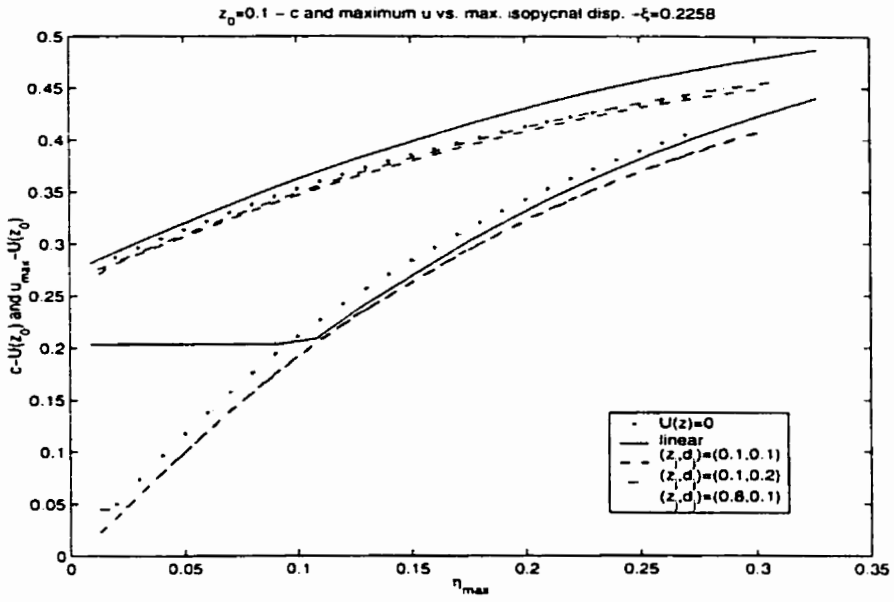

Figure 3.23: Maximum horizontal velocity and wave propagation speed as functions of the maximum isopycnal displacement. $z_0 = 0.1$, linear and shear layer currents $\xi = 0.22575$

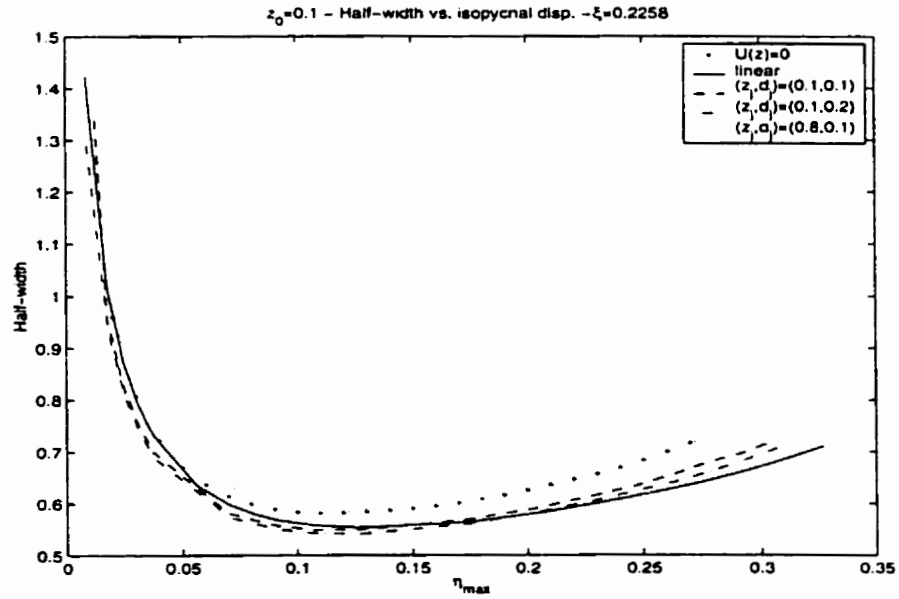

Figure 3.24: Wave half-width as a function of the maximum isopycnal displacement. $z_0 = 0.1$, linear and shear layer currents $\xi = -0.22575$

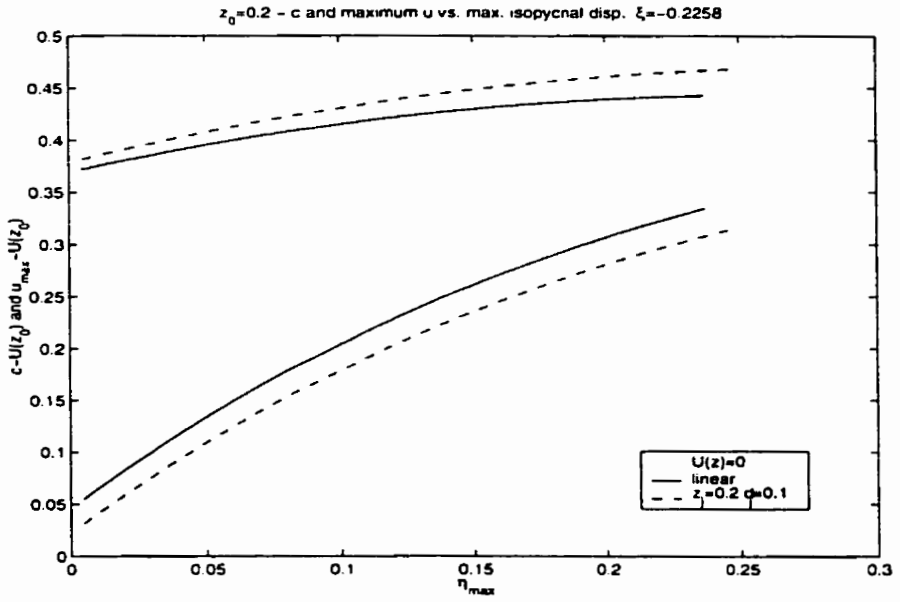

Figure 3.25: Maximum horizontal velocity and wave propagation speed as functions of the maximum isopycnal displacement. $z_0 = 0.2$, linear and shear layer currents $\xi = -0.22575$

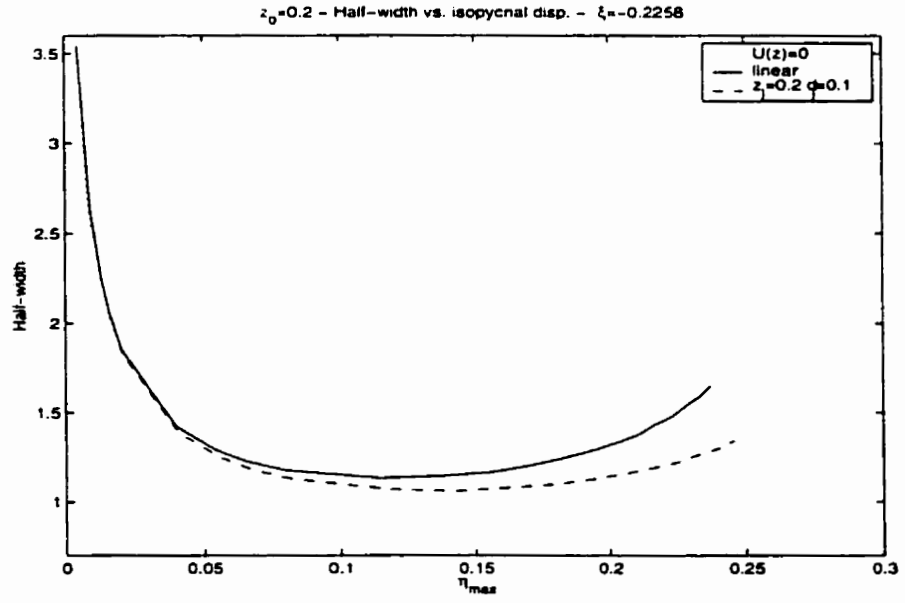

Figure 3.26: Wave half-width as a function of the maximum isopycnal displacement. $z_0 = 0.2$, linear and shear layer currents $\xi = -0.22575$

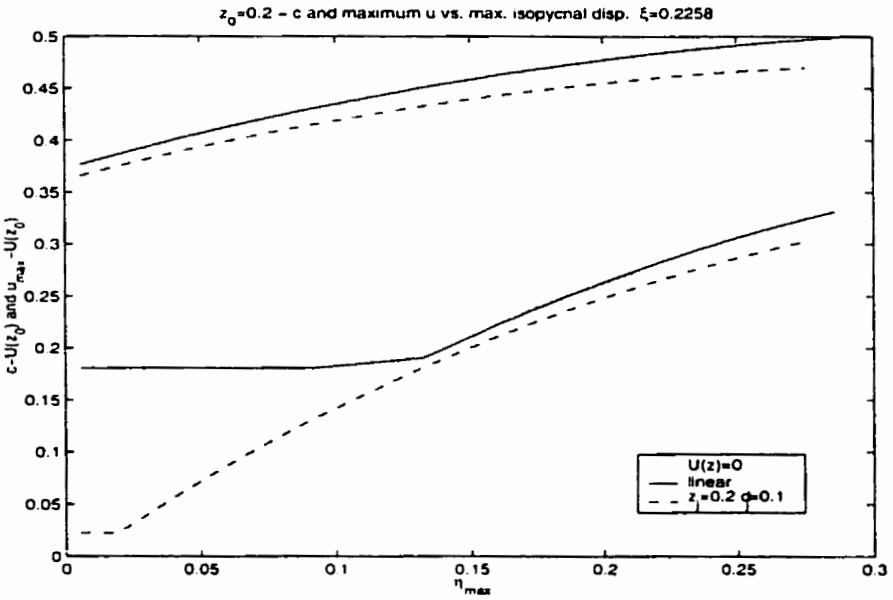

Figure 3.27: Maximum horizontal velocity and wave propagation speed as functions of the maximum isopycnal displacement. $z_0 = 0.2$, linear and shear layer currents $\xi = 0.22575$

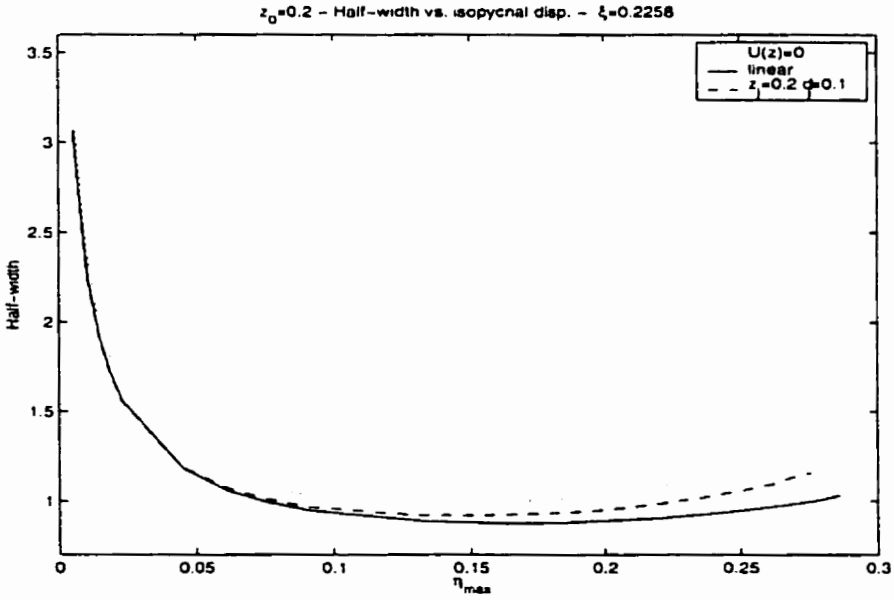

Figure 3.28: Wave half-width as a function of the maximum isopycnal displacement. $z_0 = 0.2$, linear and shear layer currents $\xi = -0.22575$

can be found in figures 3.22 and 3.24. From figure 3.21 we can see that only the linear, and shear layer with $(z_j, d_j) = (0.1, 0.2)$ cases lead to wave breaking. In fact for the shear layer with $z_j = 0.1$, $d_j = 0.2$ case, wave breaking occurs very close to the shear instability limit and some care had to be taken to actually compute waves past breaking. From all four graphs it appears that ISWs computed using the $z_j = 0.8$ background current are very close to the waves that result when there is no background current. In fact there appear to be only two differences between the no background current and $z_j = 0.8$, $d_j = 0.1$ cases. First, as evidenced by figure 3.13, the maximum wave amplitude computable changes slightly as ξ varies for the $z_j = 0.8$, $d_j = 0.1$ case. Second, for the shear layer with $z_j = 0.8$, $d_j = 0.1$ case, when ξ becomes large enough in magnitude the variational method stops being able to compute ISWs at all.

For the $\xi = 0.22575$ cases figure 3.23 shows that all shear layer cases have a maximum wave amplitude smaller than the linear current case. From the same figure we also see that the region where u_{max} lies outside the wave occurs only for the linear background current, and $z_j = 0.1$, $d_j = 0.2$ cases. Since we fix ξ (as opposed to U^{par}) the amplitude of the background currents for the linear and $z_j = 0.1$, $d_j = 0.2$ cases is larger than for the corresponding $z_j = 0.1$, $d_j = 0.1$ case, and hence the above result is not unexpected.

The corresponding figures for the $(z_j, d_j) = (0.8, 0.1)$ and $(z_j, d_j) = (0.1, 0.2)$ cases have been produced. They confirmed the qualitative comments made about these cases in the text, but were not deemed by the author to be sufficiently different from the above to merit their inclusion in the text.

To ensure that the above results are not special to the $z_0 = 0.1$ case we show a similar comparison for the $z_0 = 0.2$ case. In figures 3.25 and 3.27 we show the u_{max} and c curves for no background current, linear background current and shear layer background current with $z_j = 0.2$, $d_j = 0.1$, all with $\xi = -0.22575$ and 0.22575, respectively. The corresponding curves for half-width can be found in figures 3.26 and 3.28.

From figure 3.25 we see that for $\xi < 0$ all three cases are qualitatively very similar, with the no background current case exhibiting the largest, and the linear background current case the smallest maximum wave amplitudes. Figure 3.26 shows that the half-width versus η_{max} curve for

the shear layer case lies below and above the curves for the linear, and no background currents, respectively.

Figures 3.27 and 3.28 give the corresponding results for ξ positive. In particular we can see again that the shear layer background current (which is nonzero only on a subset of the total water column) has less of an effect on wave properties than the linear current for a corresponding value of ξ.

3.1.6 Fully nonlinear results: fixed wave amplitude, ξ varies

So far we have allowed η_{max} to vary. However it would be useful to get some idea of how wave properties change when η_{max} is fixed. Since the variational algorithm does not fix η_{max} *a priori* it can be rather time consuming to find ISWs with η_{max} fixed for various stratifications and background currents. We have chosen to present one set of results for $z_0 = 0.1$, 0.2 and 0.3. We take $\eta_{max} = 0.1$ and consider linear background currents for various values of ξ.

In general, it is not possible to find a wave with $\eta_{max} = 0.1$ for all values of ξ for which we can compute waves. There are four possible reasons for this. For cases like the $z_0 = 0.1$ case where wave breaking is possible it may be that the largest non-breaking wave has $\eta_{max} < 0.1$. On the other hand, for cases where conjugate flows exist it may be that the conjugate flow amplitude (the amplitude of the largest conjugate flow for cases in which more than one conjugate flow exists) is smaller than 0.1. For large, positive values of ξ we have found that it is possible to have a lower bound on η_{max} (to avoid critical layer formation). To find waves with $\eta_{max} = 0.1$ the lower bound must be smaller than 0.1. Finally it is possible that shear instability may prevent the variational algorithm from computing a wave with $\eta_{max} = 0.1$ (though this never occurred in the present calculations).

In figure 3.29 we show the u_{max} and c versus ξ curves for $\eta_{max} = 0.1$. We again account for the advection of the pycnocline by the depth averaged background current by subtracting $U(z_0)$ from both u_{max} and c in the figure. We can see that the propagation speed increases linearly with ξ for all three cases. All three u_{max} curves show a kink where u_{max} moves from inside the wave (induced by the wave) to outside the wave (induced by the background current). We can

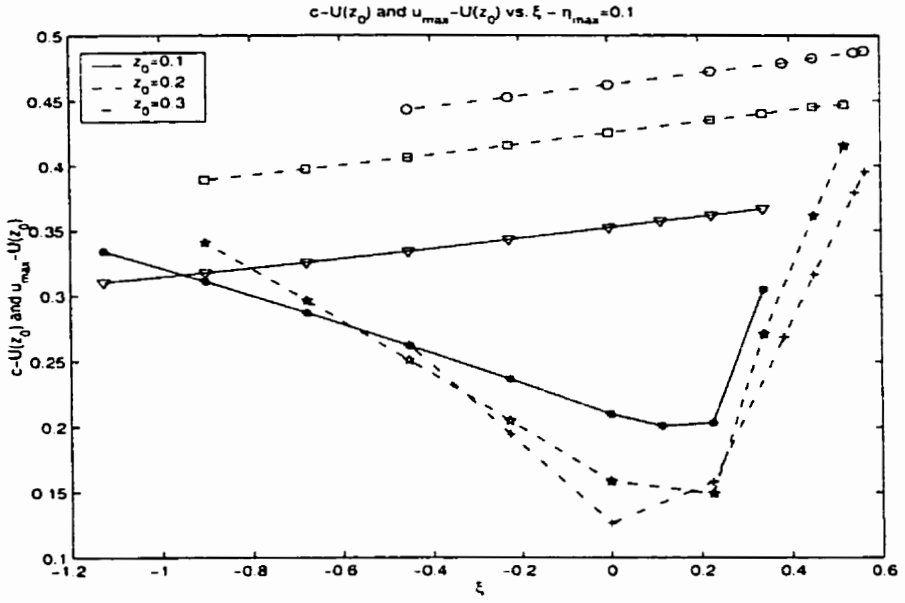

Figure 3.29: Maximum horizontal velocity and wave propagation speed as functions ξ for wave of amplitude $\eta_{max} = 0.1$

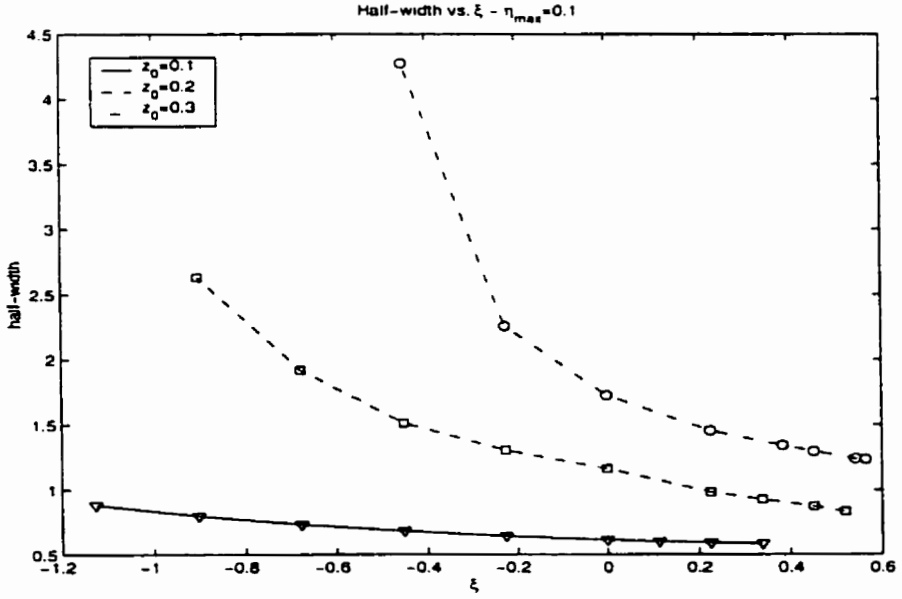

Figure 3.30: Half-width versus ξ. $\eta_{max} = 0.1$

also note that at approximately $\xi = -0.85$ waves with $\eta_{max} = 0.1$ break for the $z_0 = 0.1$ case, in agrrement with figure 3.13. This is clear from the figure since the u_{max} and c curves cross.

In figure 3.30 we show the half-width versus ξ curves for $\eta_{max} = 0.1$. We can see that for all three values of z_0 the waves become narrower as ξ increases. The large increases in half-width for the $z_0 = 0.2$ and 0.3 cases can again be understood in terms of conjugate flows (see above). The wave half-width becomes unbounded at the value of ξ at which the conjugate flow amplitude is 0.1. Finally we can see from the figure that as z_0 increases, the maximum value of ξ for which it was possible to compute a wave with $\eta_{max} = 0.1$ also increases.

3.1.7 Fully nonlinear results: sample profiles

We now turn to the examination of actual vertical profiles of η, u and Ri (the Richardson number) versus z. These profiles are plotted at the crest of the wave ($x = 0$ by symmetry). We also examine the horizontal profile of the wave-induced, horizontal velocity at the surface versus x.

We begin with the $z_0 = 0.1$ case. For each background current considered we show four waves ranging over the computable, non-breaking amplitudes. The largest, non-breaking wave computable is always plotted with a solid line. To compare the various cases of background current we keep the scale for the various quantities plotted the same for all background currents. This means that for certain cases the whole domain will not be used.

In figures 3.31, 3.32 we compare isopycnal displacements for various values of ξ, for a linear background current and a shear layer background current with $(z_j, d_j) = (0.1, 0.1)$, respectively. We can see that the linear background current has a much greater effect on η_b than the shear layer current. In particular, more negative values of ξ lead to lower values of η_b (this will also imply smaller wave-induced velocities, as discussed below). We can also see that as ξ becomes more negative the η versus z profiles become more concave up in the upper portion of the water column. Also note that the location of the maximum isopycnal displacement moves upward as waves grow in amplitude. This result is independent of the background current chosen.

In figures 3.33, 3.34 we compare the wave-induced horizontal current at the surface. We find the results for the maximum magnitude of the wave-induced horizontal current agree with the

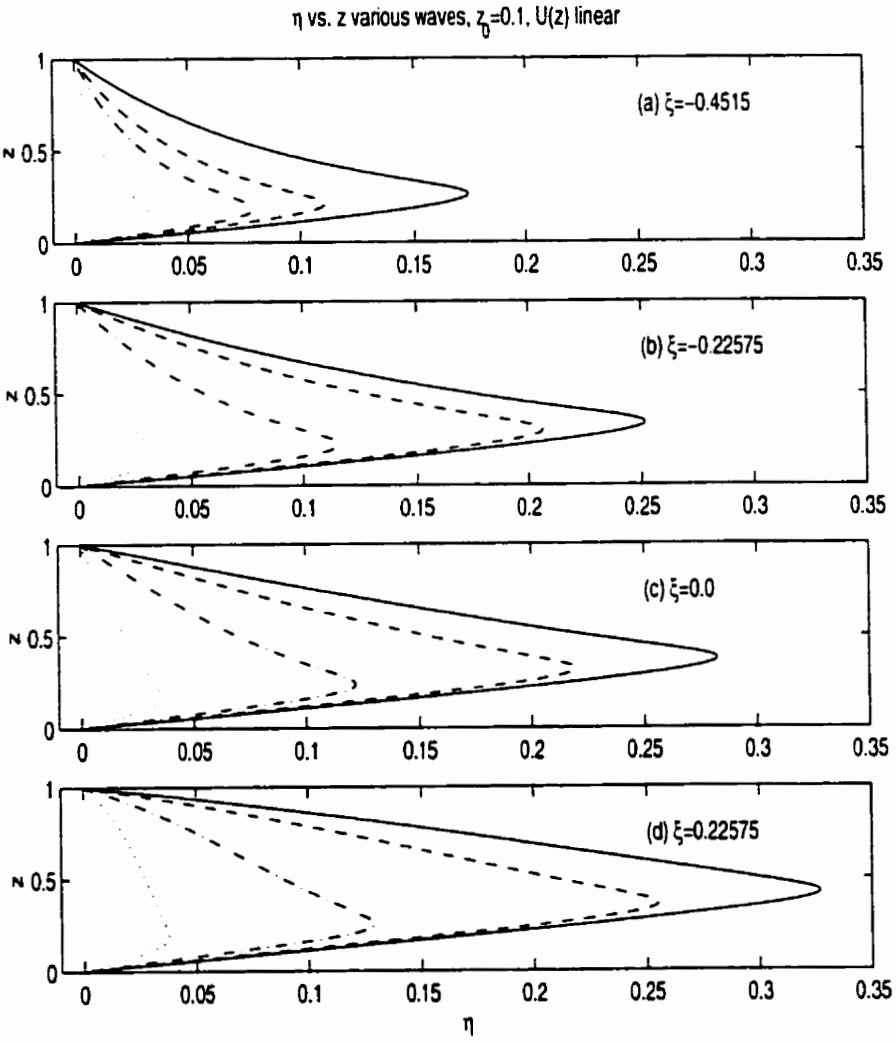

Figure 3.31: η versus z. $(z_0, d) = (0.1, 0.05)$, $U(z)$ linear, various values of ξ

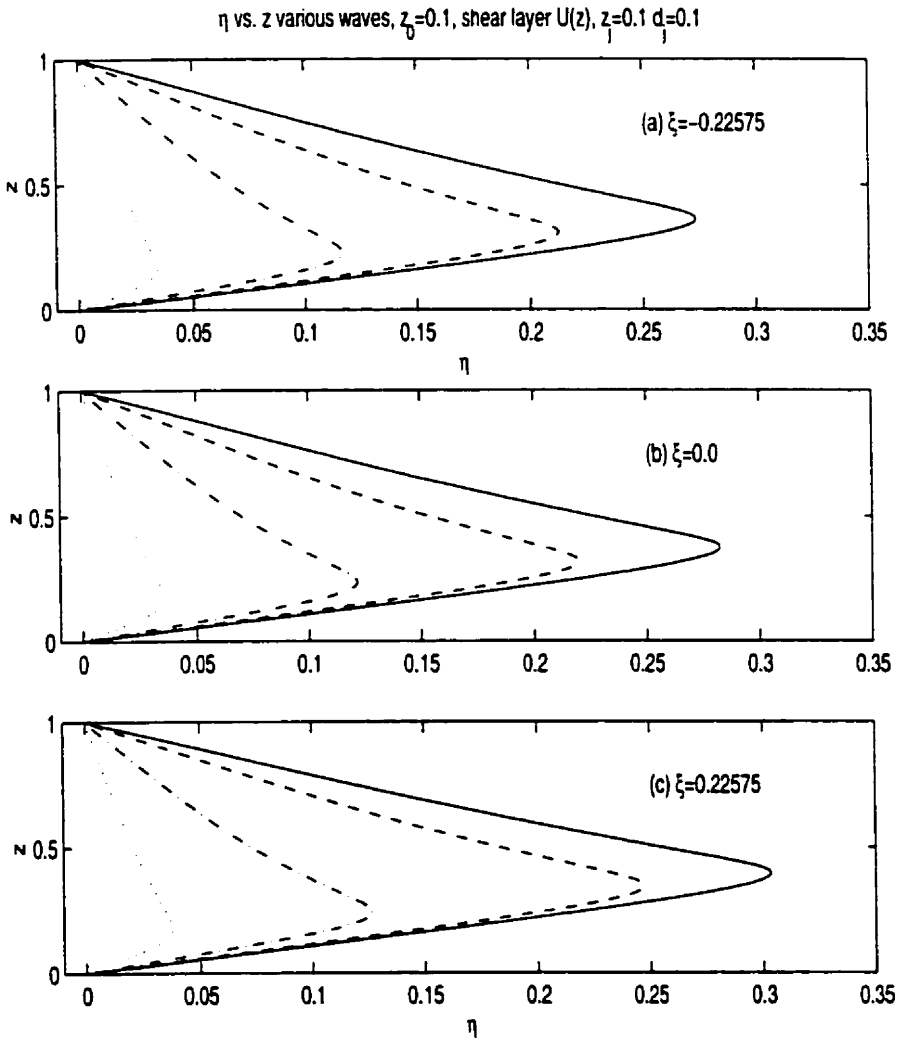

Figure 3.32: η versus z. $(z_0, d) = (0.1, 0.05)$, $U(z)$ shear layer with $(z_j, d_j) = (0.1, 0.1)$, various values of ξ

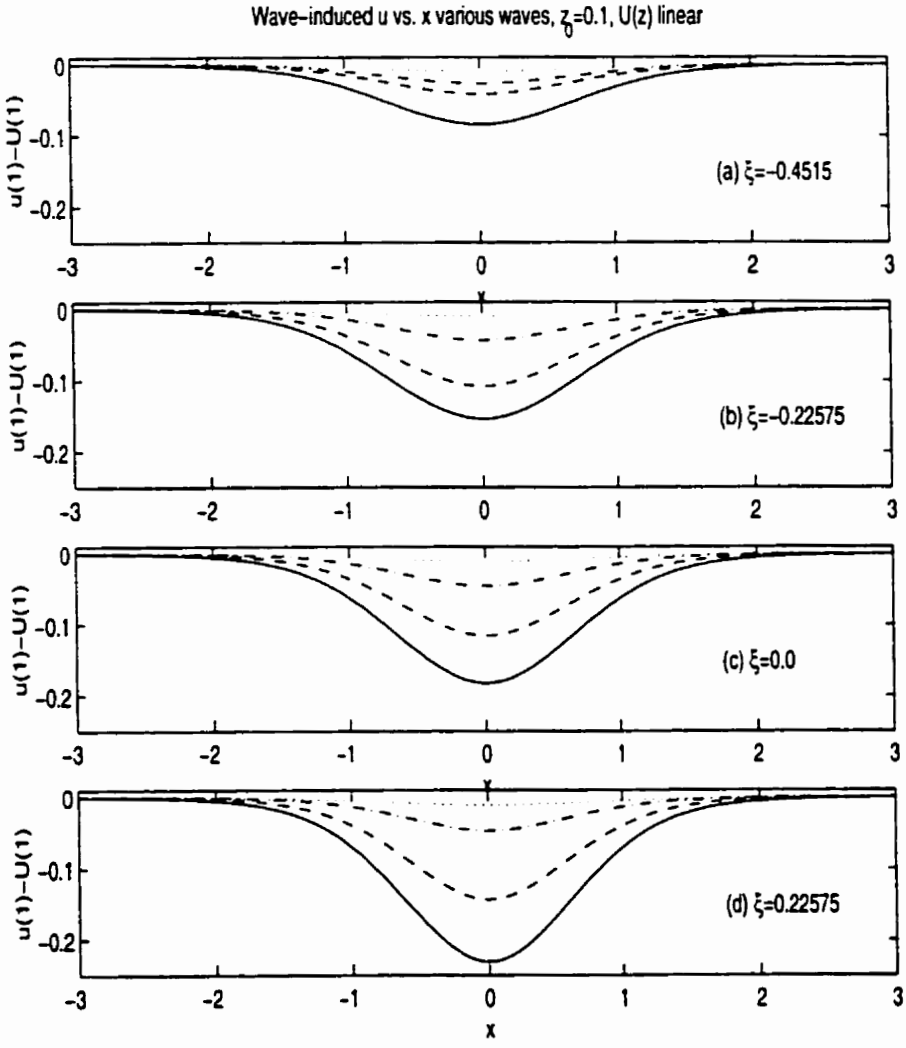

Figure 3.33: Wave-induced u versus x. $(z_0, d) = (0.1, 0.05)$, $U(z)$ linear, various values of ξ

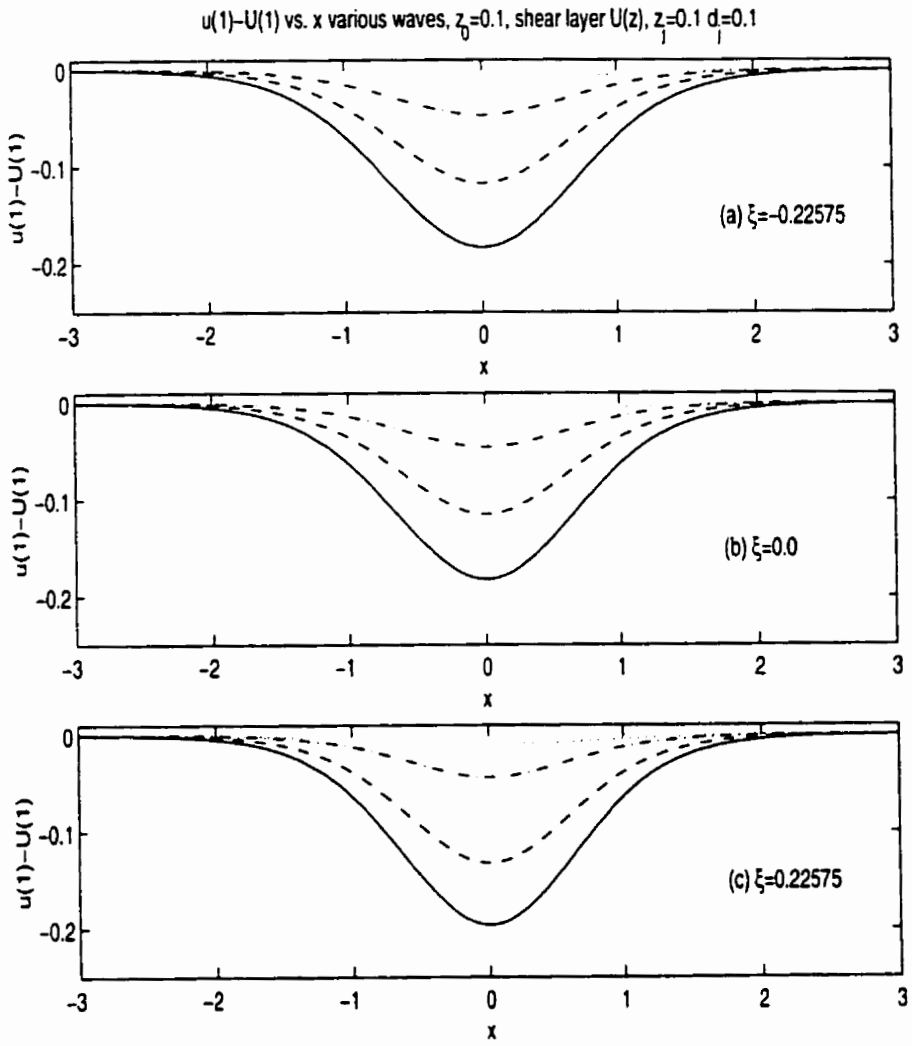

Figure 3.34: Wave-induced u at the surface versus x. $(z_0, d) = (0.1, 0.05)$, $U(z)$ shear layer with $(z_j, d_j) = (0.1, 0.1)$, various values of ξ

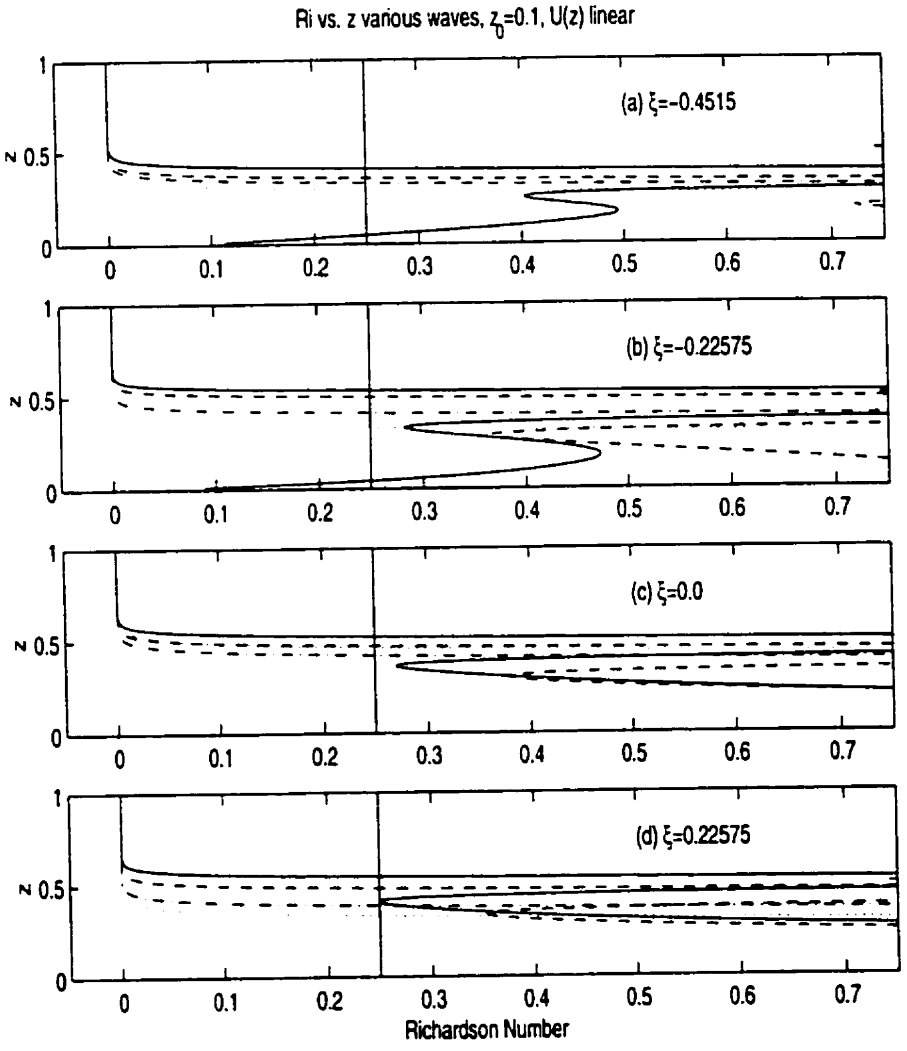

Figure 3.35: Richardson number versus z. $(z_0, d) = (0.1, 0.05)$, $U(z)$ linear, various values of ξ

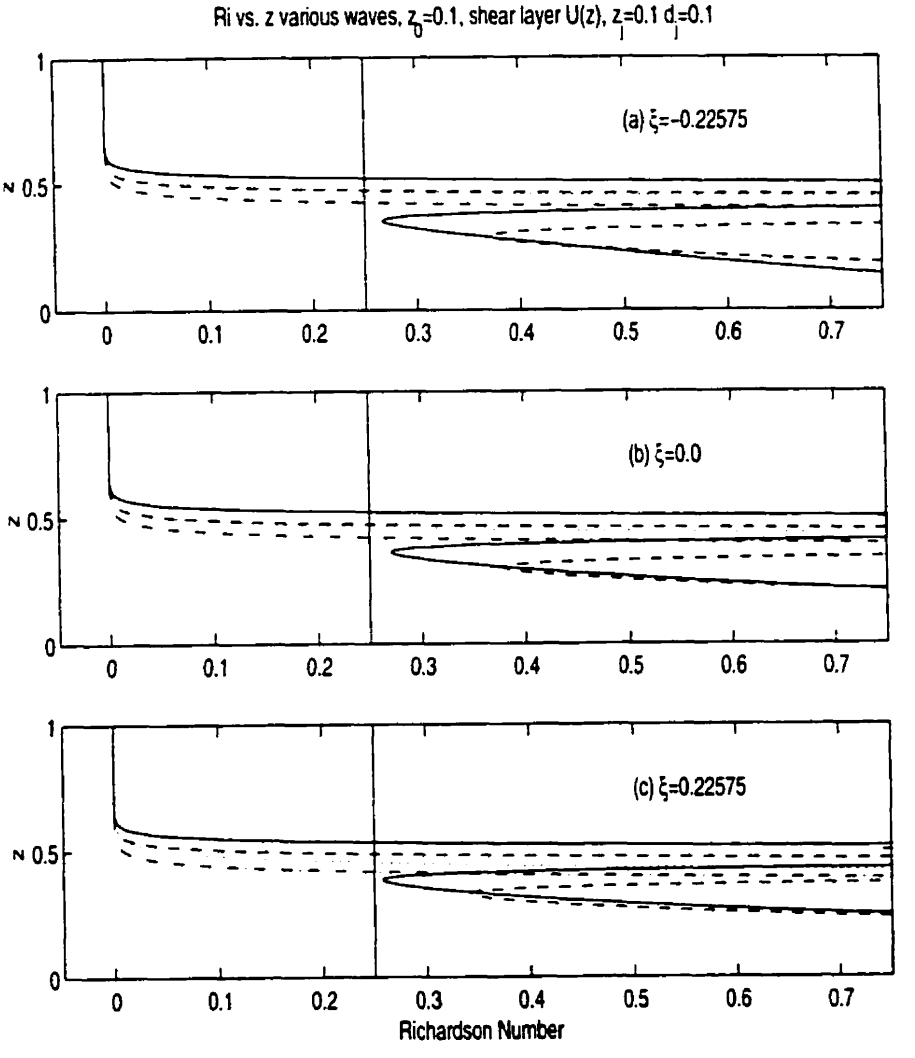

Figure 3.36: Richardson number versus z. $(z_0, d) = (0.1, 0.05)$, $U(z)$ shear layer with $(z_j, d_j) = (0.1, 0.1)$, various values of ξ

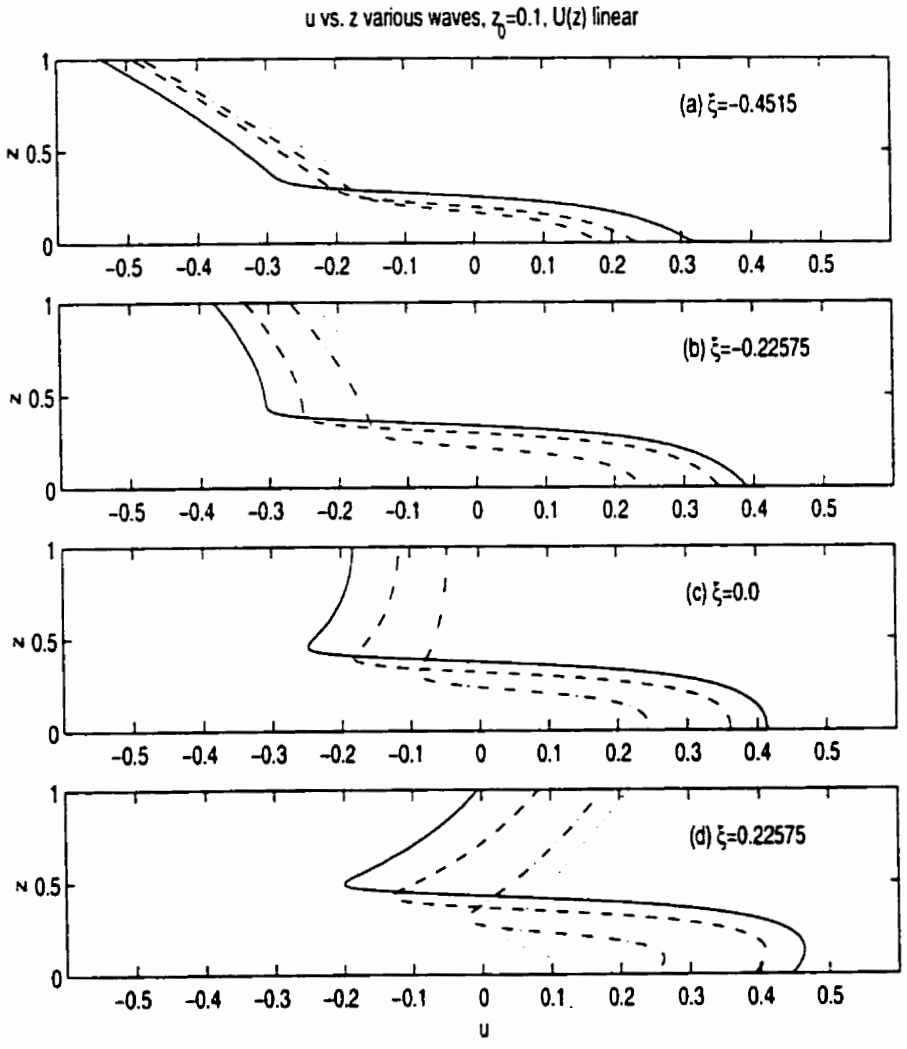

Figure 3.37: u versus z. $(z_0, d) = (0.1, 0.05)$, $U(z)$ linear, various values of ξ

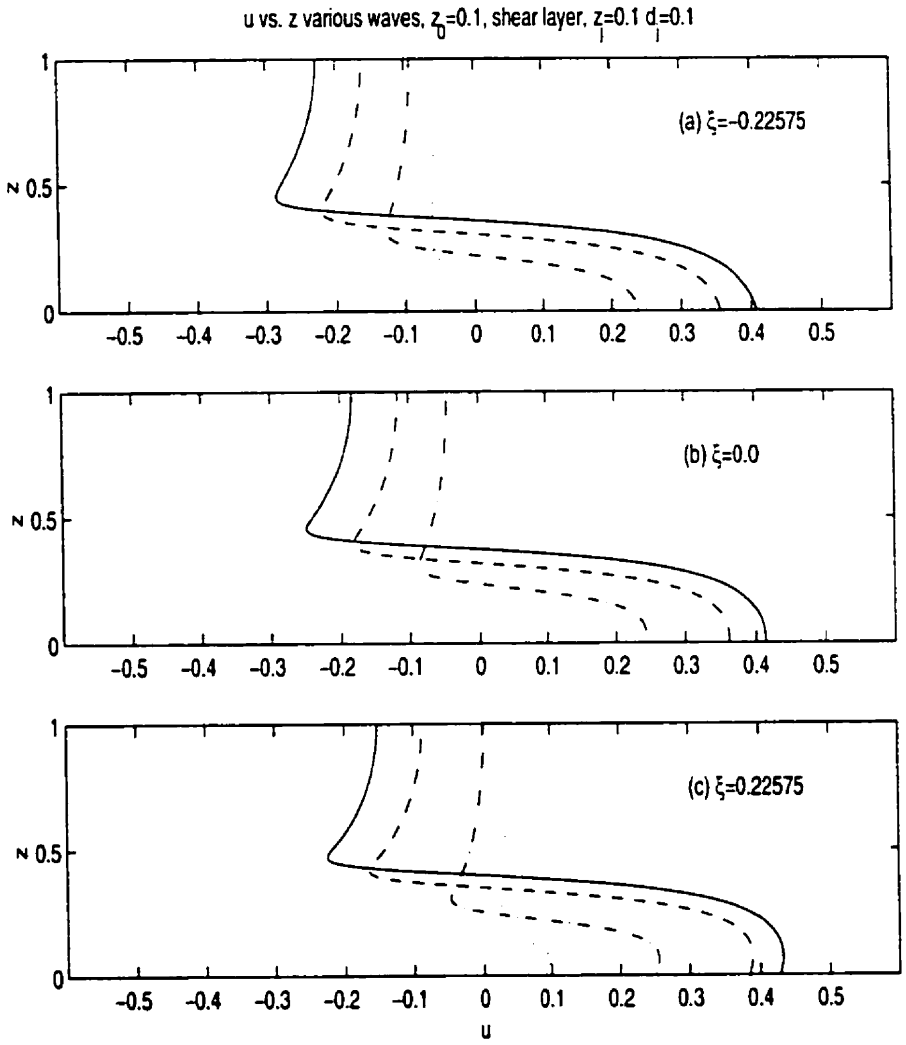

Figure 3.38: u versus z. $(z_0, d) = (0.1, 0.05)$, $U(z)$ shear layer with $(z_j, d_j) = (0.1, 0.1)$, various values of ξ

above results for maximum isopycnal displacement. The figures also show that for the ξ values shown, the increase in wave half-width is mainly due to a change in the shape of the $u(x, H)-U(H)$ versus x curve, as opposed to an increase in the width of the overall disturbance. Such an increase occurs for the $z_0 = 0.2$ case discussed below.

Despite of some reservations on the part of the author as to its utility for non-parallel flows (see for example the article [43]), figures 3.35, 3.36 show profiles of the Richardson number (Ri) versus z at the crest of the wave. It can be seen that the Richardson number decreases to very near zero in the unstratified portions of the water column for all cases. Furthermore, in the weakly stratified near bottom region the Richardson number dips to below 0.1 for linear background currents with $\xi < 0$. In the stratified region the Richardson number stays above 0.25, reaching 0.25 for the linear background current case with $\xi = 0.22575$ which has η_b given by shear instability.

In figures 3.37, 3.38 we show the vertical profiles of the total horizontal velocity u versus z at the wave crest. In general, the largest positive currents are found near or at the bottom (where the background current is weak), while the most negative currents are found either at the top of the advected pycnocline (when $\xi \geq 0.0$ for the linear currents and for both shear layer cases shown) or at the surface (when $\xi < 0.0$ for the linear background currents). It can thus be seen that the linear background current affects the top and bottom portions of the water column in a different way. In the bottom quarter of the water column the weak background current mainly modifies the geometric shape of the wave induced horizontal velocity versus z profile (of course for the no background current case the total and wave induced currents are the same). For example the $\xi = 0.22575$, linear background current case has the maximum current well above the bottom, unlike the other linear cases. In the upper portion of the water column the strong background current is the dominant portion of u, with the wave-induced current modifying the geometric shape. As in the cases discussed above, the shear layer background currents have a much smaller effect when compared to their linear counterparts.

A different perspective on the effects of linear versus shear layer currents is provided by figures 3.39, 3.40, 3.41, 3.42. In these figures the largest non-breaking waves computable for linear and shear layer background currents with $\xi \pm 0.22575$ are shown on the same set of axes (again we

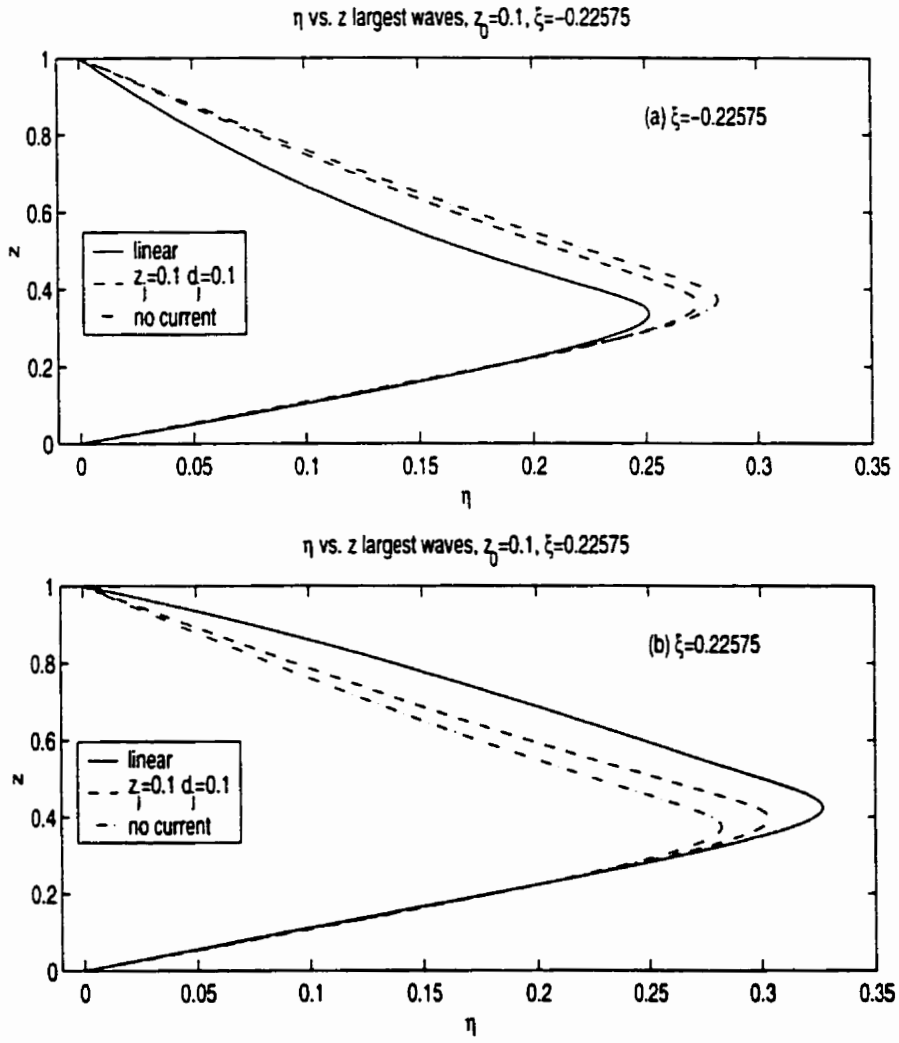

Figure 3.39: η versus z, largest non-breaking wave. $z_0 = 0.1$, upper panel - $\xi = 0.22575$, lower panel - $\xi = -0.22575$. solid - linear background current, dashed - shear layer current $z_j = 0.1$, $d_j = 0.1$, dot-dashed - no current

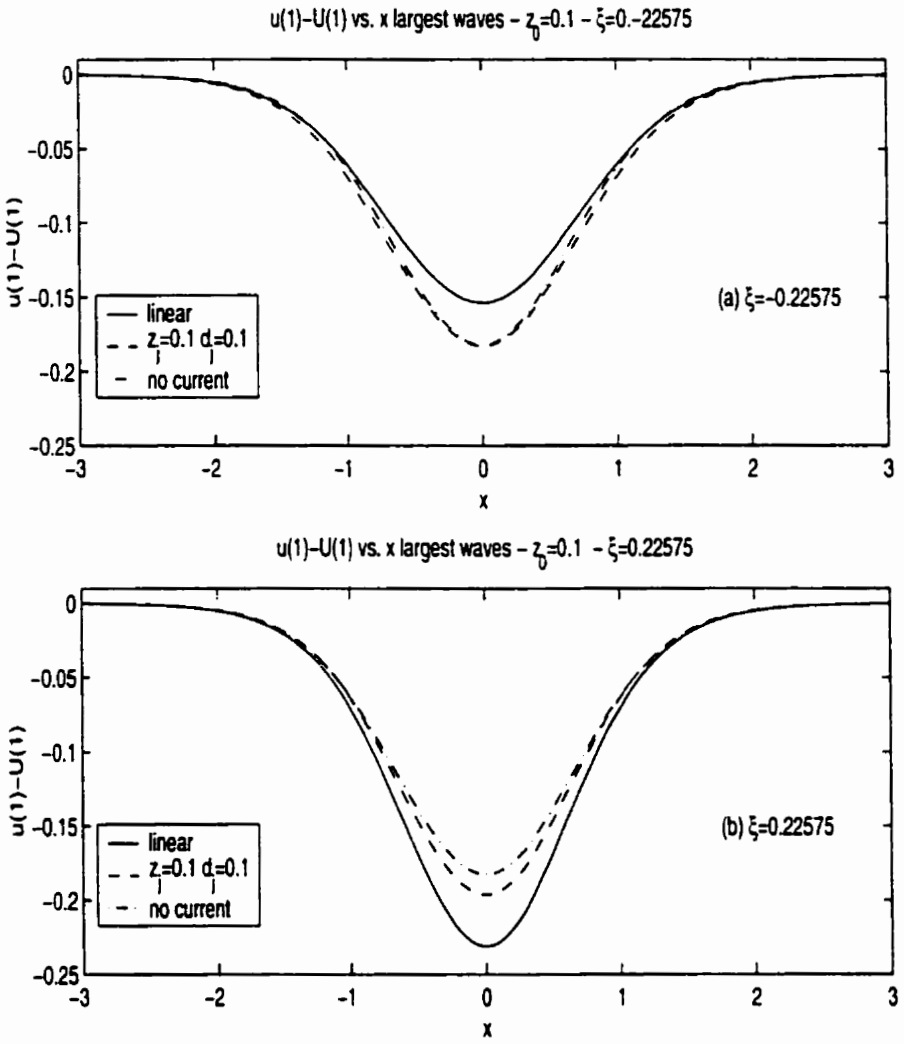

Figure 3.40: wave induced horizontal current at the surface versus x, largest non-breaking wave. $z_0 = 0.1$, upper panel - $\xi = 0.22575$, lower panel - $\xi = -0.22575$. solid - linear background current, dashed - shear layer current $z_j = 0.1$, $d_j = 0.1$, dot-dashed - no current

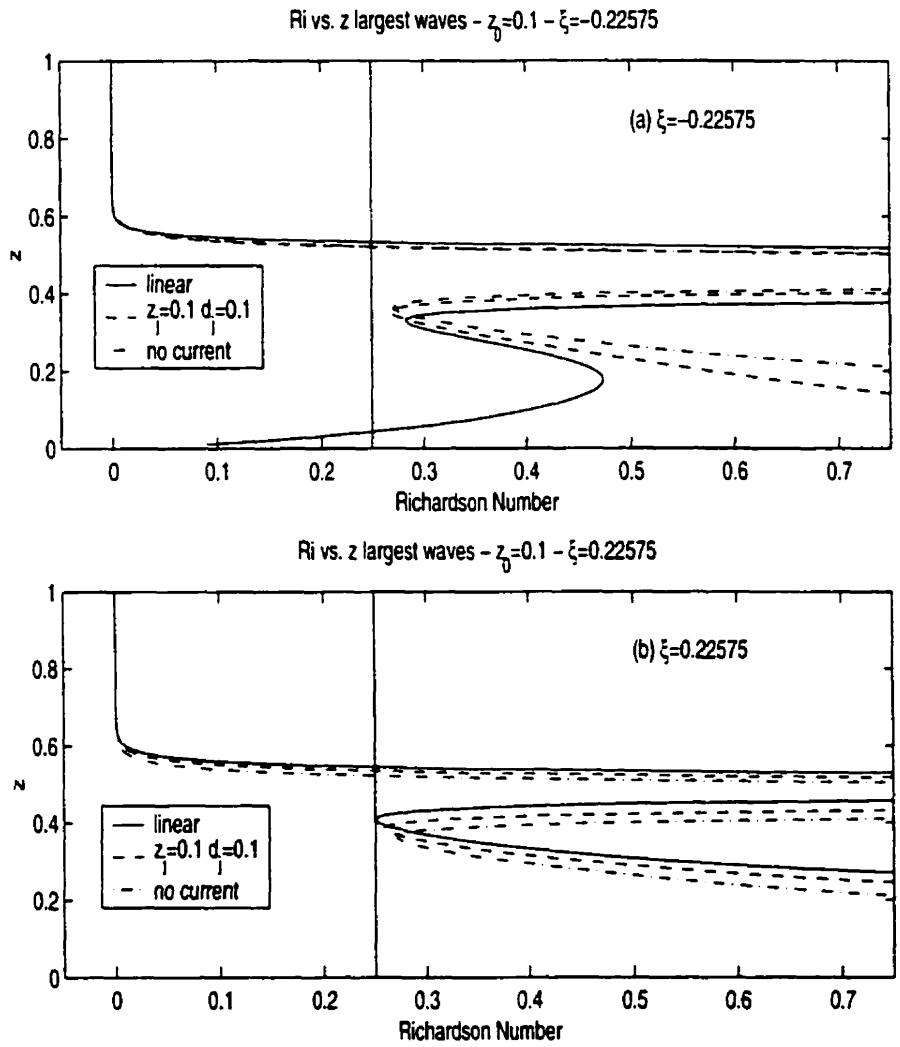

Figure 3.41: Richardson number versus z, largest non-breaking wave. $z_0 = 0.1$, upper panel - $\xi = 0.22575$, lower panel - $\xi = -0.22575$. solid - linear background current, dashed - shear layer current $z_j = 0.1$, $d_j = 0.1$, dot-dashed - no current

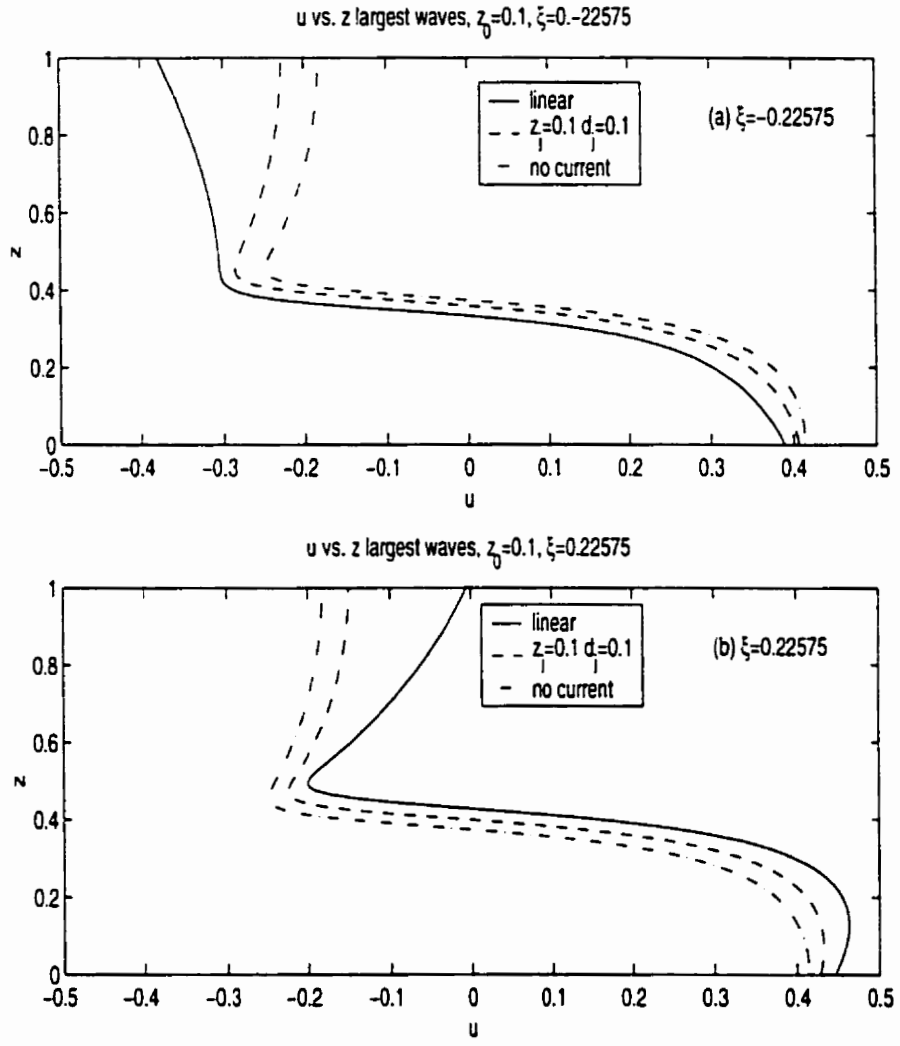

Figure 3.42: u versus z, largest non-breaking wave. $z_0 = 0.1$, upper panel - $\xi = 0.22575$, lower panel - $\xi = -0.22575$. solid - linear background current, dashed - shear layer current $z_j = 0.1$, $d_j = 0.1$, dot-dashed - no current

show the vertical profiles at the wave crest of the isopycnal displacement, the Richardson number, and the total horizontal velocity along with the horizontal profile of the wave-induced horizontal velocity at the surface). Recall that the linear and shear layer background currents have matching shear (ξ) and hence do not have the same value of U^{par}.

Next we consider the $z_0 = 0.2$ case. Again we plot four waves ranging from small to large. For cases bounded above by shear instability, the largest wave possible to compute is plotted using solid lines. For cases in which the upper bound on isopycnal displacement is given by the conjugate flow amplitude a similar choice cannot be made. We chose to plot vertical profiles and horizontal profiles based on the broadest wave computed. Another valid choice would have been to plot vertical profiles based on the conjugate flow, and horizontal profiles based on an ISW computed. We have taken some care to confirm that this alternate choice would not alter the results presented.

In figure 3.43 we compare isopycnal displacements for a linear background current with four values of ξ ($\xi = -0.4515$, -0.22575, 0.0 and 0.22575). We find that η_b decreases by about one third between the $\xi = 0.22575$ and $\xi = -0.4515$ case. As in the $z_0 = 0.1$ case, we find that the location of the maximum isopycnal displacement moves upward in the water column as wave amplitude increases. Also, while the negative values of ξ yield waves that are slightly concave up in the upper part of the water column, the effect is not nearly as pronounced as in the $z_0 = 0.1$ case.

In figure 3.44 we plot the wave-induced horizontal velocity at the surface for the cases discussed above. We can see that when $\xi < 0$ the width of the wave increases markedly as the waves get bigger. Again, this is a manifestation of the decrease in conjugate flow amplitude as ξ becomes more negative.

In figure 3.45 we plot the vertical Richardson number profiles. As in the $z_0 = 0.1$ case we see that the Richardson number drops to near zero in the unstratified portions of the water column (this time there is an unstratified near-bottom region). Also, as in the $z_0 = 0.1$ case there is a tongue of reduced Richardson number in the (upward advected) stratified region, but in the $z_0 = 0.2$ case the Richardson numbers in this region do not dip below 0.3.

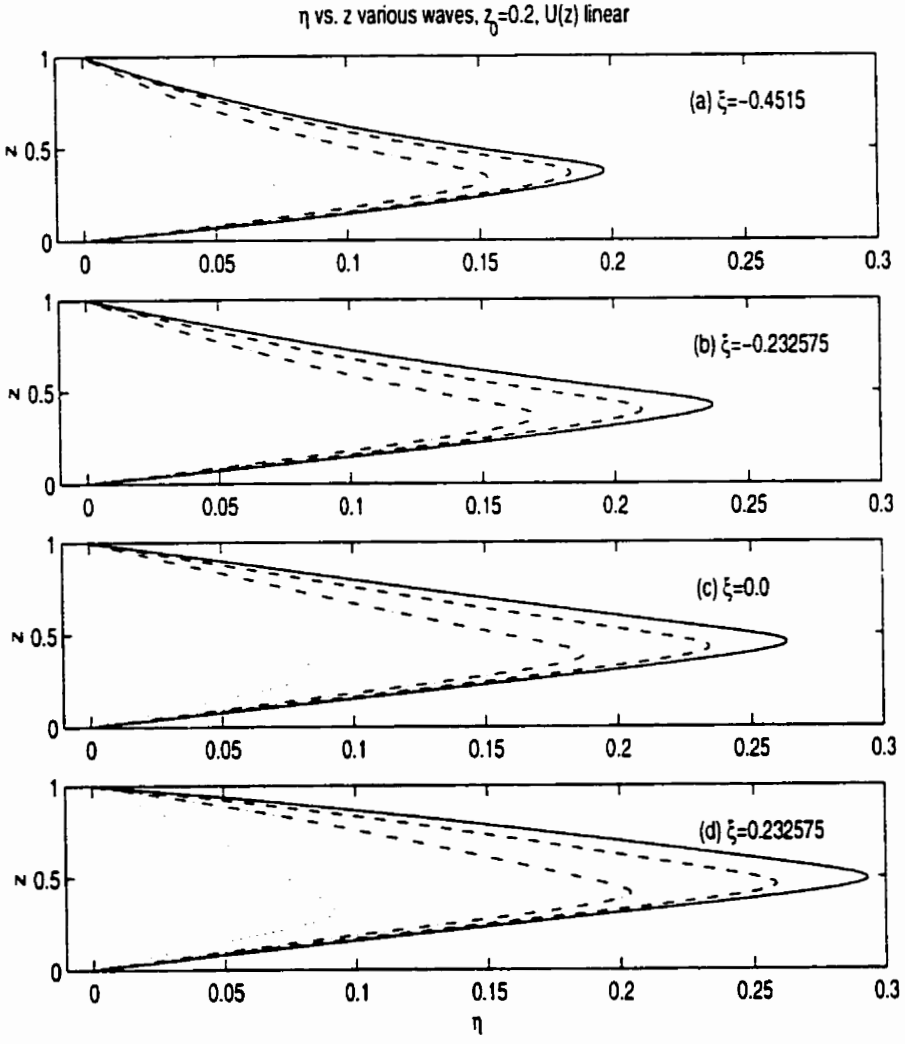

Figure 3.43: η versus z. $z_0 = 0.2$, $U(z)$ linear, various values of ξ

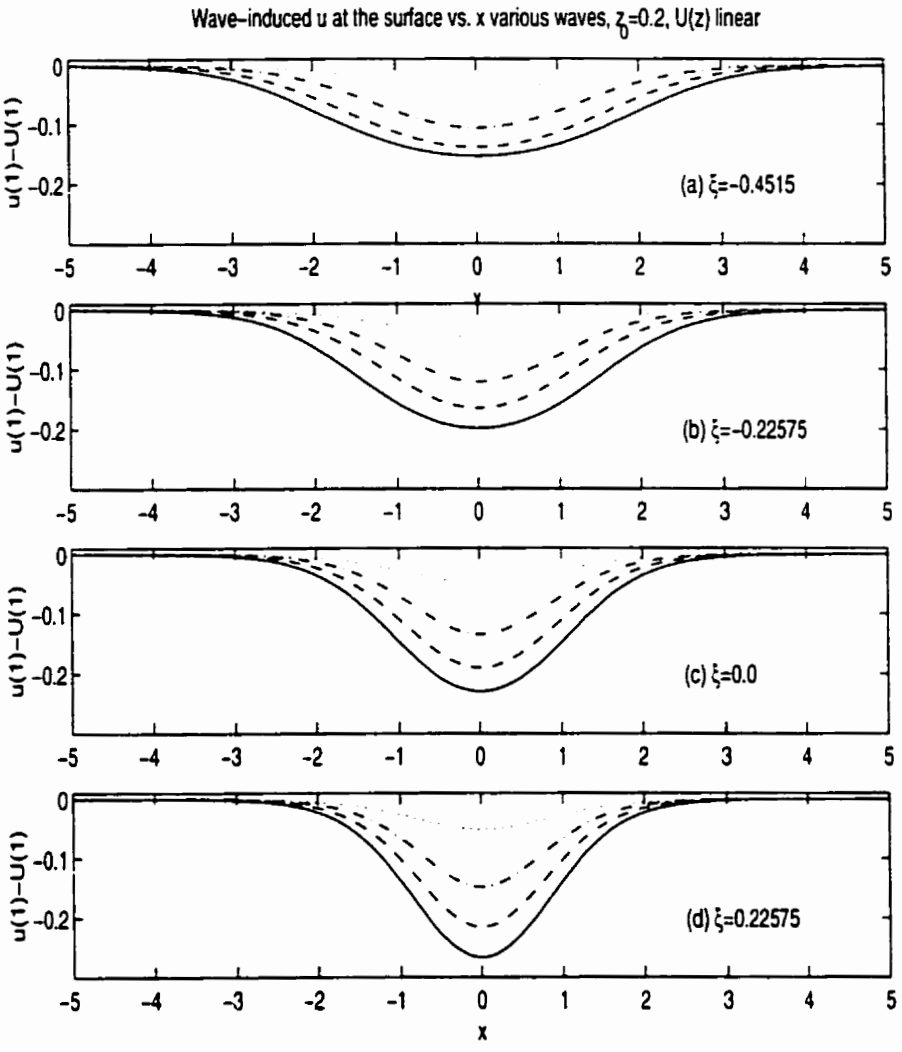

Figure 3.44: Wave-induced u versus x. $z_0 = 0.2$, $U(z)$ linear, various values of ξ

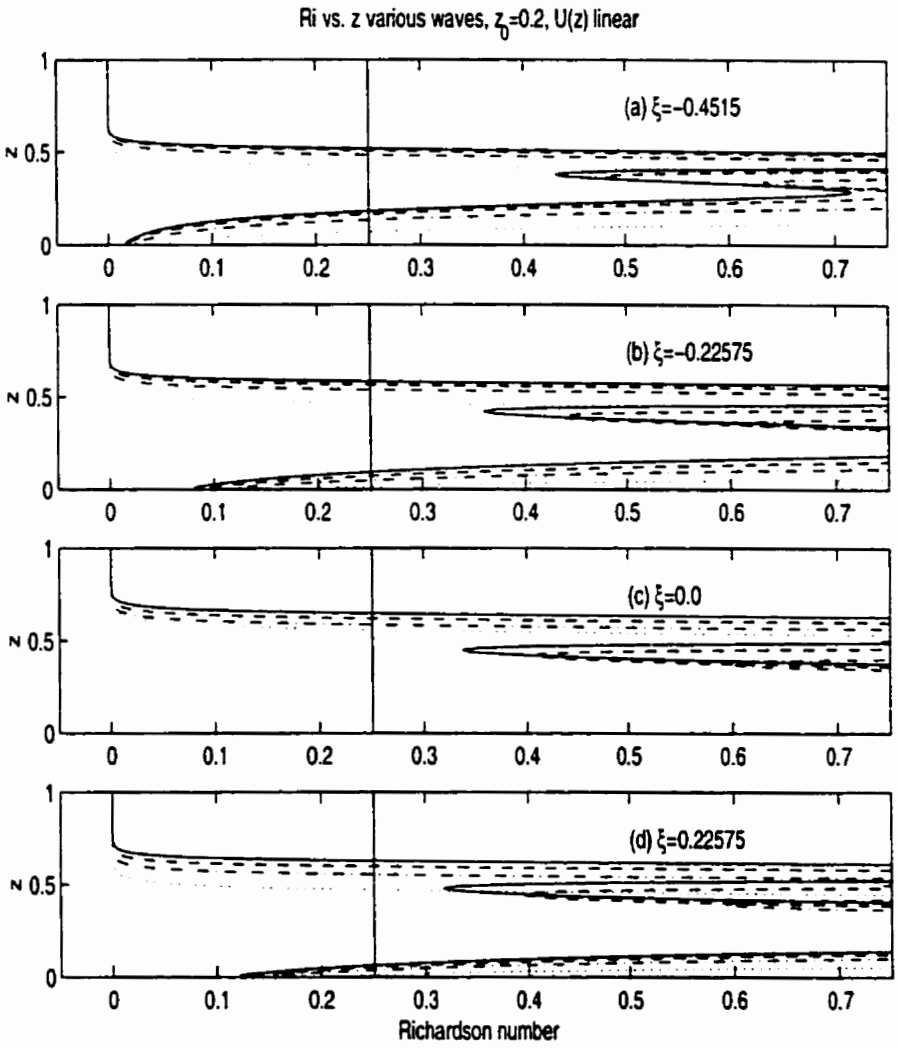

Figure 3.45: Richardson number versus z. $z_0 = 0.2$, $U(z)$ linear, various values of ξ

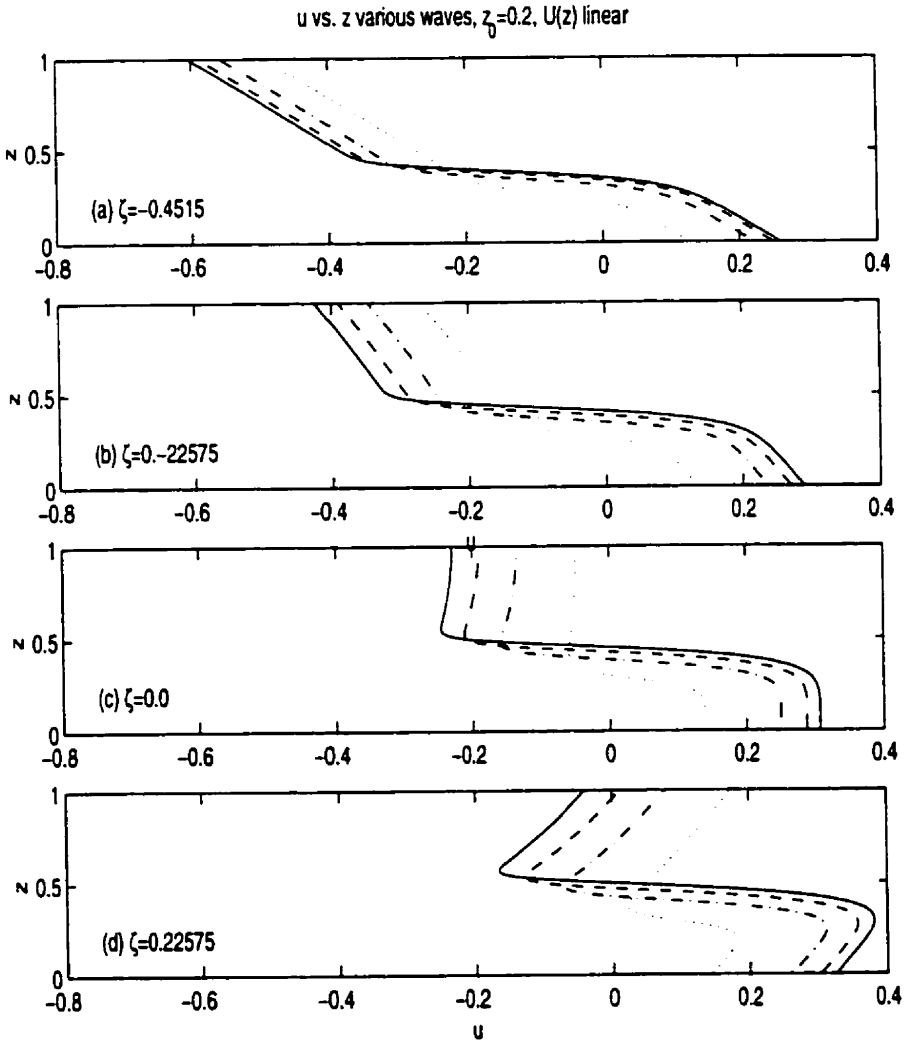

Figure 3.46: u versus z. $z_0 = 0.2$, $U(z)$ linear, various values of ξ

In figure 3.46 we plot the vertical profiles of the total horizontal velocity. Perhaps the most obvious effect is the strong role played by the background current (as seen by comparing the top and bottom panels). Also, note that for $\xi > 0$ the maximum horizontal velocity occurs well above the bottom (near $z = 0.3$ for the $\xi = 0.22575$ case).

In figure 3.47 we show the vertical profiles of η and the Richardson number at the wave crest, for the largest non-breaking wave computed for various values of ξ, and all three values of z_0. Again we can see that as ξ becomes more negative the wave amplitude decreases quite profoundly. We can also note that the wave amplitude decreases as z_0 increases. Note also that in the bottom portion of the water column the larger z_0 is, the slower the increase in η with z.

While all cases have η_b approach zero as ξ decreases, only the $z_0 = 0.3$ exhibits polarity reversal. The wave of depression shown for the $z_0 = 0.3$ case has a markedly different vertical structure from the waves of elevation.

For the Richardson number versus z curves, due to the scale chosen, not all of the waves are clearly visible. It can be readily seen that only the $z_0 = 0.1$ case has the Richardson number dip to near (in fact slightly below in one case) 0.25 in the stratified portion of the water column.

Before concluding this section, we make a couple of comments about the effect of the geometric shape of the background current: We have found that shear layers centered at the center of the pycnocline have a much greater effect on the wave properties than a shear layer centered well away from the pycnocline. Furthermore, thicker shear layers yield results closer to the case of a linear background current. We found that changing the geometric shape of the background current did not change the qualitative nature of the half-width versus η_{max} curves. However, changing the geometric shape of the background current does influence whether η_{max} is bounded above by wave breaking, shear instability, or the conjugate flow amplitude. In particular strong shears in the interior of the water column can lead to shear instability. As there are many possible geometric configurations for the background current the present work merely scratches the surface of what is possible. It thus seems sensible to the author, to proceed by using oceanic measurements on a case by case basis in the future (with the results for linear currents providing a guide to what is expected to occur).

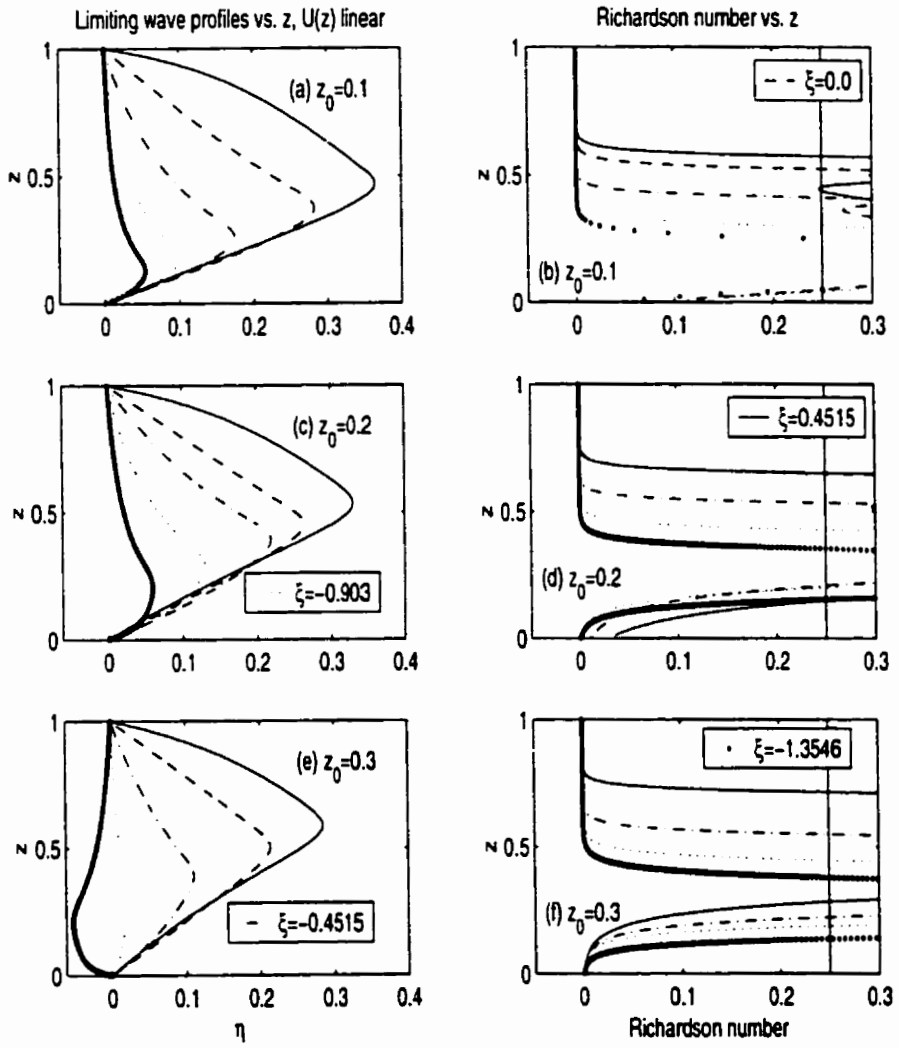

Figure 3.47: η and Richardson number versus z for largest, non-breaking wave computable, $z_0 = 0.1, 0.2, 0.3$, $U(z)$ linear, various values of ξ

3.1.8 A summary of findings

To summarize, then, it was found that the presence of a background current affects wave properties ranging from the amplitude of the maximum, non-breaking wave computable using the variational algorithm to the shape of the η versus z profile at the crest of the wave. The effects of a weak background current were consistent for stratifications with and without a conjugate flow. However, for stratifications for which a conjugate flow can be found, the presence of a background current can strongly affect the conjugate flow amplitude when the background currents are strong. This means that cases with background currents with $\xi < 0$ can exhibit very wide waves at what would be moderate amplitudes if no background current was present. Conversely, cases with background currents with $\xi > 0$ may exhibit waves that displace the center of the pycnocline well past the mid-depth before reaching the conjugate flow amplitude. Often the amplitude of waves with $\xi > 0$ is bounded above by shear instability of the variational algorithm rather than the conjugate flow amplitude.

For stratifications in which wave breaking is possible the presence of a background current with $\xi < 0$ can greatly reduce the breaking amplitude. Conversely a background current with $\xi > 0$ can lead to shear instability of the variational algorithm before a breaking wave is reached.

While it is impossible to be exhaustive on the question, an attempt was made to investigate the role of the geometric shape of the background current. It was found that shear layers centered at the center of the pycnocline had much more pronounced effects on the wave properties compared to shear layers centered outside the pycnocline. It was also found that broader shear layers with the same maximum vorticity, behaved more like linear background currents than narrower shear layers. Waves with regions of strong shear in the interior of the water column tended to have η_b bounded by shear instability.

In conclusion, the author believes that the results clearly show that the presence of a background current can have a much more pronounced effect on ISWs than merely to change the wave half-width and propagation speed. This is even more apparent when time dependent phenomena are considered, as will be done (briefly) in the following section.

Finally, at the risk of belabouring an obvious point, we make a comment on symmetry of waves

of depression and elevation under the Boussinesq approximation and in the presence of currents. Recall that the Boussinesq approximation implies that with no background current ISWs with the same amplitude of maximum isopycnal displacement for the case $(z_0, d) = (0.2, 0.05)$ and the case $(z_0, d) = (0.8, 0.05)$ will be antisymmetric in the sense that the former are waves of elevation, and the later waves of depression. What is more, the wave induced currents at the bottom for the former, match those at the surface for the latter, and *vice versa*. The propagation speed is identical. However if we now add a non-constant background current to both stratifications, say,

$$U(z) = z$$

To recover the symmetry, say we add the above current to the case $(z_0, d) = (0.2, 0.05)$, then we must add the current,

$$U(z) = 1 - z$$

to the $(z_0, d) = (0.8, 0.05)$ case (recall all quantities are dimensionless).

3.2 Miscellaneous Consequences

The results for steady waves of the previous section have various consequences for the time evolution of both ISWs and more general disturbances. In this section we briefly outline some time dependent phenomena and discuss how they are related to the results of the previous section. We discuss solutions of the Euler equations only, using the numerical model of Lamb ([31]). All simulations are discussed in dimensional variables.

We begin by examining the phenomenon of polarity reversal. Recall that in the previous section we found that with $z_0 = 30.0$ ($z_0 = 0.3$ in dimensionless form) and a large enough linear background current oriented against the direction of wave propagation, a stratification of the type given by (3.7), which would produce waves of elevation with no background current yielded waves of depression. To test this prediction we consider an initial disturbance given by (3.6) and impose a background current given by

$$U(z) = 6.0\frac{z}{H}.$$

The computational grid is regular in both the horizontal and vertical, with a grid spacing of 2 m and 1 m in the two directions, respectively. The initial disturbance breaks up into two wave trains. For the train propagating rightward the background current is oriented with the direction of propagation, and hence will not change wave polarity. For the wave train propagating leftward, however, the background current is oriented against the direction of propagation and the results of the previous section predict ISWs with an opposite polarity. To demonstrate this consider the series of contour plots of the density fields in figure 3.48. After approximately 700s the rightward propagating train of ISWs leaves the computational domain and hence the final panel shows only the leftward propagating disturbance which takes the form of a steadily broadening undular bore. Recall that according to WNL for the KdV equation (consistent with inverse scattering theory) an undular bore evolves from a disturbance that has the opposite polarity to solitary waves.

In figure 3.49 we show the contours of the horizontal velocity. At 600 s we can see the leftward propagating bore in an early stage of development as well as the rank-ordered, rightward propagating train of ISWs. Notice that the background current is strong enough that the wave

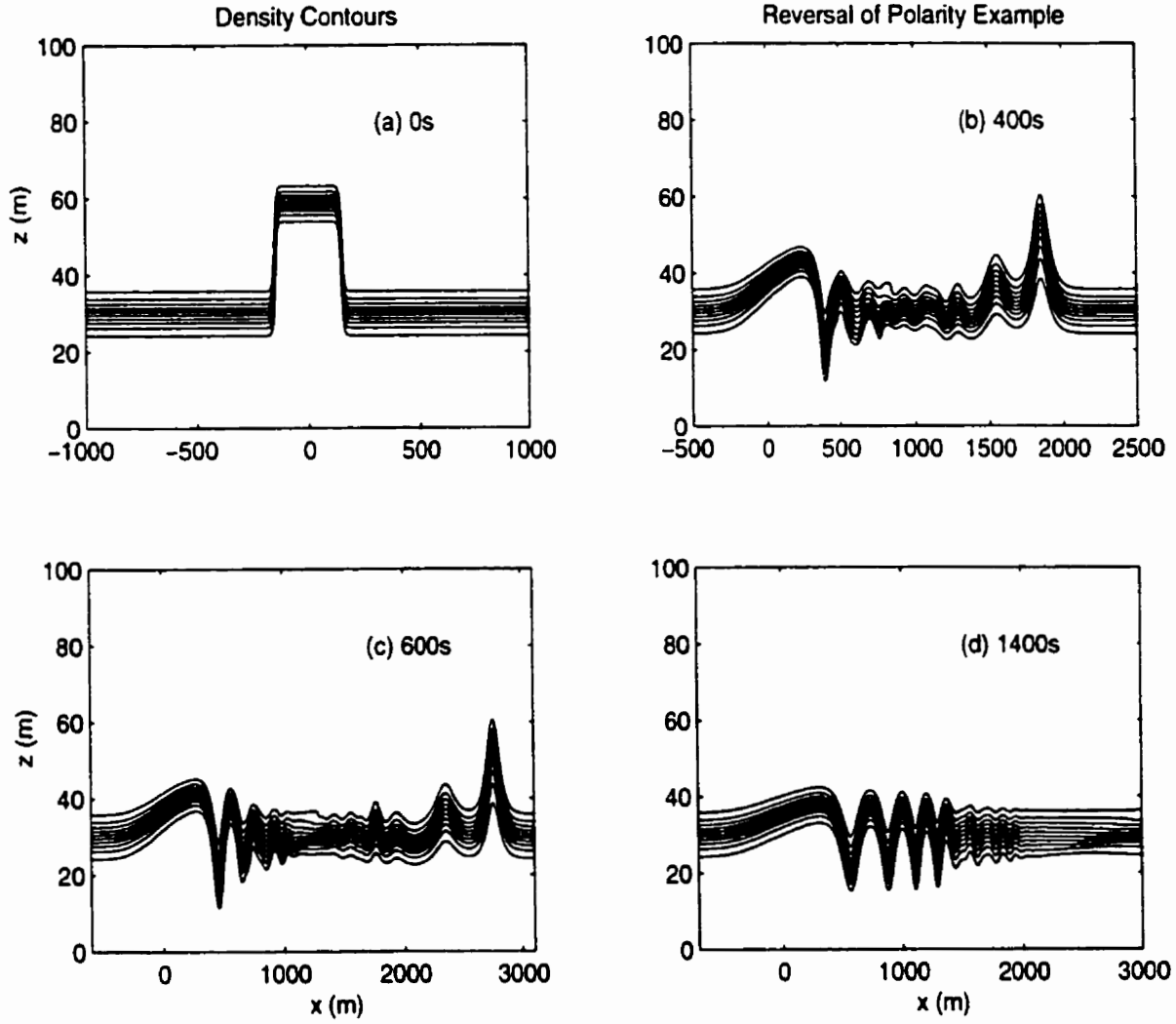

Figure 3.48: Density contours for sample run with background current strong enough to influence wave polarity.

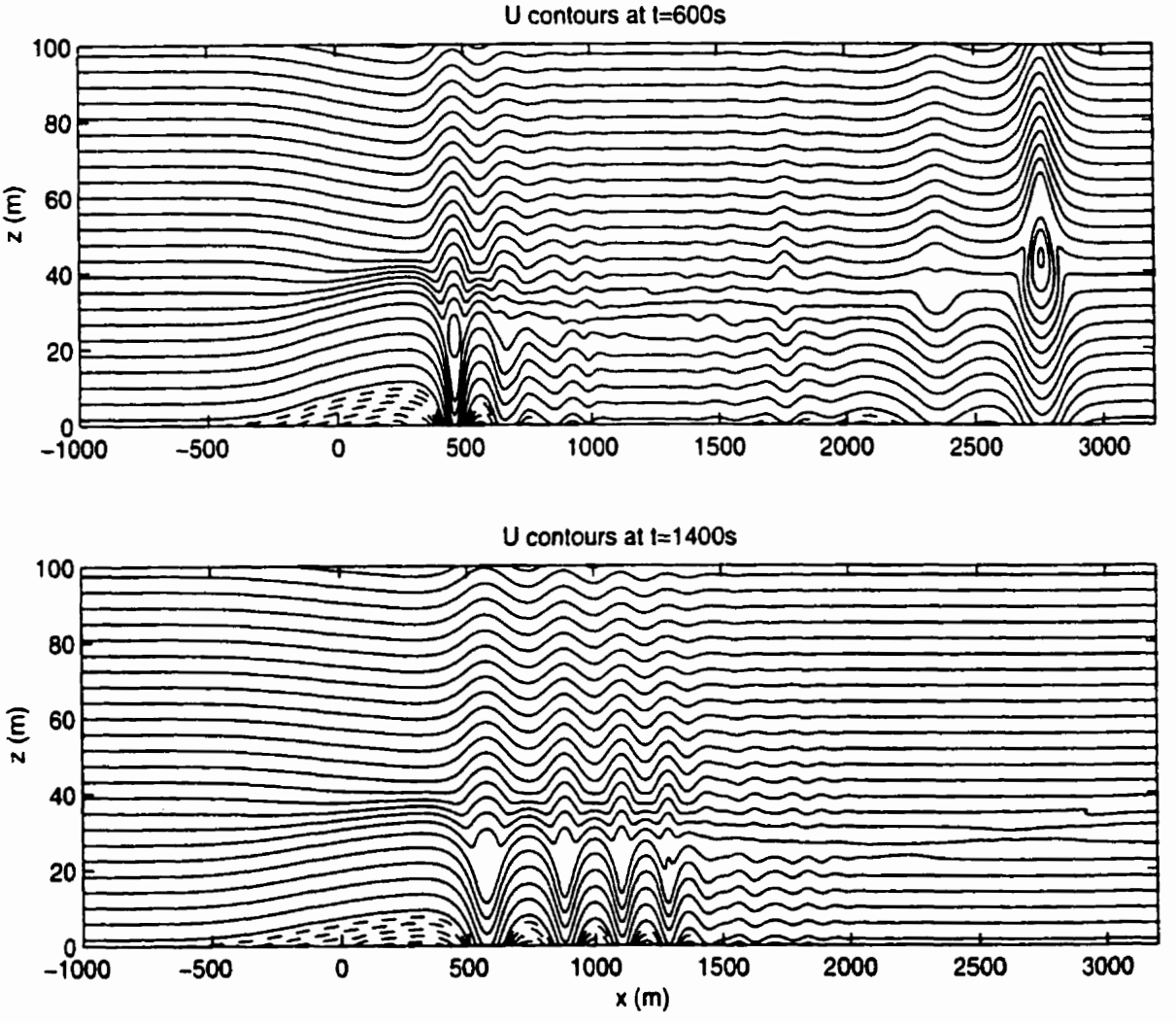

Figure 3.49: Horizontal velocity contours for sample run with background current strong enough to influence wave polarity

induced currents due to the rightward propagating waves do not induce negative (total) horizontal currents. In contrast the leftward propagating bore does induce (total) negative currents (in the near bottom region where the background current is weak).

Finally, in figure 3.50 we plot vertical profiles of horizontal velocity (left panel) and horizontal wave-induced velocity (right panel) at three different locations. Two of the profiles shown are at the crest of the leading rightward propagating ISW and the trough of the leading wave of the leftward propagating undular bore. The crest and trough are identified by using the local maxima/minima of the horizontal velocity at the surface. The third vertical profile is taken near the maximum of the rise which leads the undular bore. As such there is no unique way to choose its location and hence this profile is meant only for a qualitative comparison with the other two. These profiles are included to point out the profound difference in vertical structure between the ISW propagating with the current and the undular bore propagating against it.

In conclusion, then, the predictions of reversal of polarity based on the results of the variational method discussed in the previous section are borne out in time dependent calculations.

We wish to examine whether some of the ISWs that fission from an initial condition exhibit a critical layer. Towards this end we consider a 2000 by 100m domain with a grid resolution of 1 by 1m. To keep the computational domain as small as possible (and hence the resolution as high as possible) we take

$$U(z) = 3.0 - 3.0\frac{z}{H}.$$

We also move the center of the initial step-like disturbance to $x = -500.0$. The initialization is otherwise unchanged from subsection 3.1.1 ($(z_0, d) = (0.3, 0.05)$ and the initial density is given by equations 3.5 and 3.6). This choice of grid and initialization keeps the waves of interest in the computational domain for a long enough time for the ISWs to fission from the initial disturbance. In figure 3.51 we show the density contours at $t = 0$, 200 and 2000s. At 200s we can see that the waves furthest to the right in the contour plots are broader then those furthest to the left. Note that both trains of ISWs shown propagate to the right. It is the slower moving wave train that we are interested in, and by 2000s it is clear that only the leading two waves of this wave train remain in the computational domain.

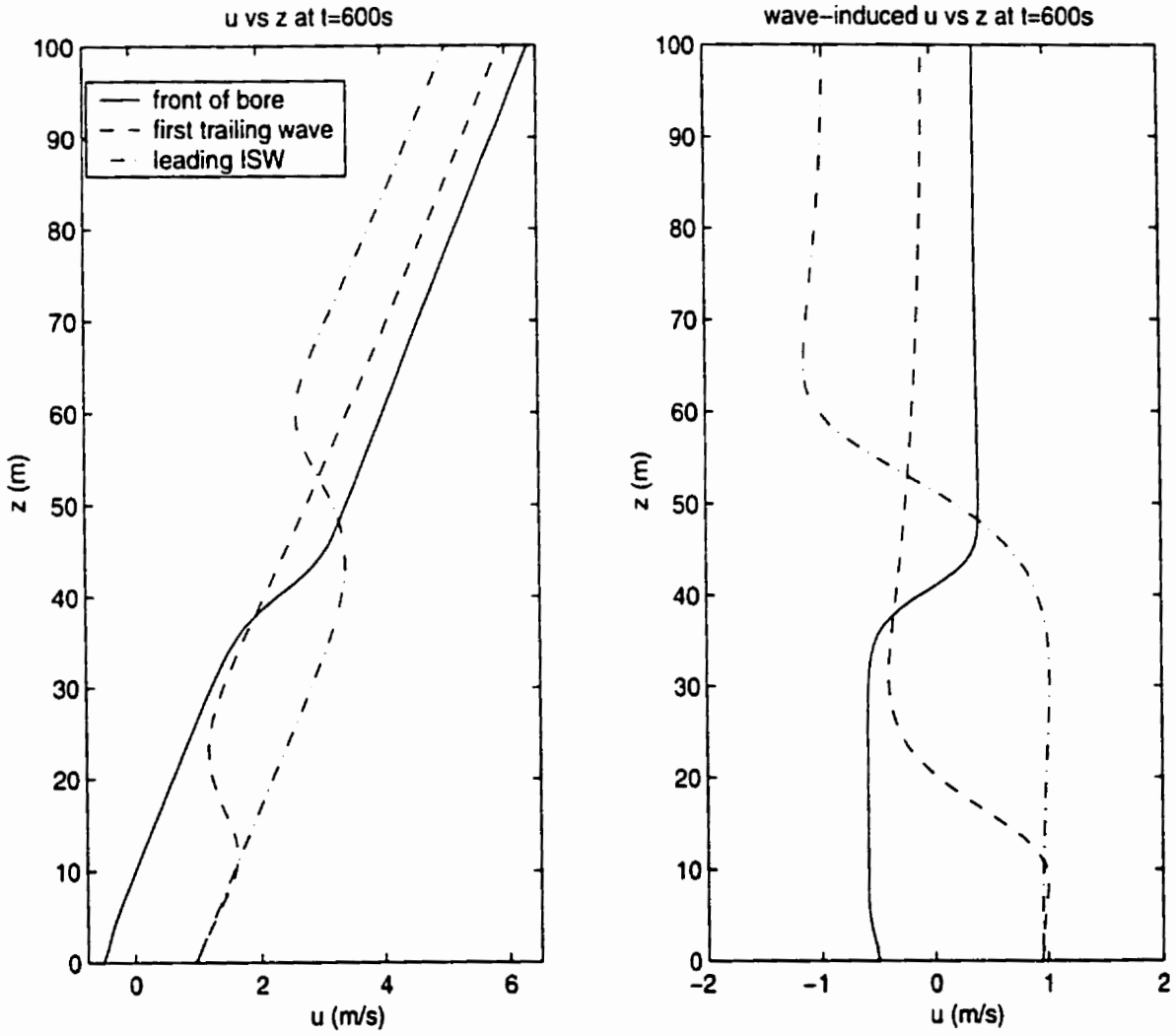

Figure 3.50: Horizontal velocity (left panel) and wave-induced horizontal velocity (right panel) vs. z at $t = 600$s. Crest of elevation at front of undular bore - solid, crest of first wave in the undular bore - dashed, crest of leading ISW - dot-dashed

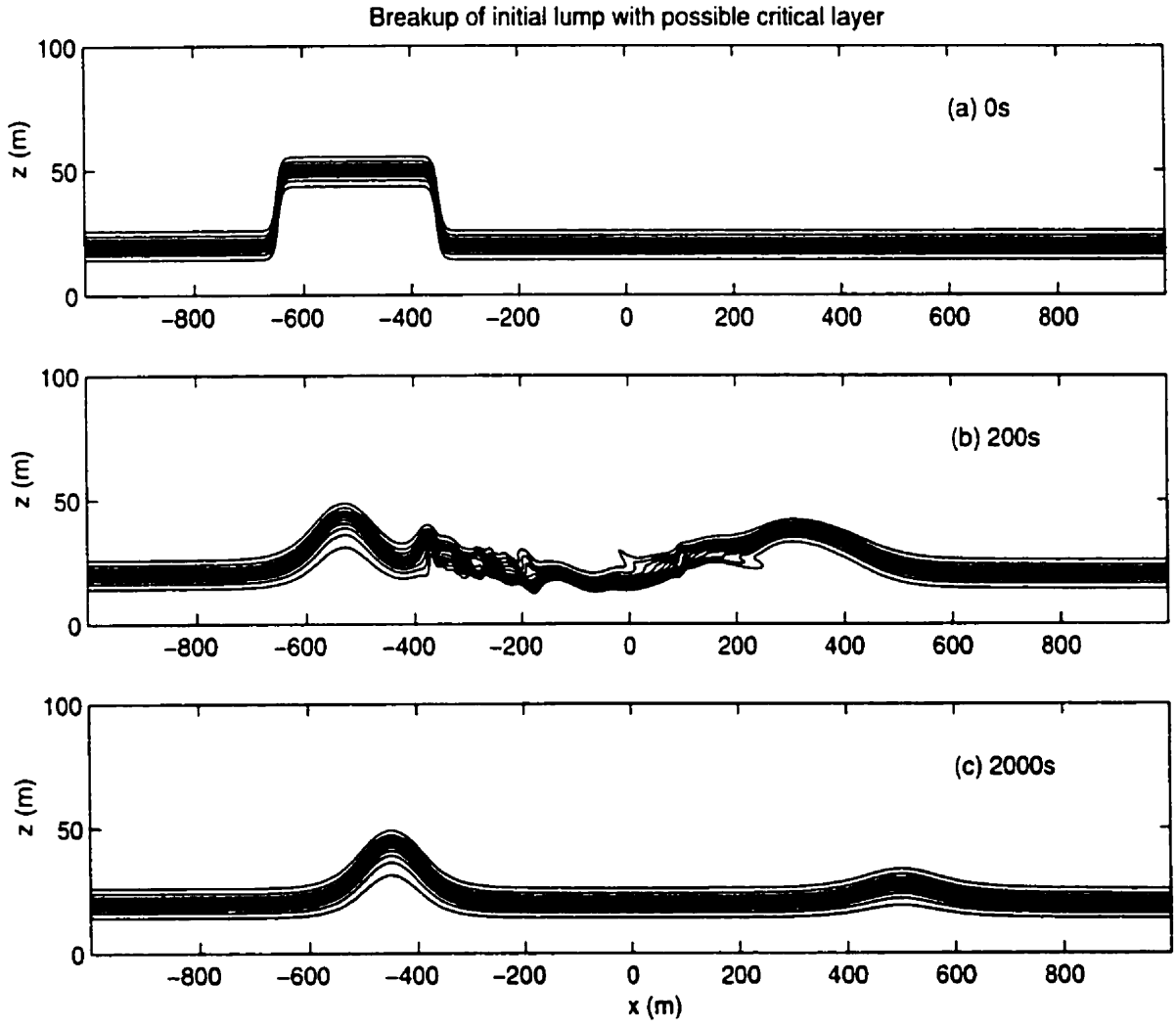

Figure 3.51: Density contours $t = 0$, 200 and 2000s

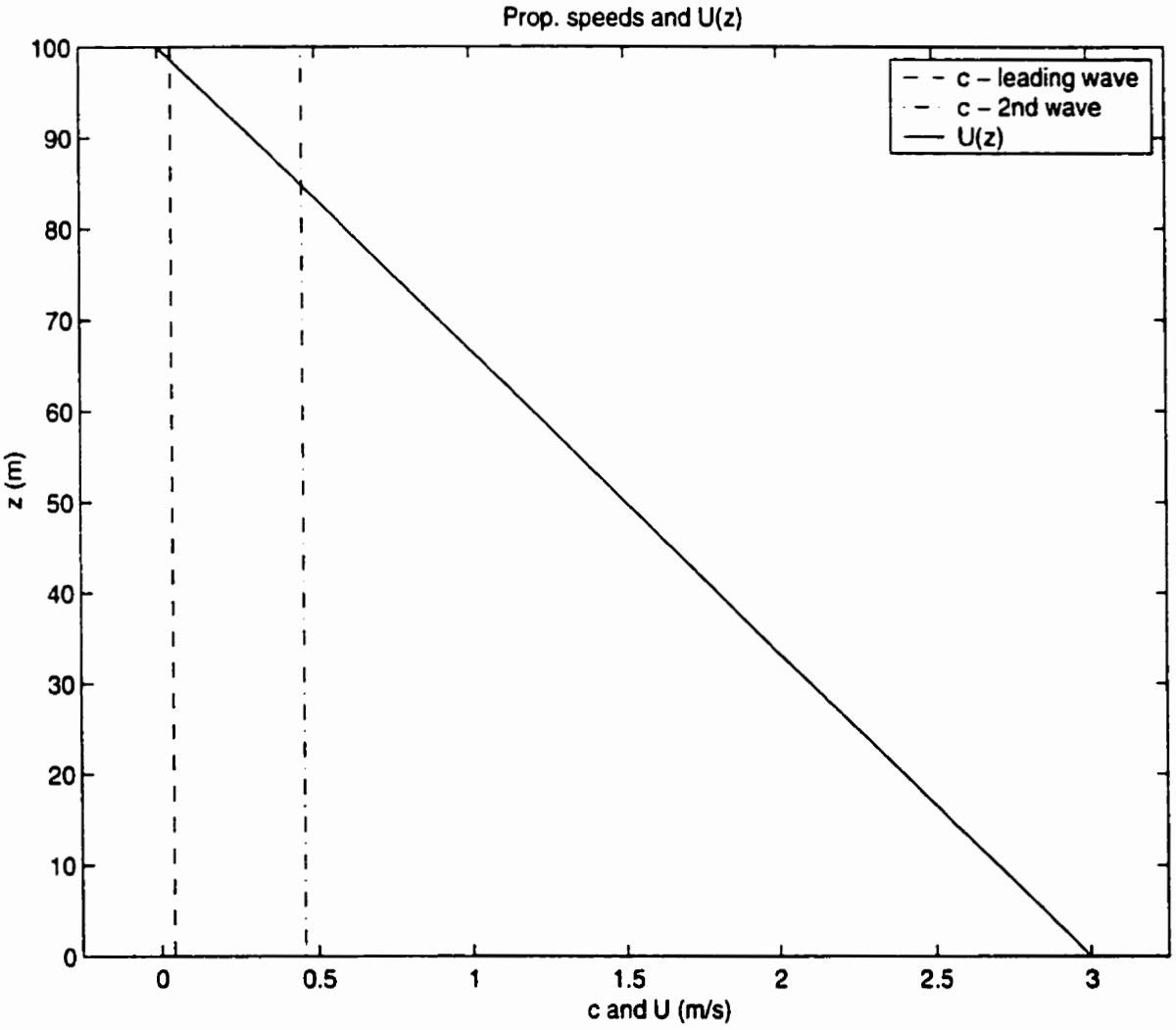

Figure 3.52: Background horizontal velocity profile and approximate propagation speeds of the two leading rightward propagating ISWs

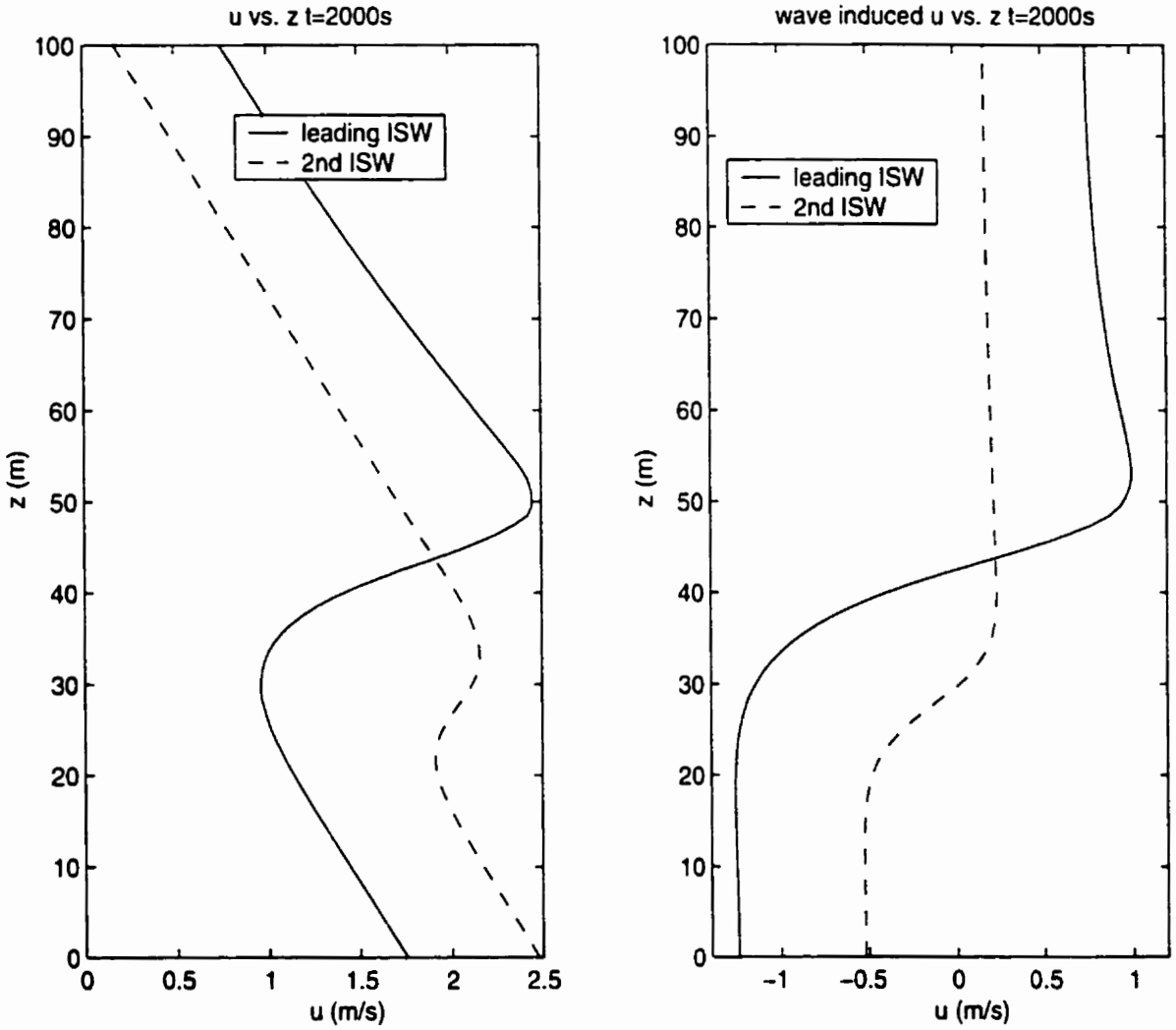

Figure 3.53: Horizontal velocity (left panel) and horizontal wave-induced velocity (right panel) profiles. leading wave - solid, 2nd wave - dashed, $t = 2000$s.

The approximate propagation speeds of the two waves of interest are calculated in the following manner. We find the location of local maxima of the horizontal, wave-induced velocity at the surface at successive output times. The difference between the successive locations divided by the time interval between output times then gives an estimate for the wave propagation speed. Due to the discretization of the space variable the values calculated using the above described method will vary slightly with time. For this reason we calculate approximate propagation speeds for output times separated by 100s starting at 1000s and ending at 2000s. We then average the resulting values to get final estimates. Using this technique for the present grid spacing the results shown in figure 3.52 are accurate to two decimal places, more than enough for our purposes. From figure 3.52 we see that both the leading and second waves have a propagation speed between the minimum and maximum value of the background current. Since both WNL and the fully nonlinear algorithm utilize terms of the form

$$\frac{G}{U(z)-c}$$

where G is not identically zero, neither can successfully compute waves when $U(z) = c$ for some z. Yet the time evolution proceeds much as predicted by KdV theory. What is more, neither the contours of horizontal velocity shown in figure 3.51 nor the vertical profiles of horizontal velocity shown in figure 3.53 show any appreciable differences from waves calculated using the variational algorithm. Thus we can conclude that the fully nonlinear, time-dependent simulations yield ISWs for a broader range of background current maxima and minima than the variational algorithm. The variational algorithm in turn yields ISWs for a broader range of background current maxima and minima than WNL (as was discussed in the previous section).

Finally we can ask whether we can construct a simple situation in which an initial condition like the one used above does not yield any ISWs. Towards this end consider a density profile of the type 3.7 with $z_0 = 20.0$ ($z_0 = 0.2$ in dimensionless form) $d = 5.0$ ($d = 0.05$ in dimensionless form), a step-like initial condition centered at $x = 0.0$ (details as in the above examples) and a horizontal background velocity given by

$$U(z) = 4.0 - 8.5\frac{z}{H}.$$

This current is chosen so that a rightward propagating undular bore (hence no ISWs) fissions from the initial disturbance. We are interested in whether an ISW wave train fissions to the left of $x = 0$. The computational domain is 3000m wide and 100m deep with a grid spacing of 1.5 by 1m.

In figure 3.54 we plot the density contours of the disturbance at times ranging between 0 and 7000s. From this figure we see that instead of a rank ordered train of ISWs, a pair of waves fissions from the initial condition. This pair of waves appear to move with the same speed (and hence maintain the same distance from one another). At $t = 1000$s the leading, leftmost wave appears to be slightly smaller in amplitude. Subsequently the pair decays, with the second, or rightmost wave decaying more quickly. This behaviour is reminiscent of the breather solution of the mKdV equation (see [53] for example). In the breather, however, the two disturbances pulsate without losing energy.

To get a more precise idea of what is happening we focus on the wave-induced horizontal velocity at the surface.

In figure 3.55 we plot the wave-induced horizontal velocity at the surface for a sequence of times at 200 s intervals, starting at 600 s and ending with 2000 s. From this sequence it is clear that the initially larger leftmost disturbance decays until about 1200s. At the same time the rightmost disturbance grows slightly. After this, the rightmost disturbance decays, while the leftmost disturbance remains virtually unchanged, decaying slightly. The total disturbance decays with each cycle. This decay is clearly shown in figure 3.56 where the wave-induced horizontal velocity at the surface is plotted at 1000 s intervals ranging from $t = 1000$ s to $t = 7000$ s. The evolution of the amplitudes of the two waves at early times is seen much more clearly in figure 3.57 where we plot the values of $u(H)$ at the two local maximuma as functions of time, as well as the ratio of $u(H, t)$ to $u(H, 1400)$ for the leftmost maximum. Furthermore, it is clear that the total disturbance decays with each cycle. This decay is clearly shown in figure 3.56 where the wave-induced horizontal velocity at the surface is plotted for a sequence of times ranging from 1000s to 7000s, separated by 1000s. From this figure we can also see that as the breather-like wave decreases in amplitude its leftward propagation speed decreases and it is advected to the

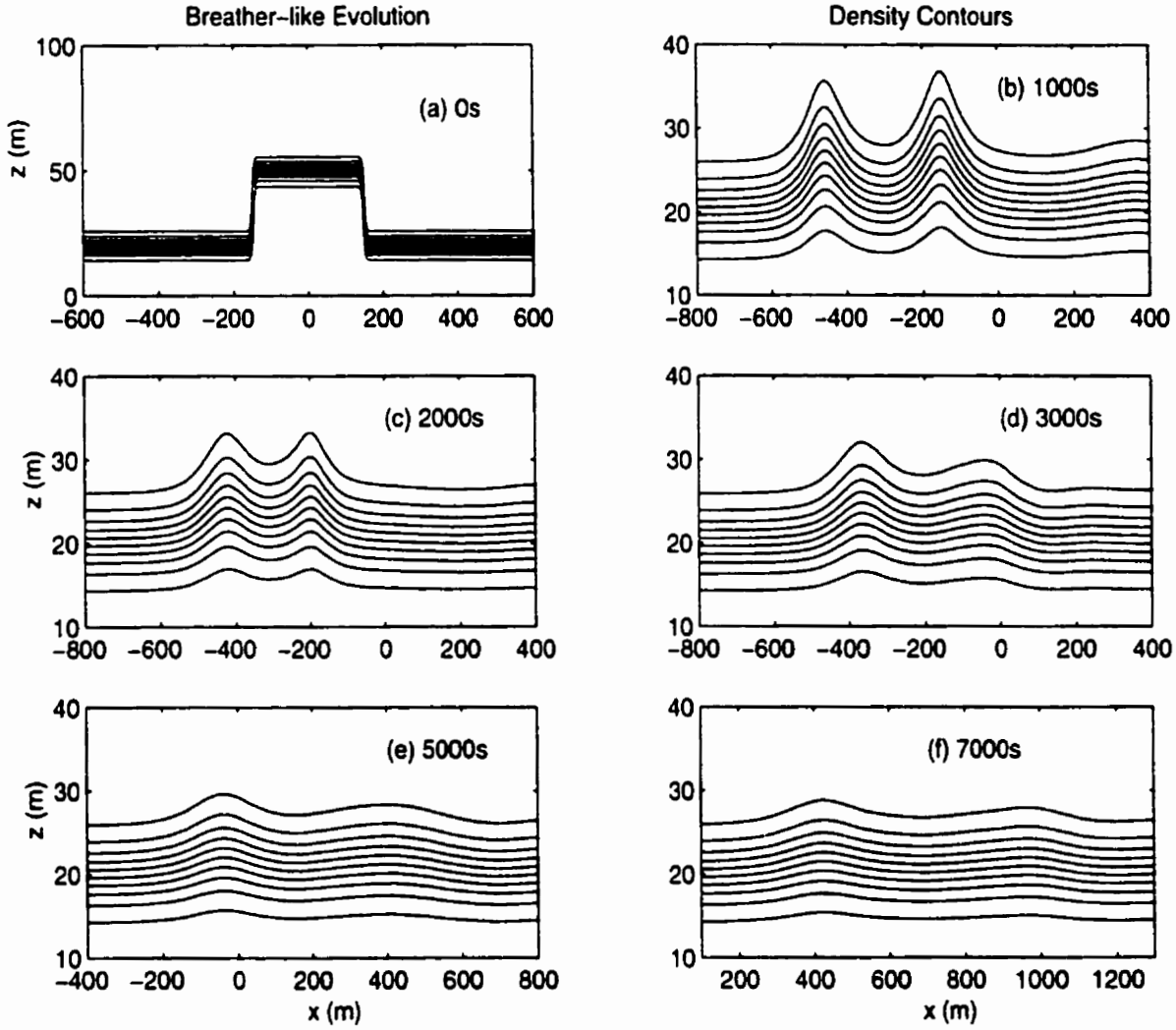

Figure 3.54: Density contours for leftward propagating, breather-like disturbance $t = 0$, 1000, 2000, 3000, 5000 and 7000s

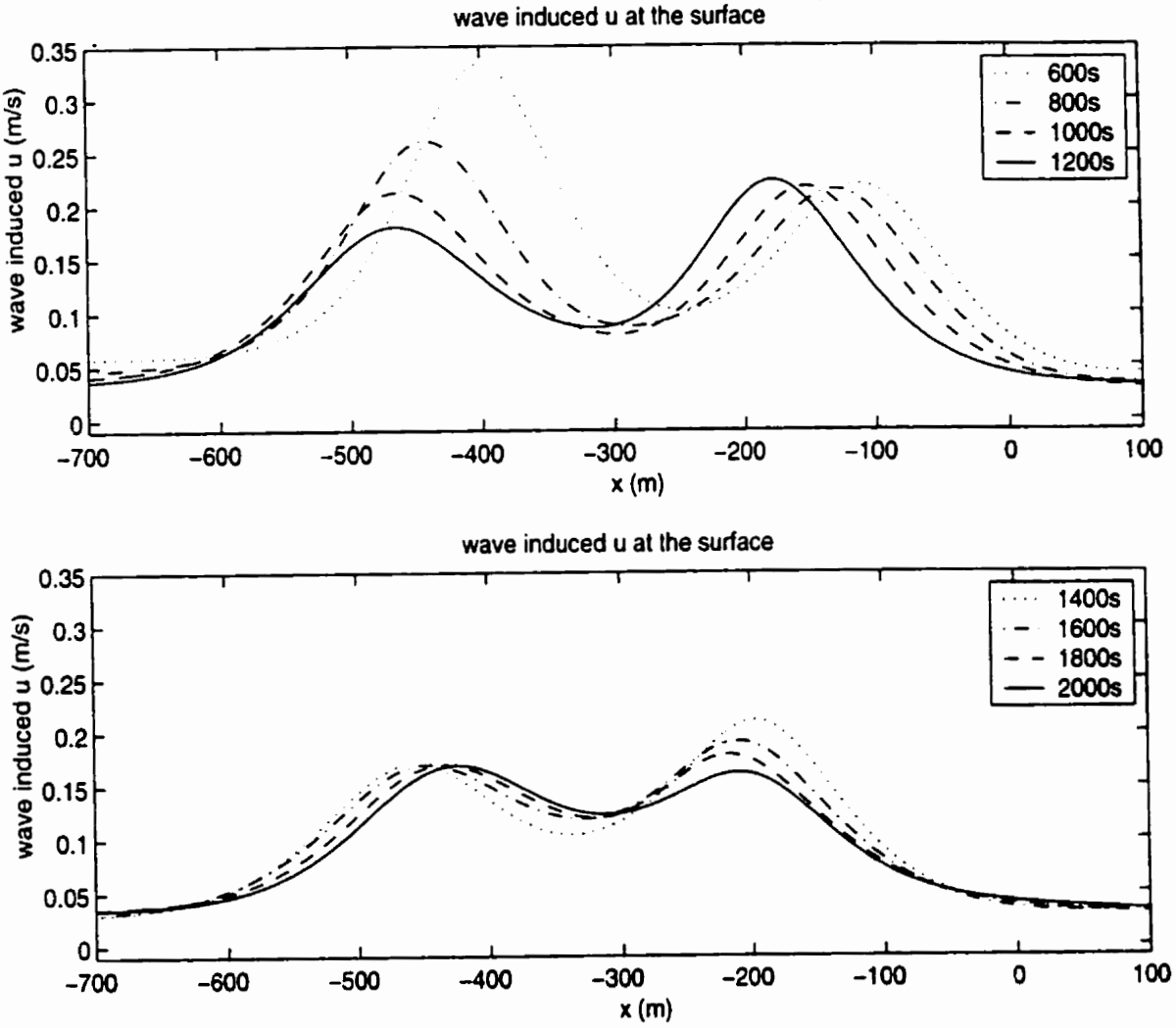

Figure 3.55: Wave-induced horizontal velocity at the surface. t = 600, 800, 1000, 1200, 1400, 1600 and 2000s

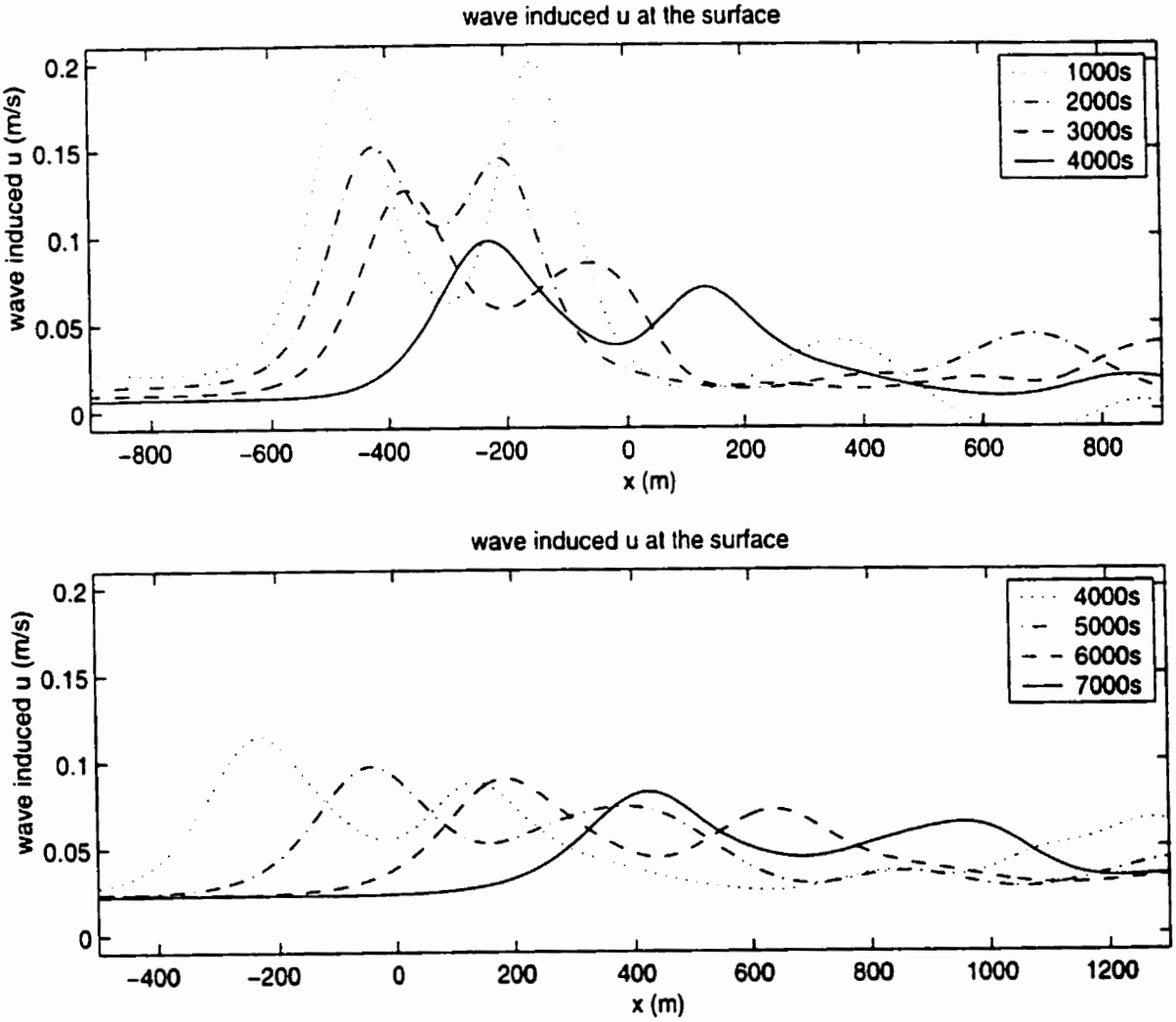

Figure 3.56: Wave-induced horizontal velocity at the surface. t = 1000, 2000, 3000, 4000, 5000, 6000 and 7000s

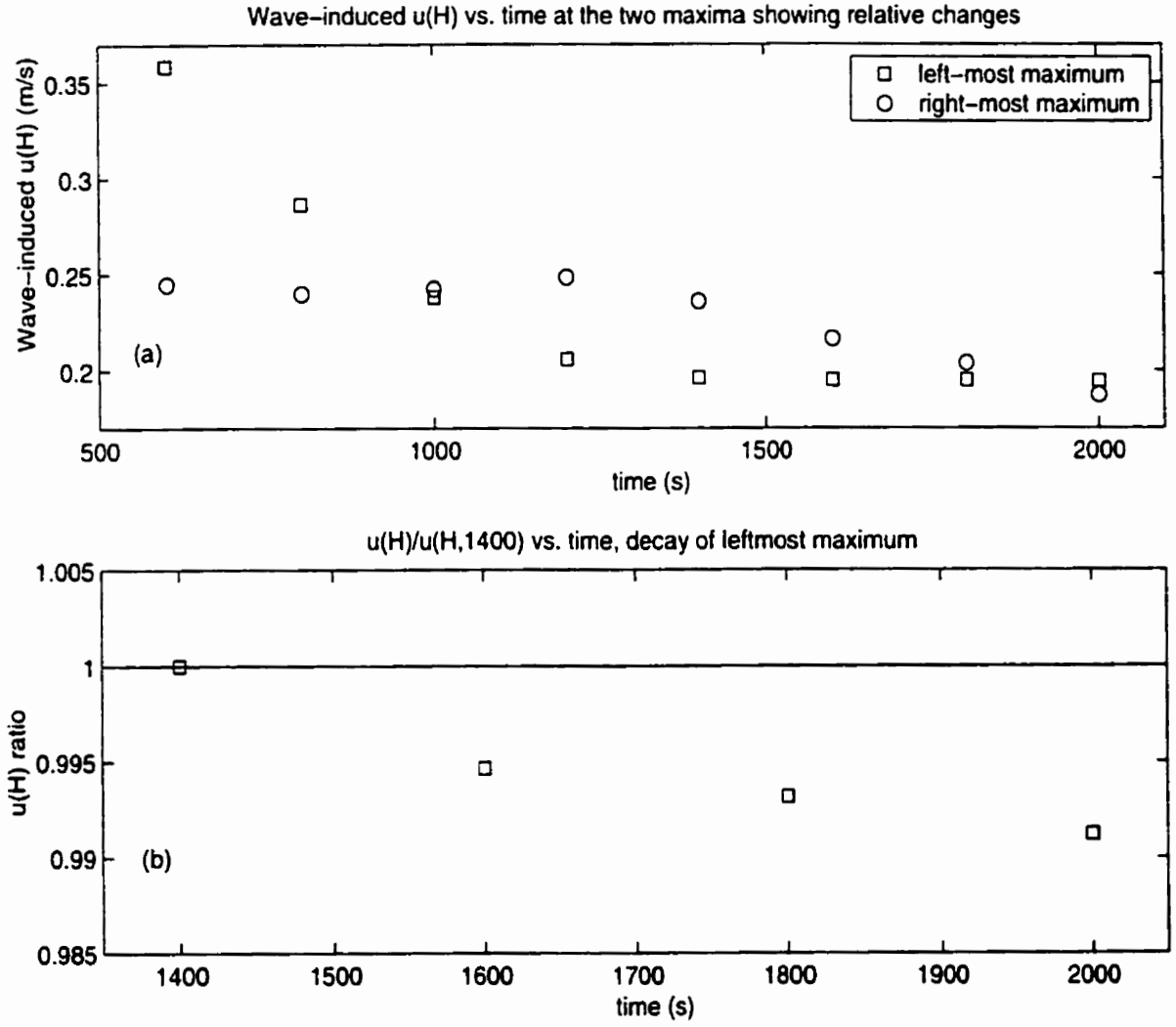

Figure 3.57: Wave-induced velocity at the two maxima vs. time, (panel (a)), and the ratio of $u(H,t)$ to $u(H,1400)$ vs. time, (panel (b)), showing the slow decay of the left-most disturbance

right by the depth averaged background current.

Thus, using the results of the previous section, we were able to construct a rather simple situation in which an initial disturbance did not yield a train of ISWs in either direction. At the time this section is being written there is no theoretical explanation available for the appearance of the breather-like wave. This concludes our brief examination of some time dependent consequences of the steady wave results found in the previous section.

3.3 Conclusions and Literature

In this chapter we have explored in some detail, the behaviour of large, fully nonlinear ISWs. We began by showing that, for a stratification taken from field measurements, WNL cannot successfully be used to represent the spatial structure of large ISWs (as calculated by the variational technique presented in the previous chapter).

The major issue addressed in this chapter is the effect of background currents on fully nonlinear ISW properties. In general we found that the presence of a background current can greatly alter the wave properties (such as the wave half-width and the shape of the vertical profile of η at $x = 0$, the wave crest). Perhaps more importantly, as the amplitude of the background current varies, so does η_b, the maximum isopycnal displacement of the largest non-breaking wave computable. Furthermore the type of upper bound may change, i.e. for stratifications with density change right to the ocean bottom, waves of elevation may be bounded above by wave-breaking or by shear instability, while for stratifications with a mixed layer adjacent to the ocean bottom waves of elevation may be bounded above by the conjugate flow amplitude or by shear instability. Note however that in no circumstances did the presence of a background current change an upper bound due to conjugate flow to one due to wave-breaking. This is due to the thin pycnoclines used in the present study. A stratification with a thicker pycnocline (such as $(z_0, d) = (0.3, 0.15)$ can have the upper bound change from one due to conjugate flow to one due to breaking, as ξ becomes more negative (with a linear background current).

An attempt was also made to investigate what role the geometric shape of the background current plays. While it is not possible to be exhaustive, we have found that shear layer background currents centered at the center of the pycnocline had a much larger effect on the wave properties compared to shear layer background currents centered in the unstratified region well away from the pycnocline. Also, as can be expected, thicker shear layers led to effects more closely matching those of linear currents. Finally, background currents with strong shears in the interior of the water column had upper bounds on the wave amplitude due to shear instability of the variational algorithm.

Overall the time dependent simulations performed showed that the predictions made based on

steady ISWs computed with the variational algorithm were borne out in the simulations. The fully nonlinear waves, in turn, agreed with the qualitative predictions of WNL. Thus the variational algorithm (as well as the conjugate flow calculator, when applicable) provide a new set of tools for understanding ISWs and similar phenomena in the ocean. Notably, we also constructed a simple case for which the break up of an initial disturbance led to no ISWs in either direction. This construction used results of the variational algorithm for fully nonlinear waves that WNL simply could not provide.

In terms of the literature the present study is another chapter in a series of papers by Lamb and co-workers. Lamb and Yan ([38]) compared the evolution of an undular bore governed by the full Euler equations and various versions of WNL. They found that higher order asymptotics provided a better fit to the actual evolution, but that even these showed discrepancies in the WNL. Lamb and Wan ([37]) then addressed the correspondence between broad ISWs with a flat center and conjugate flows. In a subsequent study Lamb ([36]) discussed the simpler case of conjugate flows in a three layer fluid. This case allows a more analytically based approach. In tangential, but relevant work, Lamb discussed Lagrangian particle transport by ISWs ([32]) using both WNL and fully nonlinear waves. The generation of ISWs (an issue completely ignored in the present work) by tidal flow over the continental shelf was discussed in ([31]). Finally, in an extensive, but as of yet unpublished manuscript Lamb ([34]) showed how and when the two formulations of WNL succeed and fail to descirbe large, fully nonlinear ISWs for different classes of standard background density profiles at leading, first and second order (without a background current). The present work is an attempt to outline the need for, and utility of, the variational algorithm for ISW calculation when it comes to undertsanding ISWs in the ocean. As such it is a fairly new piece of work with little in the way of precursors. The study of Brown and Christie ([12]) is the only instance in the literature (to the author's knowledge) where fully nonlinear ISWs are calculated for continuous stratifications with an eye towards oceanic or atmospheric applications (the paper of Turkington *et al.* ([64]) which formulates the variational method extended in the previous chapter computes ISWs only to show that the algorithm works). The paper ([12]), however, attempts to put together a great many issues (ISWs, ISW broadening, ISWs past breaking, etc.) ending up, in

the author's opinion, with a somewhat unclear picture. In particular the conjugate flow concept is not utilized, and hence wave broadening is not clearly explained. ISW-like waves with trapped cores merit detailed attention and will be discussed in the following chapter.

Older work is generally based on WNL, starting with the papers of Benney ([7]) and Benjamin ([4], [5]). The former provides the basis for the WNL used in this work and the latter provides an alternative approach based on variational techniques. The extensions of WNL are many and include extensions to second order ([20]), discussion of critical layers ([44]), discussion of shear ([62]), and incorporating variable currents and topography ([69]). The survey article by Grimshaw ([22]) is a good compendium of these ideas as well as providing a full set of references. The same survey article also discusses the many attempts to compare experiment and WNL.

Finally we should note that the work of Turkington *et al.* on large, fully nonlinear ISWs is preceded by the work of Tung et al. ([63]) on fully nonlinear, mode-2 ISWs. The latter uses a different numerical approach, and in fact treats mode-1 waves only, recovering mode-2 waves from a symmetry condition. The focus on waves with closed streamlines makes this article more relevant to the material of the next chapter.

To conclude then, the present work addresses many of the questions that have appeared and re-appeared in the literature in the past 30 years. In particular, we show that the qualitative predictions of WNL are often borne out by large, fully nonlinear ISWs. However, the present results also show that large, fully nonlinear objects are more complex than the tidy solitons of WNL (see for example ([33])). The rich phenomenology of ISWs in the ocean will be explored further in the next two chapters.

Chapter 4

ISW-like Objects With Trapped Cores

To motivate the study of waves with trapped cores consider the situation of an initial ISW computed using the fully nonlinear solitary wave calculator, propagating leftward in a fluid with no current. The fluid is forced by a steady, user imposed body force that sets up a steady, linear background current. The forcing occurs over the first 1000 s of the simulation and the final background current has the form,

$$U(z) = 4.5\frac{z}{H}.$$

For the simulation shown below the forcing is simply switched off after 1000 s. Tests with a rapid damping that ensured the forcing was C^∞ revealed no change from the simulation shown below. We consider the adjustment of the ISW for two tanh-type densities (i.e. given by equation 3.7), one with $z_0 = 10.0$ m and the other with $z_0 = 20.0$ m. The computational domain is 6000.0 m long and 100.0 m deep and has a resolution of 6 by 1 meters.

In figures 4.1 and 4.2 we plot the density contours for the $z_0 = 10.0$ m and $z_0 = 20.0$ m cases respectively. It can be readily seen that the $z_0 = 20.0$ m case undergoes a great deal more wave shedding behind the initial ISW during its adjustment to the imposed current. Indeed the initial

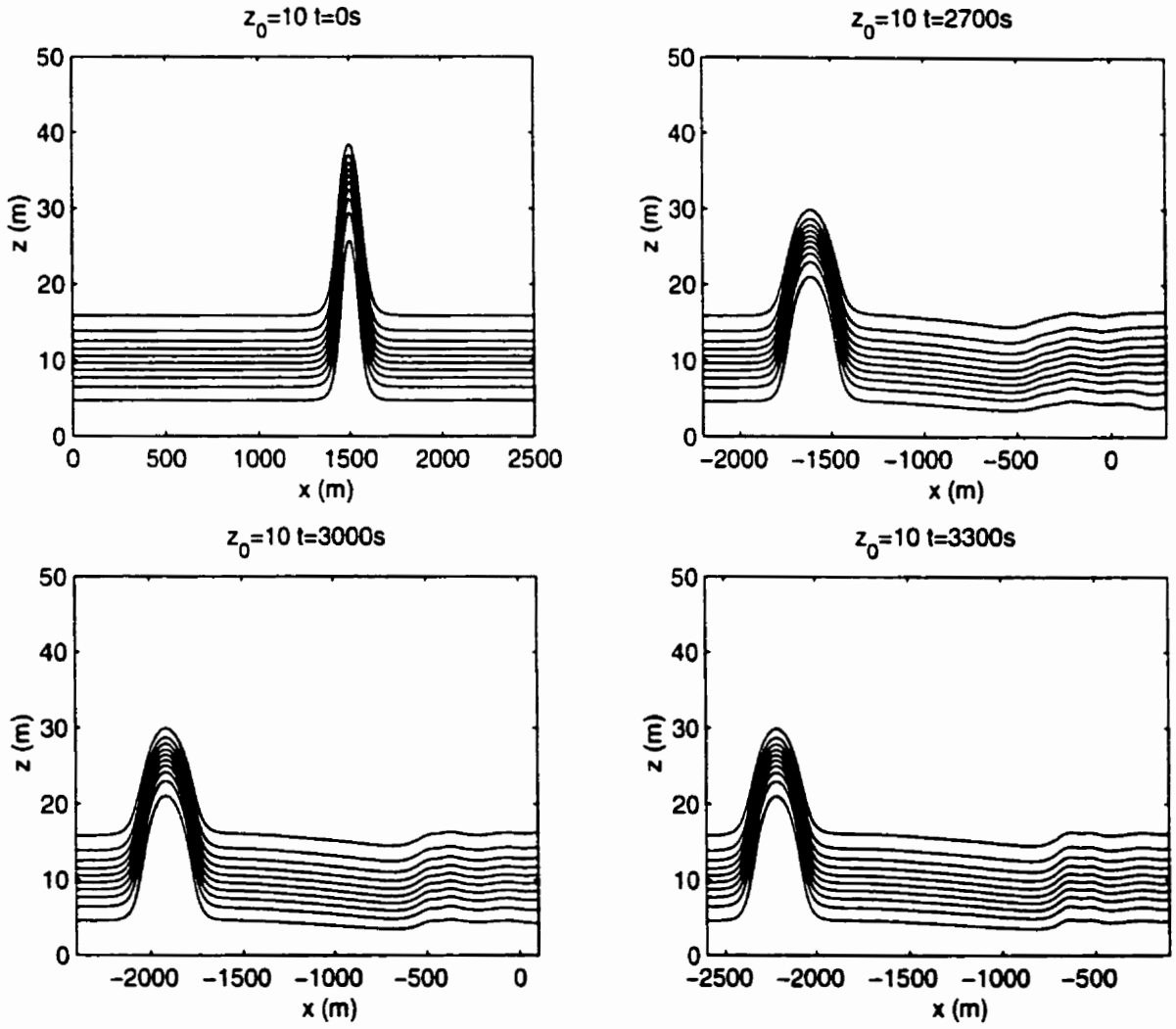

Figure 4.1: Density contours for $z_0 = 10.0$ m stratification at various times.

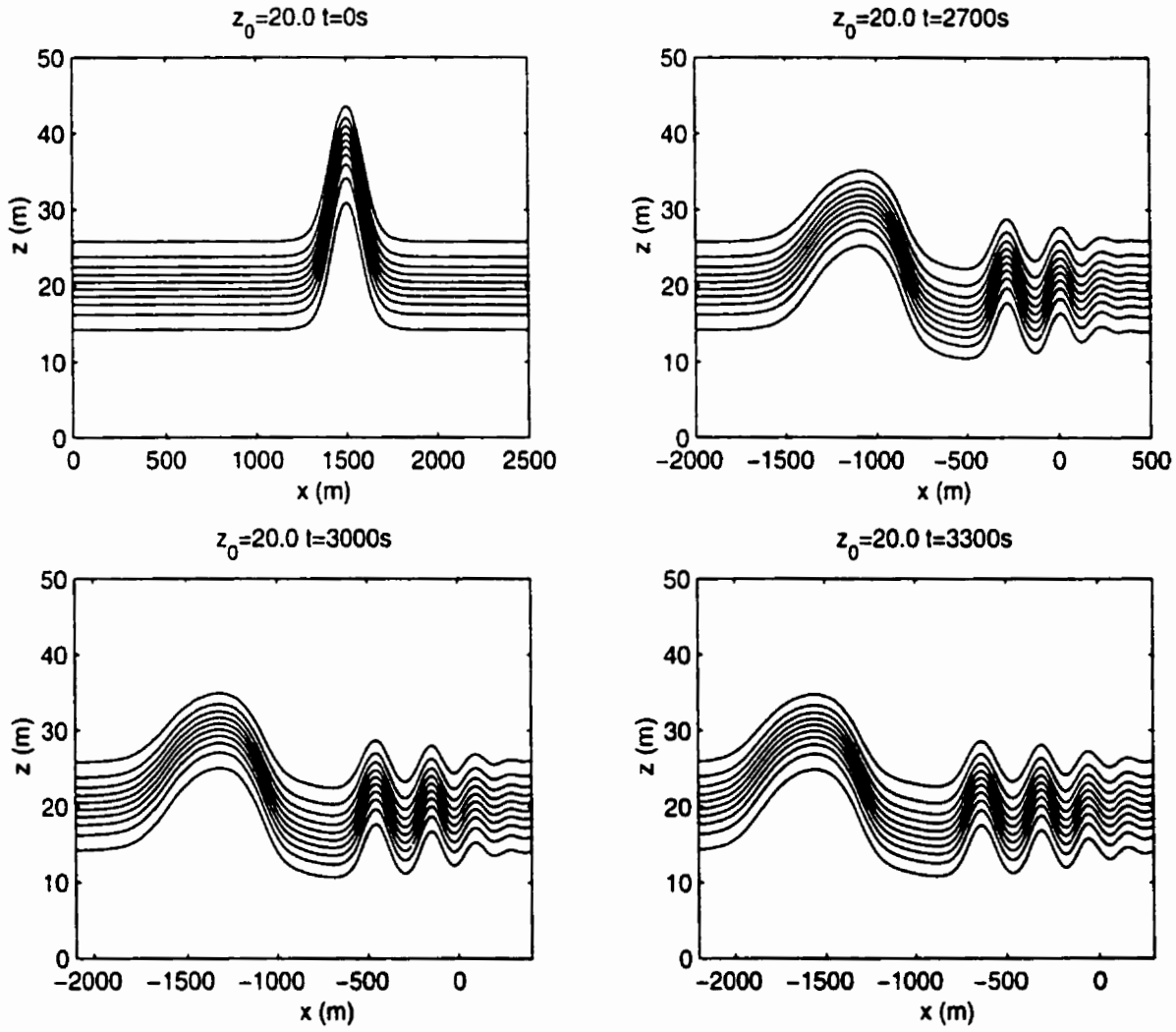

Figure 4.2: Density contours for $z_0 = 20.0$ m stratification at various times.

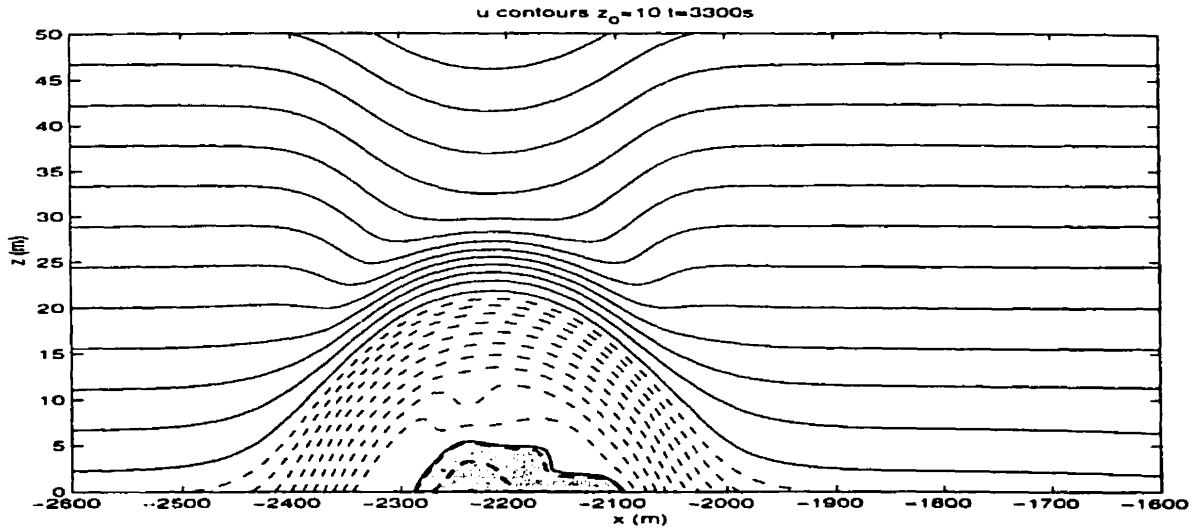

Figure 4.3: Horizontal Velocity contours for $z_0 = 10.0$ m stratification positive values in solid, negative values dashed, and the region where $u < c$ shaded.

ISW appears to fission into a smaller amplitude, wider leading ISW followed by a small amplitude shelf ending in an undular bore. After a longer time (not shown) the undular bore evolves into a train of smaller ISWs and is left behind the leading wave. In sharp contrast the $z_0 = 10.0$ m case appears to consist of a single ISW-like object which, while smaller and broader than the original ISW sheds only small dispersive waves and non-coherent noise (visible in the 2700 s panel).

From figures 4.3 and 4.4 we can see that only the $z_0 = 10.0$ m case undergoes wave breaking ($u_{total} < c$ since the waves are propagating to the left). Here c is calculated approximately from the time-dependent results by finding the location of the maximum surface current at successive times and dividing by the time interval. The actual wave overturning begins in the first 1000 s of the simulation, while the forcing is turned on. Some sample density contours illustrating the overturning after the forcing has been turned off are given in figure 4.5. From figures 4.1 and 4.5 we can see that the results of the wave adjustment process in the $z_0 = 10.0$ m case consist of a large ISW-like wave with a dynamically active core that is trapped near the bottom and some small-scale shedding behind the wave that does not propagate with the leading ISW-like object. For the $z_0 = 20.0$ m case the wave shedding during the wave adjustment process is much larger,

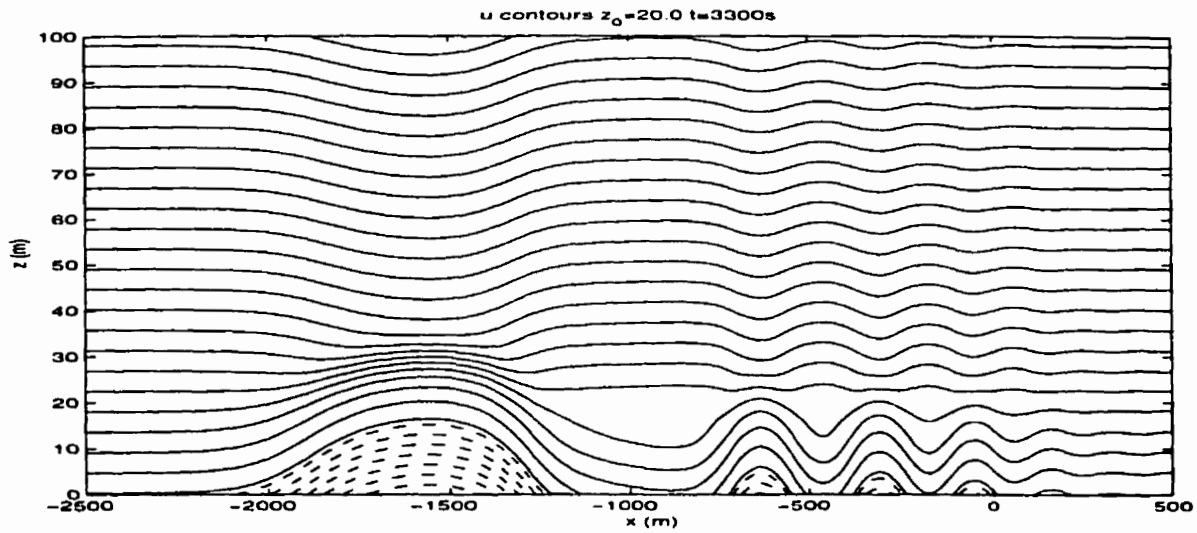

Figure 4.4: Horizontal Velocity contours for $z_0 = 20.0$ m stratification positive values in solid, negative values dashed.

and propagates leftward much faster than in the $z_0 = 10.0$ m case. This is clear from figures 4.1 and 4.2, or figures 4.3 and 4.4.

These results are, of course, consistent with the previous chapter where it was found that only the $z_0 = 10.0$ m case had maximum wave amplitude bounded above by wave breaking. The body forcing to set-up a background current used in the time-stepping simulations merely provides one illustration of an ISW adjustment process. A more common one from an oceanographic point of view is that of shoaling as discussed in ([35]). The apparently coherent response of the initial ISW in the $z_0 = 10.0$ m case provides the motivation of this chapter. An interesting question to answer is whether the dynamically active core settles to an eventual steady or quasi-steady state, and if it does, what sort of velocity and density profiles result. We should note that overturning similar to the above has been thoroughly discussed in the context of ISW (waves of depression) shoaling onto the continental shelf by Lamb ([35]).

There are several reasons to be interested in waves with trapped cores. First and foremost it appears that time-dependent simulations of ISWs under various types of forcing can lead to ISWs with trapped cores. From a physical point of view, an active core must lead to enhanced rates of

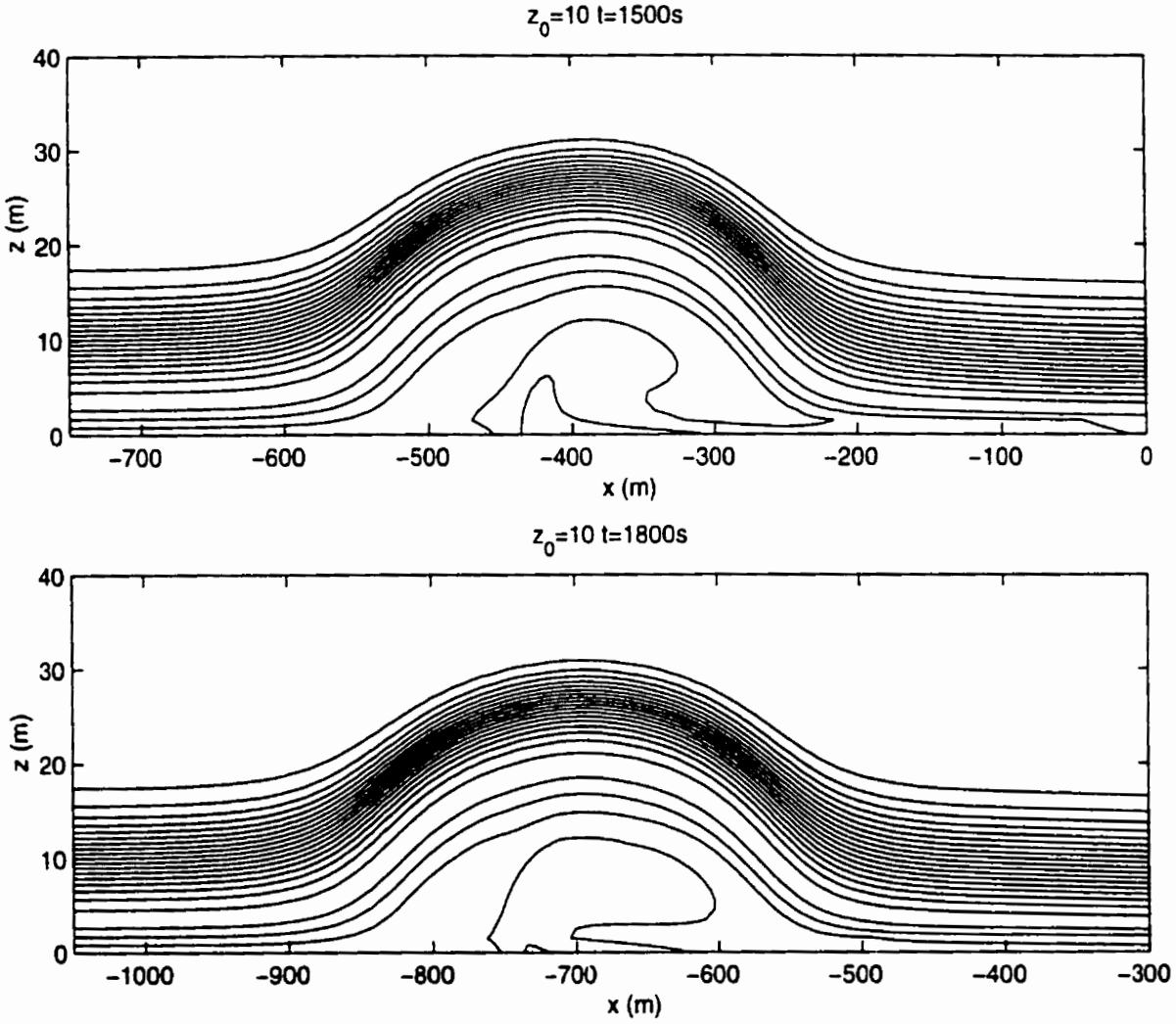

Figure 4.5: Density contours for $z_0 = 10.0$ m stratification at various times showing wave overturning. The highest four contours are chosen to highlight the near bottom region where overturning occurs.

mixing (of passively advected nutrients or sediment, for example), and even a stagnant core could lead to enhanced vertical transport of sediment into the water column due to passive advection of material up and over the core. Moreover, particles trapped in the core may be transported long distances by the wave before they are expelled (if they are expelled at all). ISW interaction with the bottom boundary layer has been hypothesized as a mechanism for increased resuspension of sediments measured beneath ISWs ([8]), but one can imagine a trapped, active core leading to significant sediment resuspension independently of any viscous effects. From a theoretical point of view the question of whether a final steady (or more reasonably quasi-steady) state emerges from a given initial wave is interesting in its own right. Derzho and Grimshaw ([15]) have argued on the basis of a finite amplitude asymptotic theory for a fluid with a nearly linear stratification (nearly constant N) that the small, but finite-sized core should be stagnant in a frame moving with the wave. Recent experiments by Grue *et al.* ([23]) agree with this prediction up to a point, though the details of the flow in the core observed in the experiments are likely dependent on the method used to generate the wave. ISW-like objects with a trapped core were discussed by Brown and Christie ([12] within the framework of a broader paper on steady ISWs. However their work exhibits at least one major short-coming (discussed in the presentation of the core calculation method) and as such is not of direct relevance to the present study.

This chapter is organized in the following manner. First a technique for computing ISW-like objects with a trapped core is introduced. In particular, we show that the variational solitary wave calculator can provide an initial condition that evolves to a quasi-steady ISW-like object with a trapped core. This is followed by a detailed discussion of the evolution process and eventual quasi-steady outcome for a particular initial condition (that is chosen to be representative of the general behaviour). Next the variation of the adjustment process and its quasi-steady outcome are discussed for various parameters. The most detailed attention is paid to varying the initial core size. The effect of how the core is initialized on the quasi-steady state is subsequently discussed. The effect of background currents and the possibility of waves with trapped cores for a background density profile that allows a conjugate flow (i.e. has a mixed layer near the top and bottom boundary) are discussed in the final section of conclusions and directions for future study.

The final section also discusses how the results of this chapter relate to the relevant literature.

4.1 Method

Given a suitable stratification and background current, the variational method discussed in Chapter 2 can be used to compute ISWs with closed streamlines. These waves are past breaking (i.e. $u_{total} > c$ somewhere). The region of closed streamlines corresponds to locations in which the mathematical algorithm sets the density in the wave to be equal to values found below the ocean bottom, or since the ambient density is a strictly decreasing function of z, to values larger than the value of the ambient density at the bottom (see figure 4.6). While this presents no problem for the algorithm, it is clearly unphysical and the region of closed streamlines must be modified to yield physically valid objects. In their study Brown and Christie ([12]) did not modify the density within the core and for this reason the details of their results do not appear relevant to the present work. We have chosen to replace the unphysical values of density in the closed streamline region with $\tilde{\rho}(0)$, the value of the density at the bottom of the ocean, far upstream of the wave. The initial velocities in the core region can be modified in many ways. We consider two possibilities, either the velocities are left as given by the ISW calculator or they are set according to $(u, w) = (c, 0)$ in agreement with ([15]). The latter approach introduces velocity discontinuities at the core boundary. The initial wave is not a solution of the steady Euler's equations, but we expect that by using it as the initial condition in a time dependent simulation we will get an ISW-like object with a trapped core after some time. We find that the object which eventually emerges does not depend on how the velocities in the initial core were defined. The variational method allows us to have some control over the size of the core and to set up an initial state quickly and inexpensively. The domain used for the simulations is rectangular (flat bottom). In order to minimize the spatial domain needed for the computations the evolution is performed in a moving frame of reference. We would like the noise and smaller waves shed behind the ISW-like object during adjustment to leave the computational domain without disturbing the main object of interest. For this reason the initial ISW is chosen to propagate leftward ($c < 0$). For consistency, we present the velocity fields in a frame moving with the initial (as given by the ISW calculator) propagation speed, unless otherwise specified.

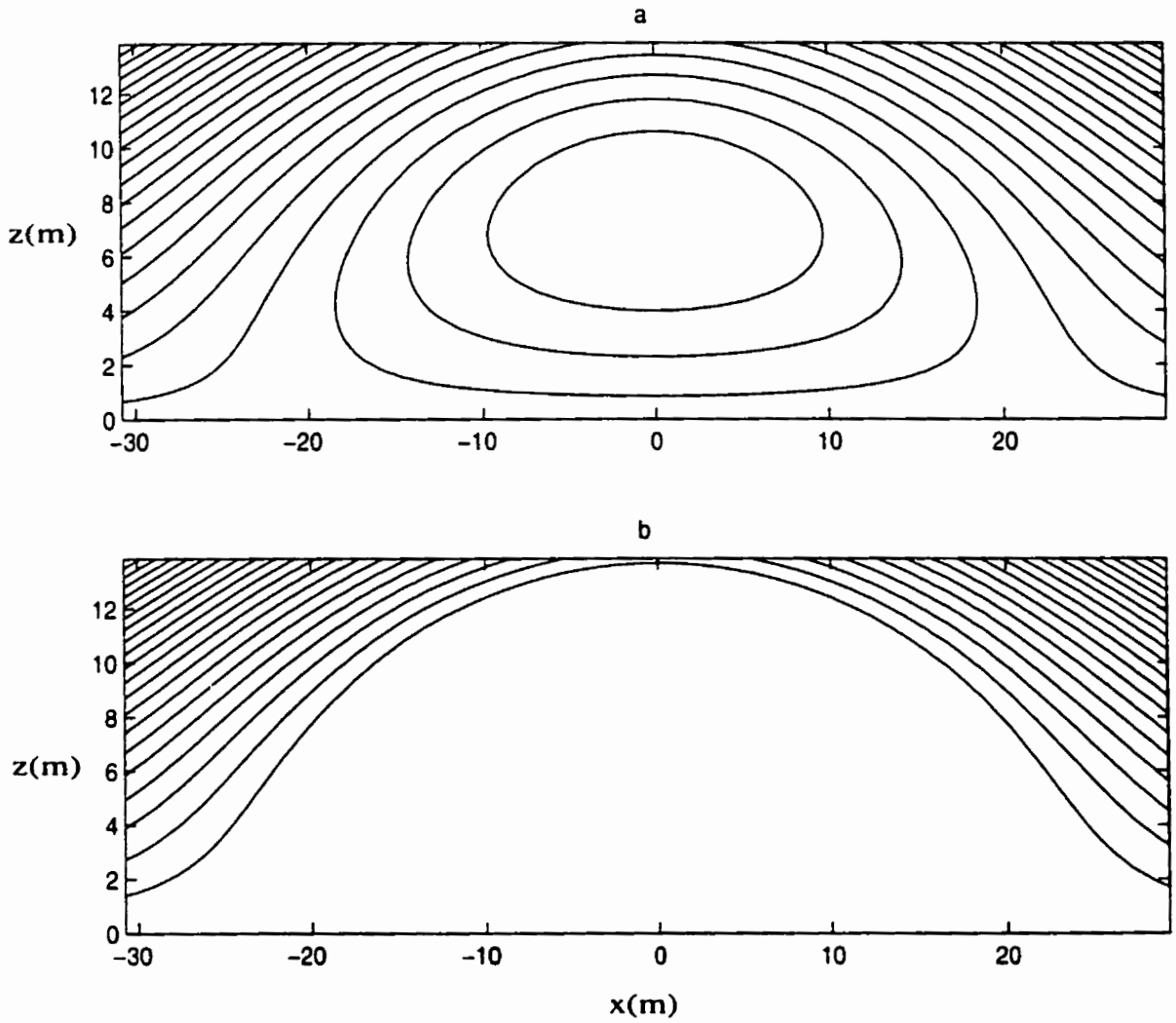

Figure 4.6: Density contours a) as given by ISW calculator b) after modification.

4.2 A Sample Core

In this section we consider in detail the evolution and final state of one particular test run. The background density used is the theoretical fit to the measurements of Bogucki, Dickey and Redekopp (BDR) off the California coast, and is given by (3.1). For this section we assume no background current is present. The water is 60 m deep and the computational domain is 1500 m long. For the run presented we take 1000 points regularly spaced in the horizontal (horizontal resolution 1.5 m) and 100 points quadratically spaced in the vertical so that 10 points lie in the bottom 1 m, 27 points lie in the bottom 5 m, and 57 points lie in the bottom 20 m (the stratified region in the undisturbed state). Upon comparison with runs using a refined grid (double the resolution in the horizontal, and with 150 points in the vertical), it was found that the 1000x100 run resolves the ISW-like object well and runs in a reasonable amount of time using computing resources presently available to the author. The qualitative results presented in this section are not altered by grid refinement, though quantitative results in the active core would be (of course 3-D effects, completely ignored in the present computations, would be most important in this region as well). For the chosen density the largest nonbreaking ISW possible to calculate using the ISW calculator has $A = 0.042$. For the sample of core evolution we consider a wave computed by the ISW calculator with $A = 0.06$.

In figure 4.7 we show the initial density and velocity fields. A clock-wise rotating vortex centered at the line of symmetry and about 7 m above the bottom can be seen to dominate the core. The size of the initial core is indicated by plotting the contour of density at the first grid-point above the bottom ($z_1 = 0.03$ m). This is essentially the value of the density throughout the core. We choose the value at the first grid point instead of right at the bottom in order to minimize numerical noise in the contour plotting routine. The region in which $\rho = \bar{\rho}(z_1)$ is about 13 m high and has a half-width of approximately 20 m at the bottom. We also plot the smaller regions enclosed by the contours $u = 0.02|c|$ and $u = c$.

In figure 4.8 we show the early development of the core as it tilts away from the direction of propagation (1000 s), begins a complex mixing (2000 s) and loses a tail of dense fluid in a thin layer trapped near the bottom (3000 s). Note that at 1000 s the velocities in the region of the

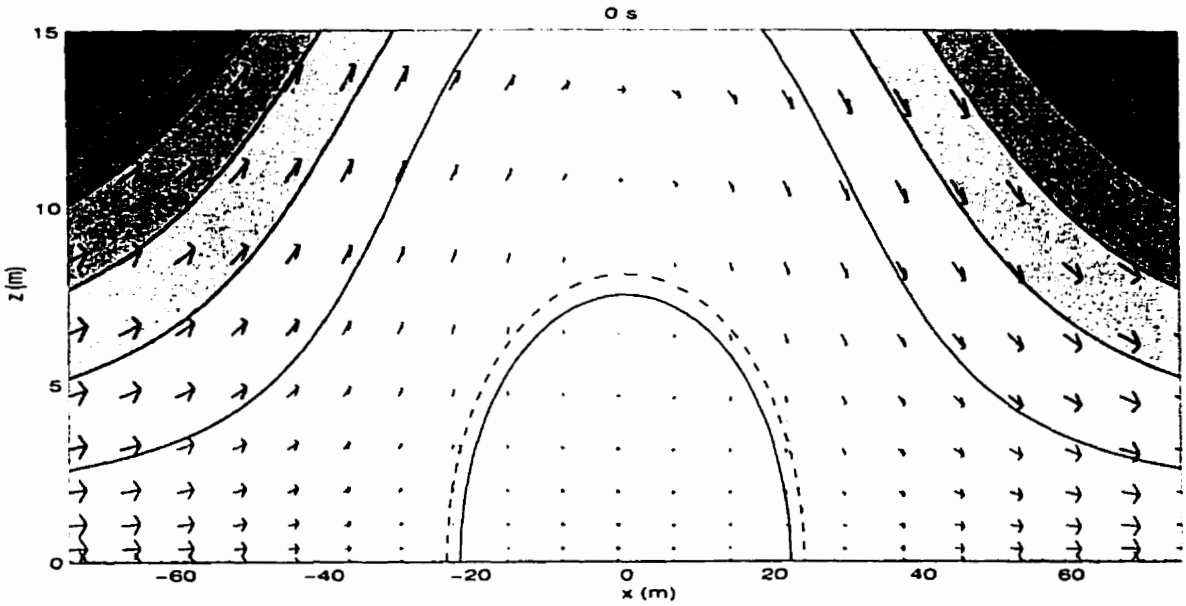

Figure 4.7: Initial density contours and velocity field in a frame moving with the wave speed for a leftward propagating wave. Density contours - shaded, contour of $\bar{\rho}(z_1)$ where z_1 is the first grid point above the bottom - dotted, contour of $u = 0.02|c|$ - dashed, contour of $u = c$ - solid

core overhang are oriented leftward and downward. The contour $u = c$ (not shown) now touches the bottom at $x = 27$ m. By 8000 s the core has decreased slightly in size.

In figure 4.9 we show the density contours and velocity fields for 8000, 16000, 24000 and 32000 s. The initial vortex remains reasonably coherent at 8000 s and strengthens at 16000 and 24000 s (this is difficult to see in the figure). At 32000 s the vortex has decreased in height and a complex motion is visible at the back of the wave. This complex motion drifts rightward and out of the computational domain.

In figure 4.10 we consider density and velocity fields at later times in the core adjustment process. The figure shows that the core region stabilizes to a quasi-steady state dominated by an asymmetric region where the horizontal velocity is very low (in the frame moving with the initial wave propagation speed). We choose to outline the region in which the horizontal velocity is less than two percent of the original propagation speed. This asymmetric region reaches down to the bottom near the front of the core then lifts up off the bottom, forming an approximately

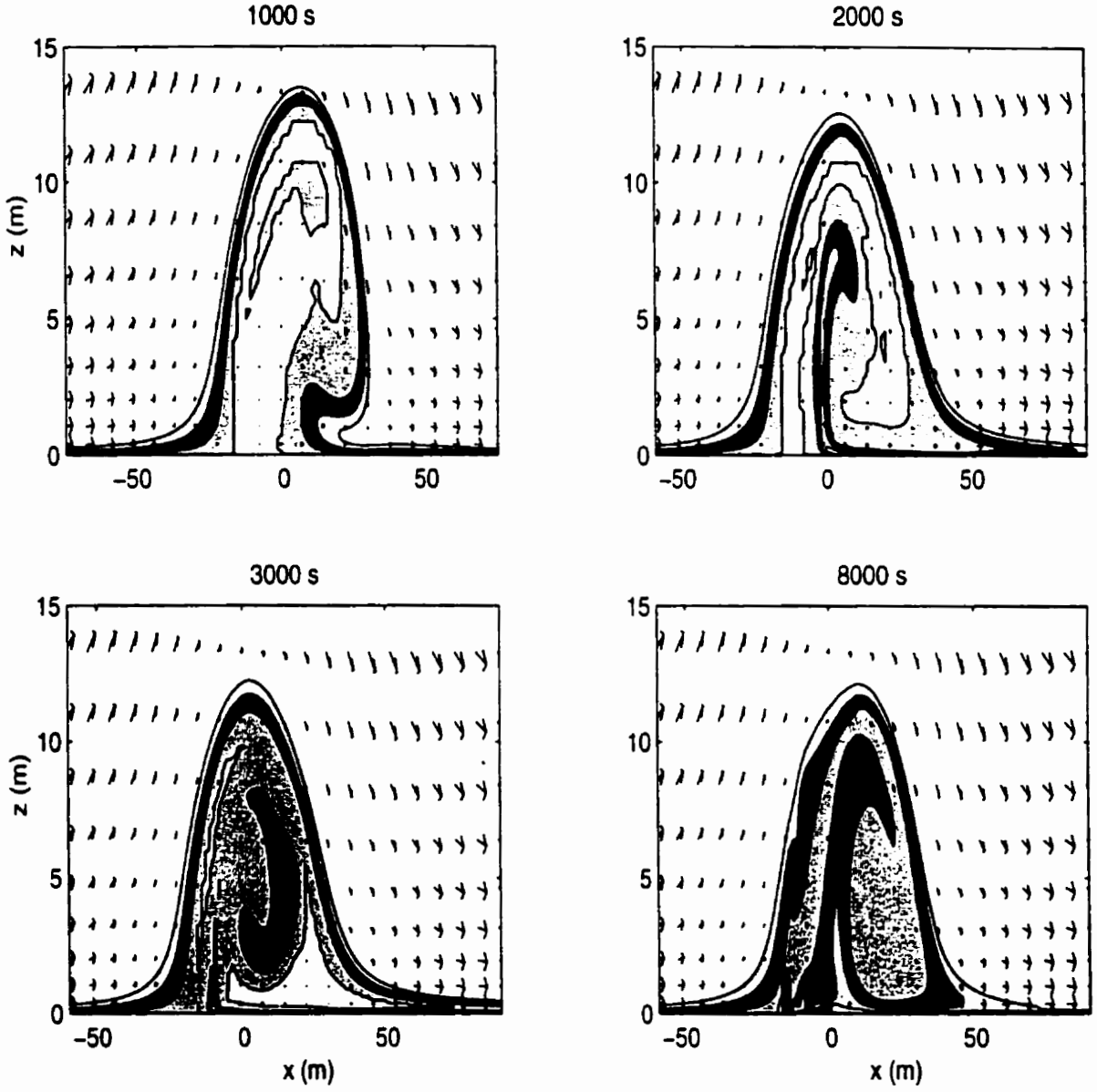

Figure 4.8: Velocity field and near bottom density contours (shaded) at 1000, 2000, 3000 and 8000 s.

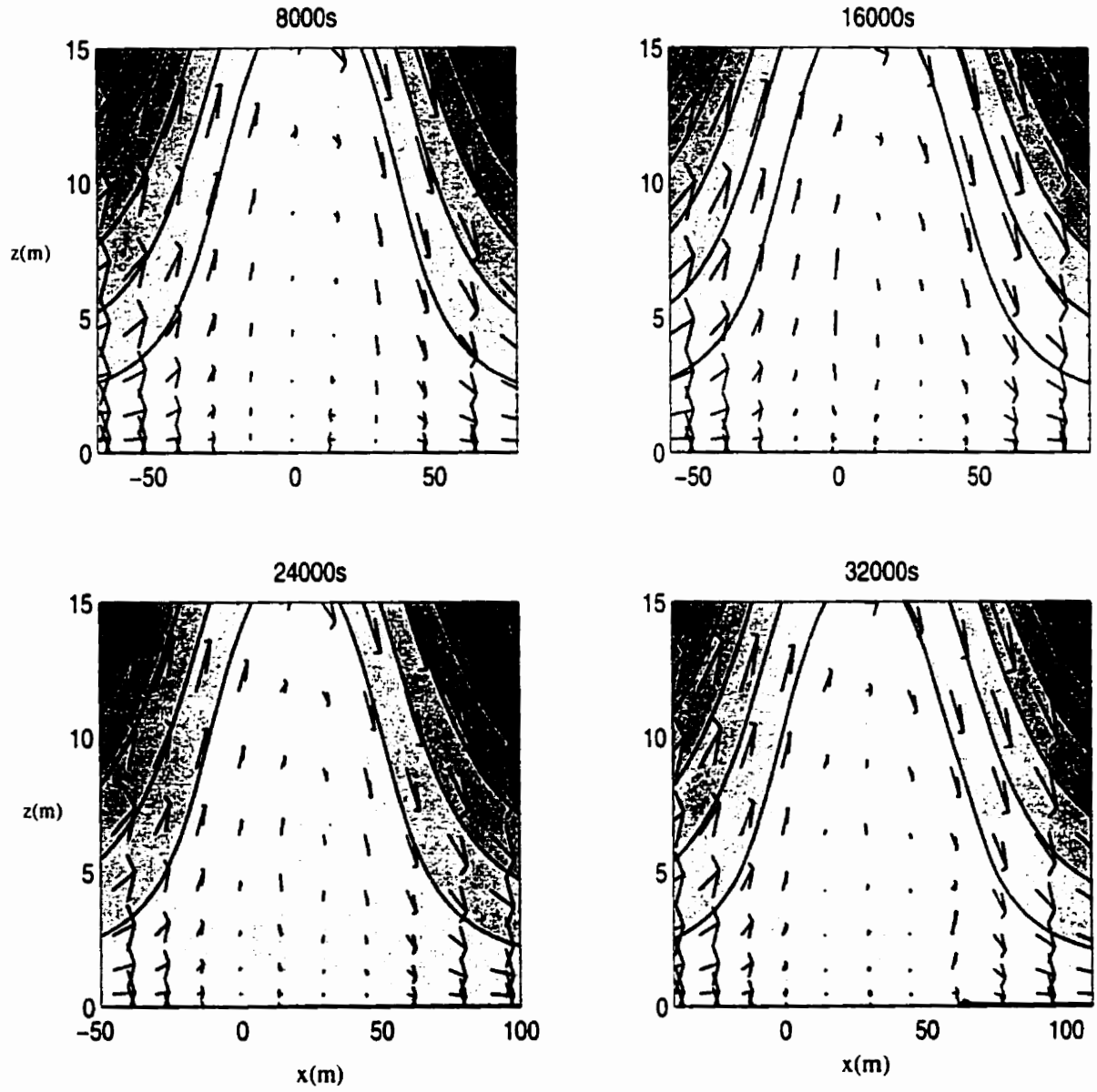

Figure 4.9: Density contours (shaded) and velocity field at 8000, 16000, 24000 and 32000 s.

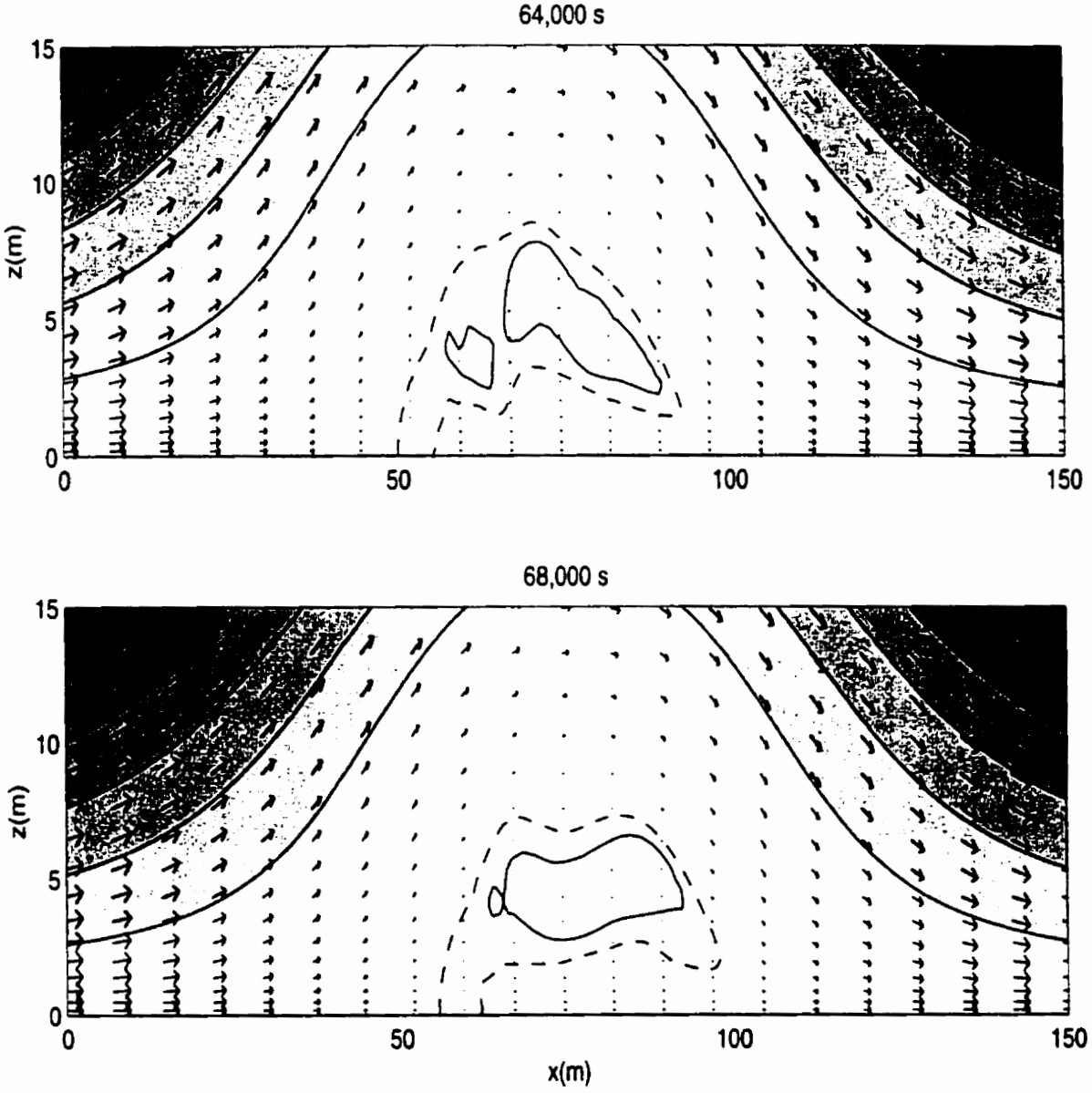

Figure 4.10: Density contours (shaded) and velocity field at 64000 and 68000 s. Contours of region where $u < 0.02|c|$ (dashed line), $u = 0.0$ (solid line).

triangular region with a base of 40 m and a height of 5 m. It can be seen from figure 4.10 that while the shape of this region is not steady, it does not change much with time. It is for this reason that we call the final state of the core quasi-steady.

In figure 4.11 we reconsider the velocity field at 72000 s in detail. The region of low velocities can now be clearly seen. Furthermore we can note that the region $u < 0$ is lifted off the bottom, in contrast to figure 4.7 where it is widest at the bottom. The area of the region where $u < 0$ is reduced by approximately one third from the initial to the final state. We should note that the magnitude of the propagation speed of the final wave is lower than magnitude of the propagation speed given by the ISW calculator. For this example, however, this reduction is less than 1% of the original propagation speed value. It is unlikely that this reduction could be detected in oceanic measurements.

To further examine the difference between the initial and final state we consider the contours of horizontal velocity for both states.

From figure 4.12 we can see that the contours for $u = 0.02$ and $u = 0.03$ are largely unaffected by the adjustment process save for a small region at the back of the wave extending to about 1.5 m above the bottom. The region of negative velocities in the initial core is replaced in the final quasi-steady state by a region of small positive velocities trapped near the bottom and an approximately triangular region of slightly negative velocities lying between about 2 and 7 m above the bottom, as discussed above. Since the computations was performed in a frame moving with the original wave propagation speed, the figure also shows the slight reduction of wave propagation speed during adjustment that results in the wave's small rightward drift.

The vertical velocities have a rather different spatial distribution and for this reason it was found that the visualisation technique used above to compare the horizontal velocities was too cluttered. Instead, shaded contours of the density along with contours of vertical velocity (solid line - positive, dashed line - negative) for the initial and final states are presented in two separate panels in figure 4.13.

From the figure we see that, in the final state, the core consists of an approximately triangular region marked by regions of weak downdrafts and updrafts. The core has a base length of about

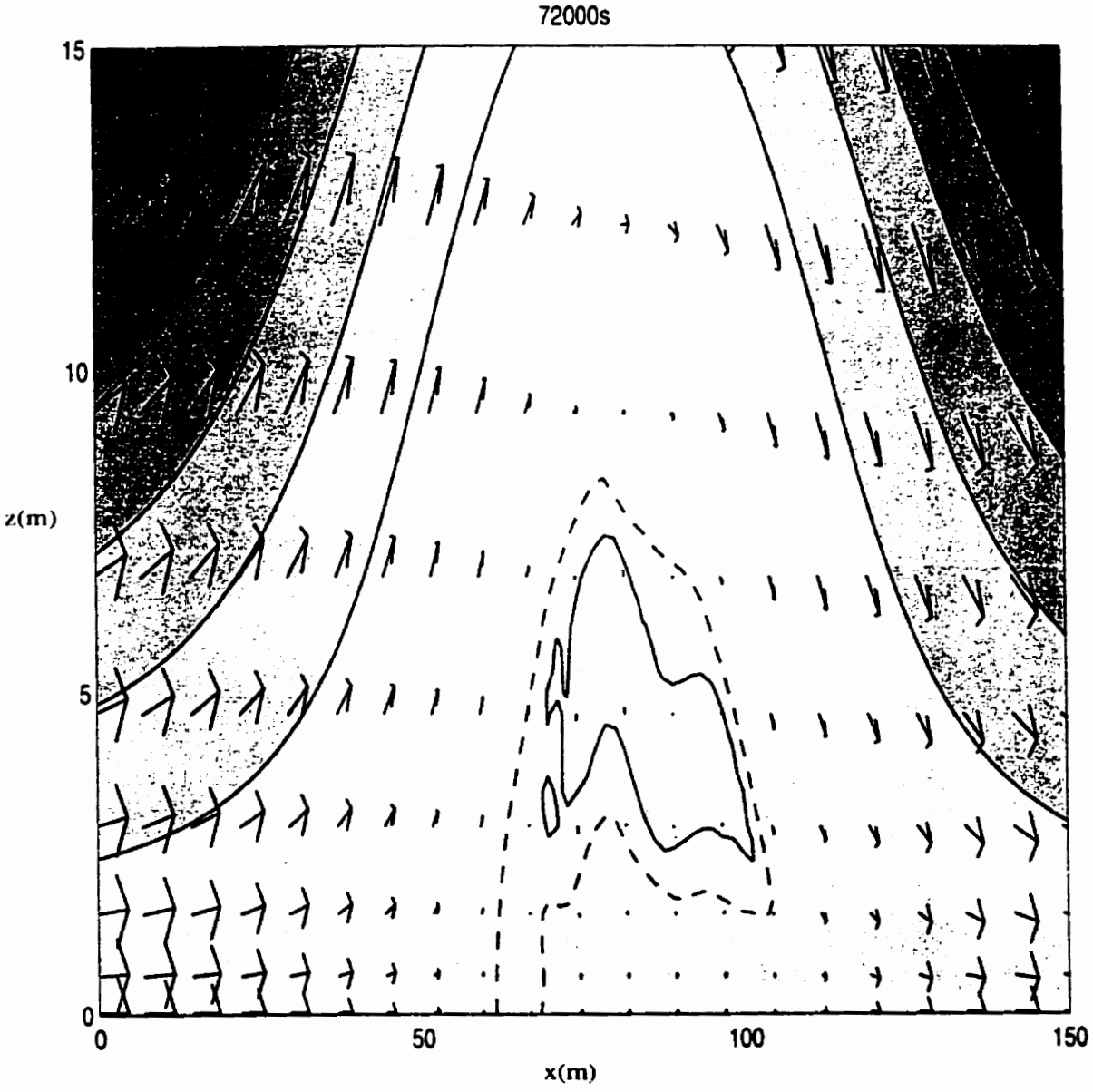

Figure 4.11: Density contours and velocity field at 72000 s. Contour of region where $u = 0.0$ solid, $u = 0.02|c|$ dashed.

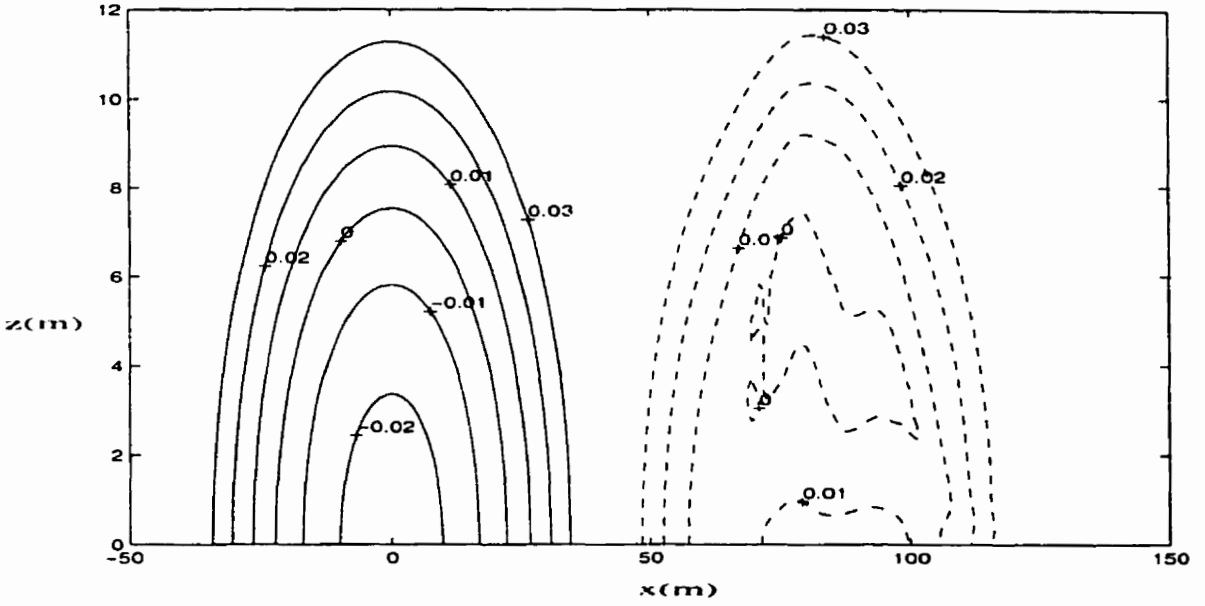

Figure 4.12: Horizontal velocity contours at 0 s (solid) and 72000 s (dashed).

40 m along the bottom and a height of about 7 m. The vertical velocities in the core region are very weak and hence the flow is nearly horizontal. Outside the core region the contours appear largely unchanged from the initial to the final state. In other words the final ISW-like object consists of a weakly active core with a velocity profile very different from that of a nonbreaking ISW and wave body with a velocity profile virtually indistinguishable from a nonbreaking ISW. A very clear illustration of this splitting is furnished by examining the vertical profile down the middle of the wave of the horizontal velocity (figure 4.14). In the majority of the water column the only difference from the initial to the final state is a small decrease in magnitude (due to the shedding of material behind the wave during the adjustment phase). In the near-bottom, or core region, the final profile is blunted with the most negative velocity occuring just below 6 m above the bottom. For the initial state the largest negative velocity occurs right at the bottom.

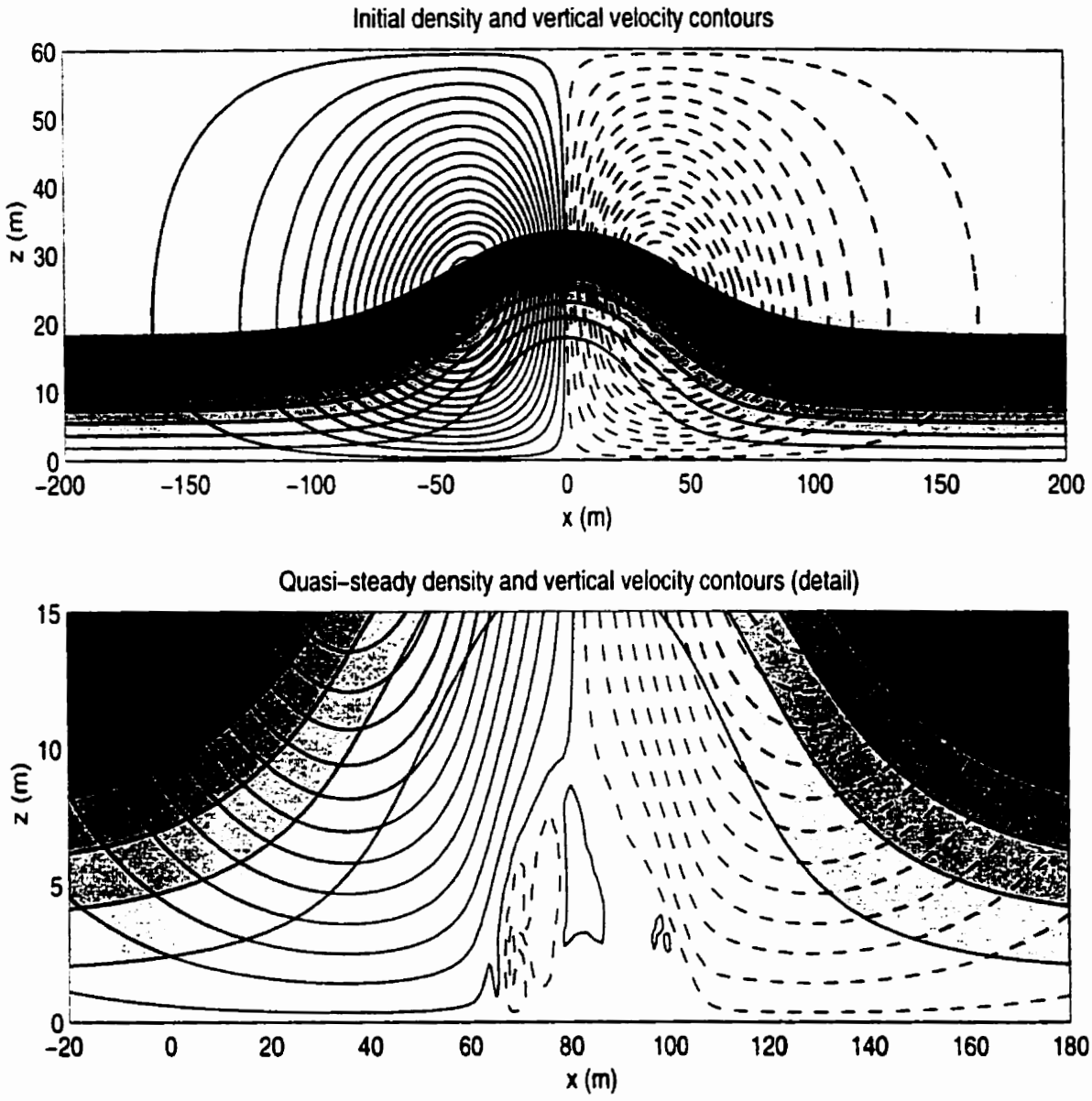

Figure 4.13: Density (shaded) and vertical velocity contours at 0s (top) and 72000 s (bottom). Positive values - solid, negative values - dashed

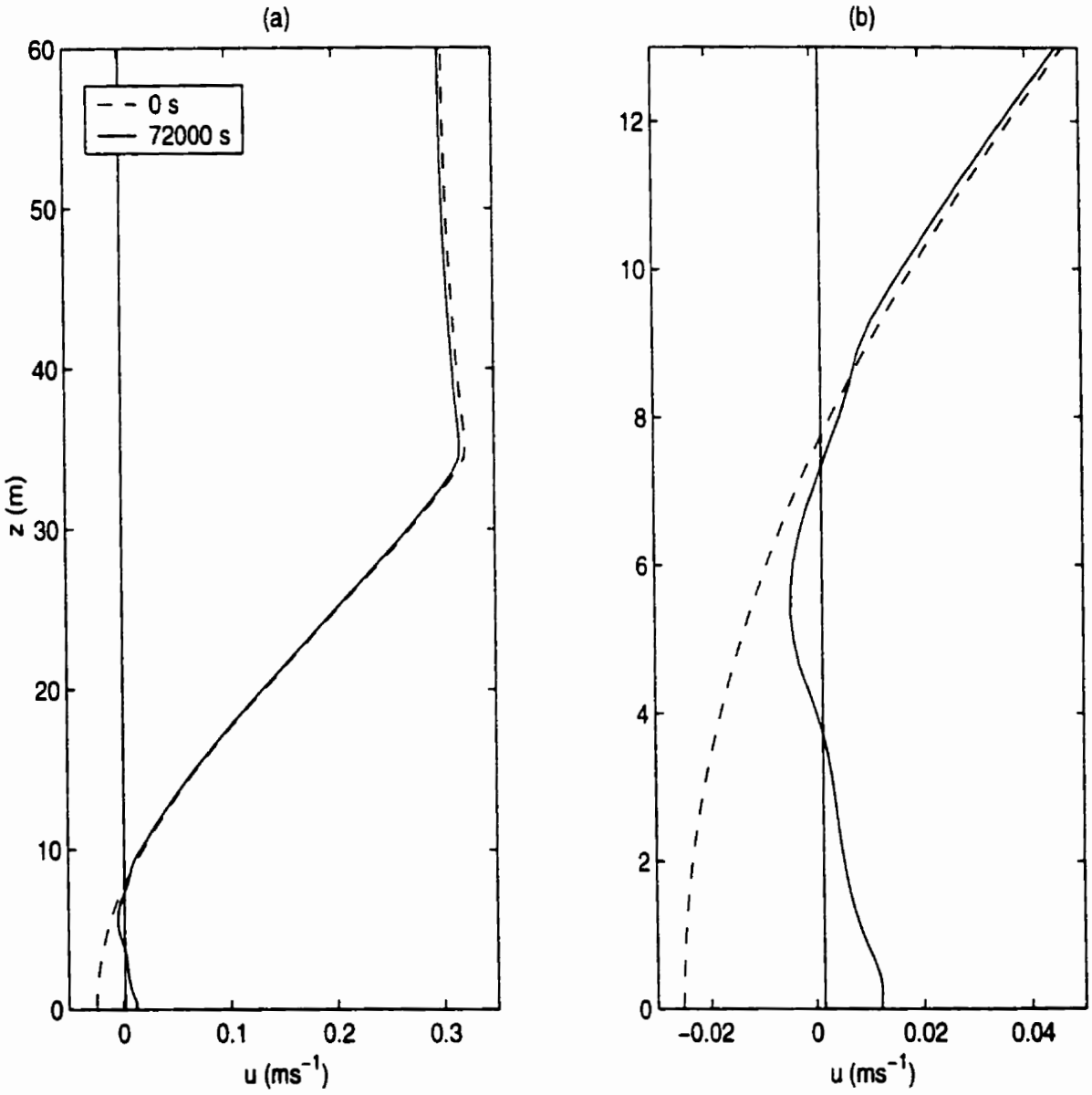

Figure 4.14: Vertical profiles of the horizontal velocity down the middle of the wave. The final propagation speed (in a frame moving with the initial propagation speed) is indicated by a vertical line. Final state - solid, initial state - dashed. a) entire water column b) near bottom region only.

4.3 Comparison of Quasi-steady States

Having established the qualitative features of the adjustment process we now turn to the important task of comparing the resulting trapped cores as various physical parameters are changed. In particular we wish to examine the effect of initial core size and the choice of velocity initialization in the initial core.

4.3.1 Comparison by Initial Core Size

Recall that the variational algorithm used to compute the initial candidate wave does not specify maximum isopycnal displacement. Instead the algorithm fixes the available potential energy, A, (see equations 2.43, 2.44, and 2.45). This means that while we have some control over the size of the initial core, this control is not exact.

We consider eight test cases using the ambient density profile (3.1) used in the previous section. The values of A used range from $A = 0.05$ to $A = 0.12$ incremented by 0.01. As in the previous section all waves propagate from right to left (hence c is negative). The relevant properties of the waves computed by the variational ISW calculator are shown in table 4.3.1.

A	$\lvert c\rvert$ (ms^{-1})	η_{max} (m)	$\lvert u_{min}\rvert$ (ms^{-1})
0.05	0.19477	16.37	0.20634
0.06	0.19778	17.72	0.22300
0.07	0.20034	18.92	0.23791
0.08	0.20012	20.01	0.25144
0.09	0.20450	21.01	0.26390
0.10	0.20637	21.94	0.27546
0.11	0.20780	22.81	0.28628
0.12	0.20921	23.62	0.29645

Table 4.3.1 Available potential energy, propagation speed, η_{max} and largest wave induced current for ISWs past breaking as computed by the ISW calculator. The breaking amplitude is $\eta_b = 15.6$ m.

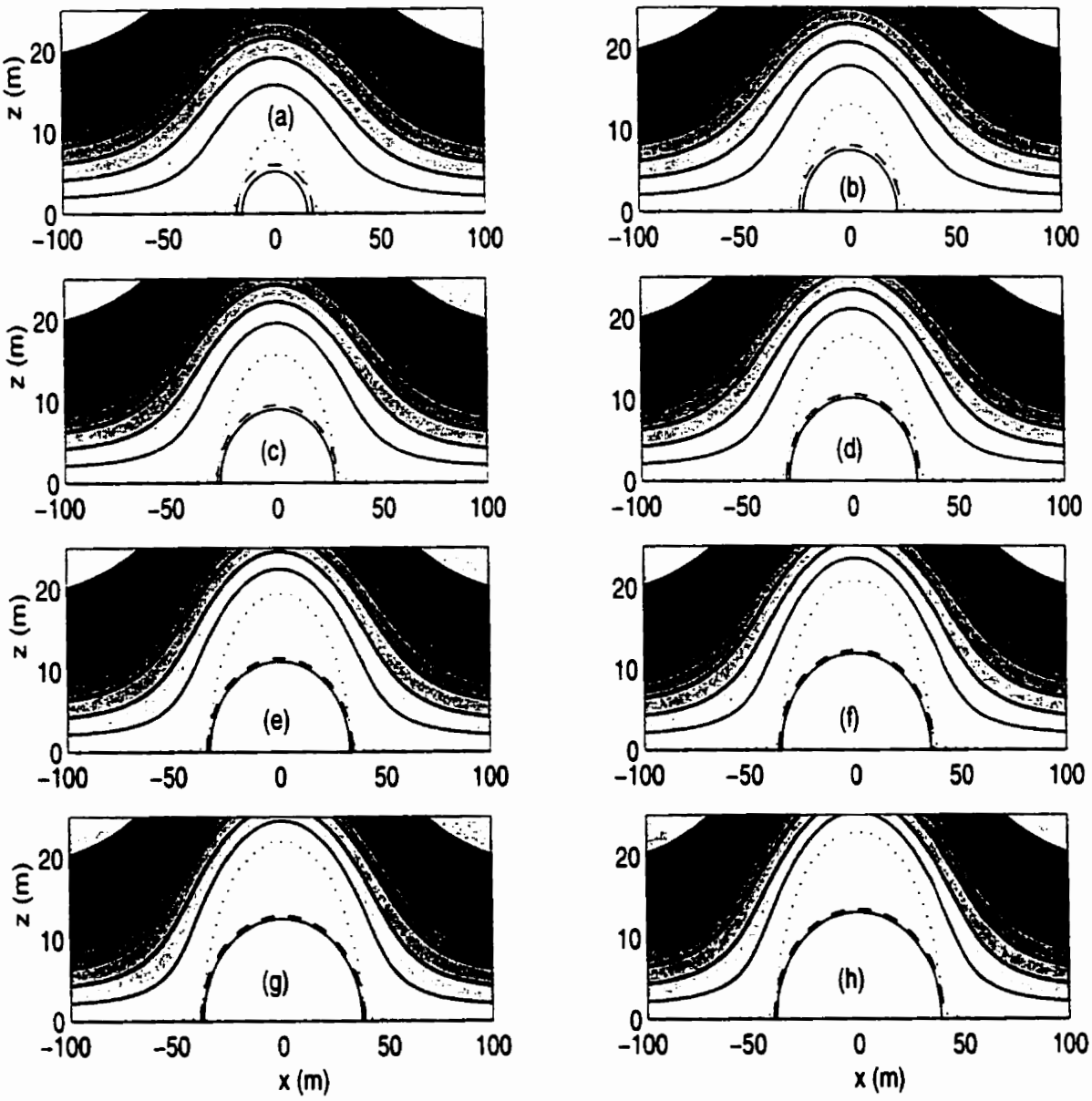

Figure 4.15: Initial wave states. Density contours - shaded, contour of $\bar{\rho}(z_1)$ - dotted, contour of $u = 0.02|c|$ - dashed, contour of $u = 0$ - solid. (a) A=0.05, (b) A=0.06, (c) A=0.07, (d) A=0.08, (e) A=0.09, (f) A=0.10, (g) A=0.11, (h) A=0.12

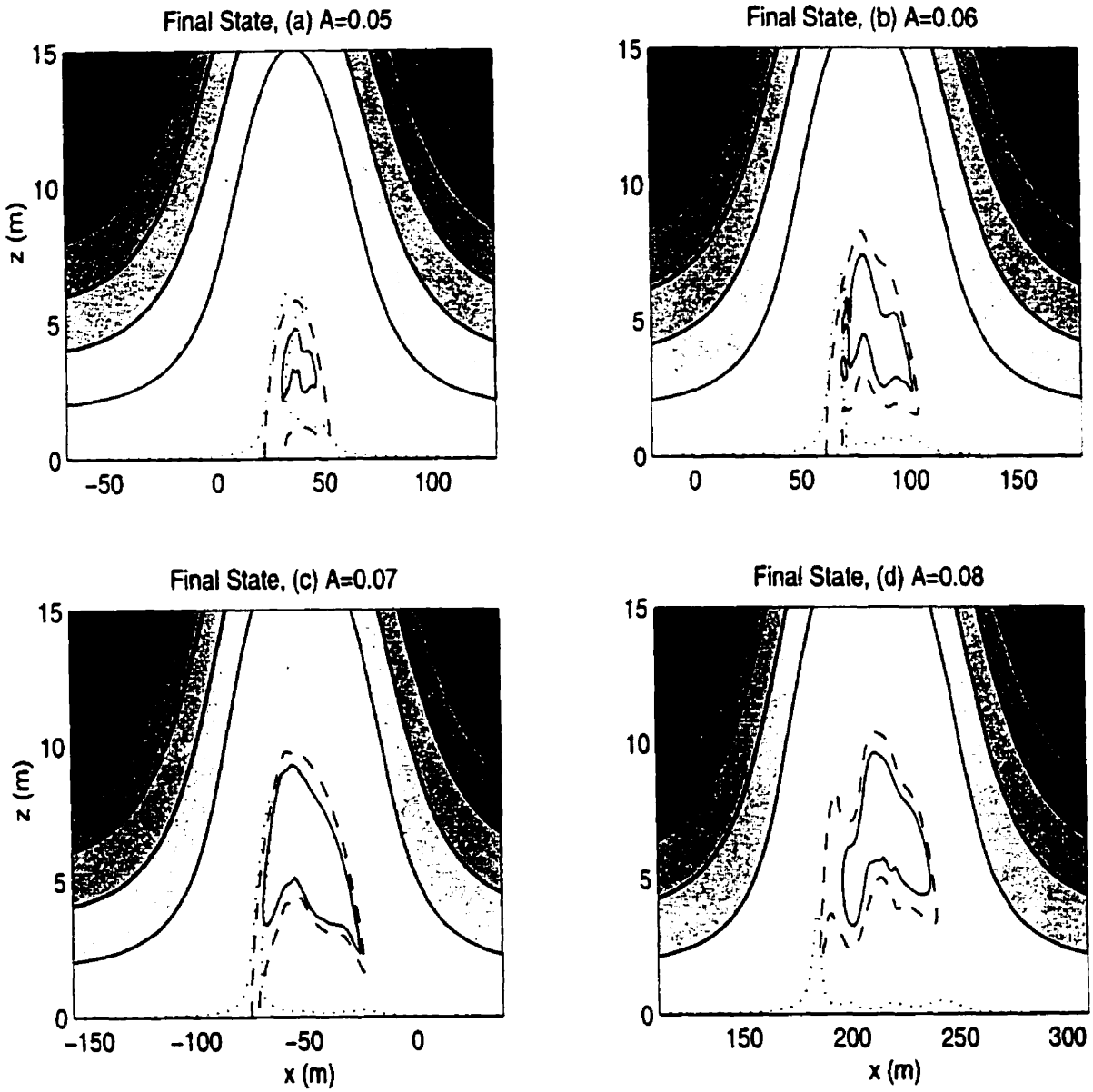

Figure 4.16: Final wave states, four smallest waves. Density contours - shaded, contour of $\bar{\rho}(z_1)$ - dotted, contour of $u = 0.02|c|$ - dashed, contour of $u = 0$ - solid.

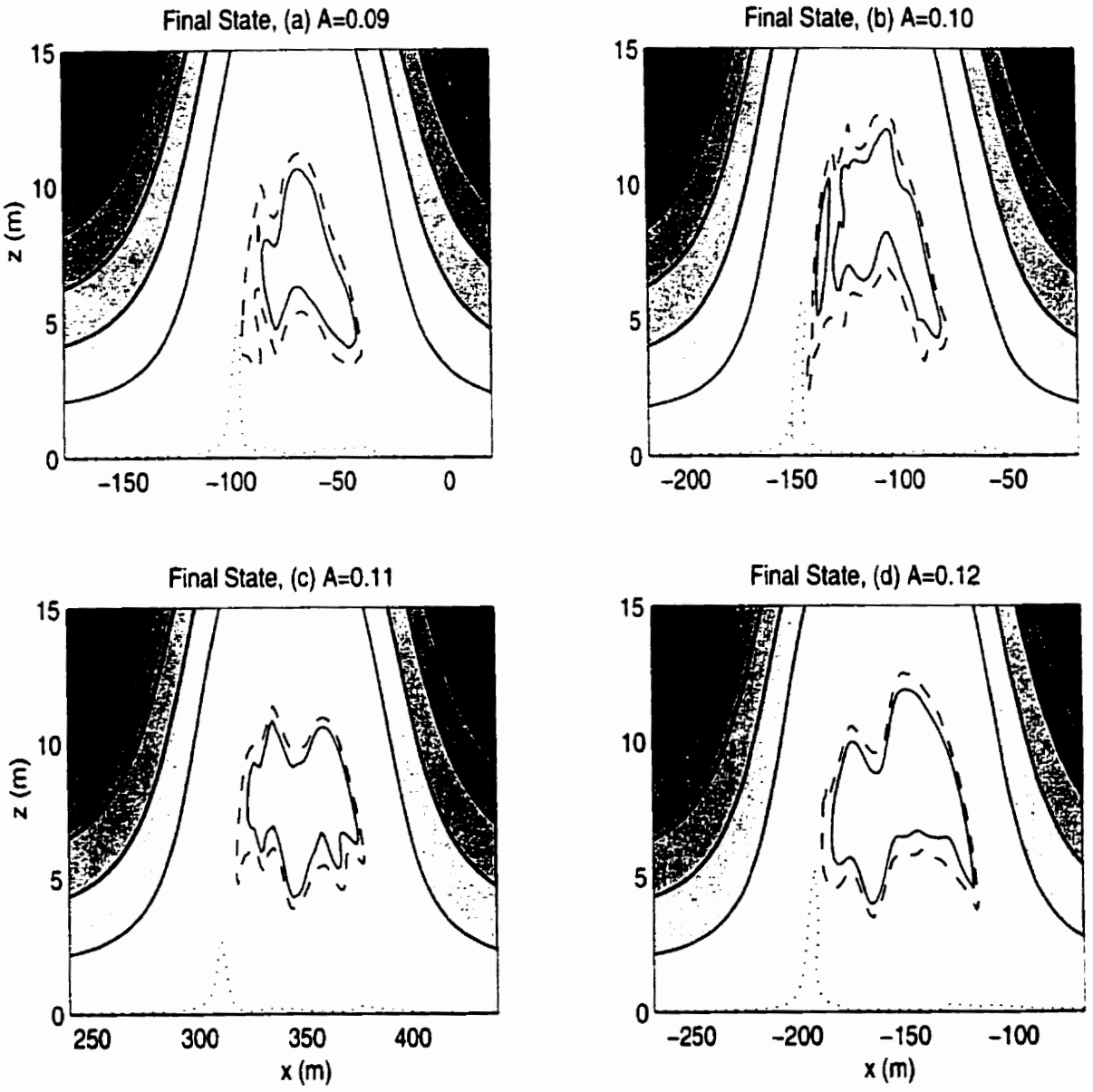

Figure 4.17: Final wave states, four largest waves. Density contours - shaded, contour of $\bar{\rho}(z_1)$ - dotted, contour of $u = 0.02|c|$ - dashed, contour of $u = 0$ - solid.

We begin by comparing the initial and final states for the various waves. In figure 4.15 we show the inital conditions (after adjustment) for all eight waves. We can see that the initial core height down the center and half-width at the bottom grow from about 8.5 m and 15 m, respectively, for $A = 0.05$, to about 20.5 m and 45 m, respectively, for $A = 0.12$. We can also see that the region where $u < 0$ (in a frame moving with the initial propagation speed) is about half the core height. As for the case discussed in the last section, all quasi-steady waves have a lower propagation speed than the initial waves (as given by the ISW calculator) used to compute them. We will discuss this point in more detail below, however we should point out that the reduction is less than 4% for all waves considered. We will consider all contours of velocity to be in a frame moving with the initial wave propagation speed.

In figures 4.16 and 4.17 we show the final, quasi-steady states of the cores for the four smallest and four largest waves, respectively. The general features of all the final states are in qualitative agreement with the example discussed at length in the previous section. Namely the final core is a region of nearly stagnant fluid in a frame moving with the original propagation speed. All plots are shown at 72,000 s. From figure 4.16 we can see that for all four waves shown, the region of small horizontal velocities (we show contours of $u = 0$ and $u = 0.02|c|$) occupies an approximately triangular region centered at least 4 m above the bottom. The three smallest initial cores also have a region of reduced horizontal velocities that reaches right to the bottom at the front of the core. Starting with $A = 0.08$ and for all four cases shown in figure 4.17 the region of reduced horizontal velocities does not reach the bottom. For the four larger waves, the final core is characterized by an approximately 5 m tall, 100 m wide region of nearly stagnant fluid centered at about 7 m above the bottom.

An increase in the size of the initial core leads to an increase in the size of the quasi-steady core. However, increasing the size of the initial core also leads to a more violent adjustment process. Thus doubling the size of the initial core will not lead to a doubling of the quasi-steady core size. An example of the rather violent adjustment for the larger initial cores is given in figure 4.18 where we show two contour plots of the adjustment phase of the $A = 0.12$ case. It can be expected that 3D effects would play a large role in the adjustment phase of the larger initial

cores.

Another way to look at how the quasi-steady state changes as the initial core size increases is to look at plots of the horizontal velocity at fixed heights. In figure 4.19 we show horizontal plots of the wave-induced, horizontal velocity for the initial state along with the difference between the initial and quasi-steady states for four waves (A = 0.05, 0.06, 0.08 and 0.12). We can see that all four waves shown experience adjustment at 1 m above the bottom. However, at 5 m above the bottom only the A = 0.08 and 0.12 cases show significant adjustment, and at 10 m above the bottom only the largest wave shows significant adjustment. We can also see that larger initial cores experience larger adjustment. This is consistent with the contour plots 4.16 and 4.17.

The core adjustment process results in a solitary-like wave that has a propagation speed, maximum isopycnal displacement, and wave-induced horizontal velocity of smaller magnitude. Strictly speaking we can only speak of an average final propagation speed since we calculate the final propagation speed from horizontal velocity values at the surface, which are output only every 4000s. It seems reasonable to focus on the wave induced horizontal velocity at the surface since the final adjusted wave is very close to the initial wave in the near surface region. In contrast, the near bottom region changes markedly, as discussed above.

In figure 4.20 we show the initial and final values of maximum horizontal velocity at the surface, propagation speed and maximum isopycnal displacement. The comparisons are done as a function of A. Since A does not have a clear meaning for the final, adjusted ISW-like object it makes sense to consider the propagation speed as a function of either the maximum isopycnal displacement or the maximum wave induced horizontal velocity at the surface. This is done in figure 4.21. It is clear from this figure that the decreases in all quantities considered are larger for larger initial cores. Furthermore, it appears that the maximum isopycnal displacement and propagation speed of the final state have an upper bound (approx. 21.0 m and 0.203, respectively).

In figure 4.22 we consider the propagation speed as a function of maximum isopycnal displacement for the four largest nonbreaking ISWs as well as ISW-like objects resulting from the eight initial core regions. It can be seen that decreases in both the maximum isopycnal displacement and propagation speed appear to follow a smooth relationship for the four (arguably five) smallest

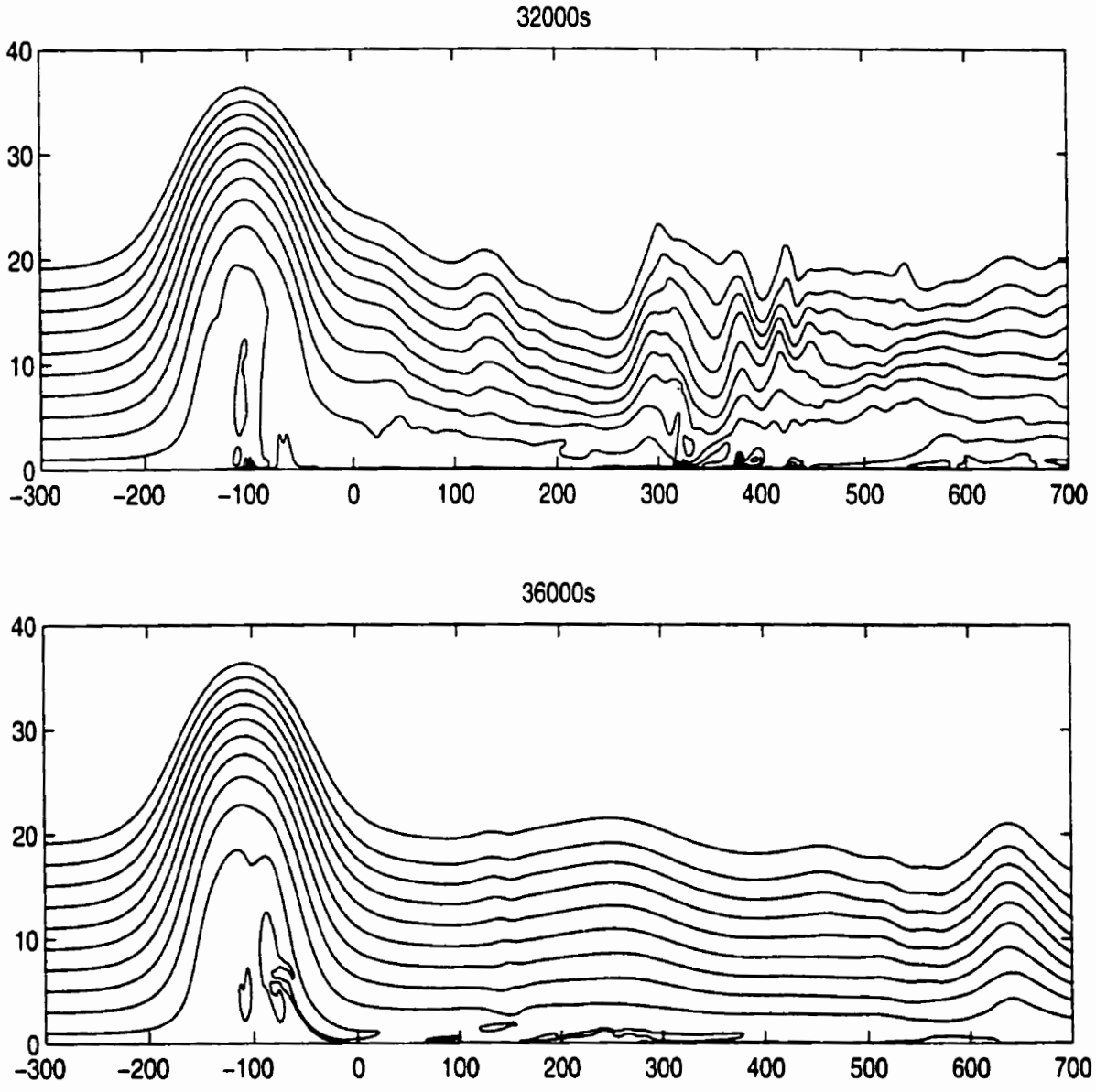

Figure 4.18: Density contours during the adjustment phase of the $A = 0.12$ case

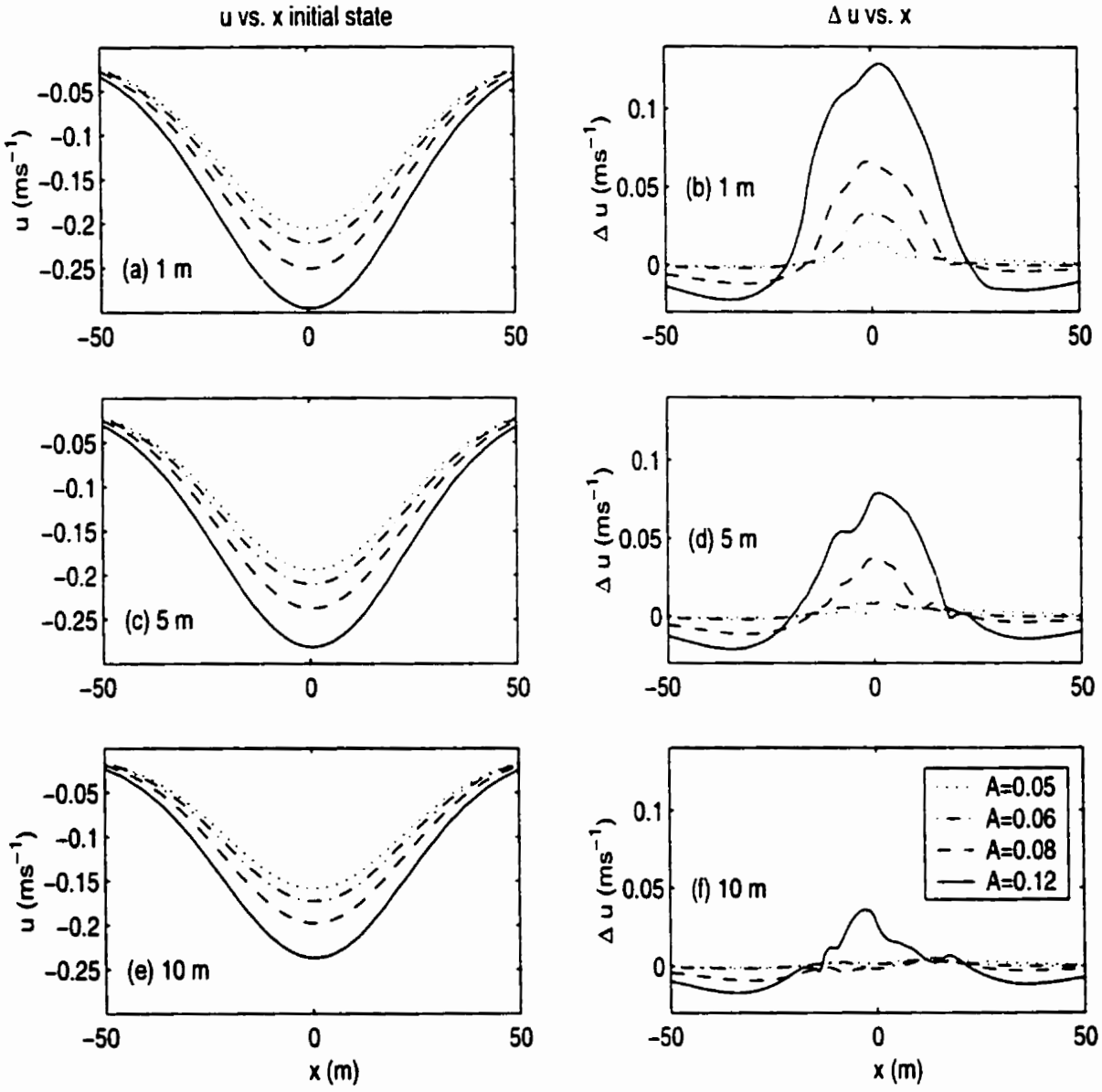

Figure 4.19: Wave-induced horizontal velocity vs. x at a $t = 0$ s and fixed heights, (a) 1 m, (c) 5 m, (e) 10 m along with the difference between initial and quasi-steady wave-induced horizontal velocities vs. x at fixed heights, (b) 1 m, (d) 5 m, (f) 10 m. Four waves shown, $A = 0.05$ - dotted, $A = 0.06$ - dot-dashed, $A = 0.08$ - dashed, $A = 0.12$ - solid.

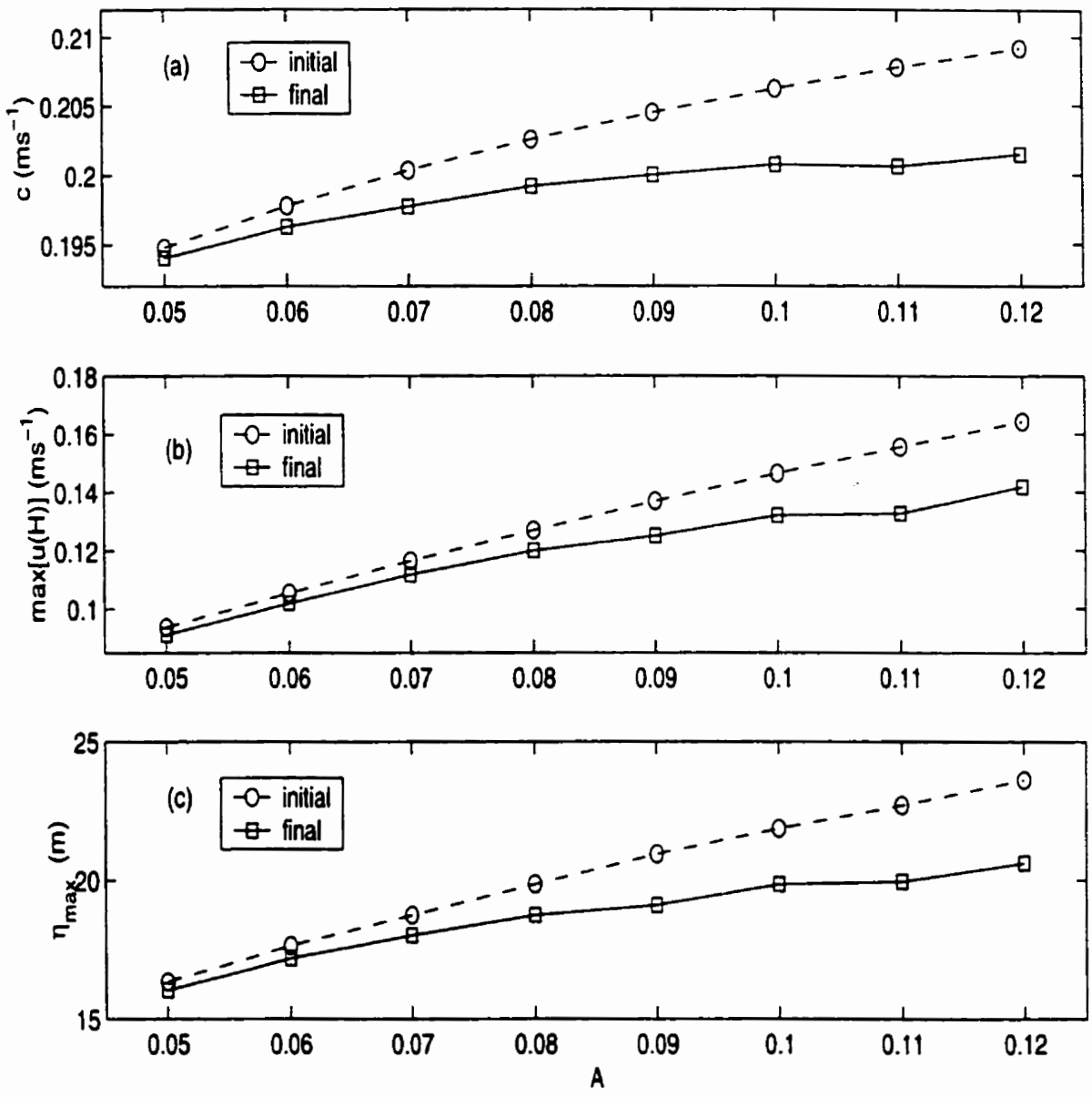

Figure 4.20: Initial and final values of (a) the propagation speed, (b) the maximum wave induced velocity at the surface, (c) maximum isopycnal displacement as a function of A. Magnitudes plotted.

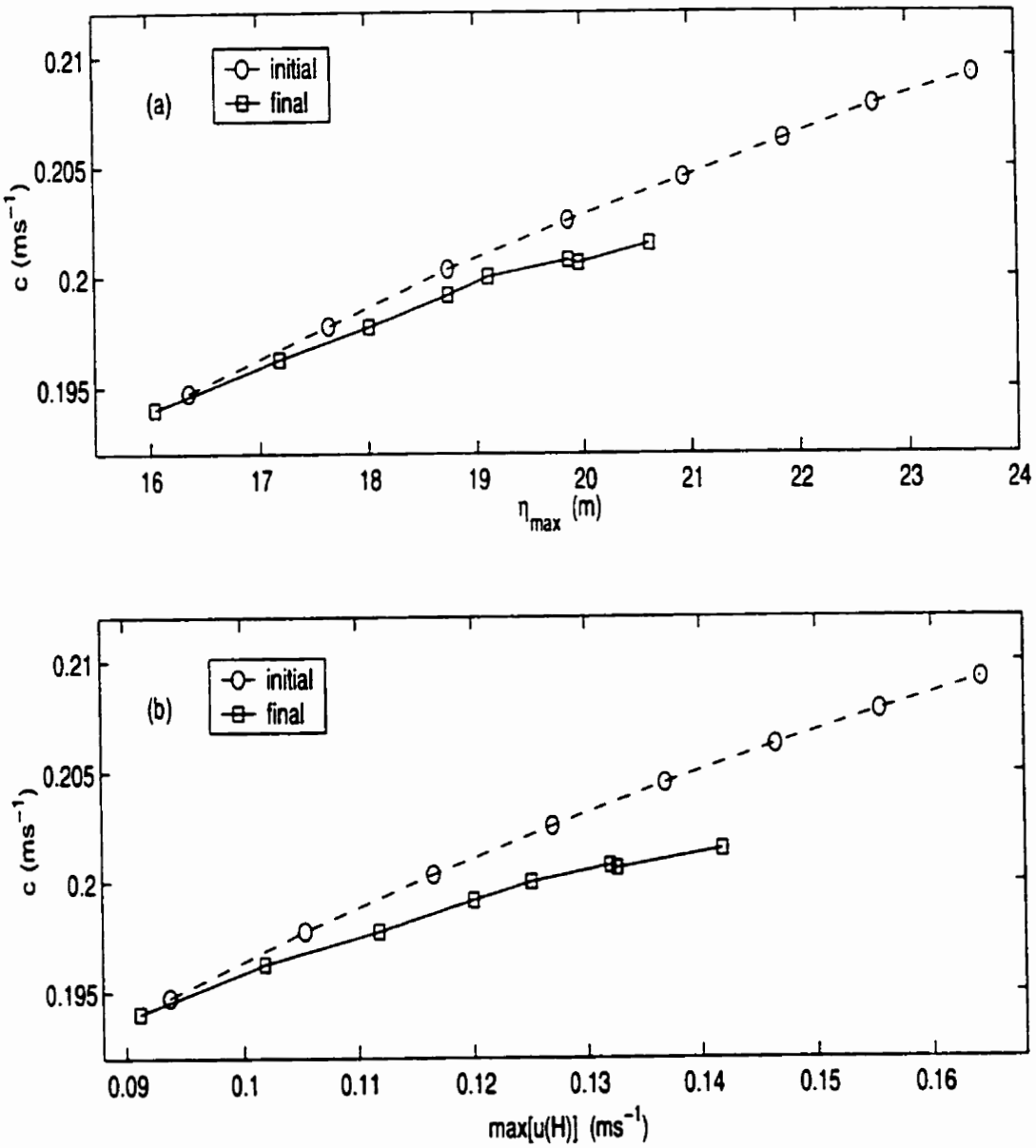

Figure 4.21: Initial and final values of the propagation speed as a function of (a) the maximum isopycnal displacement, (b) the maximum wave induced horizontal velocity at the surface. Magnitudes plotted.

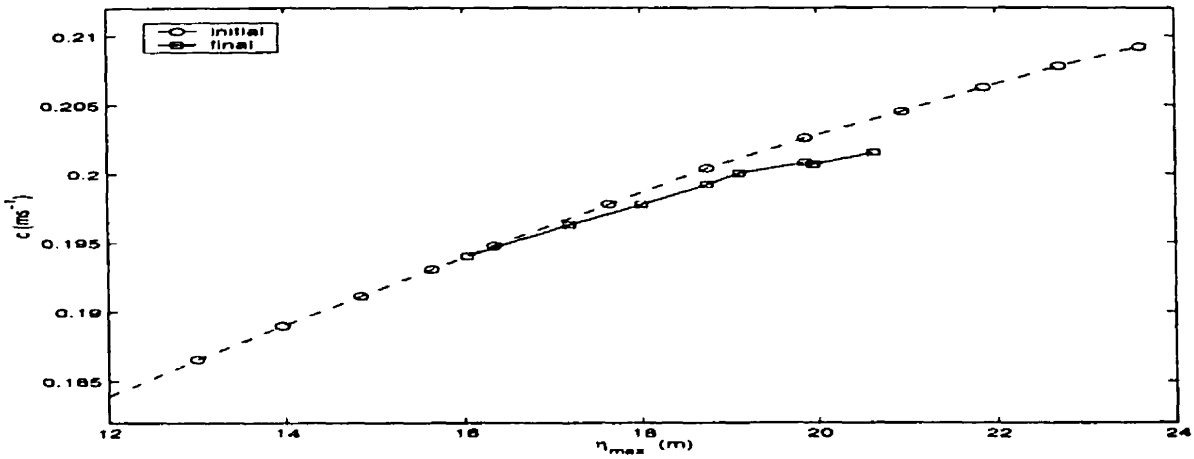

Figure 4.22: Initial and final values of the propagation speed as a function of the maximum isopycnal displacement for the four largest nonbreaking ISWs as well as the eight ISW-like objects with trapped cores. Magnitudes plotted.

cores, but that this smooth relationship does not hold for the larger cores.

We now turn to vertical profiles of the horizontal velocity. As in the previous section we consider profiles taken at the center of the wave where the largest wave induced horizontal currents occur. In figures 4.23 and 4.24 we compare initial and quasi-steady states for $A = 0.06, 0.08, 0.10$ and 0.12. Figure 4.23 shows the entire water column while figure 4.24 focuses on the near bottom core region. We can see that while for $A = 0.06$ the decay of the velocity profile over the top 20.0 m of the water column is nearly negligible, it increases with increasing initial core size (A) becoming clearly visible for $A = 0.10$ and 0.12. The profile in the near bottom region is blunted in the quasi-steady state with the most negative current occurring between 5.0 and 10.0 m above the bottom. Figure 4.24 shows some of the details of the core region. In particular, one can note that the oscillations in the profile appear to grow with increasing initial core size (A). It is nevertheless interesting that the larger initial core cases, which undergo a more violent adjustment, end up with essentially unchanged characteristics from the smaller cases.

Finally we examine the vorticity contours in the quasi-steady core region. From figure 4.25 we can see that for smaller initial cores the core region remains largely free of vorticity while large vorticity variations form a ring around the core. For larger cores there is more variation in the

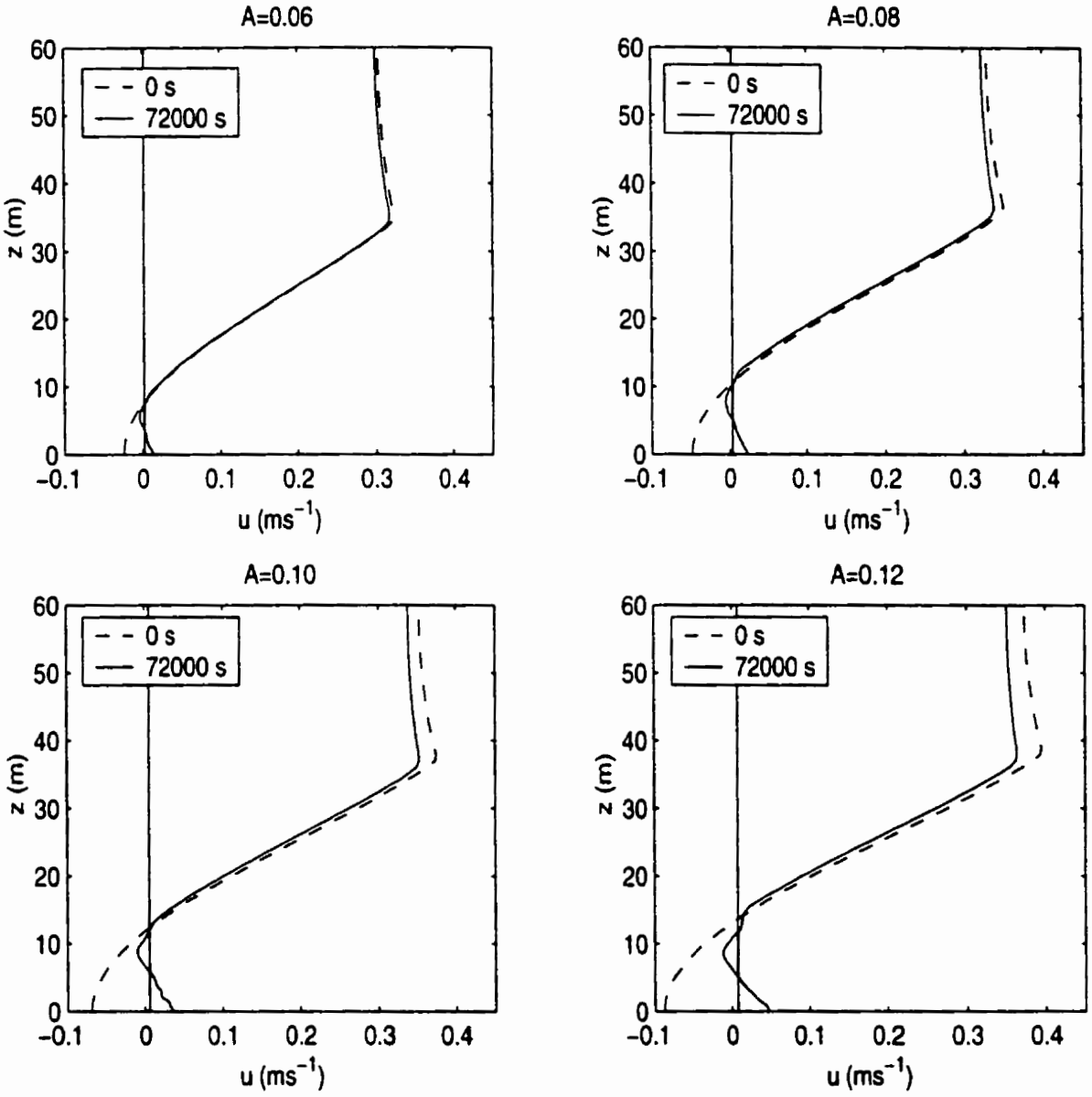

Figure 4.23: Vertical profile of the horizontal velocity at the wave crest: Comparisons of initial (dashed) and quasi-steady (solid) states. Final propagation speed indicated by solid line.

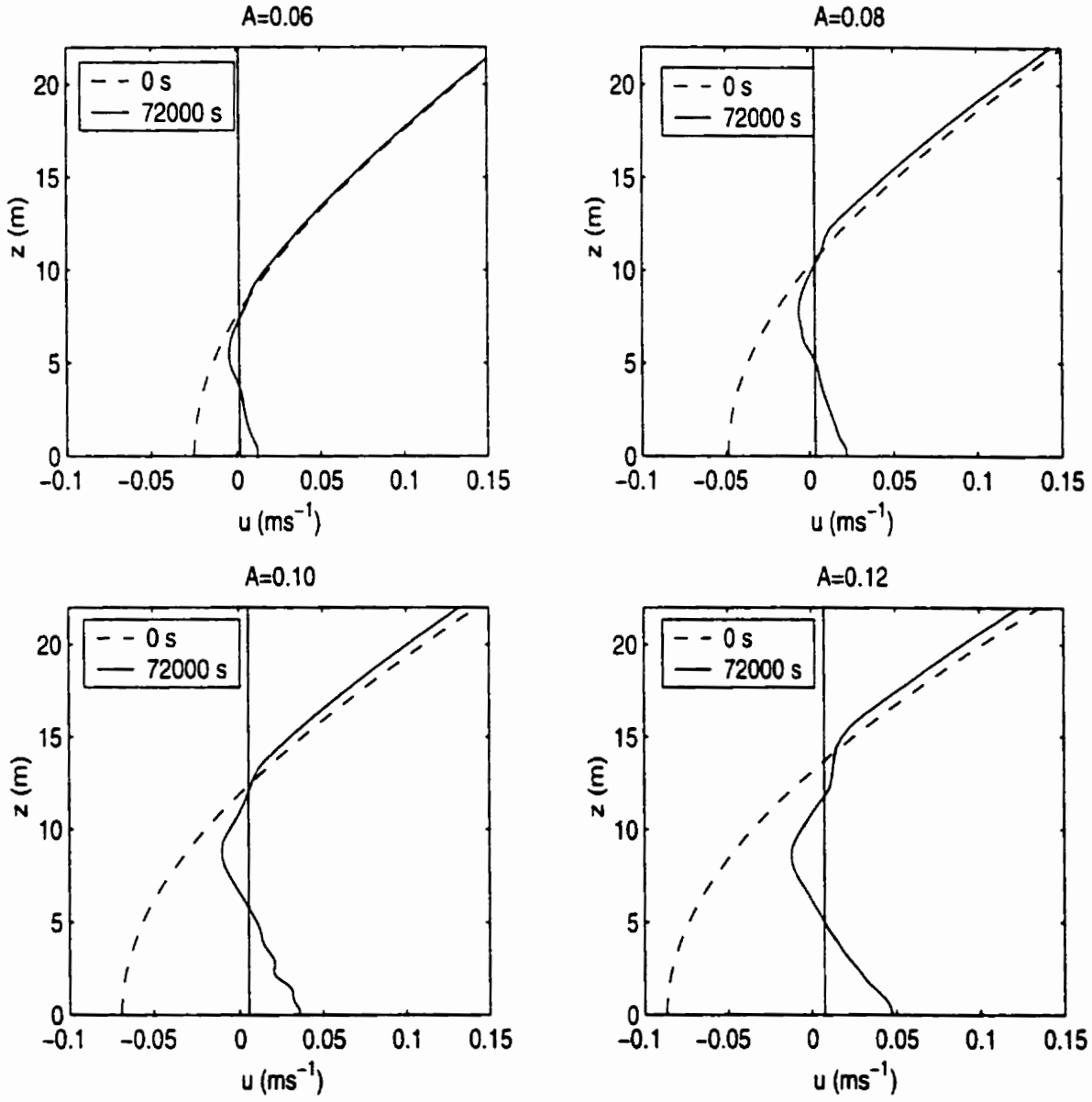

Figure 4.24: Vertical profile of the horizontal velocity at the wave crest: Comparisons of initial (dashed) and quasi-steady (solid) states. Final propagations speed indicated by solid line.

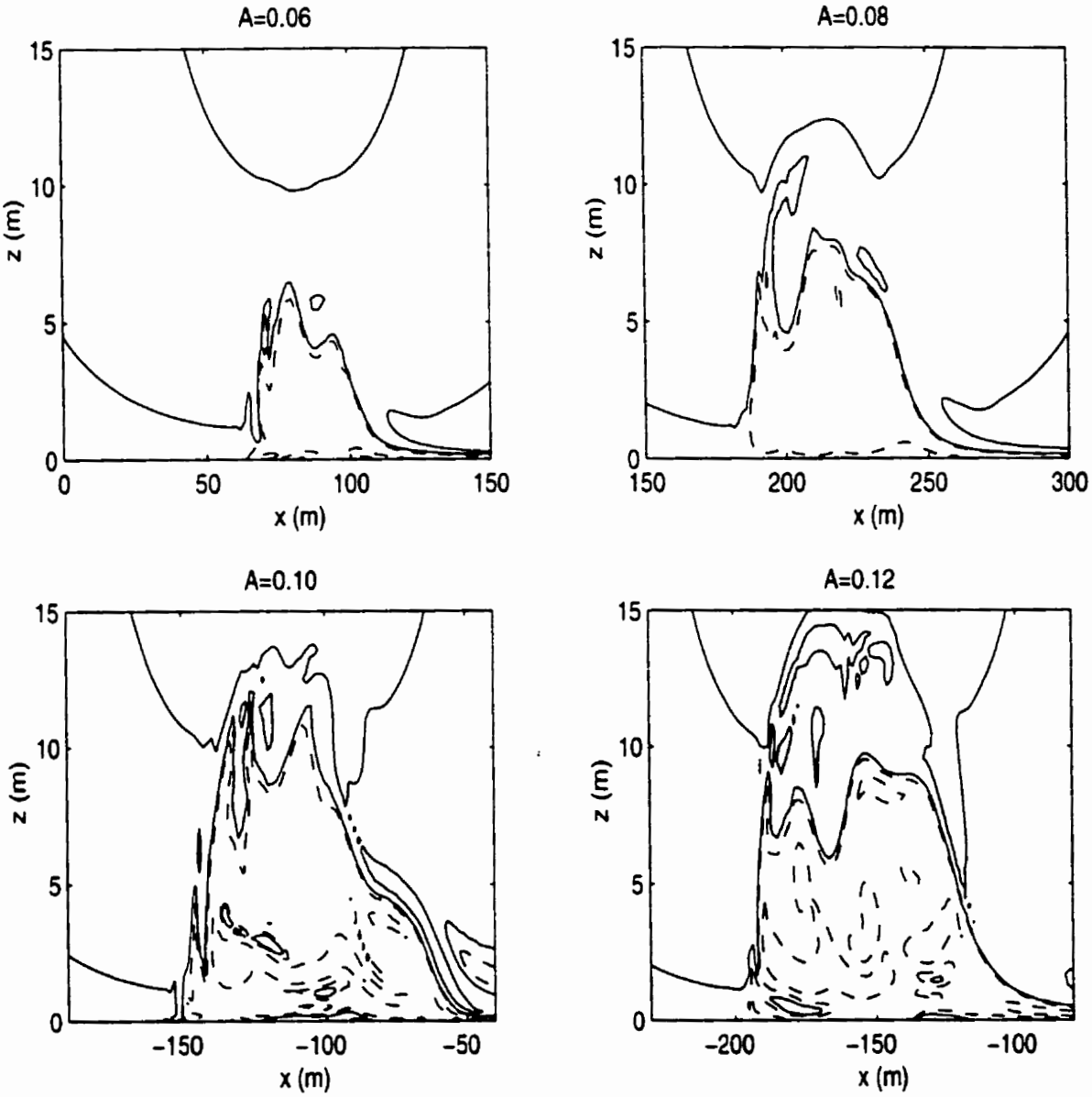

Figure 4.25: Contours of the vorticity in the core region for $A = 0.06, 0.08, 0.10$ and 0.12. Positive values - solid, negative values - dashed.

vorticity field within the core itself. However, for $A = 0.10$ we can see that a sizable region free of vorticity (corresponding to stagnant fluid) is found roughly 5 m above the bottom.

In summary then, as the initial core size (A) is increased we find that the size of the quasi-steady, nearly stagnant core increases, initially keeping an asymmetric shape consisting of a main area of reduced velocities found several meters above the bottom and a small region of reduced velocities reaching the bottom at the front of the core. When the initial core size is increased past a certain point, the region of reduced velocities that reaches right to the bottom disappears and the entire quasi-steady core is found in a broad (approx. 60.0 m), region lying between 5.0 and 15.0 m above the bottom. The adjustment for the larger initial core values is quite violent and hence could be significantly modified by 3D effects. Nevertheless, for all cores (values of A) used the vertical profiles of the horizontal velocity at the crest of the wave, were remarkably similar.

The adjustment process leads to a decrease in propagation speed and maximum isopycnal displacement for all waves. This change increases in magnitude as the initial core amplitude is increased. The results for the larger initial cores appear to indicate that the wave amplitude as defined by the maximum isopycnal displacement cannot be increased arbitrarily. In other words past a certain point increasing the size of the initial core will lead to a more violent adjustment during which more material is shed behind the wave, but will not yield a final, quasi-steady wave with a larger amplitude.

We next turn to the effect of the core initialization

4.3.2 Core Initialization Effects

As mentioned in the Methods section, the manner in which we have chosen to set the velocities in the initial core is not unique. Recall that the initial core is defined as the set of points at which the variational algorithm sets the density to be larger than the density at the bottom of the ocean. To ensure that our initial wave is a physically reasonable object we set the density in this region to equal the density at the bottom, far upstream of the wave. At this point we must also make a choice as to what to do about the velocities in this region. The choice made in the above discussion is to simply keep the velocities as given by the variational ISW calculator (this

is referred to as the original initialization in the figures and discussion below). Of course we do not expect the final quasi-steady state of the ISW-like object to necessarily reflect these velocities, however there seems no *a priori* reason to modify the velocities. Other choices are possible. For example we could set the entire core region to be stagnant with respect to the initial wave speed. This makes some sense as we found that the final quasi-steady state had a nearly stagnant core region. Furthermore it agrees with the theory of Derzho and Grimshaw ([15]). This initialization (referred to as the $u = c$ initialization in the figures and discussion below), however, is not perfect from the point of view of the numerical solver as it introduces discontinuities in the velocity field at the edge of the core. In practice these discontinuities lead to small scale noise, but no other profound effects on the resulting ISW-like object. The level of noise increases as the initial core region increases in size.

Setting $(u, w) = (c, 0)$ modifies the velocities in the bottom region. For small cores the change is small (i.e. the change in u is less than 6% of the maximum wave induced u value for the $A = 0.05$ case), but increases with the initial core size (the change in u is about 25% of the maximum wave induced u value for the $A = 0.08$ case).

In this sub-section we compare and contrast the results of the two above-mentioned initializations for three values of A ($A = 0.05$, $A = 0.06$ and $A = 0.08$). We choose to focus on the smaller initial cores in order to avoid questions regarding the violent adjustment phase for larger initial cores.

In figure 4.26 we show the final quasi-steady velocity fields for the three waves for both initializations. For fixed A the shape of the nearly stagnant region is not greatly changed by a change of initialization. There is a clear difference for the smaller cores in that there is no region where $u < 0$. However, as the negative currents for the original initialization (in the quasi-steady state) have a small magnitude, the quantitative difference between the two initialization cases is very small. The fact that a region with $u < 0$ results for the larger initial core corresponding to $A = 0.08$ can be explained by noting that the final, quasi-steady region is much smaller than the initial core and hence for $A = 0.08$ a more violent adjustment process can induce negative velocities in the core region. Recall the adjustment consists of instability at the edge of the core

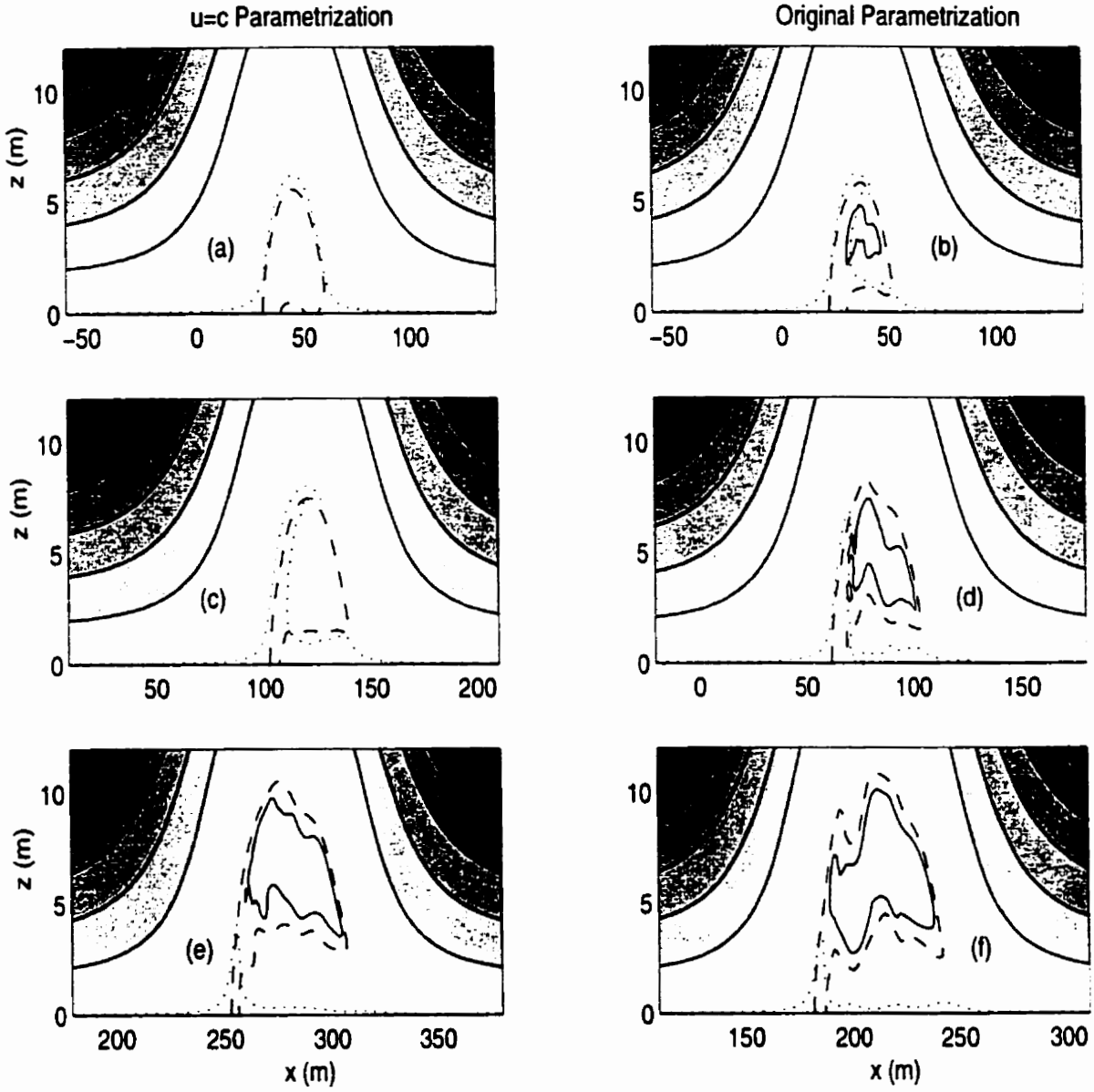

Figure 4.26: Quasi-steady state comparison for the two initializations used, density contours (shaded), bottom density contour (dotted), contour of $u = 0.02|c|$ (dashed), contour of $u = 0$ (solid). (a) $A = 0.05$ $u = c$ initialization, (b) $A = 0.05$ original parametrization, (c) $A = 0.06$ $u = c$ initialization, (d) $A = 0.06$ original initialization, (e) $A = 0.08$ $u = c$ initialization, (f) $A = 0.08$ original initialization.

region, followed by intrusion into the core itself as well as downstream washout of material in the core. At the risk of being repetitious, we remind the reader that we are talking about negative velocities in a frame of reference moving with the initial wave propagation speed.

The two initializations lead to different values for the final propagation speed. In particular, the $u = c$ initialization yields a larger drop in propagation speed from the value given by the solitary wave solver. More quantitatively if we define the ratio

$$R_c = \frac{c_{original} - c_{final}}{c_{original}} \tag{4.1}$$

we find that for the original initialization $R_c = 0.0038$, 0.0076 and 0.0167 and for the $u = c$ initialization $R_c = 0.0058$, 0.0114 and 0.0204 for $A = 0.05$, 0.06 and 0.08, respectively. Thus neither the difference in the drop between the two initializations, nor the drop in propagation speed itself are very large. Note that due to the drop in propagation speed it is the dashed contours representing $0.02|c|$ in figure 4.26 that give the nearly stagnant region for the quasi-steady state.

In figure 4.27 we show the contours of vorticity for the initial and quasi-steady states for the $A = 0.08$ case with both the original and the $u = c$ initialization. The $u = c$ initialization leads to slightly more vorticity in the core interior, but in general the two plots are qualitatively similar.

Finally we consider vertical profiles of the horizontal velocity at the center of the wave (the wave crest). In figure 4.28 we compare the two initializations. It can be seen that when examining the entire water column the results of the two initializations are indistinguishable for $A = 0.05$ and very nearly identical for both $A = 0.06$ and 0.08. If we focus on the near bottom or core region we can see that there are indeed small differences for all values of A. However the major characteristics noted in the previous subsection (i.e. the blunted profile with a minimum velocity found some ways above the bottom) are common to both initializations.

The above results suggest that ISW-like objects with a main body very close to a solitary wave and a smaller (though possibly quite large in physical space) core region of nearly stagnant fluid are largely independent of the way the velocities in the initial core are initialized. Of course the above results are not exhaustive. Still there seems little evidence that a different quasi-steady

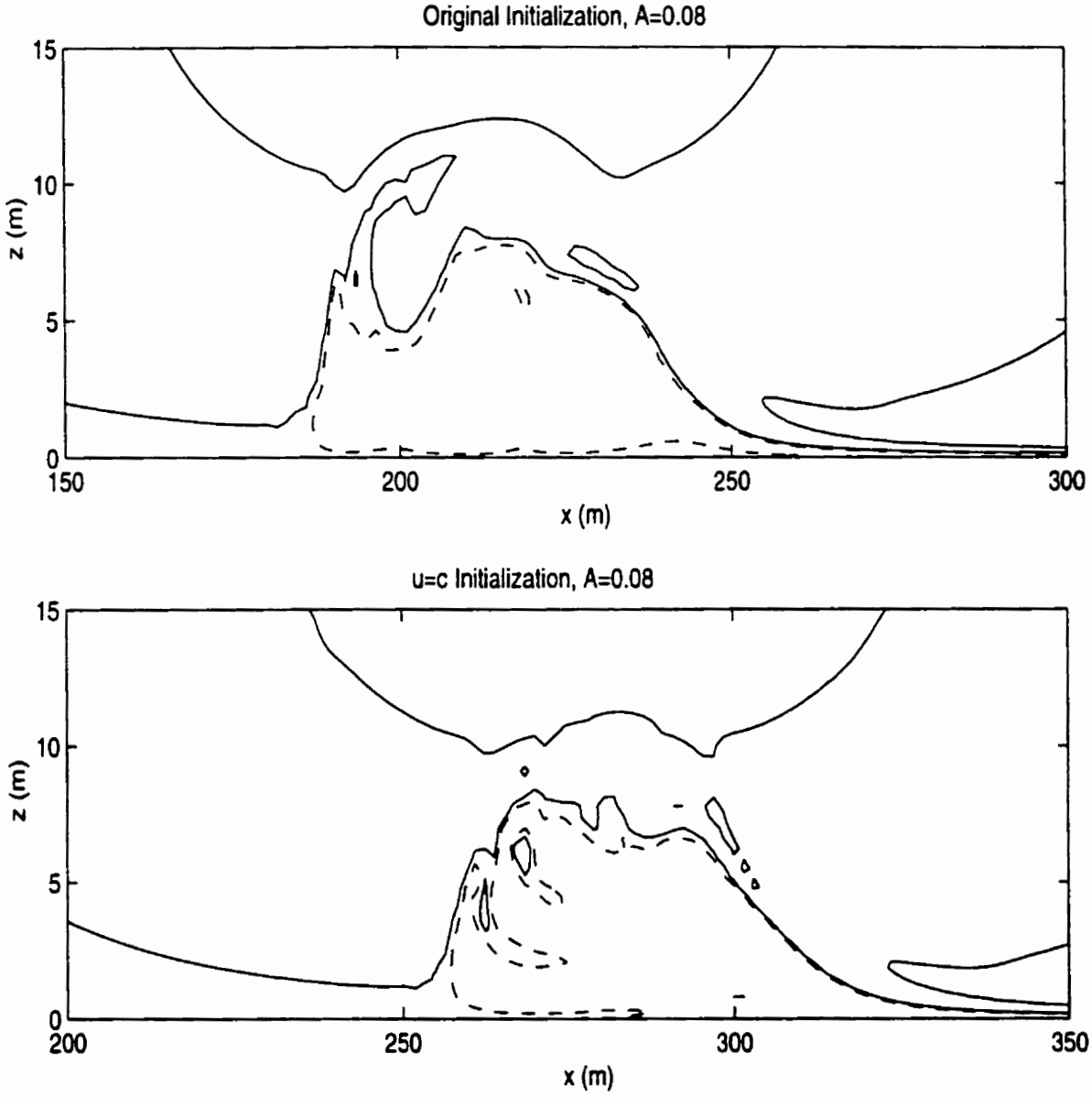

Figure 4.27: Contours of the quasi-steady vorticity in the core region for $A = 0.08$ with the original initialization (top panel) and the $u = c$ initilization (bottom panel) for the velocities in the initial core. Positive values - solid, negative values - dashed.

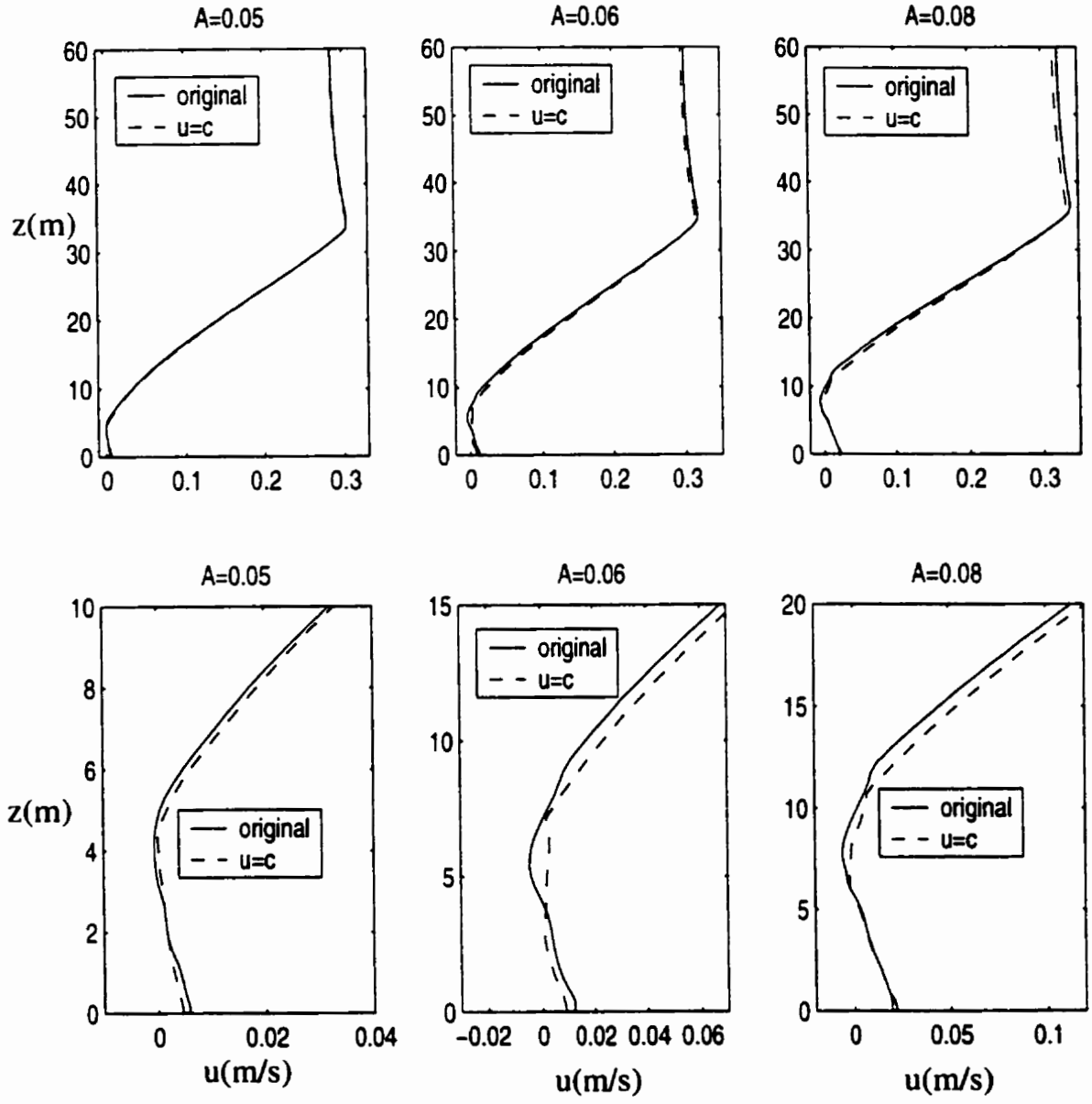

Figure 4.28: Comparisons of vertical profiles of the horizontal velocity at the wave crest for the two core initializations as A varies: original (solid), $u = c$ (dashed). Top three panels show entire water column, bottom three focus on core region.

state (for example a vortex core) from that described above could be achieved.

4.4 Conclusions and Future Work

In the previous sections we have outlined a method for calculating internal solitary-like waves with a trapped core and discussed some of the properties of these waves. In particular we have shown that it is possible to find waves that are quasi-steady. These waves are made up of a main body that is virtually indistinguishable from a nonbreaking ISW and a nearly stagnant core (in a frame moving with the wave propagation speed). The waves were computed by first using the variational solitary wave calculating algorithm to prepare an initial state. The wave calculated by the variational method must be modified by adjusting the density (and possibly the velocities) in the closed streamline region. Once modified, the wave is allowed to evolve until a quasi-steady state is reached. In all cases a quasi-steady state was reached. Two different initializations for the velocity field in the core were tried, but these did not seem to have much bearing on the final quasi-steady state. We also ran several test cases with a non-zero, linear background current. Again we found that, aside from a change in η_b (as discussed in Chapter 3), the presence of the background current did not affect the final quasi-steady outcome, as evidenced by the example in figure 4.29.

In figure 4.29 we show the initial and quasi-steady contours for two waves with $U(z) = 0.1\frac{z}{H}$ and one wave with no background current for comparison. The maximum value of the background current is approximately 69% of the linear longwave speed.

Though the variational algorithm does not specify the wave amplitude, it does allow us to have some control of the size of the initial core region. For all cases, the adjustment time needed for the initial state to reach the final, or quasi-steady state is quite long (50,000 s for a stratification with a linear long wave speed of 0.14 ms^{-1}). This long adjustment time makes it difficult to envision a situation in which quasi-steady cores would be observed in the ocean. During the adjustment process both the amplitude and propagation of the initial wave decrease. For smaller initial cores it was found that the propagation speed versus maximum isopycnal displacement curve (after adjustment) for waves with a trapped core can be smoothly joined to the same curve for nonbreaking ISWs. For larger initial cores this was not possible. This can be attributed to the fact that the adjustment process is much more violent for larger initial cores. While 3D effects

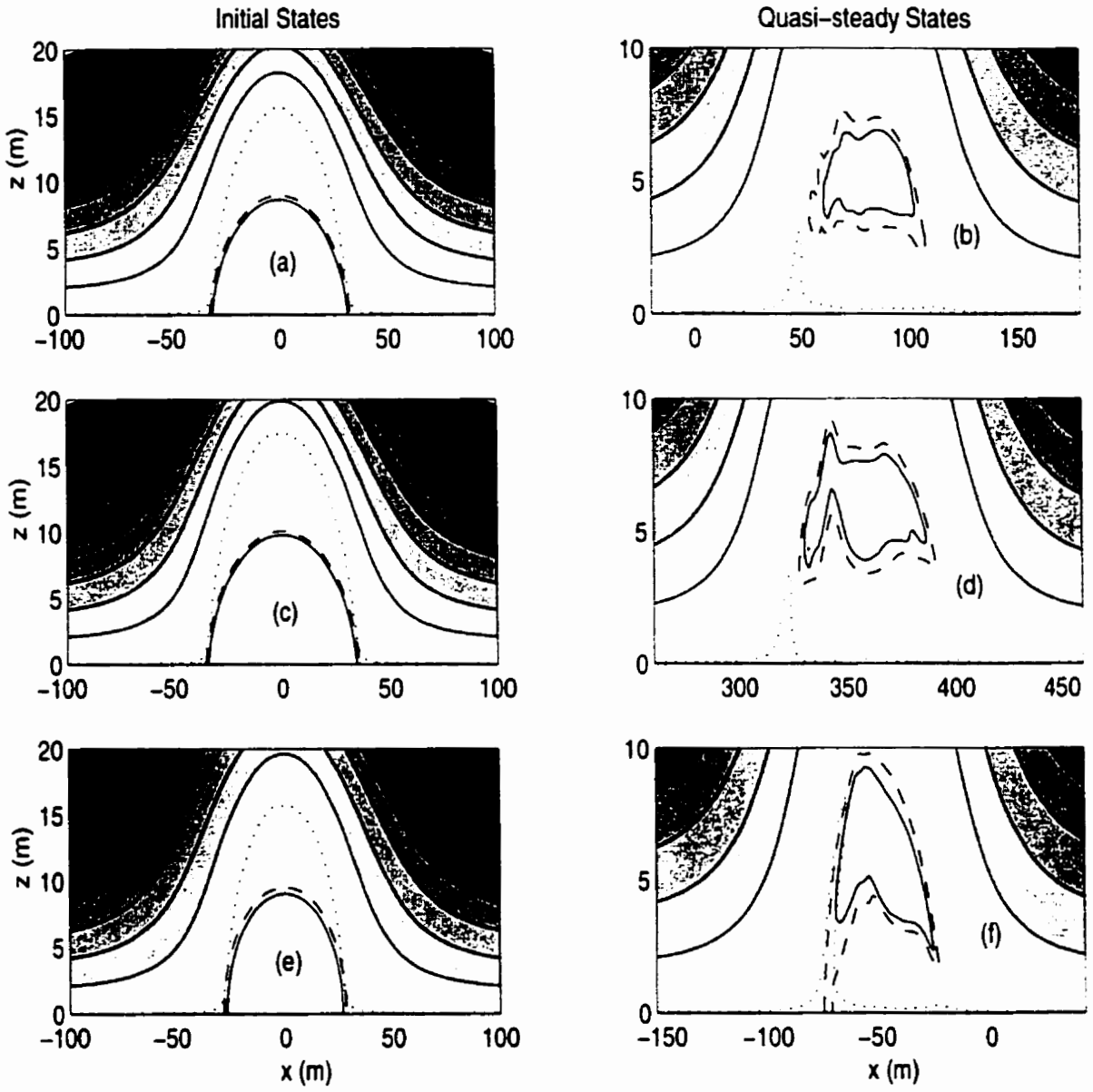

Figure 4.29: Initial and quasi-steady states, (a)-(d) with linear background current. Density contours (shaded), bottom density contour (dotted), contour of $u = 0.02|c|$ (dashed), contour of $u = 0$ (solid). (a) $(A, U(H)) = (0.05, 0.1)$ initial, (b) as (a) quasi-steady, (c) $(A, U(H)) = (0.06, 0.1)$ initial, (d) as (c) quasi-steady, (e) $(A, U(H)) = (0.07, 0.0)$ initial, (f) as (e) quasi-steady

would undoubtedly play some part in the adjustment process, it is interesting that even the largest waves tried eventually reached a quasi-steady state.

All cases shown in this chapter used a stratification for which the wave amplitude, η_{max}, is bounded above by wave breaking. For stratifications with conjugate flows it is impossible to use the variational algorithm to calculate waves past breaking. We attempted to produce waves with trapped cores for such stratifications using first-order WNL (which predicts breaking waves for all stratifications). Despite considerable effort, it was found that the cores did not remain trapped and the steady state reached was a nonbreaking ISW (confirmed by the variational algorithm).

The literature on waves with trapped cores is not nearly as extensive as for nonbreaking ISWs. The numerical study of shoaling ISWs of depression by Lamb ([35]) serves as the main comparison to the present study. Lamb finds that shoaling waves will not form trapped cores if a mixed layer is found near the surface (or in other words, for stratifications which admit a conjugate flow solution). He discusses the evolution of the trapped cores as the waves propagate in the shallow (on shelf) region. However Lamb does not follow the waves long enough to see whether quasi-steady cores form. For stratifications with the pycnocline found in the bottom half of the water column (resulting in waves of elevation) it is perhaps more likely that the water column is stratified right to the bottom, and hence that shoaling will lead to waves with trapped cores. In fact for waves of elevation, very small changes in the total depth can lead to wave breaking and the formation of trapped cores. For example a change in total depth from 60 m to 55 m over 100 m was found to lead to breaking and core formation for the density profile discussed in this chapter. Observations of ISWs of elevation on the Pechora shelf by Serebryany and Shapiro ([56]) show several waves consistent with the properties described in this chapter. While the waves observed did not likely have quasi-steady cores (as they were likely formed during shoaling and had not had time to settle to the quasi-steady state), it would be interesting to compare the measurements with the present results in more detail.

The experiments of Grue *et al.* ([23]) were mentioned in the introductory section of this chapter. These experiments follow the formation and propagation of an ISW that is formed by the collapse of a rectangular region (kept apart from the main tank) with a density profile that is

different from the profile found in the main portion of the experimental wave tank. The technique used to create the waves leads to a very active core region. The tank length is sufficiently large so that an ISW with a trapped core is observed before the wave reaches the end of the tank. Given the long adjustment time it is unlikely that the ISWs studied by Grue *et al.* have quasi-steady cores. Grue *et al.* find that the main wave body is well described by nonbreaking, theoretical predictions (their theory can be thought of as a special case of the general formulation used to construct the variational ISW calculating algorithm). However, their theory cannot describe the core region. Given the results in this chapter, it is difficult to imagine a simple theory for the motions in the core. Even for nearly linear stratifications, as Derzho and Grimshaw's theory breaks down for large cores since the core is no longer adjacent to the bottom and the fluid in the core is not stagnant.

In summary, the experiments of Grue *et al.* are an excellent complement to the results of this chapter. Given that the two studies attempt to answer somewhat different questions (Grue *et al.* make no mention of a quasi-steady state and there is some question of how dependent the details of their waves are on the generation technique) the agreement between the two sets of results speaks to the robust nature of the phenomena being discussed. Numerical simulations that mimic the experimental set-up of Grue *et al.* provide an obvious avenue for future work.

We should briefly mention that experimental and numerical work on trapped cores for mode 2 waves is much more extensive (i.e. [14], [63], [58], [60]). However the case of mode-2 waves is complicated by the fact that it is possible to have small, mode-1, oscillatory tails that propagate with the wave and drain energy from it (hence the wave is not solitary, see [2]). Preliminary investigations by the author indicate that mode-2 waves with trapped cores are possible for density profiles which have conjugate flow solutions. Space and time considerations relegate further investigation to the future.

We should note that the numerical simulations of both Terez and Knio ([60]) and Tung *et al.* ([63]) actually involve mode-1 waves (mode-2 waves are then plotted using a line of symmetry), and as such are somewhat relevant to the present work. The study of Tung *et al.* provides an alternative numerical technique (same governing equation) for calculating ISWs as well as some

preliminary discussion of waves with closed streamlines (along the lines, and with many of the shortcomings of the previously discussed ([12])). In the study of Terez and Knio, the waves are generated by collapsing an initially mixed region in a main domain that is a stably stratified, two-layer fluid. The resulting waves appear qualitatively similar to both the present work and the experiments of Grue *et al.*, though the authors do not provide quantitative discussion of the velocity fields, concentrating instead on Lagrangian particle tracking for short times and wave-wave collisions.

In summary then the present work shows that it is possible to calculate quasi-steady waves with a trapped core in a systematic manner. For small initial cores, these waves are in reasonably good agreement with the theoretical prediction of Derzho and Grimshaw ([15]) that the trapped core should be stagnant in a frame moving with the wave. It is found that the waves are only approximately stagnant and that their propagation speed is over-estimated by the variational ISW calculation algorithm (the drop in propagation speed increases with initial core size). For larger initial cores the quasi-steady core is found well above the ocean bottom, something not predicted by ([15]). In nature it is possible that waves of elevation with trapped cores can be formed as an initially nonbreaking ISW shoals onto bottom topography of relatively small size (compared, for example with that used in [35]). We should note, however, that the interaction of an ISW with realistic topography would likely be more complex than to simply form a trapped core. Preliminary simulations performed by the author indicate that even for long (100 m), small amplitude (2 m) sinusoidal topography the near bottom region of the wave is modified a great deal. This issue requires careful exploration in the future.

Chapter 5

ISW-BL Interaction

The previous two chapters considered waves governed by inviscid governing equations. This is often a good approximation in the ocean, particularly if there is no background current, as the bottom boundary layer (BL) will be thin and the loss of energy from the ISW to viscous dissipation small. However there is some question whether the interaction between the wave and the bottom boundary layer could lead to qualitatively different dynamics (from a slowly changing solitary-like wave). The measurements of Bogucki *et al.* (or BDR) ([8]) off the California coast indicate that the passage of an internal wave packet of elevation leads to an increase in the amount of sediment in the water column well above the bottom (8 m above the bottom in water 60.0 m deep). These measurements imply that the interaction of the wave-induced currents with the bottom boundary layer leads to sediment resuspension. In ([8]) the authors hypothesize, based on WNL, that the resuspension sets in due to shear instability in the boundary layer, with the shear instability being crucially dependent on the presence of a (non-constant) background current. We calculated fully nonlinear ISWs for the situation outlined in ([8]) and found that for all nonbreaking ISWs the Richardson number (Ri) did not dip below 0.3. While $Ri > 0.25$ does not guarantee stability for non-parallel flows, our results appear to invalidate the predictions in ([8]). The problem of resuspension was revisited by Bogucki and Redekopp in the short paper ([10]). This paper presented direct numerical simulations of the bottom layer in a two-layer fluid (however the top

boundary was held fixed), and argued that (WNL) waves larger than a certain amplitude exhibited a global instability. While the implications of the given results were clear, the same could not be said for the numerical methodology and hence ([10]) served more as an impetus for further work than as a valid explanation of the sediment resuspension process measured by BDR. A particular concern for the author was the reliance in ([10]) on WNL for the velocity profiles (though even this was not done in a clear manner). Further observations of resuspension events due to ISW passage were presented by Bogucki and Redekopp in the proceedings of the Fifth International Symposium on Stratified Flows ([11]). These observations indicated that resuspension of sediment by ISWs in coastal seas occurs quite often and underlined further the need for a theoretical understanding of the resuspension process.

As the present work aims to clarify the work of Bogucki and Redekopp it makes sense to comment on their paper ([10]) more extensively. The authors argue that below a critical amplitude the flow in the BL beneath the WNL wave is given by a reasonably symmetric, stationary eddy. Above the critical amplitude (which is based on the magnitude of the WNL horizontal velocity perturbation) spontaneous vortex shedding occurs. The authors interpret the vortex shedding as a global instability of the initial separation bubble. To the present author, this seems rather odd, as Bogucki and Redekopp never discuss whether a fully nonlinear ISW is allowed to evolve from their initial conditions at all.

Indeed the work of Bogucki and Redekopp is perhaps best understood in terms of previous work on separation bubbles in the boundary layer ([51], [52]). In ([51]) separation bubbles induced by suction at the upper boundary of a two-dimensional channel and their instability were studied by direct numerical simulation. The authors found that below a certain critical suction rate the separation bubbles induced by the adverse pressure gradient were steady. Above this critical suction rate vortex shedding resulted. The authors found, somewhat surprisingly, that vortex shedding began to occur when 11% of the incoming fluid was removed from the computational domain by suction for the entire range of Reynolds numbers tried. The remainder of the paper provided a comparison of numerical and experimental results on boundary layer separation. As such it is not relevant to the present work. The results of ([51]) were repeated for a more complex

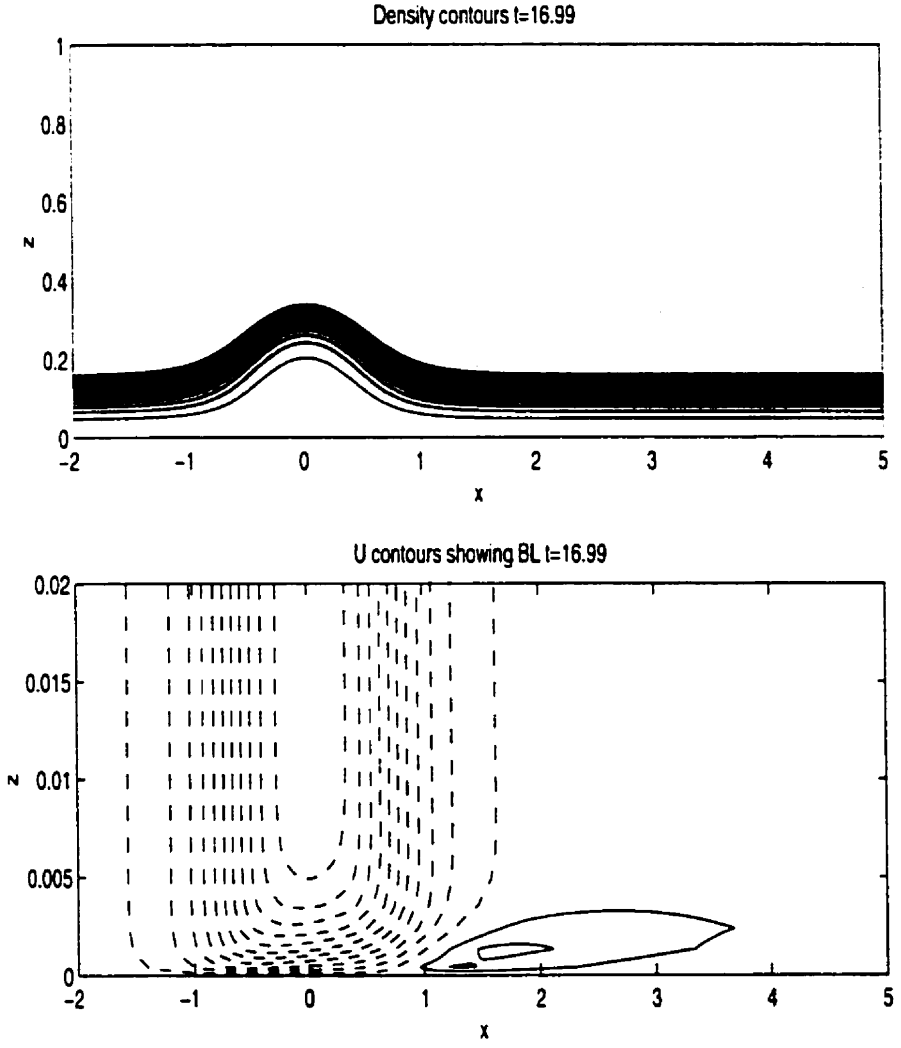

Figure 5.1: Density and horizontal velocity contours (in aframe fixed with the ground) for ISW with well developed bottom BL. $(U_s, \nu) = (0.0, 10^{-4})$

flow at the upper boundary in ([52]), again to provide a comparison with experiment. Later in this chapter we will present work attempting to reproduce some of the results of ([51], [52]).

Returning to the paper of Bogucki and Redekopp, it seems reasonable to adopt the viewpoint that an instability may occur in the BL beneath large, fully nonlinear ISWs. However, the details of the instability may not be accurately described by the WNL based simulations of Bogucki and Redekopp.

There are two methods available to us for computing solitary-like waves in the presence of no slip boundary conditions on the ocean bottom. First we could simply allow an initial disturbance in the density field to break up into a rank ordered wave train of solitary-like waves (though the resulting wave amplitudes would be largely uncontrolled). Second we could use an inviscid ISW as an initial condition with the hope that the adjustment to the no slip bottom boundary conditions proceeds in a physically reasonable manner. There is no guarantee *a priori* that this will be the case. However, several computations for different sized ISWs (as well as different density profiles) have demonstrated quite conclusively that the initial wave remains largely unchanged, save for the formation of a bottom boundary layer whose thickness depends on the choice of eddy viscosity value. For these runs we compute a leftward propagating wave, switch to a frame moving with the wave, and then begin time-stepping with no slip boundary conditions applied at the moving bottom (this setup means smaller waves will propagate to the right and out of the computational domain). In figure 5.1 we show an example of a leftward propagating ISW with a well developed BL. The details of the grid used will be given in the following section. From the figure it is clear that the wave remains essentially solitary with a narrow BL attached to the bottom. An area of weak horizontal velocities directed opposite to the direction of propagation is seen to trail the wave in the bottom BL.

The same result was found for waves of various size and in the presence of a background current provided that $U(0) = 0$, or in other words the velocity of the background current at the bottom was zero. When the velocity of the background current at the bottom is not zero (in the inviscid case) a boundary layer forms upstream of the wave as soon as the no slip bottom boundary condition is applied. This means vorticity is produced upstream of the wave. This

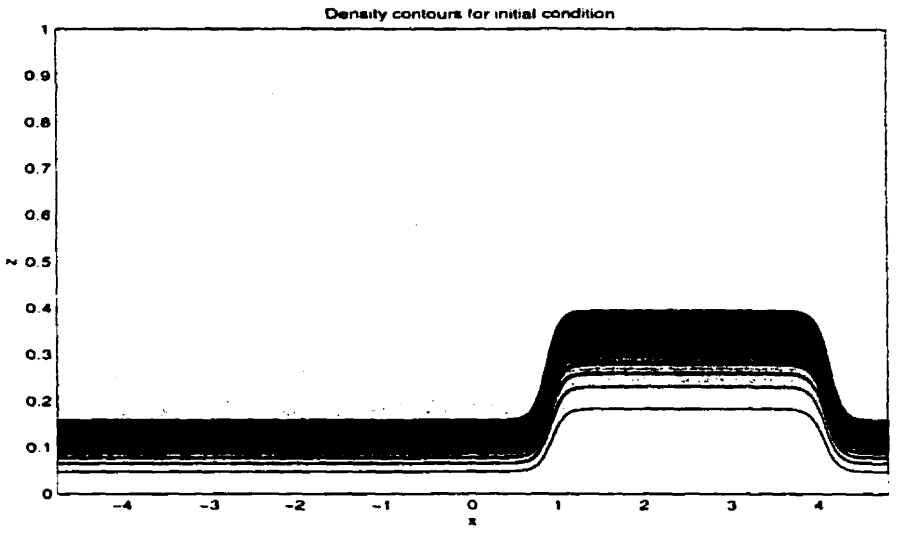

Figure 5.2: Density contours of initial condition for ISW fissioning with bottom BL. $(U_s, \nu) = (0.5, 10^-5)$

vorticity is subsequently advected into (and interacts with) the main wave body. We will show that this interaction can lead to large instabilities within the bottom boundary layer.

We will look at the the simplest possible background currents, namely non-zero constants (we will label these U_s). These can be thought of as a model of the barotropic internal tide. To motivate the remainder of the chapter consider the evolution of an initial disturbance shown in figure 5.2. The length scales in the figure have been non-dimensionalized by the total depth. The computation was carried out in a domain 10 units wide and 1 unit deep using a grid of 3000 by 150 points. All lengths were nondimensionalized by the water column height of 60 m. The horizontal spacing was regular giving a resolution of 0.0033 (0.2 m). The vertical spacing was quadratic with 20 points in the bottom 0.0167 (1 m) and 80 points in the bottom 0.0833 (5 m), giving excellent resolution of the boundary layer region as well as the remainder of the water column. The initial background current is fixed to be a constant, approximately one half of the propagation speed of the expected, leading ISW. We take the eddy viscosity to be $10^{-5}\ m^2\ s^{-1}$, and the Prandtl number to be unity. This simulation has the highest resolution of any presented in this thesis. The Reynolds number (Re) based on the estimated value of the maximum magnitude of the

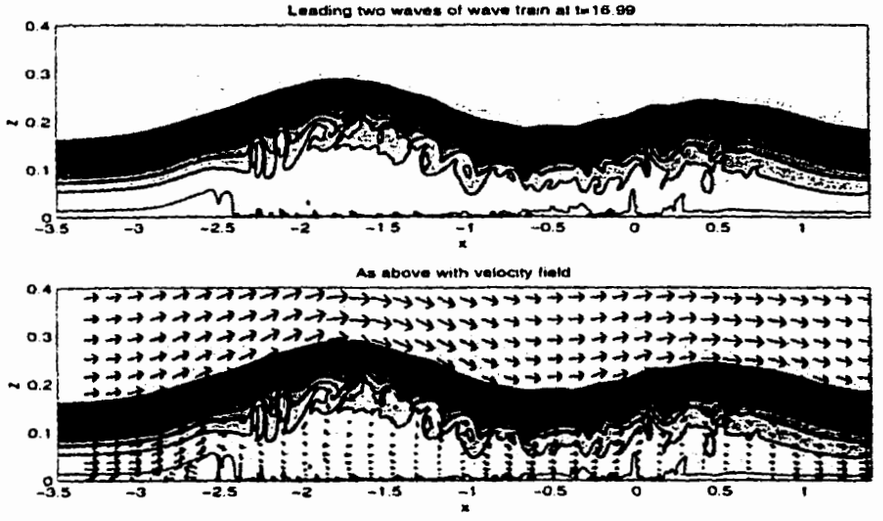

Figure 5.3: Density contours and velocity field for leading two ISWs . Instability and vortex shedding are well developed. $(U_s, \nu) = (0.5, 10^{-}5)$

wave-induced horizontal velocity due to the leading wave, the total depth and the eddy viscosity is approximately $Re = 7.5 \times 10^6$.

The initial disturbance will break up into two rank ordered trains of ISWs, with the rightward propagating train being swept out of the computational domain. In figure 5.3 we show the leftward propagating train well after it has fissioned from the initial disturbance and the bottom BL has had plenty of time to develop. We show both the density and the velocity field. We can note immediately that the two waves that are visible have a much more active and complex structure than the inviscid ISWs (even the waves with trapped cores). Further note that several regions of heavy fluid (in white) have been advected up into the pycnocline. In fact it appears that large vortices are shed from the bottom boundary layer near the front of the leading wave (white region near $x = -2.5$) and are advected up into the pycnocline and over the main wave body. In the remainder of the chapter we aim to systematically examine the onset of the instability in the boundary layer, the values of the physical parameters for which the instability does and does not occur, and the repercussions of the instability for sediment resuspension. We will also comment on some details of the instability as well as some possible theoretical explanations for the onset

of the instability.

5.1 Methodology

The high resolution simulation presented in the previous section is not an efficient means to investigate ISW induced wave resuspension for several reasons. The primary theoretical objection is that we cannot control the size of the ISW that fissions from the initial disturbance, something we could do with the variational ISW calculating method. What is more, on a practical level, to resolve the fissioning process with the same level of accuracy as in the previous section would prove too costly in terms of computational time and storage space to make a thorough investigation of the parameter space. A compromise between what is computationally reasonable and what is desired in terms of resolution is afforded by the ISW calculating algorithm. We adopt the following approach for a given stratification profile:

- Calculate the desired ISW using the variational method on a regular grid with no background current.
- Interpolate to a grid that resolves the bottom BL using third order splines.
- Add the desired background current (which we shall call U_s).
- Switch to a frame moving with the wave (see details below)
- Run the time-stepping solver for the desired value of the eddy viscosity and diffusivity

Note that in the frame moving with the wave the bottom will be moving as well. We should note that with the no slip bottom BCs it is not possible to shift to a frame moving with the wave exactly, since the wave propagation speed is altered slightly by drag due to the bottom BL and decreases as the wave amplitude decreases. In practice this issue is irrelevant as the wave drift is nearly negligible on the time scales of interest. Also note that to run cases with varying Reynolds number (alternatively eddy viscosity) we need only repeat steps 3 through 5. Because the wave is basically still we can specify a smaller domain in the horizontal direction (thereby getting greater resolution without increasing computational cost). Plots of horizontal velocity will be given in the moving frame unless otherwise specified.

For the simulations presented in the following section we utilize a domain $L = 16.66$ by $H = 1$ units with 1000 by 120 points. All lengths are nondimensionalized by the water column depth of 60 m. The grid is regular in the horizontal direction with a resolution of 0.0167 (1 m) while the vertical grid is quadratic with 12 points in the bottom 0.0167 (1 m), 32 points in the bottom 0.0833 (5 m) and 48 points in the bottom 0.167 (10 m). Resolution tests for the horizontal spacing were performed by doubling the horizontal resolution. We found that this did not affect the occurrence or time to onset of the instability in the bottom boundary layer. However certain fine scale features that appear after the onset of the instability are affected by doubling the horizontal resolution. Resolution tests for the vertical grid yielded more interesting results and will be discussed at length in the following section. In the final analysis, however, the grid spacing mentioned above proved to be both computationally economical and capable of resolving the details of the instability to a reasonable level.

For all simulations the bottom is flat, the Prandtl number is set to unity and the eddy viscosity is constant. The value of the eddy viscosity varies from simulation to simulation. All ISWs are computed as leftward propagating so that in a frame moving with the wave all disturbances shed behind the wave propagate rightward and out of the computational domain (through an open right side boundary).

We consider several stratifications of the form

$$\bar{\rho}(z) = 1 - 0.01 \tanh\left(\frac{z - z_0}{d}\right).$$

All results will be presented in nondimensional form. We take the total depth, H, as the characteristic length, the linear long-wave propagation speed in a fluid at rest, c_{lw}, as the characteristic velocity, and hence $t^* = \frac{H}{c_{lw}}$ as the characteristic time.

Finally, we should note that the simulations presented in this work are fairly crude. They are 2D only and the turbulence modeling is extremely simplistic. As such our simulations do not attempt to reproduce nature, serving instead to provide an indication of whether an instability occurs, and if the instability occurs, some idea as to the qualitative effects of this instability. This is important since most large scale ocean models cannot hope to resolve the scales we are dealing

with and must parametrize their effects on larger scale motions.

5.2 Results

In this section we present the results of our numerical experiments. The section is broken up into four parts. First we describe the evolution of a canonical example in detail, thereby giving us a baseline case to compare the general results with. Next we turn to a more general exploration of phase space in order to attempt to answer when the instability does and does not occur. Third we return to give several different examples of the instability evolution. These examples aim to clarify the effects of initial ISW size, the effect of background current amplitude, and the effect of changing the stratification. Finally we comment on the relation of the instability to sediment resuspension.

Before discussing the results we present two tables. The first lists the dimensional linear long-wave speeds in a fluid at rest for the three stratifications used, while the second lists some relevant information about the ISWs used in this section.

z_0	d	c_{lw} $m\ s^{-1}$
0.1	0.05	0.918578
0.15	0.05	1.11795
0.33	0.05	1.52708

Table 5.3.1 z_0, d and c_{lw}, the dimensional linear longwave speed in a fluid at rest for the three stratifications used in this section.

z_0	$\|c\|$	η_{max}	$\max(\|u\|)$
0.1	1.5221	0.19	1.1385
0.1	1.2127	0.063	0.5442
0.15	1.3710	0.22	0.9628
0.33	1.0529	0.099	0.2645

Table 5.3.0 z_0 ($d = 0.05$ in all cases), propagation speed, η_{max} and $\max(|u|)$ (all in dimensionless form) for the ISWs discussed in this section.

For all cases tried $U_s < 0$ did not yield any interesting dynamics in the bottom BL region. For this reason we will consider $U_s \geq 0$ only. It should be noted however that for waves of depression cases with $U_s < 0$ would need to be examined.

In all figures showing the contours of horizontal velocity we will follow the convention that we are in a frame fixed with the ground. Unless otherwise indicated, the contours are regularly spaced.

5.2.1 An Example

We begin with a thorough discussion of a sample numerical simulation. We take $(z_0, d) = (0.1, 0.05)$, $\eta_{max} = 0.19$ and $U_s = 0.76$. The Reynolds number (Re) is set equal to 6.8×10^5. U_s and ν are chosen so that a global instability does occur. For this stratification ISW amplitudes are bounded above by shear instability and no conjugate flow exists ([37]). In figures 5.4 and 5.5 we show the density and vertical velocity contours, and density and horizontal velocity contours for the initial wave, respectively. In figure 5.6 we show the density and horizontal velocity contours early in the wave's evolution. It can be seen from the upper panel that the BL is quite thin. The detail of the BL in the lower panel shows that there is virtually no stratification in the bottom BL and that a long, thin separation region forms on the upstream side of the wave crest ($x = 0$ at $t = 0$). Note that we cannot call this region a separation bubble as there is no clear reattachment (it occurs at the rear of the wave, well away from the region shown).

In figure 5.7 we show the separation region just at the point of the instability setting in. We can see that the height of the separation region has increased from figure 5.6 and that the isolines of negative velocity have begun crowding together at about $x = -0.55$. The instability formation is perhaps better illustrated by a plot of the contours of vertical velocity, shown in figure 5.8. In this figure we can see that the region of isoline crowding in the contours of horizontal velocity corresponds to an anomalous region of negative vertical velocity.

In figures 5.9 and 5.10 we can see the development of the instability as it grows in size. By $t = 4.66$ the instability extends from deep in the BL to the bottom of the stratified region and can be seen to consist of alternating bands of strong updrafts and downdrafts. The updrafts are

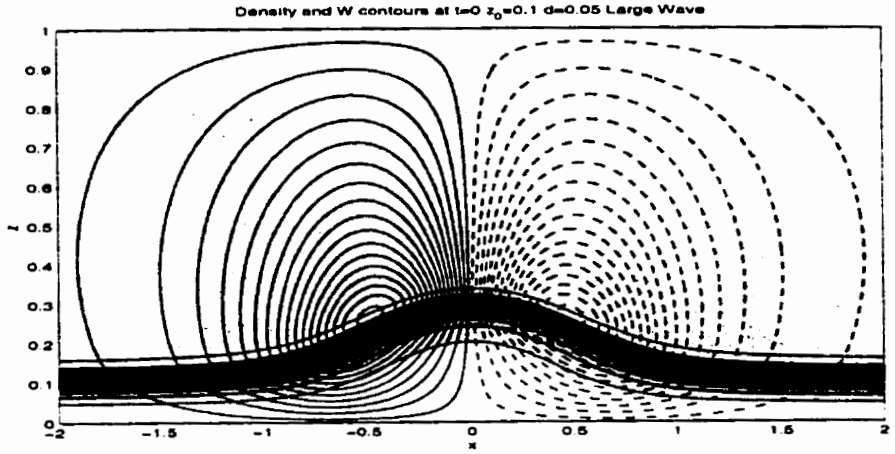

Figure 5.4: Density and vertical velocity contours for sample initial ISW with $(U_s, Re) = (0.76, 16.8 \times 10^5)$. Positive velocity (solid), negative velocity (dashed).

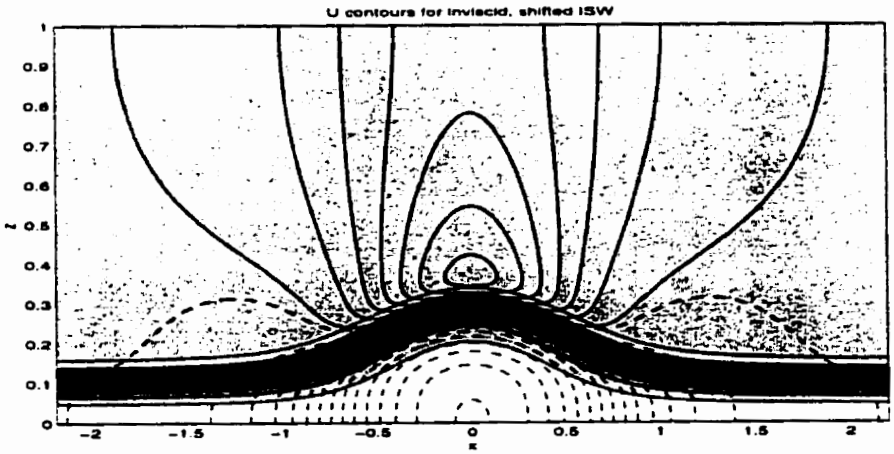

Figure 5.5: As figure 5.4 but for horizontal velocities before no slip boundary conditions are applied.

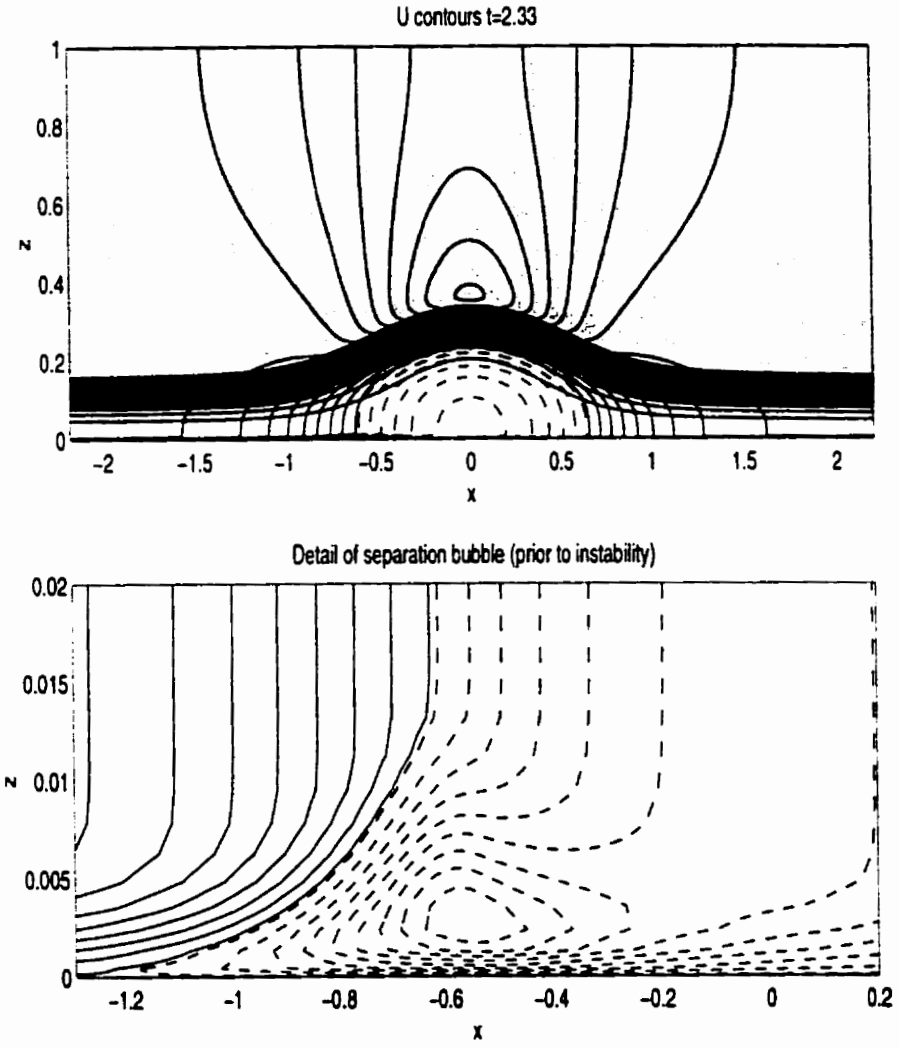

Figure 5.6: Density and horizontal velocity contours for sample ISW with $(U_s, Re) = (0.76, 6.8 \times 10^5)$ at $t = 2.33$. Positive velocity (solid), negative velocity (dashed).

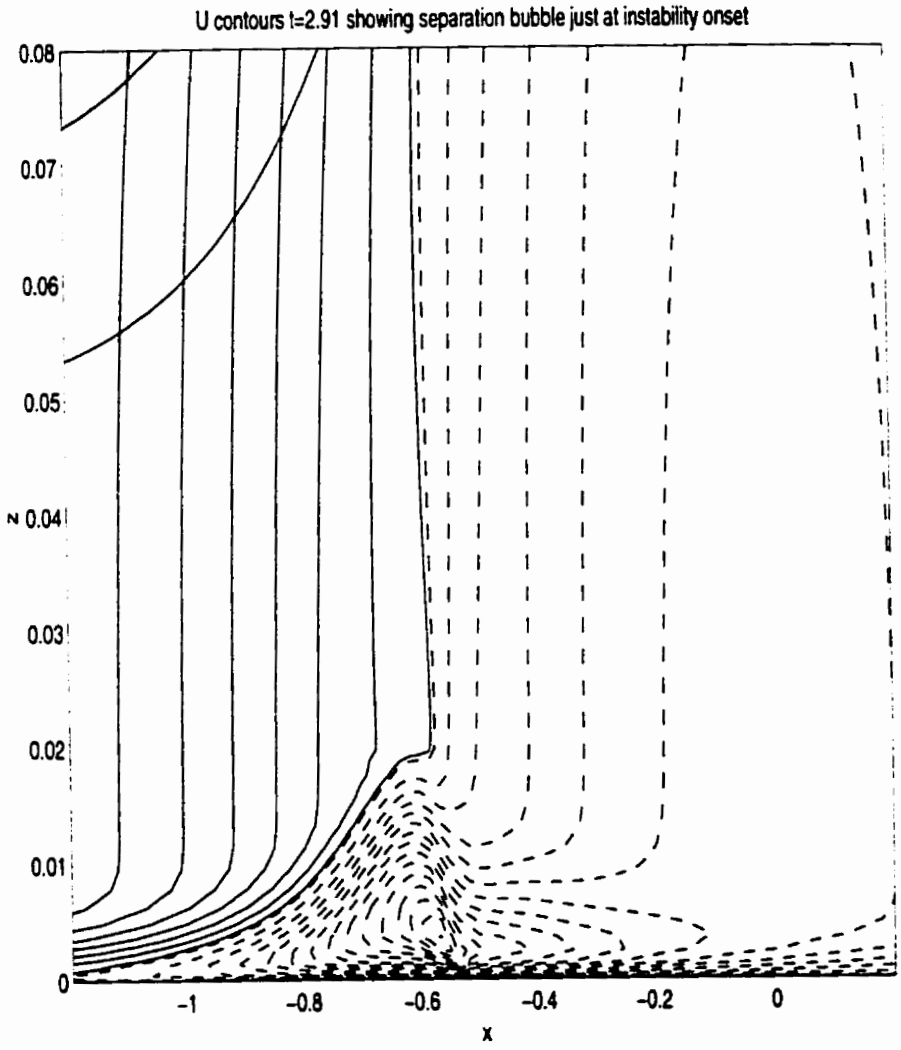

Figure 5.7: As figure 5.6 but at $t = 2.91$. Note the change in vertical scale.

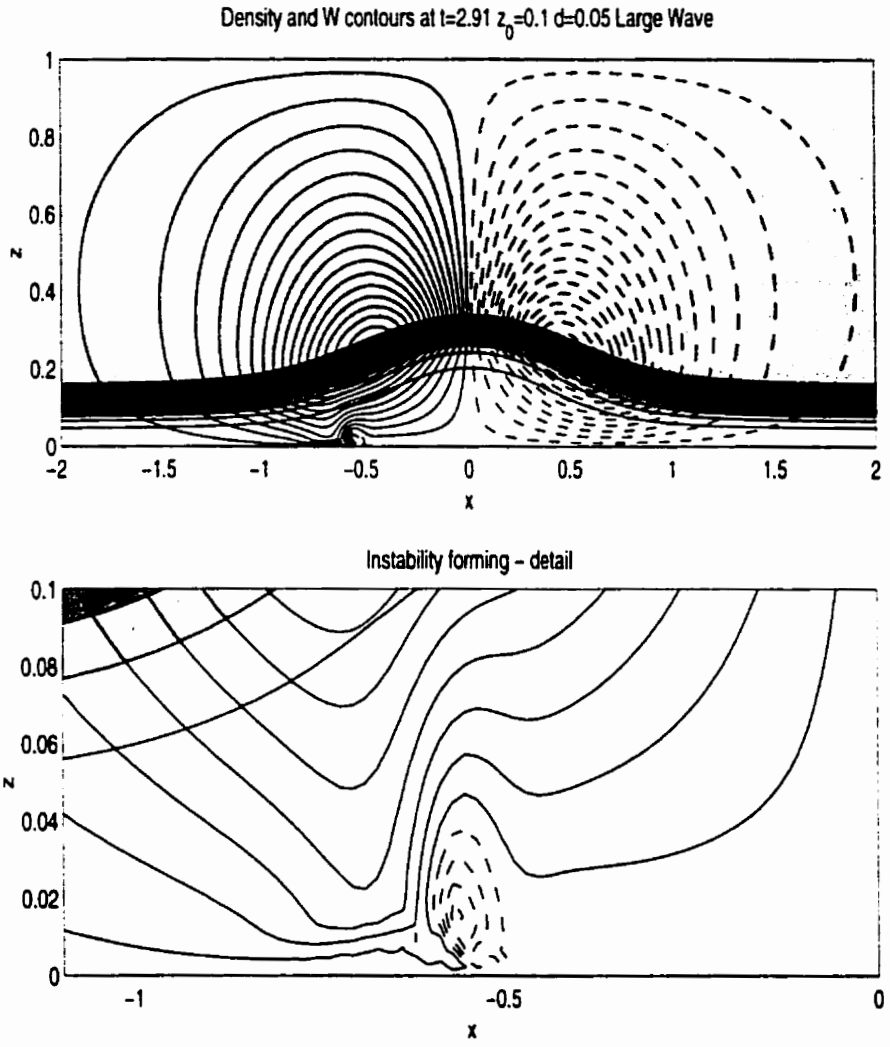

Figure 5.8: As in figure 5.7 but for vertical velocities. Note the change in vertical scale.

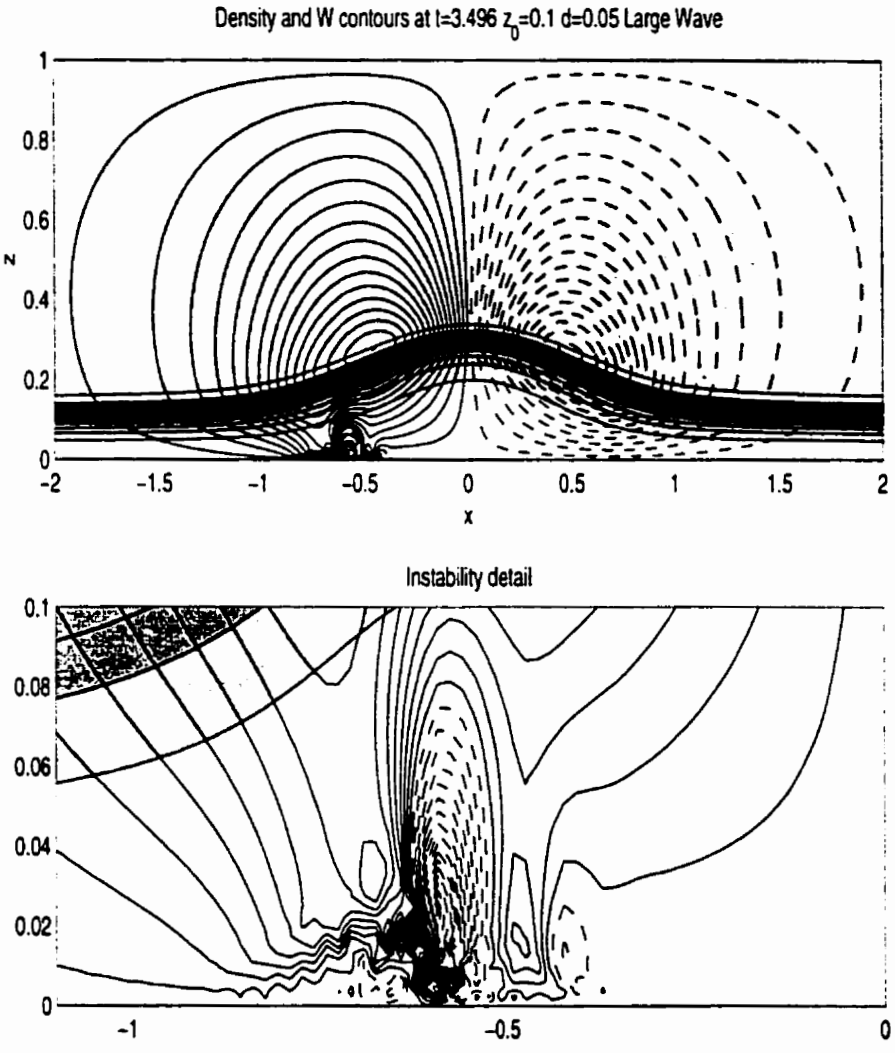

Figure 5.9: As in figure 5.8 at $t = 3.496$.

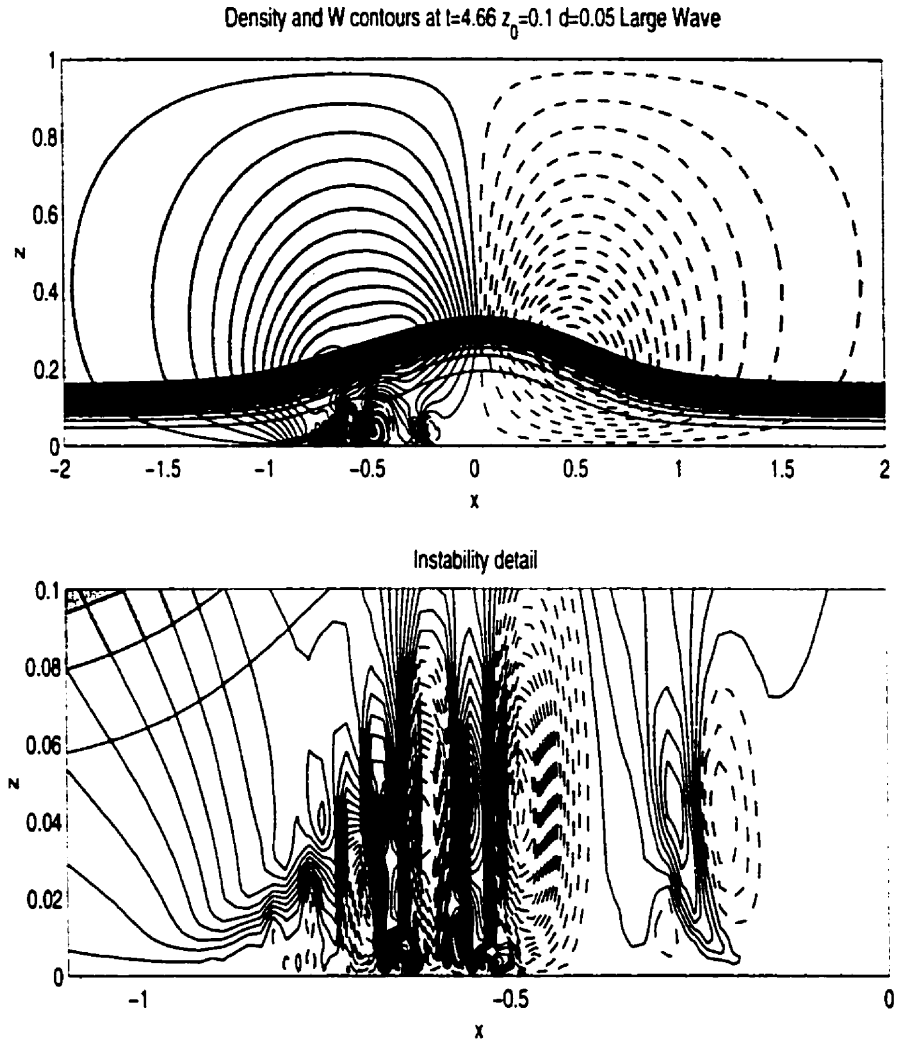

Figure 5.10: As in figure 5.8 at $t = 4.66$.

capable of transporting near bottom sediment high ($z = 0.2$) into the water column. Furthermore, the violent nature of the instability onset could induce sediment motion (more on this in the subsection on sediment transport). In figures 5.11 and 5.12 we show the contours of vorticity. Figure 5.12 shows the vorticity at times corresponding to figures 5.9 and 5.10. It can be seen that the positive vorticity advected over the separation region breaks up and by $t = 4.66$ two large positive vortices appear ready to separate and move into the stratified region.

To get a better idea of how this situation comes about, we turn to vorticity dynamics. The inviscid ISW has a certain amount of baroclinic vorticity associated with it, concentrated in the deformed pycnocline (see top left panel of figure 5.11) well away from the ocean bottom. As mentioned in the introduction, the background current and no slip BCs lead to upstream vorticity production (as a BL forms upstream of the wave). The upstream produced vorticity is positive, or clockwise, the same as the ISW vorticity. However the extent of the BL is quite small and hence the strong BL vorticity remains well away from the weaker ISW vorticity even as the former is advected into the wave body (see top right panel in figure 5.11). For this particular case, the horizontal velocity under the center of the wave (wave-induced plus background current) is initially negative in the BL region. Hence the vorticity produced beneath the ISW once the no slip BCs are applied is negative (see figure 5.11, bottom panel). As the positive upstream vorticity is advected horizontally into the wave by the background current it is advected upward by the wave-induced currents, and over the region of negative vorticity. The interaction between the two regions of vorticity leads to the creation, deformation and eventual instability of the separation region discussed above.

As mentioned in the introduction, instability of separation bubbles in the bottom BL is associated with vortex shedding (see [51], [52] for work on suction induced separation bubbles in a flat plate BL for constant density fluid). Some effort was expended in reproducing the general results of ([51]) with our numerical model. As we cannot easily impose a suction condition at the upper bounding surface, we use a body force term to induce the desired flow profile. We use

$$\vec{F}_d = \left[0, \frac{\sinh(X)\cosh(Z)}{2\cosh^2(X)}\right]$$

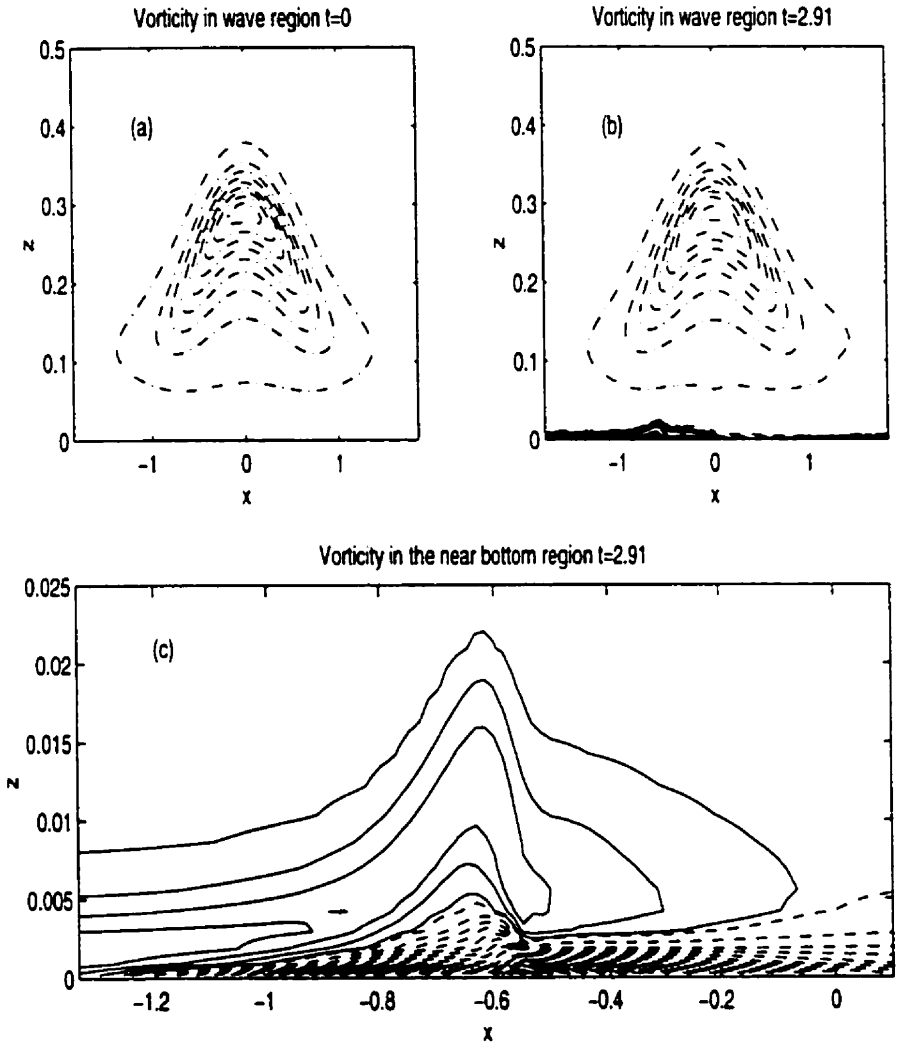

Figure 5.11: Vorticity contours for sample ISW with $(U_s, Re) = (0.76, 6.8 \times 10^5)$ at $t = 0$ and $t = 2.91$. Positive BL vorticity (solid), negative BL vorticity (dashed), smaller magnitude, positive baroclinic vorticity (dot-dashed). (a) $t = 0$, (b) $t = 2.91$, (c) $t = 2.91$ expanded view.

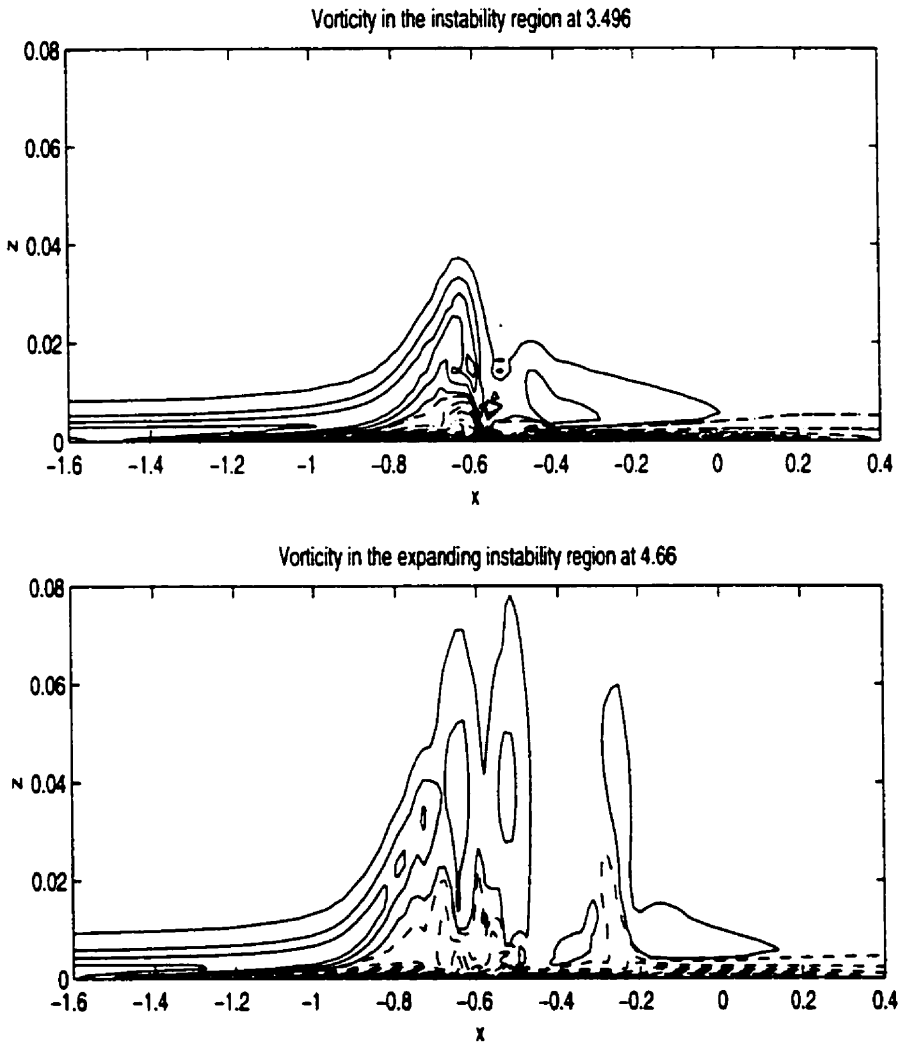

Figure 5.12: Vorticity contours for sample ISW with $(U_s, Re) = (0.76, 6.8 \times 10^5)$ at $t = 3.496$ and $t = 4.66$. Positive BL vorticity (solid), negative BL vorticity (dashed). Note the change in vertical scale from figure 5.11 (c).

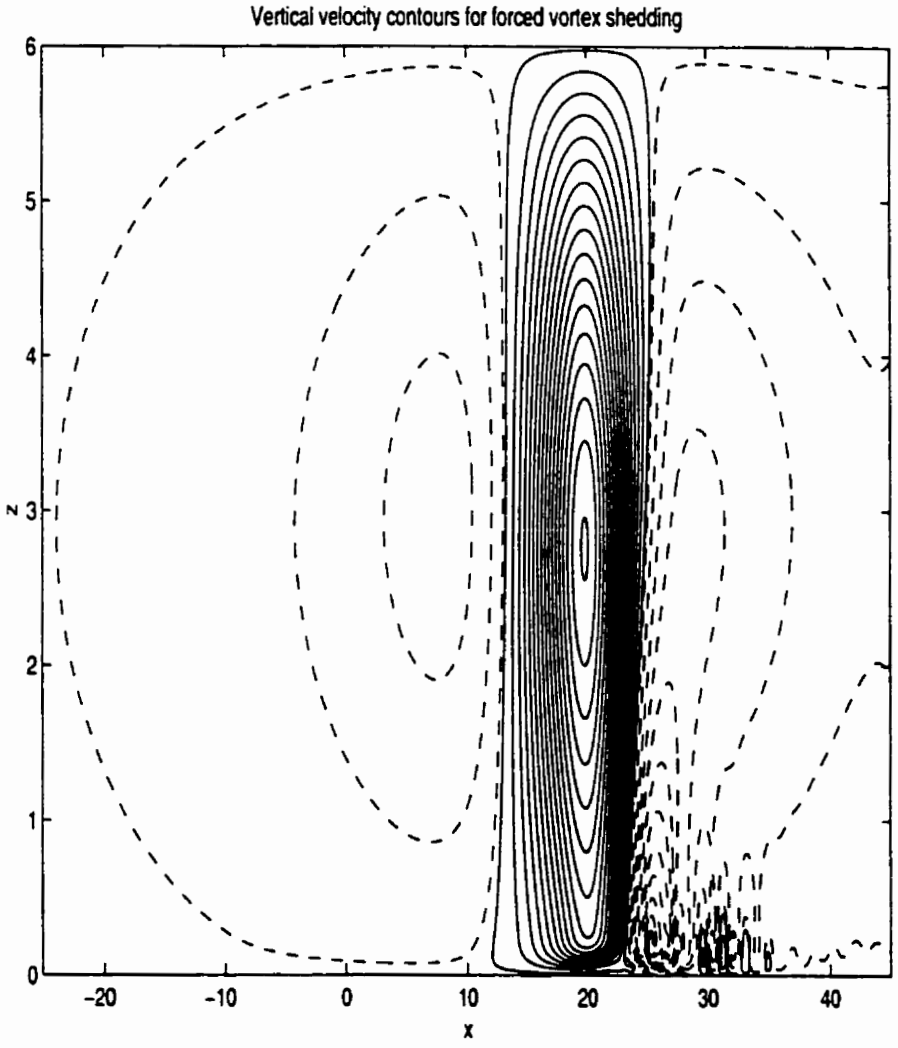

Figure 5.13: Vertical velocity contours for sample run of a separation bubble induced by suction

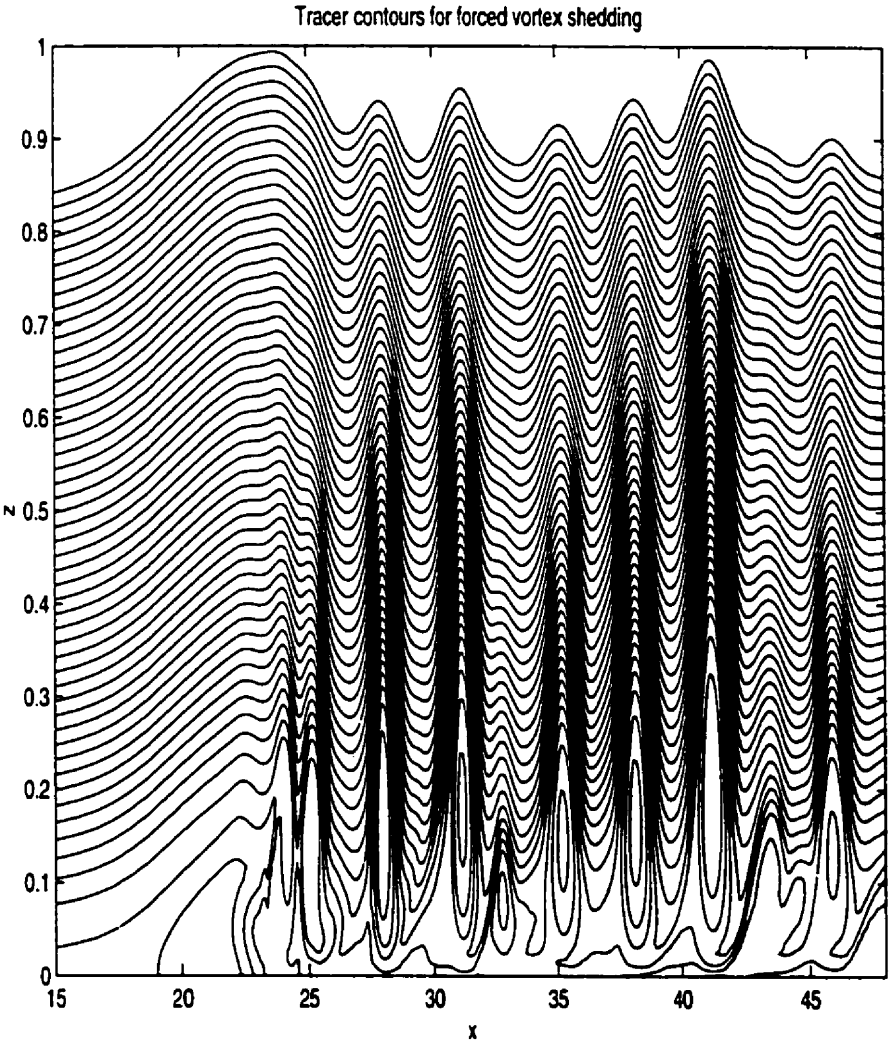

Figure 5.14: Tracer contours for sample run of a separation bubble induced by suction. Focus on the vortex shedding region.

$$X = \frac{x - 3.333}{0.5}$$
$$Z = \frac{z - 0.5}{0.1666}.$$

The forcing term that yields the desired velocity profile is found by an iterative process. We choose a forcing term and solve the steady, linearized version of the 2D Euler equations with a constant background current. If the resulting velocity field is not the one desired, we modify the forcing function and repeat the process. The solution of the 2D, steady, linearized Euler equations amounts to the solution of a Helmholtz problem for the stream-function Ψ. Once we have found a forcing that yields the desired velocity field, we utilize this forcing in the numerical solver for the Navier-Stokes equations. After an initial period of adjustment a nearly steady suction-type velocity profile is achieved. The constant background current is fixed so that all transient disturbances are advected to the right and out of the computational domain. In figure 5.13 we show an example of the vertical velocity contours while the vortex shedding is still quite small in magnitude. In figure 5.14 we show the contours of a tracer field (with a maximum concentration at the bottom) at a points in time when the vortex shedding is well developed. The results agree qualitatively with those of ([51], [52]). The sample simulation was performed on a domain 16.66 wide and 1.0 tall (where we have nondimensionalized using the domain height $H = 6.0$) or 100 m by 6 m in dimensional variables. There were 1000 regularly spaced points in the horizontal and 120 quadratically spaced points in the vertical (44 point in the bottom 0.1, or 1 m in dimensional variables).

Returning to the ISW-BL interaction we can see the effect of the separated vortices on the wave body from the sequence in figure 5.15. In this figure we plot the contours of density in the bottom 40% of the water column for various times. It can be seen that the separated vortices have a profound effect on the wave. First, they bring up heavy fluid (and possibly sediment) from the bottom BL, and second they cause a significant decay in the wave amplitude (due to wave radiation) with time. By 27.97 the wave is less than half of its original size. Interestingly it appears that the vortex shedding has greatly diminished (but not stopped completely) at this point.

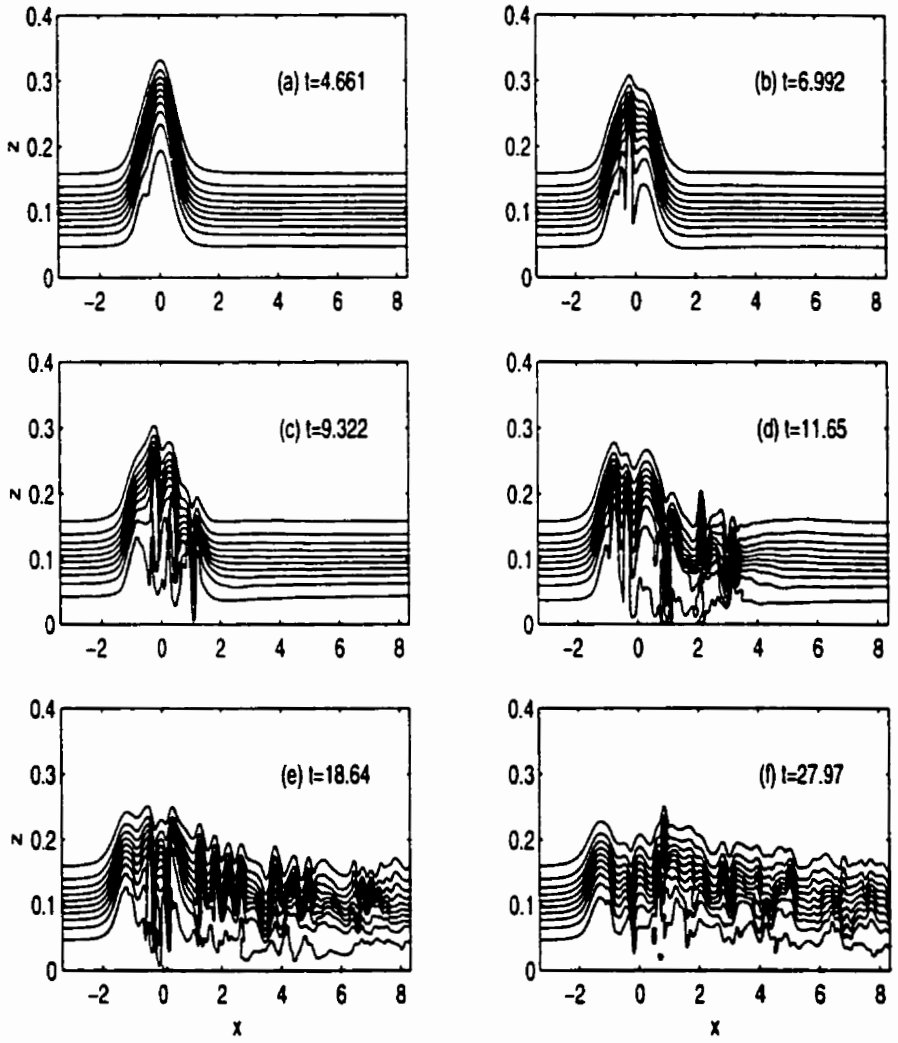

Figure 5.15: Density contours for sample ISW with $(U_s, Re) = (0.76, 6.8 \times 10^5)$ at various times, showing instability onset, vortex shedding and ISW decay.

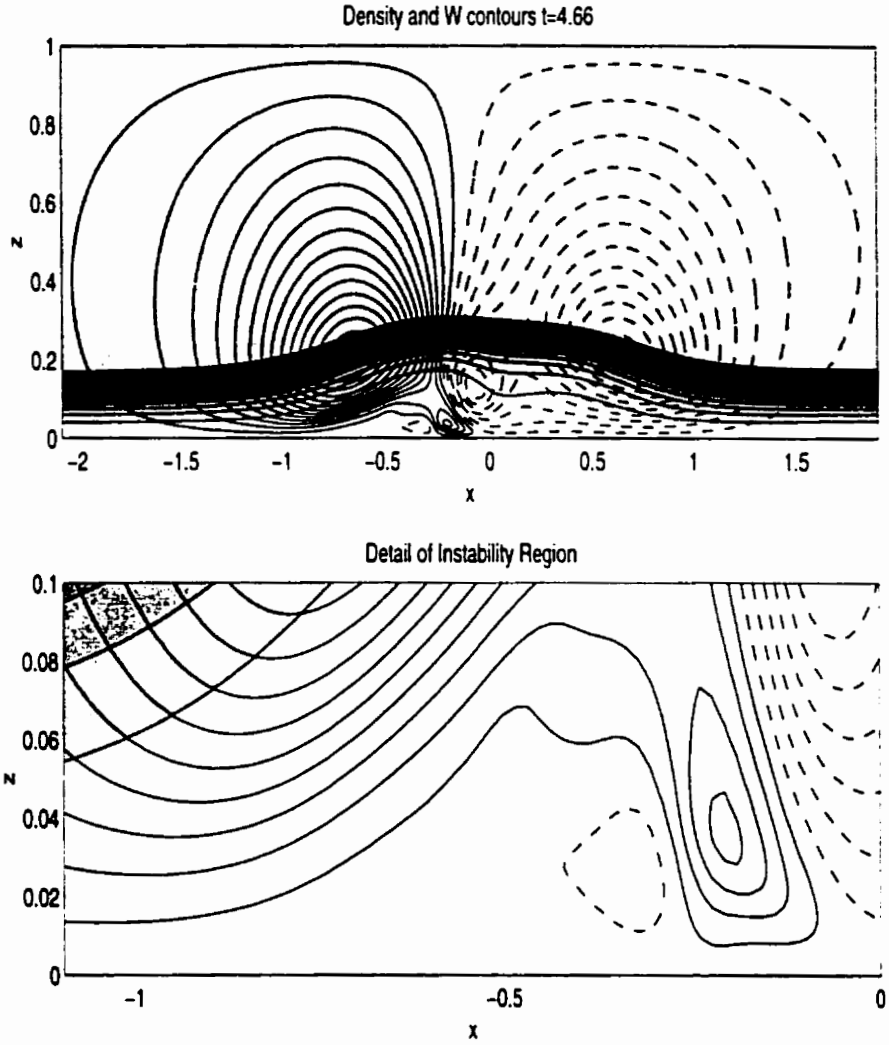

Figure 5.16: Density and vertical velocity contours for sample ISW with $(U_s, Re) = (0.76, 1.13 \times 10^4)$ at $t = 4.66$ showing the instability is suppressed. Positive velocity (solid), negative velocity (dashed)

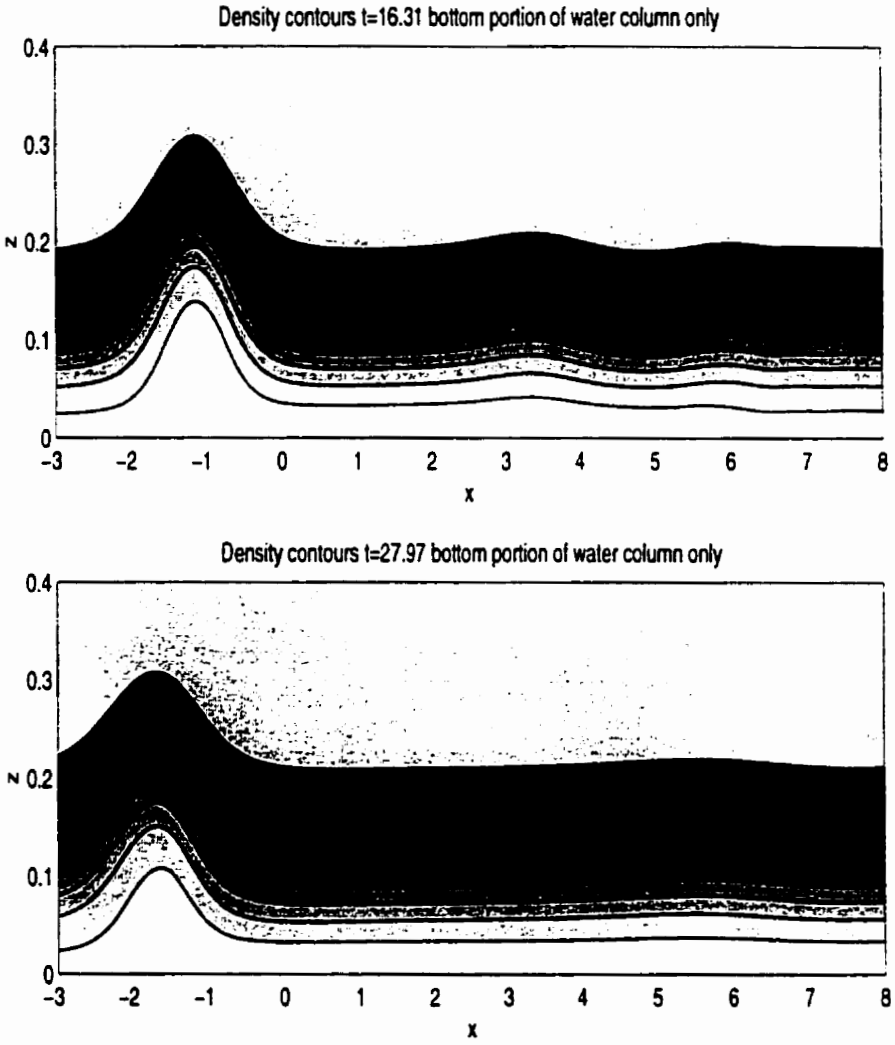

Figure 5.17: Density contours for sample ISW with $(U_s, Re) = (0.76, 1.13 \times 10^4)$ at $t = 16.31$ and $t = 27.97$ showing small ISWs being shed, but no vortex shedding.

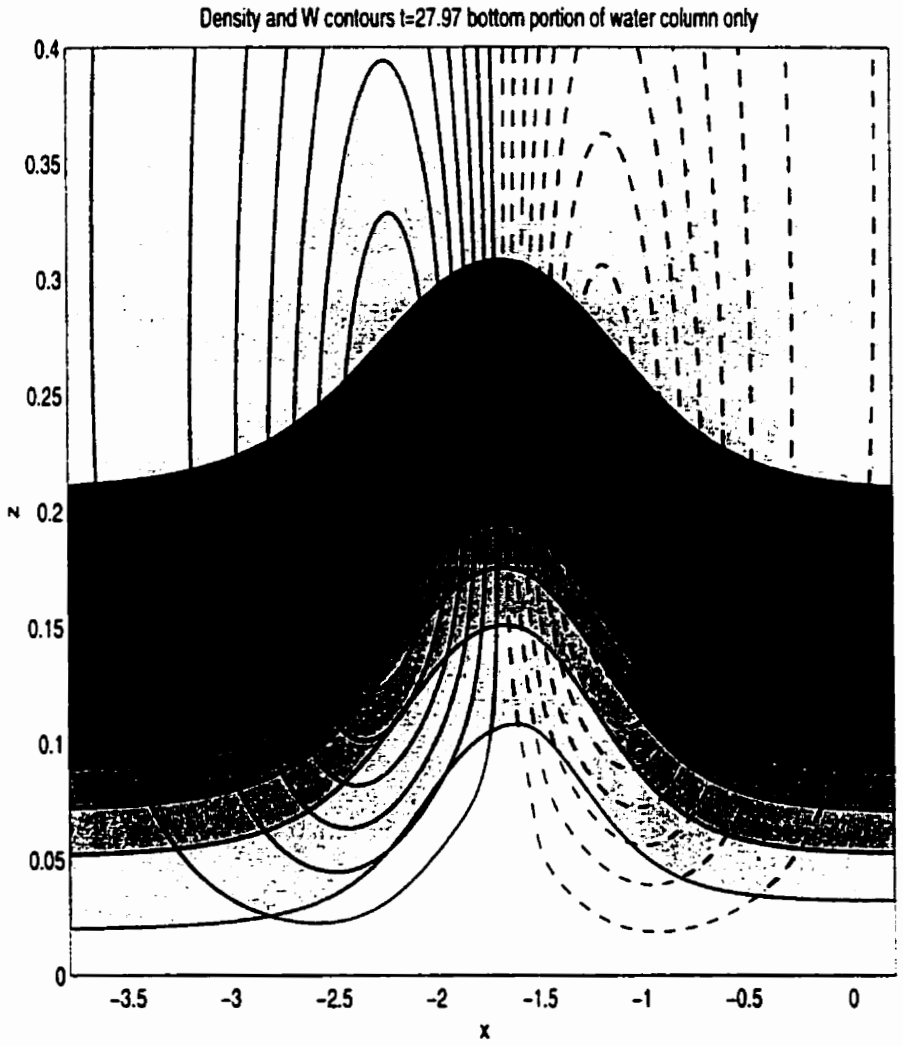

Figure 5.18: Density contours and vertical velocity for sample ISW with $(U_s, Re) = (0.76, 1.13 \times 10^4)$ at $t = 27.97$ showing that no anomalous updrafts below the wave. Positive velocity (solid), negative velocity (dashed)

An important question we sought to answer is what happens as the the Reynolds number, Re, decreases? In figure 5.16 we plot the density and vertical velocity contours at $t = 4.66$ for the same wave as discussed above with $Re = 1.13 \times 10^4$. This value of Re is chosen deliberately so that the global instability does not occur. Instead of a violent instability we see a small region of anomalous downdraft followed by a larger region of anomalous updraft. Neither appears particularly strong, nor to extend deep into the bottom BL. Indeed the density contours later in the wave's evolution ($t = 16.31$ and 27.97) found in figure 5.17 show that the adjustment to the no slip bottom BCs results in the shedding of only two small ISWs (seen to trail the main wave in the top panel). Figure 5.18 shows the density and vertical velocity contours at $t = 27.97$. We can see that while the wave is no longer symmetric about its crest, it remains very close to its initial condition (hence no global instability exists). The weak updrafts and the lack of coherent vortices shed both indicate that sediment transport from the bottom BL into the main water column would be small in this case.

Several resolution tests were performed for the vertical discretization. The number of grid points was held fixed (120). The grids used ranged from a regular grid (with the first grid point above the bottom at 0.004166 m and a vertical grid spacing of 0.00833 m) to various quadratic grids. Refining the grid in the near bottom region (the finest grid tried was a 150 point grid as described in the Introduction section) improved the resolution of the details of the instability (as expected), but did not affect the time of instability onset or the qualitative nature of the instability evolution. On the other hand, coarse grids simply could not resolve the separation region. Nevertheless, the $Re = 6.8 \times 10^5$ case developed a global instability at times within 10% of the above results for all grids tried including the regular grid. As expected, very coarse grids (such as a regular grid) could not resolve the complicated dynamics past the onset of the global instability and led to numerical instability in the solver. In figure 5.19 we show contours plots of the horizontal velocity at global instability onset for various grids. It can be seen that apart from the regular grid (the coarsest grid tried) the contours appear qualitatively similar.

For larger values of ν, or equivalently smaller values of Re, the boundary layer is thicker and hence coarser grids can do an adequate job. This has to do, in large part, with the qualitative

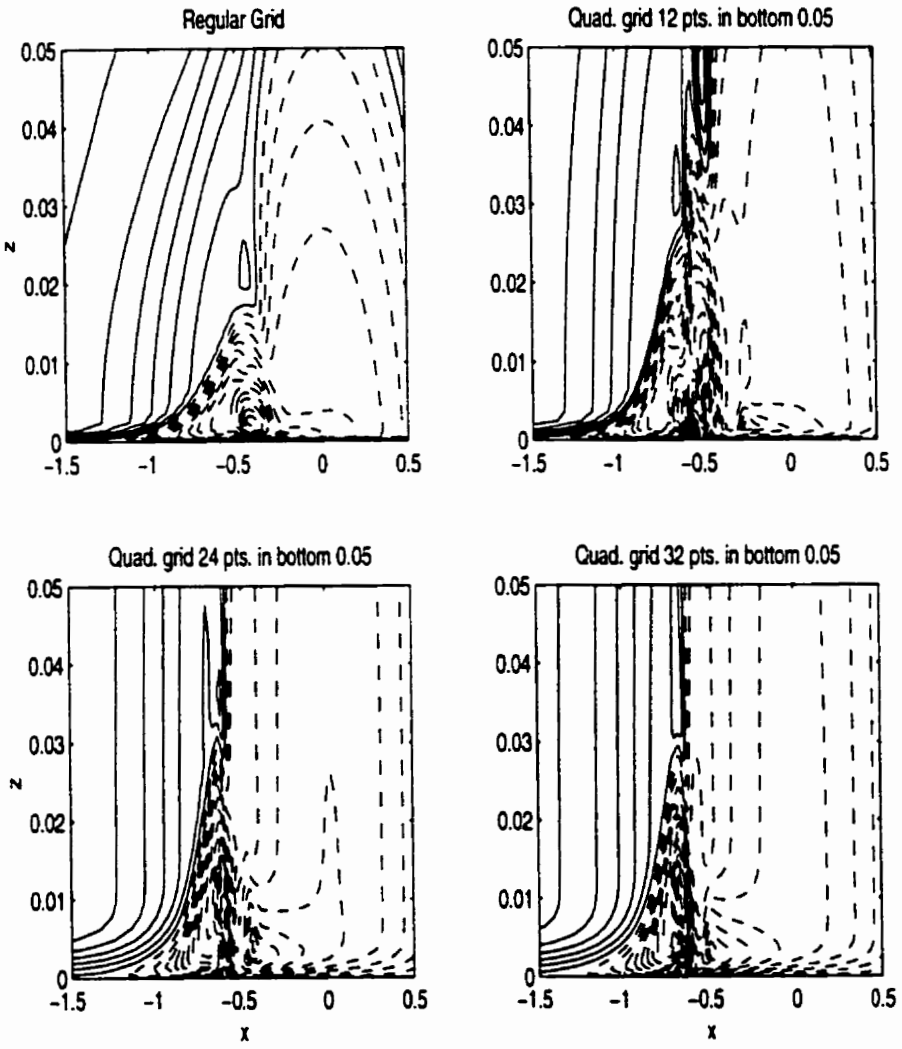

Figure 5.19: Horizontal velocity contours for various grids as global instability sets in. positive velocity (solid), negative velocity (dashed)

difference in the evolution between the two cases. In conclusion, it is quite interesting that runs on a regular grid with only 2 points in the bottom 0.0167 (1 m in dimensional units) still lead to a global instability, even if they cannot resolve its dynamics far beyond onset. However, as runs on the grid used (described in the Methodology section) can be handled by a work station in about five hours or less, there seems little incentive to try to use coarser grids. Finer grids may be possible in the future, though a 3D solver or a better turbulence model would likely prove much more useful.

5.2.2 Phase Space Bounds

A vital question to answer about the instability described in the previous section is, "Given some amount of upstream vorticity production, for what range of Reynolds numbers do we get a global instability?" As we saw in the previous subsection, large eddy viscosities damp out the global instability (and hence our proposed mechanism for sediment transport from the bottom BL into the main water column).

In order to discuss the region in parameter space in which a global instability occurs we need to have an easy to implement definition of such an instability. This is particularly difficult as any upstream vorticity production will lead to some adjustment once the vorticity is advected into the ISW, regardless of the value of ν. While we are primarily interested in ISW dynamics, we would like the present results to have some relevance to the twin issues of wave-induced sediment resuspension and sediment transport into regions of the water column well away from the bottom. For this reason it seems reasonable to make the following definition. We consider the horizontal profile of the vertical velocity at a fixed height above the bottom (we choose 0.5 m in dimensional units or 0.0083333 in non-dimensional units) for an inviscid ISW, and find the maximum value (label this value W_0^m). We consider a global instability to have occurred if the maximum value of the horizontal profile of the vertical velocity at the same height at a later time (label this value $W^m(t)$) exceeds twice the inviscid value, i.e.

$$W^m(t) > 2W_0^m. \tag{5.1}$$

In practice this criterion is very easy to implement. Moreover, the low values of W for inviscid ISWs in the near-bottom region mean that if the initial wave sheds smaller waves behind it (as opposed to a full global instability that leads to vortex shedding from the bottom BL) the above criterion for global instability will not be satisfied. A criterion based on the horizontal velocity would not have this property. Similarly a criterion based on vorticity would pose problems due to the varying BL thickness as ν changes. The above criterion has proven to be a good, if by no means unique, way to sort the various simulations.

As we will see in the following section, the manner in which (5.1) is satisfied can vary depending on the stratification. For this reason we should perhaps, for reasons of accuracy, invent some new terminology to label the event in question. Nevertheless, we will continue to use the simpler global instability to emphasize the link with the ideas of Bogucki and Redekopp ([10]).

In figure 5.20 we show the phase plane results for the case with $(z_0, d) = (0.1, 0.05)$ for two ISWs. The large and small waves have an amplitude of 0.19 and 0.063, respectively. In the figure we show only the simulations needed to show the boundary between cases of global instability and no global instability. There are several points to notice about the figure. First, the minimum background current needed to get a global instability at the largest Reynolds number used for the two waves, respectively, is more than three times larger for the small wave. Second, the shape of the boundary between the regions of instability and no instability (it would not be correct to call it a neutral curve in this case since waves we label globally stable still undergo some adjustment) is very similar for both waves. Third, with fixed, large values of U_s, the values of Re required to stabilize the small wave are nearly ten times larger then those required to stabilize the large wave. Also note from the figure that the curve for the small wave lies entirely within the curve for the large wave, and that the two curves do not collapse into a single curve.

The concept of global instability leading to possible sediment resuspension loses meaning for large values of ν because the original ISW breaks down into a train of smaller ISWs in a laminar manner, and because large eddy viscosities are associated with more turbulence. In these cases we found that the initial ISW shed several smaller ISWs, decreasing in size and propagation speed in the process. Eventually the wave was swept out of the computational domain. Since the

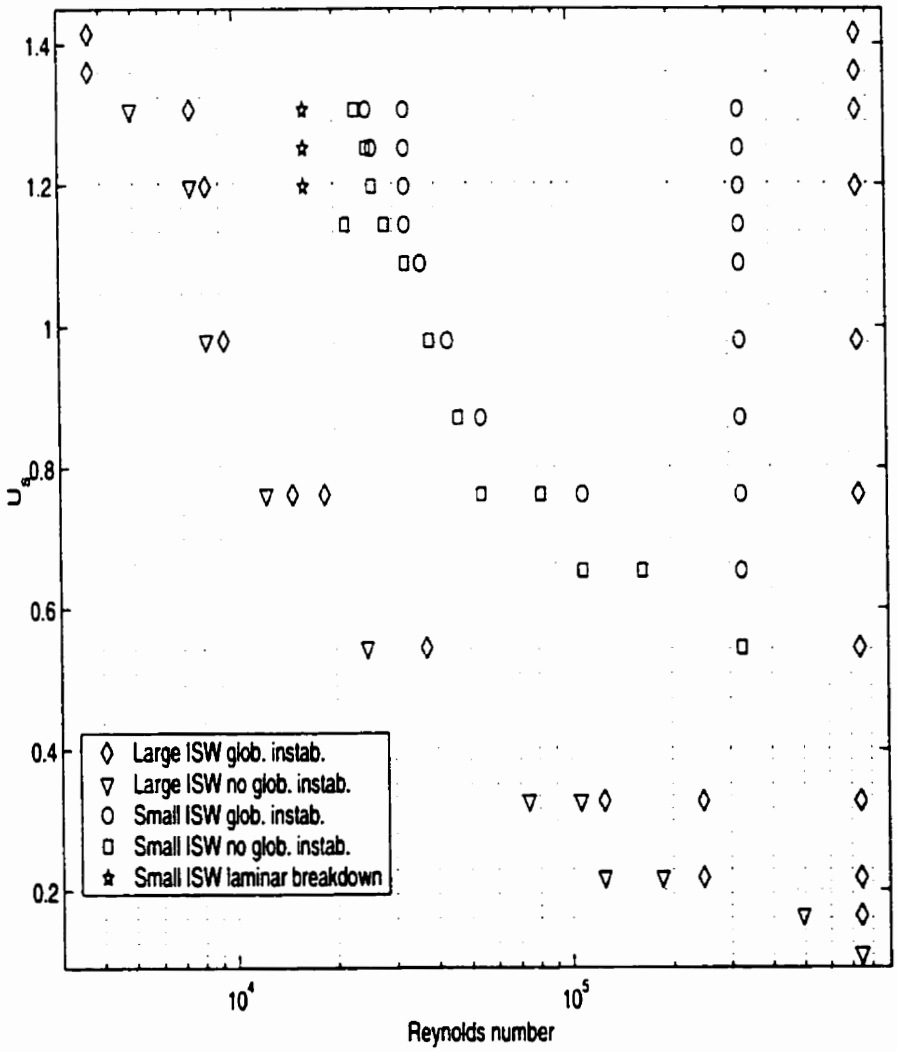

Figure 5.20: Phase space bounds for $(z_0, d) = (0.1, 0.05)$ ISWs with amplitude 0.19 and 0.063. Reynolds number based on $\max(|u|)$ used

motion did not exhibit any small scale features, we labelled this type of ISW breakdown 'laminar breakdown'.

As we mentioned previously, the $(z_0, d) = (0.1, 0.05)$ case does not have a conjugate flow solution. It thus seemed natural to ask whether a stratification that does have a conjugate flow would exhibit similar instability behaviour. Towards this end we considered two stratifications, one with $(z_0, d) = (0.15, 0.05)$ and another with $(z_0, d) = (0.33333, 0.05)$, both of which have a conjugate flow solution (though only the latter has η_{max} bounded above by the conjugate flow amplitude, the former is bounded by shear instability). The first was chosen with the hope of finding similar behaviour to that described above. The second, on the other hand, has the pycnocline situated near the mid-depth yielding very long, small amplitude ISWs.

In figure 5.21 we show the phase plane results for the $(z_0, d) = (0.15, 0.05)$ case for a wave of amplitude 0.22. We will discuss the evolution of one particular example of global instability for this case in the following subsection. The phase plane plot is quite similar to that of the larger wave in figure 5.20, except for the fact that for values of U_s larger than about 0.8 the global instability proved impossible to suppress without inducing a laminar breakdown of the initial ISW.

In figure 5.22 we show the phase plane results for the $(z_0, d) = (0.3333, 0.05)$ case for a wave of amplitude 0.099 (5.96 m, roughly 60% of the conjugate flow amplitude). The evolution for this case is markedly different from the cases mentioned above (a particular example will be discussed in detail later). The global instability sets in as a shear instability in the bottom BL. Furthermore, there are clear cases in which a sinusoidal perturbation grows to a visible size, but the global instability criterion is not satisfied. These cases are labeled as marginal in figure 5.22.

We have discussed one example of the evolution of a global instability as well as how a sufficient decrease in Reynolds number (Re) alters the evolution so that no global instability (according to our criterion) results. In the following subsections we use several examples to discuss the effects of initial wave size, the background current magnitude, and the stratification.

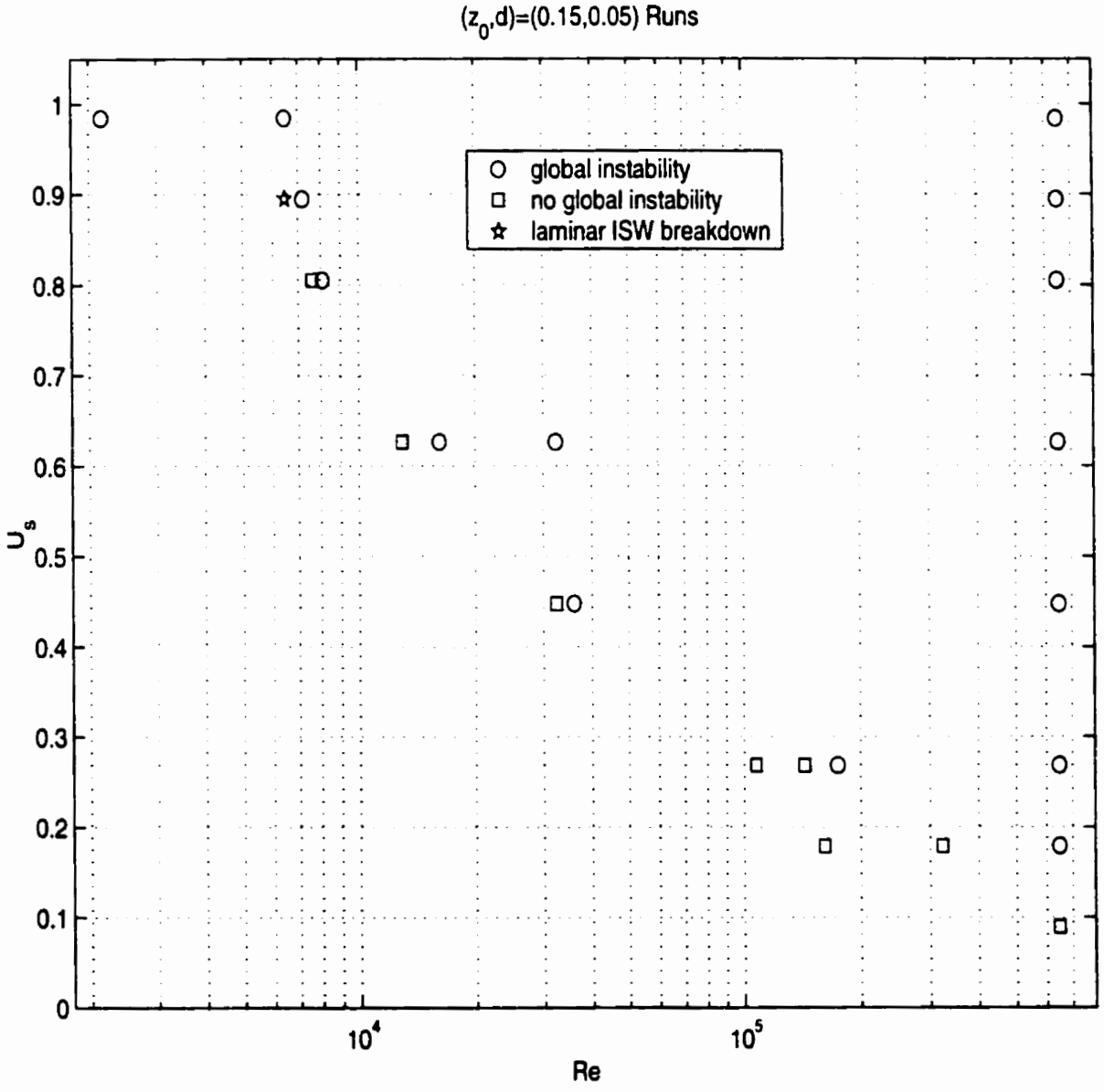

Figure 5.21: Phase space bounds for $(z_0, d) = (0.15, 0.05)$ ISW with amplitude 0.22.

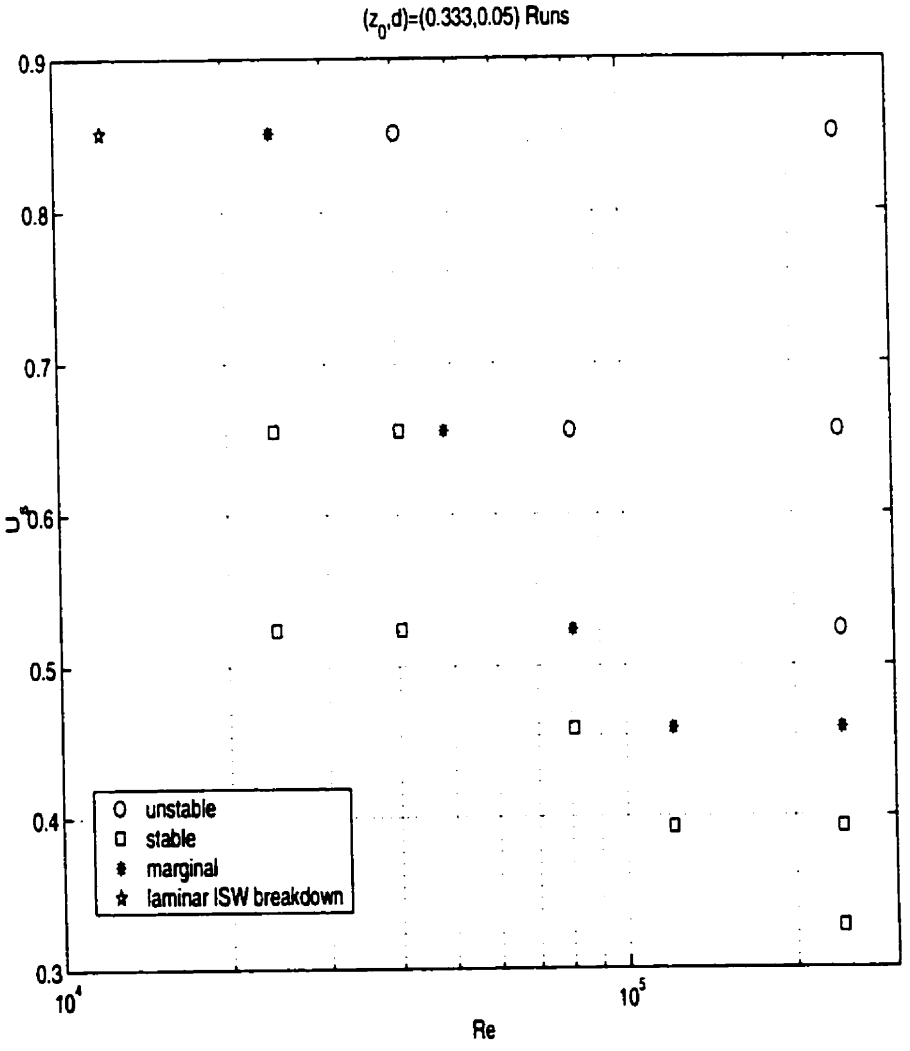

Figure 5.22: Phase space bounds for $(z_0, d) = (0.3333, 0.05)$ ISW with amplitude 0.099.

5.2.3 Effect of ISW size

We begin by returning to the $(z_0, d) = (0.1, 0.05)$ case with $U_s = 0.76$, but this time for the small wave (maximum isopycnal displacement is 0.063, and the magnitude of the maximum wave-induced horizontal current is 0.5442) discussed in the previous section. This wave is chosen so that $\max(|u|) < U_s$, in contrast to the large wave case.

In figure 5.23 we show the density contours for the initial state as well as for $t = 11.14$, well after the global instability has set in. We can see that by $t = 11.14$ the global instability has virtually swamped the initial ISW. In figure 5.24 we show the density and horizontal velocity contours with a focus on the separation bubble (in this case it is an actual separation bubble with a clear reattachment point), just as the global instability is setting in ($t = 5.57$). Figure 5.25 shows the vertical velocity contours at the same time. Figure 5.26 shows the vertical velocity contours at $t = 11.14$. In this figure we can clearly see the alternating bands of updrafts and downdrafts that indicate that the initial ISW is slowly losing energy to wave radiation.

While the details of this case are different from the case of the larger wave discussed previously, certain characteristics of the evolution appear to be robust. In particular we can note that as the positive, upstream vorticity is advected into the wave body it does not matter whether the currents in the BL within the wave body are positive or negative, only that the vorticity is reduced in the BL beneath the wave body, and that the vorticity created in the BL upstream of the wave is advected up and over the BL within the wave body. For $U_s > 0$ this will always be the case. The ISW-induced vertical current advects the upstream vorticity over the BL within the wave body and the interaction between the BL and upstream vorticity leads to the subsequent instability.

5.2.4 Effect of background current magnitude

We now return to the larger wave, $(z_0, d) = (0.1, 0.05)$, $\eta_{max} = 0.19$. We would like to get some idea as to how the amount of upstream vorticity production changes the evolution of the instability (when it happens). Towards this end consider a case with a smaller background current, $(U_s, Re) = (0.22, 6.8 \times 10^5)$. In figures 5.27 and 5.28 we show the density and vertical velocity contours during the instability onset and early development ($t = 6.991$ and 9.3.0). In contrast with

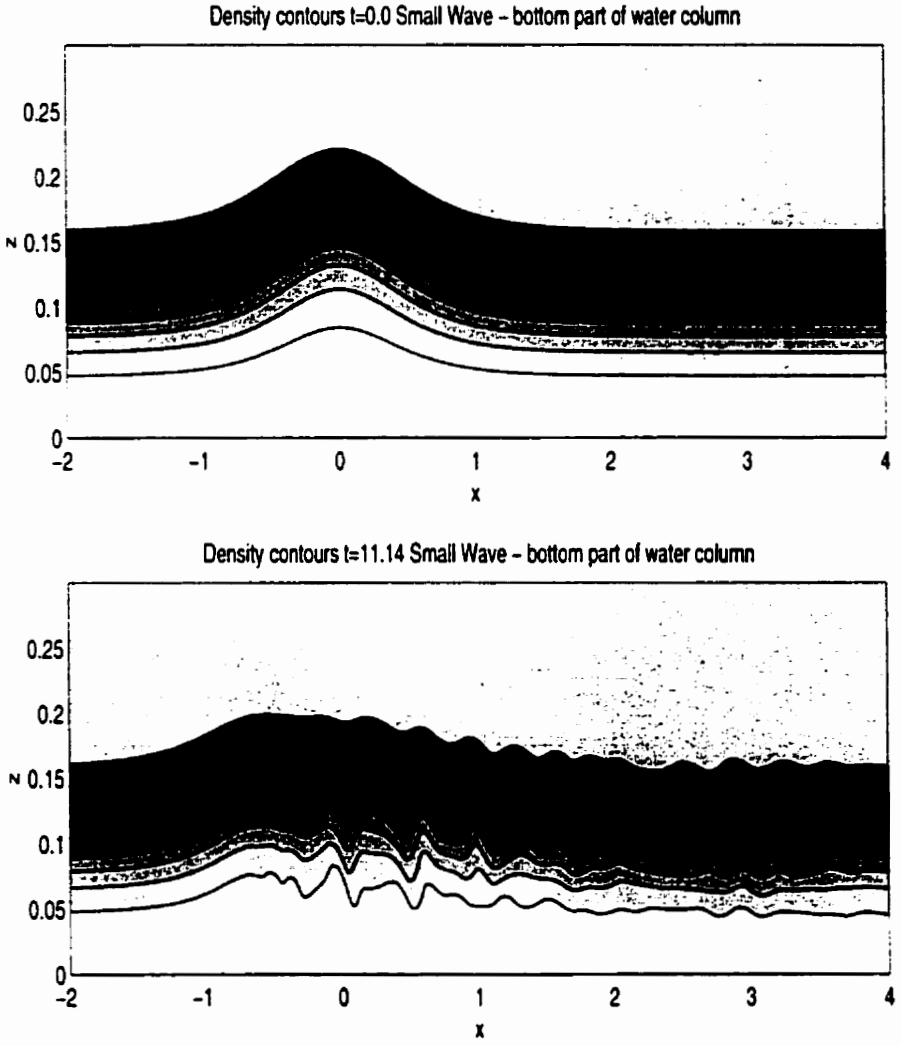

Figure 5.23: Density contours for $\eta_{max} = 0.063$ ISW with $(U_s, Re) = (0.76, 3.0 \times 10^5)$ at $t = 0.0$ and $t = 11.14$ showing ISW decay due to vortex shedding.

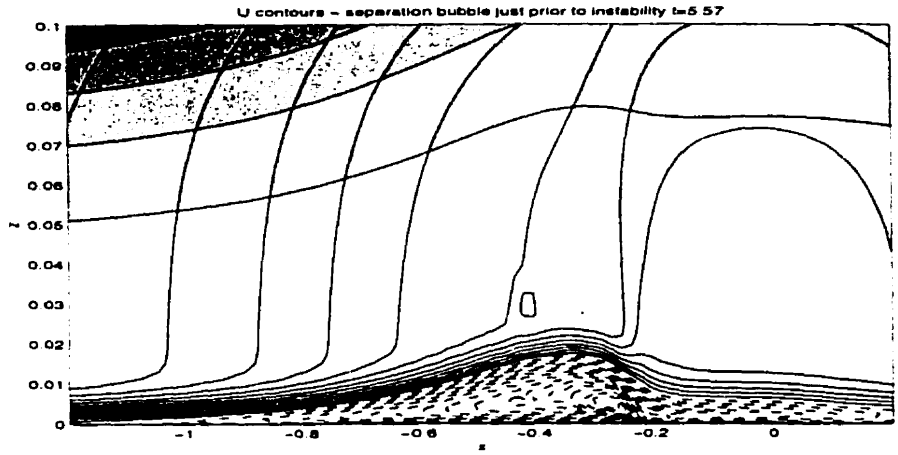

Figure 5.24: Density and horizontal velocity contours for $\eta_{max} = 0.063$ ISW with $(U_s, Re) = (0.76, 3.0 \times 10^5)$ at $t = 5.57$ during instability onset. Positive velocity (solid), negative velocity (dashed)

figures 5.8 and 5.9 the instability sets in closer to the wave crest. This is confirmed in figures 5.29 and 5.30 which show the horizontal velocity at the same times. The instability dynamics in this case do not involve the leading separation region at all. Figure 5.31 shows the vorticity at $t = 6.992$ and 9.3.0. By this time the upstream vorticity has interacted with the BL in the wave body and we can see the positive, upstream vorticity overlaying the negative vorticity. It appears that any vortex shedding that results will be small. This is confirmed in figure 5.32 which shows the density contours at $t = 16.31$ and 27.97. It can be seen that the waves radiated downstream of the ISW are quite small in this case. In figure 5.33 we plot the vertical velocity in the near bottom region at $t = 27.97$. We can see that the BL region beneath the ISW remains active even for late times (contrast this with the inviscid simulations of the previous chapter).

The above example shows that the dynamics in different parts of the parameter space can be rather different, even if our definition of global instability onset is satisfied. On reflection, this should not be unexpected (we are exploring a very large parameter space), yet this point is not discussed in the literature ([10]), perhaps because fully nonlinear ISWs are not used.

Next we would like to examine how decreasing Re affects the evolution for the above case. We consider $Re = 8.2 \times 10^4$, a case right on the brink of global instability onset according to our

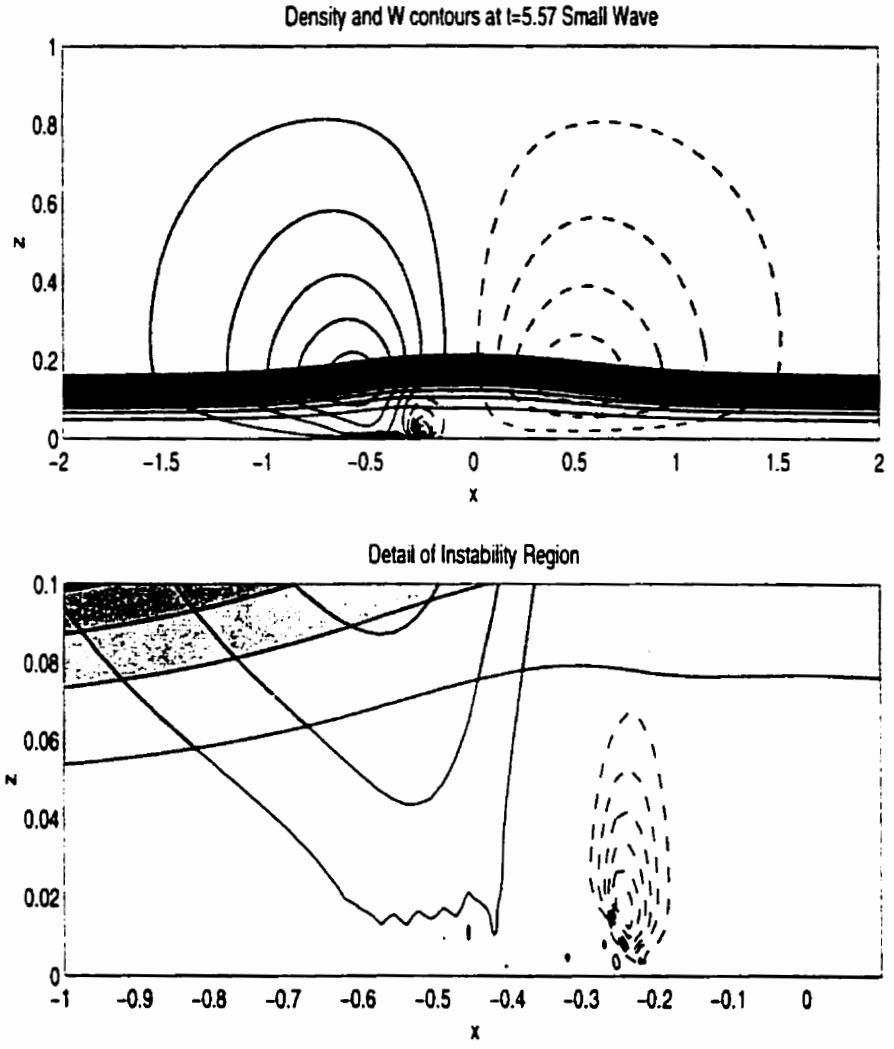

Figure 5.25: As in figure 5.24 but for vertical velocity.

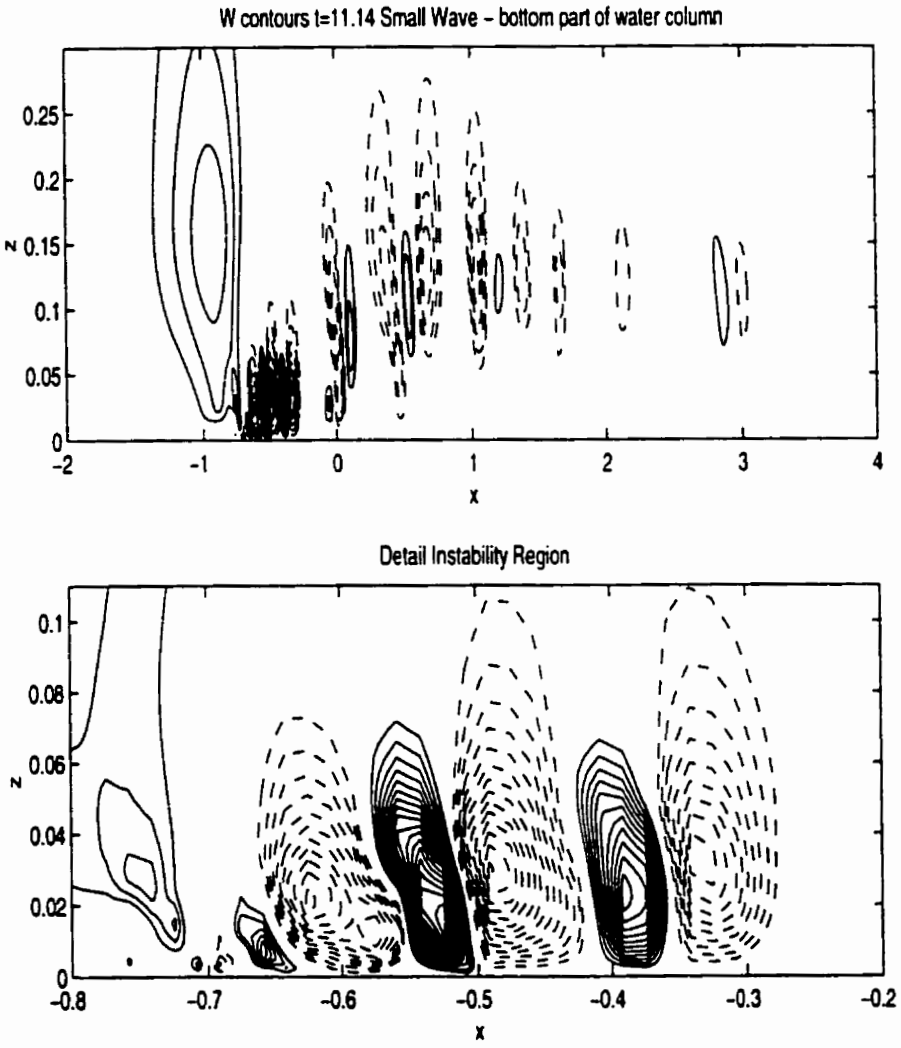

Figure 5.26: Vertical velocity contours for $\eta_{max} = 0.063$ ISW with $(U_s, Re) = (0.76, 3.0 \times 10^5)$ at $t = 11.14$ showing vortex shedding. Positive velocity (solid), negative velocity (dashed)

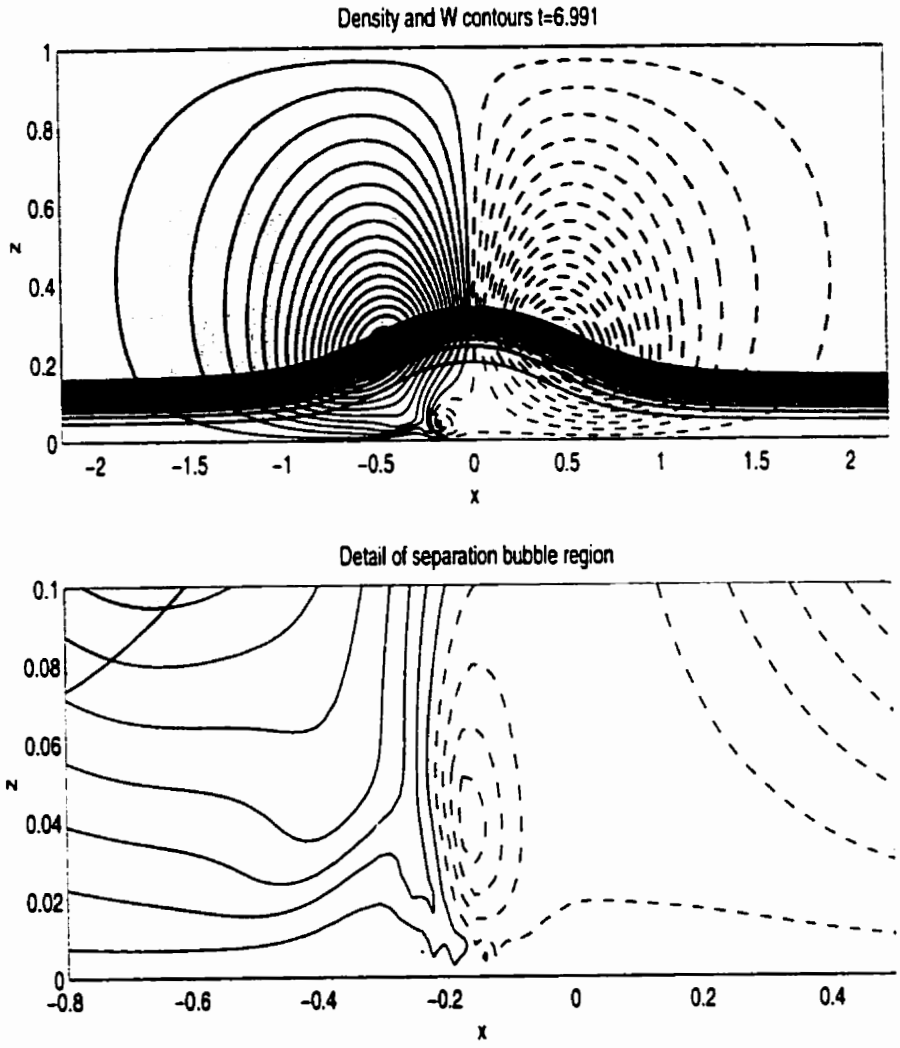

Figure 5.27: Onset of instability. Density and vertical velocity contours for ($\eta_{max} = 0.19$ ISW with $(z_0, d) = (0.1, 0.05)$, $(U_s, Re) = (0.22, 6.8 \times 10^5)$ at $t = 6.991$. Positive velocity (solid), negative velocity (dashed).

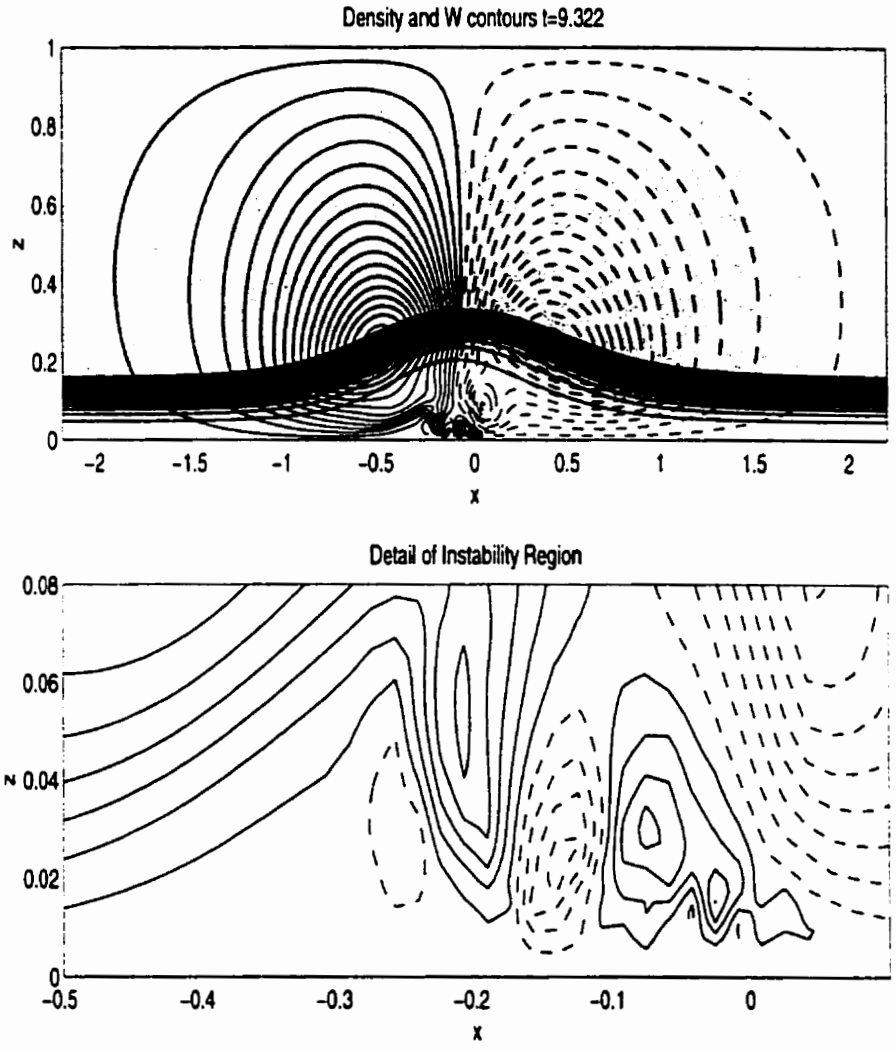

Figure 5.28: As figure 5.27 but at a later time, $t = 9.3.0$.

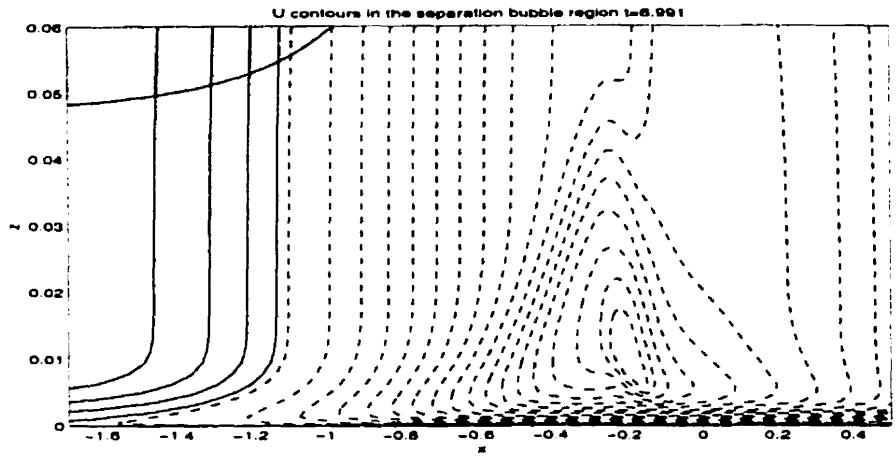

Figure 5.29: As figure 5.27 but for horizontal velocity.

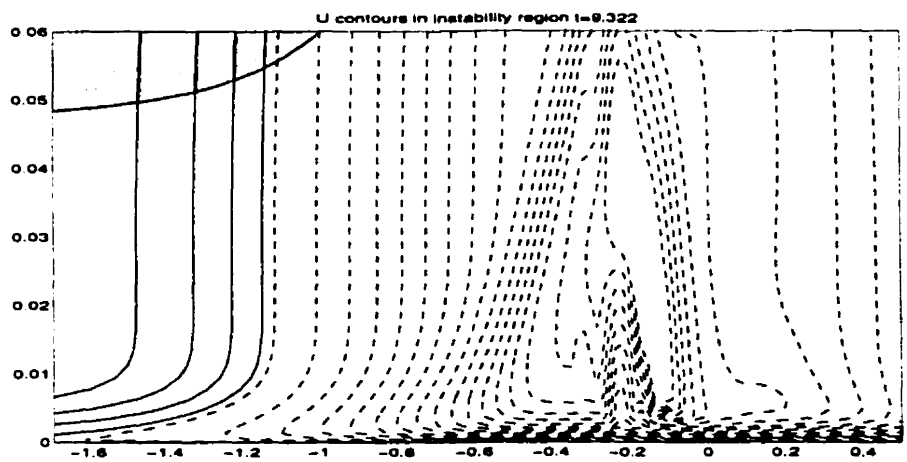

Figure 5.30: As figure 5.28 but for horizontal velocity.

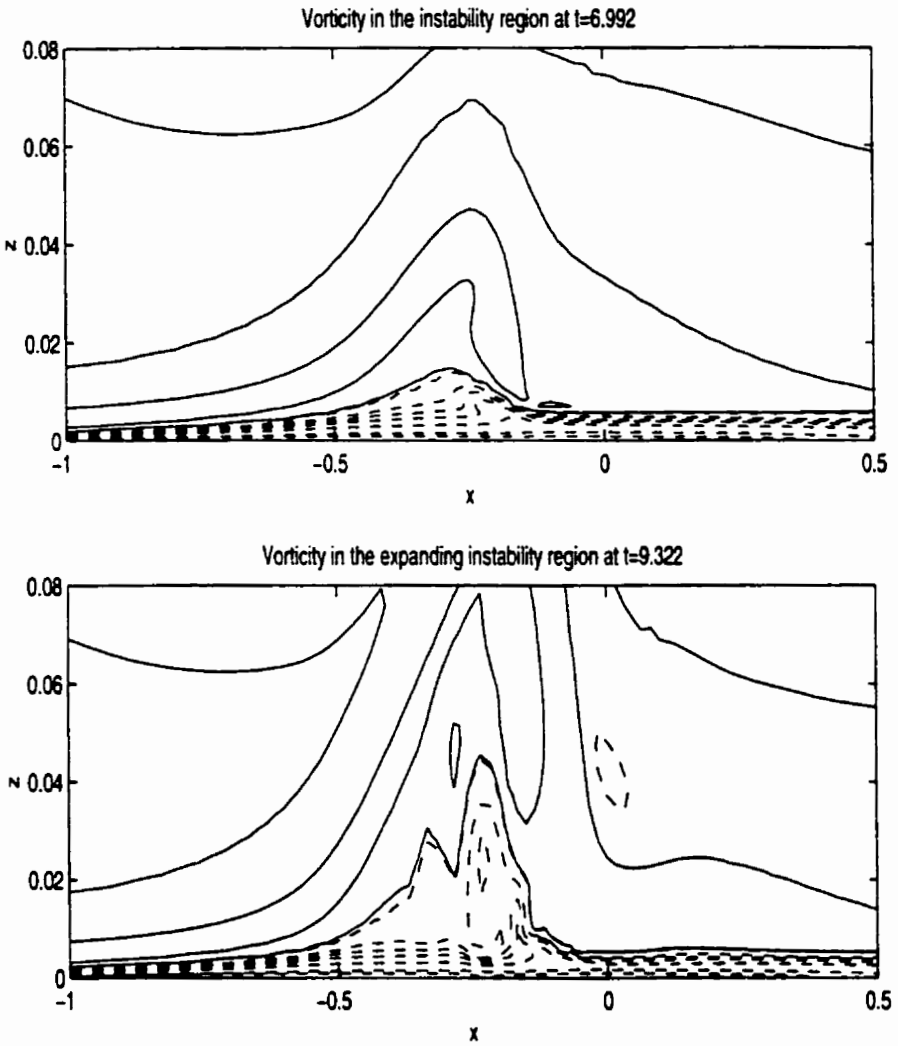

Figure 5.31: Vorticity contours for ($\eta_{max} = 0.19$ ISW with $(z_0, d) = (0.1, 0.05)$, $(U_s, Re) = (0.22, 6.8 \times 10^5)$ at $t = 6.991$. Positive BL vorticity (solid), negative BL vorticity (dashed).

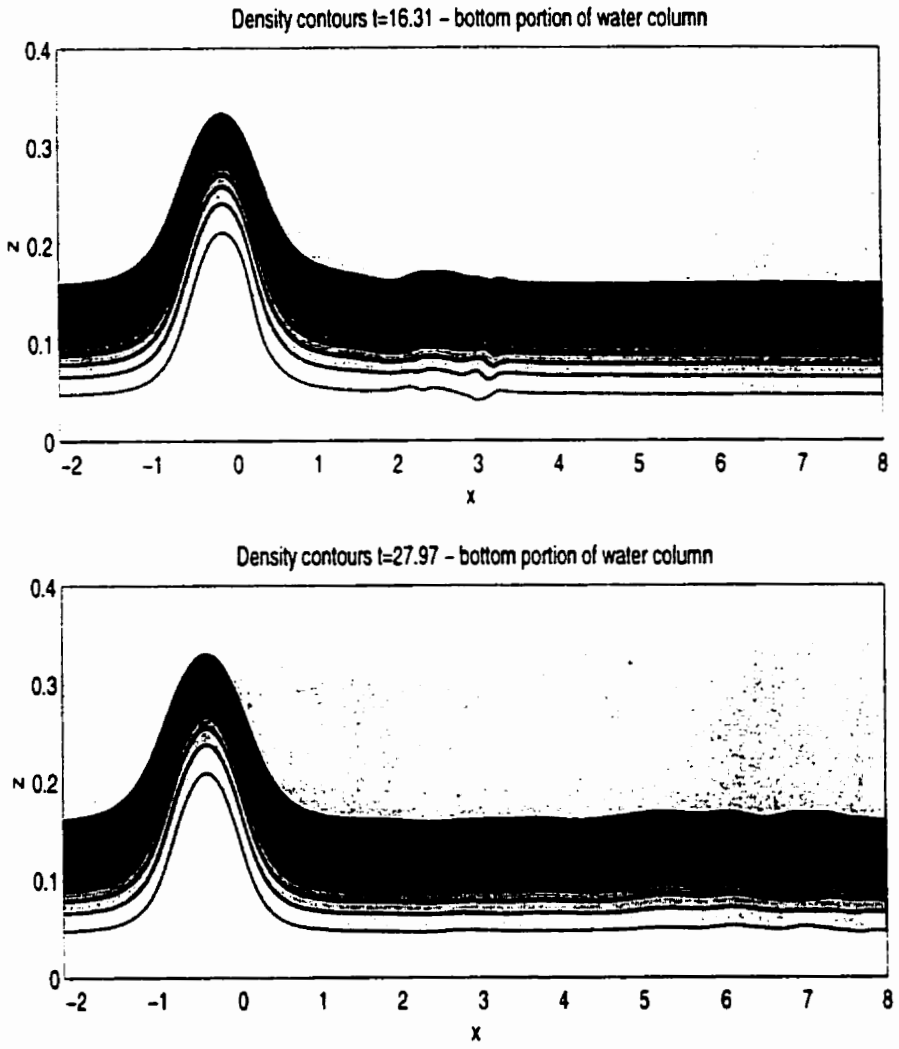

Figure 5.32: Density contours for ($\eta_{max} = 0.19$ ISW with $(z_0, d) = (0.1, 0.05)$, $(U_s, Re) = (0.22, 6.8 \times 10^5)$ at $t = 16.31$ and 27.97 showing no visible vortex shedding.

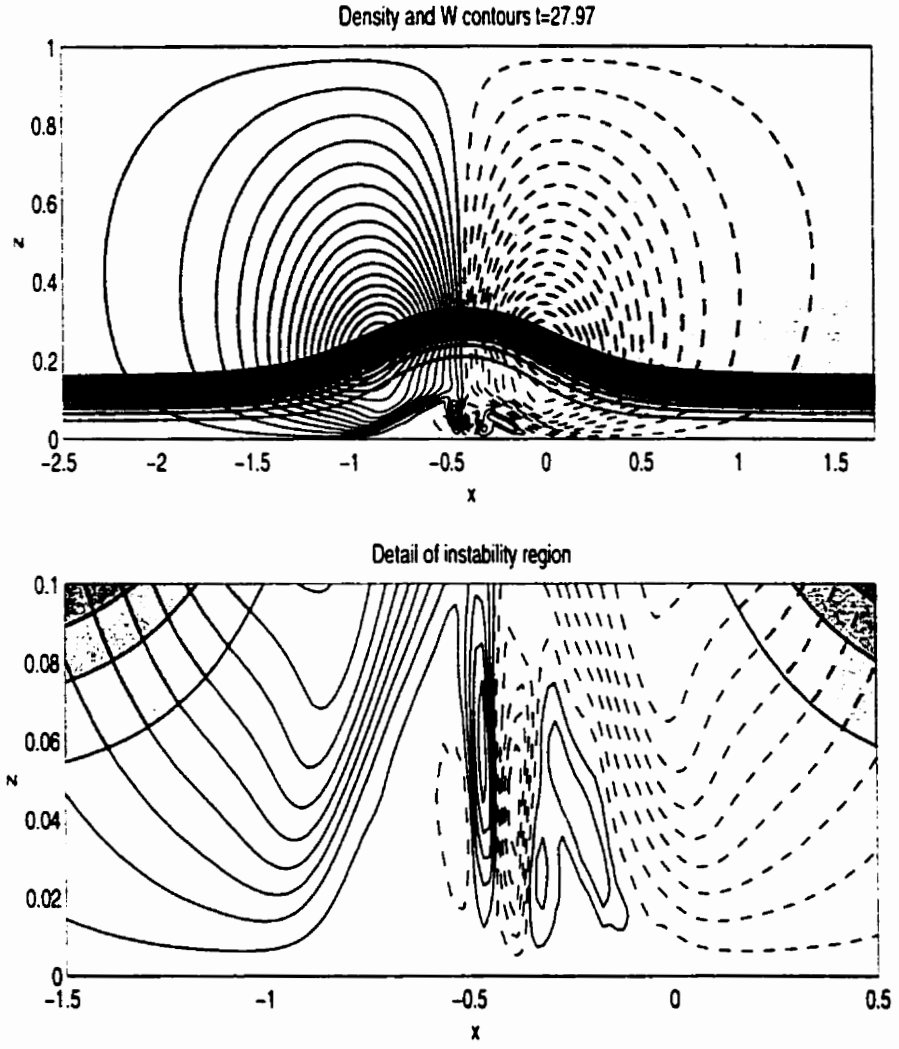

Figure 5.33: Late in the evolution process. Density and vertical velocity contours for ($\eta_{max} = 0.19$ ISW with $(z_0, d) = (0.1, 0.05)$, $(U_s, Re) = (0.22, 6.8 \times 10^5)$ at $t = 27.97$. Positive velocity (solid), negative velocity (dashed).

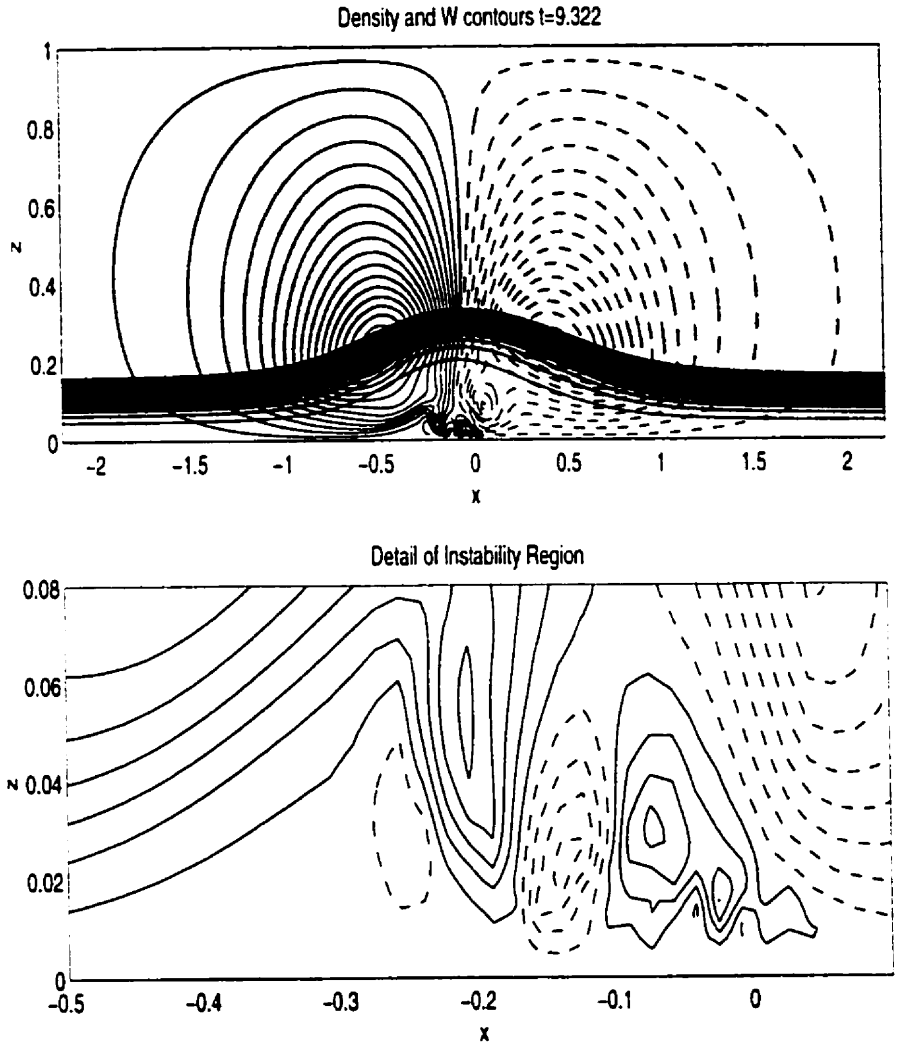

Figure 5.34: Density and vertical velocity contours for ($\eta_{max} = 0.19$ ISW with $(z_0, d) = (0.1, 0.05)$, $(U_s, Re) = (0.22, 8.2 \times 10^4)$ at $t = 9.3.0$. Positive velocity (solid), negative velocity (dashed).

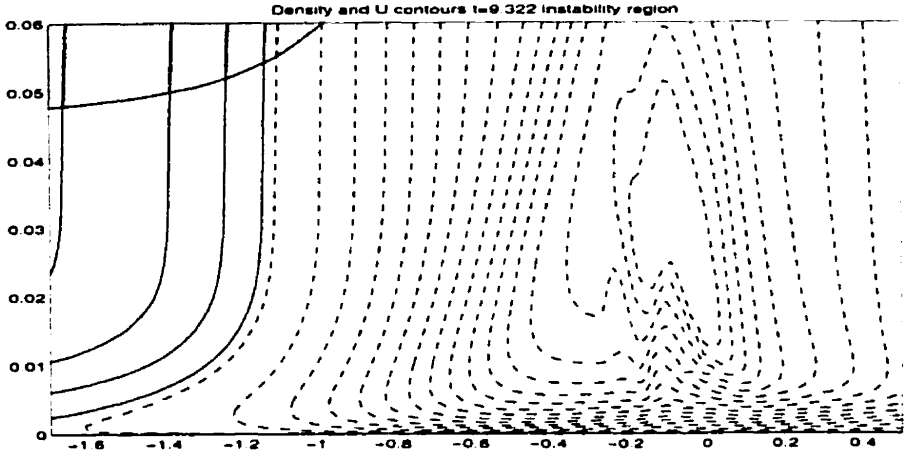

Figure 5.35: Density and horizontal velocity contours for (η_{max} = 0.19 ISW with (z_0, d) = $(0.1, 0.05)$, $(U_s, Re) = (0.22, 8.2 \times 10^4)$ at t = 9.3.0. Positive velocity (solid), negative velocity (dashed).

definition. Figures 5.34 and 5.35 show the vertical and horizontal velocity contours at t = 9.3.0, respectively. The evolution appears to be quite complex, however note that the updrafts and downdrafts in figure 5.34 as well as the isoline crowding in figure 5.35 are confined to a region well above z = 0.01. In other words, the large thickness of the BL precludes global instability onset according to our definition. Furthermore, as can be seen in figure 5.36, the stronger diffusion leads to a much less active region beneath the ISW at t = 27.97.

In figures 5.37, 5.38 and 5.39 we show the vertical velocity contours at t = 9.3.0, the horizontal velocity contours at t = 9.3.0 and the vertical velocity contours at t = 27.92, respectively, for an even smaller Reynolds number ($Re = 3.3 \times 10^4$). We can see that in this case the diffusion keeps the interaction between the upstream vorticity and the ISW very smooth and uneventful. In its late stages, it appears the interaction cannot cause sediment resuspension beneath the wave. Though setting the eddy viscosity to be large implies more sub-scale turbulence that could lead to sediment resuspension.

From the previous two subsections we see that the interaction between a fixed upstream vorticity and the ISW for small waves changes gradually as we change the Reynolds number. For larger waves the range of Reynolds numbers for which global instability sets in is larger and hence

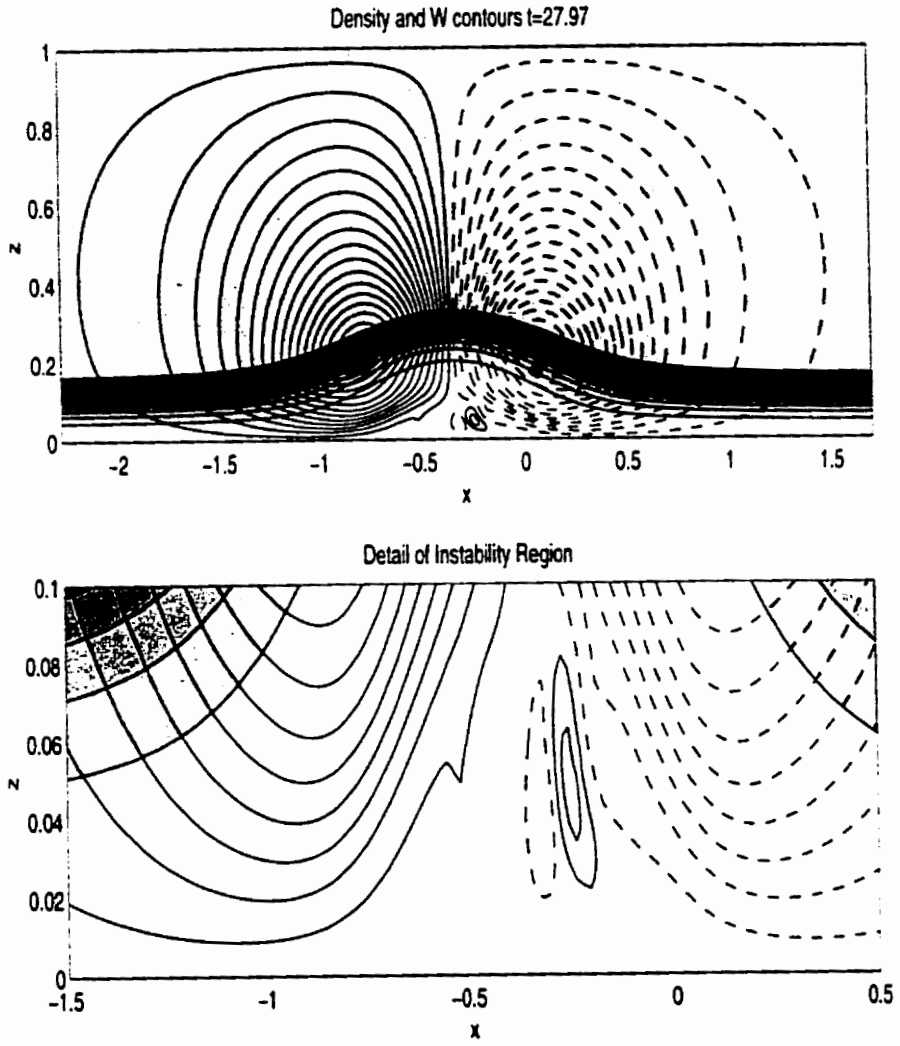

Figure 5.36: As figure 5.34 at a later time, $t = 27.97$

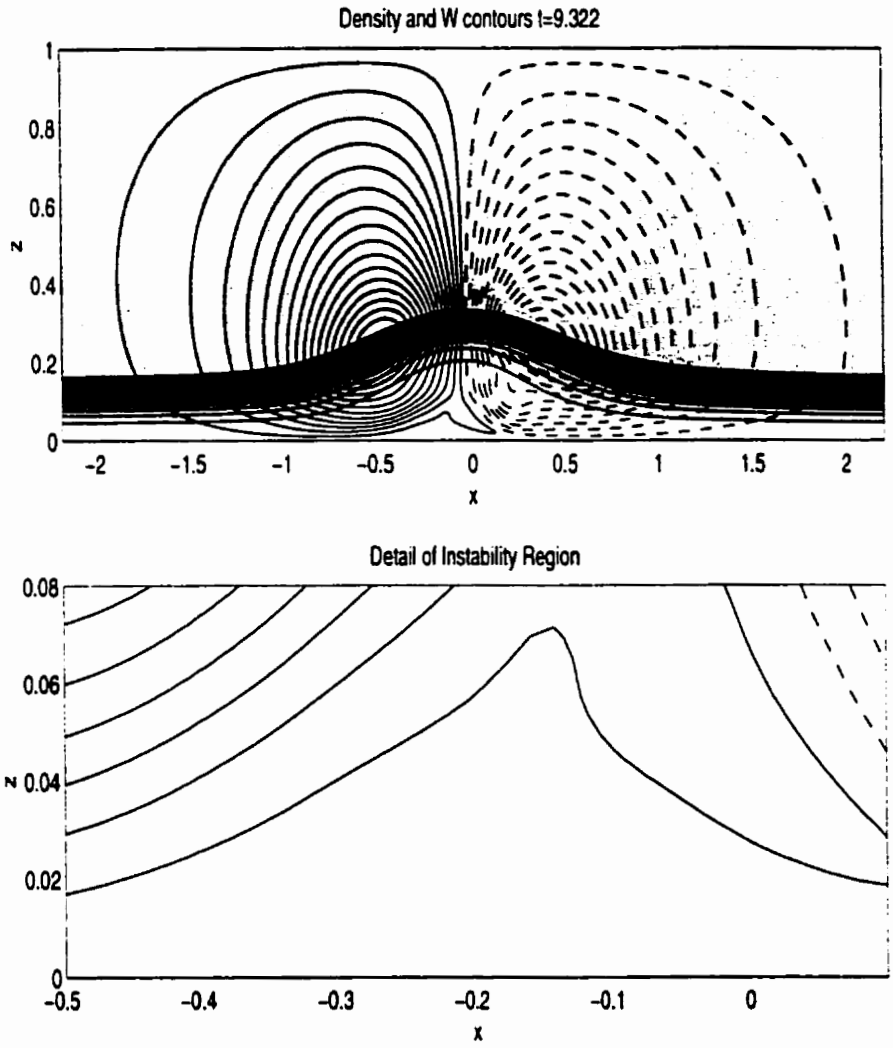

Figure 5.37: Density and vertical velocity contours for ($\eta_{max} = 0.19$ ISW with $(z_0, d) = (0.1, 0.05)$, $(U_s, Re) = (0.22, 3.3 \times 10^4)$ at $t = 9.3.0$. Positive velocity (solid), negative velocity (dashed).

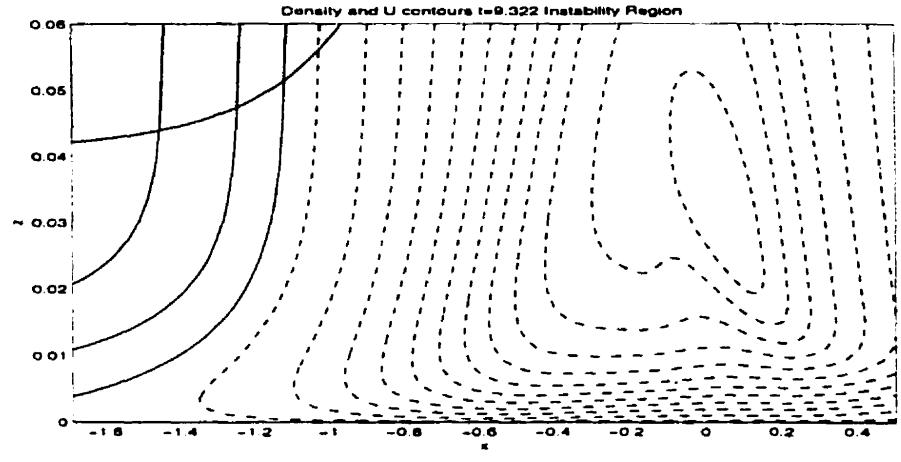

Figure 5.38: Density and horizontal velocity contours for (η_{max} = 0.19 ISW with (z_0, d) = $(0.1, 0.05)$, (U_s, Re) = $(0.22, 3.3 \times 10^4)$ at t = 9.3.0. Positive velocity (solid), negative velocity (dashed).

large parts of parameter space show similar behaviour. This is another issue that is hinted at, but not really explored in ([10]).

5.2.5 Effects of stratification

All of the cases discussed so far have set $(z_0, d) = (0.1, 0.05)$. In this subsection we briefly explore what effect varying the stratification has on the instability dynamics. We begin by reconsidering the case $(z_0, d) = (0.15, 0.05)$ and $\eta_{max} = 0.22$, fixing $U_s = 0.626$ and $Re = 6.46 \times 10^5$. From table 5.3.2 we can see that $max(|u|) > U_s$. As mentioned previously, this stratification has a conjugate flow, however η_{max} is bounded above by shear instability of the variational algorithm and not the conjugate flow amplitude. In figure 5.40 we show the density and vertical velocity contours for the initial wave. On comparison with figure 5.4 (the $(z_0, d) = (0.1, 0.05)$ and η_{max} = 0.19 case) we see that the present wave is roughly 1.5 times wider. In figures 5.41 and 5.42 we show the vertical and horizontal velocity contours during the onset of the instability, respectively. Figures 5.43 and 5.44 show the vortex shedding process later in the instability's evolution. It is worth noting that the vortex shedding in figure 5.44 has the closest resemblance to the vortex shedding found by Pauley and Moin ([51]) of all the simulations examined. Figure 5.45 shows

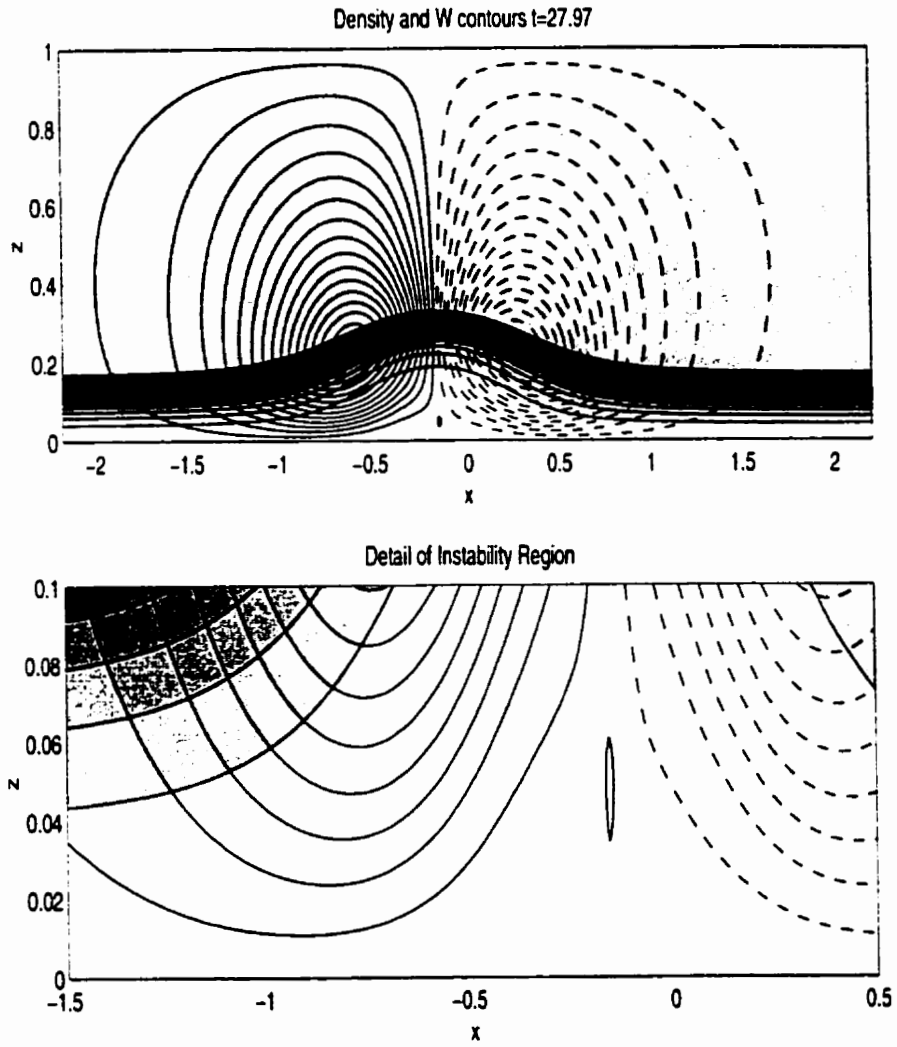

Figure 5.39: As figure 5.37 at a later time, $t = 27.97$

the evolution of the density field. It can be clearly seen that heavy fluid from near the bottom intrudes into the pycnocline. Furthermore, the initial wave is seen to decay dramatically due to wave radiation. This is very similar to the $(z_0, d) = (0.1, 0.05)$ and $\eta_{max} = 0.19$ case described previously.

Finally we could ask what sort of dynamics we get if η_{max} is bounded above by the conjugate flow amplitude. This was the motivation for the previously discussed $(z_0, d) = (0.3333, 0.05)$ and $\eta_{max} = 0.099$ case, which we will presently revisit. We take $Re = 2.4 \times 10^5$ and fix $U_s = 0.85$. From table 5.3.2 we see that $\max(|u|) < U_s$. From figure 5.46, where we plot the initial density and vertical velocity contours, we can see that the initial ISW is extremely broad (nearly four times the cases discussed previously). We can also note that the maximum wave-induced vertical current is weaker in this case than in all other cases shown so far. In figure 5.47 we show the horizontal velocity contours at the point where a shear instability has begun to form behind the separation bubble. We can see that the separation bubble in this case is extremely broad and very short. Thus the flow is nearly parallel over this entire region. In figures 5.48 and 5.49 we show the vertical velocity contours as the shear instability grows. It can be seen that by $t = 21.44$ the shear instability stretches over about three quarters of the ISW's length and that it extends well above the bottom BL. No vortex shedding is apparent, and indeed no vortex shedding was observed for this stratification regardless of the values of U_s and Re used. It is possible that no vortex shedding occurs due to the large length and weak wave induced currents found in the ISW.

In summary we have shown that a global instability consisting of vortex shedding occurs for stratifications with and without a conjugate flow. Stratifications with a center near the mid-depth, for which ISWs are small and broad, exhibits a shear instability instead. This shear instability produces strong enough vertical currents to satisfy our global instability criterion, despite being qualitatively different from the vortex shedding instability. We have found that as the initial ISW decayed due to wave radiation caused by vortex shedding the intensity of the vortex shedding decreased. The intensity of vortex shedding also decreased when the amount of upstream vorticity was decreased (the background current was smaller).

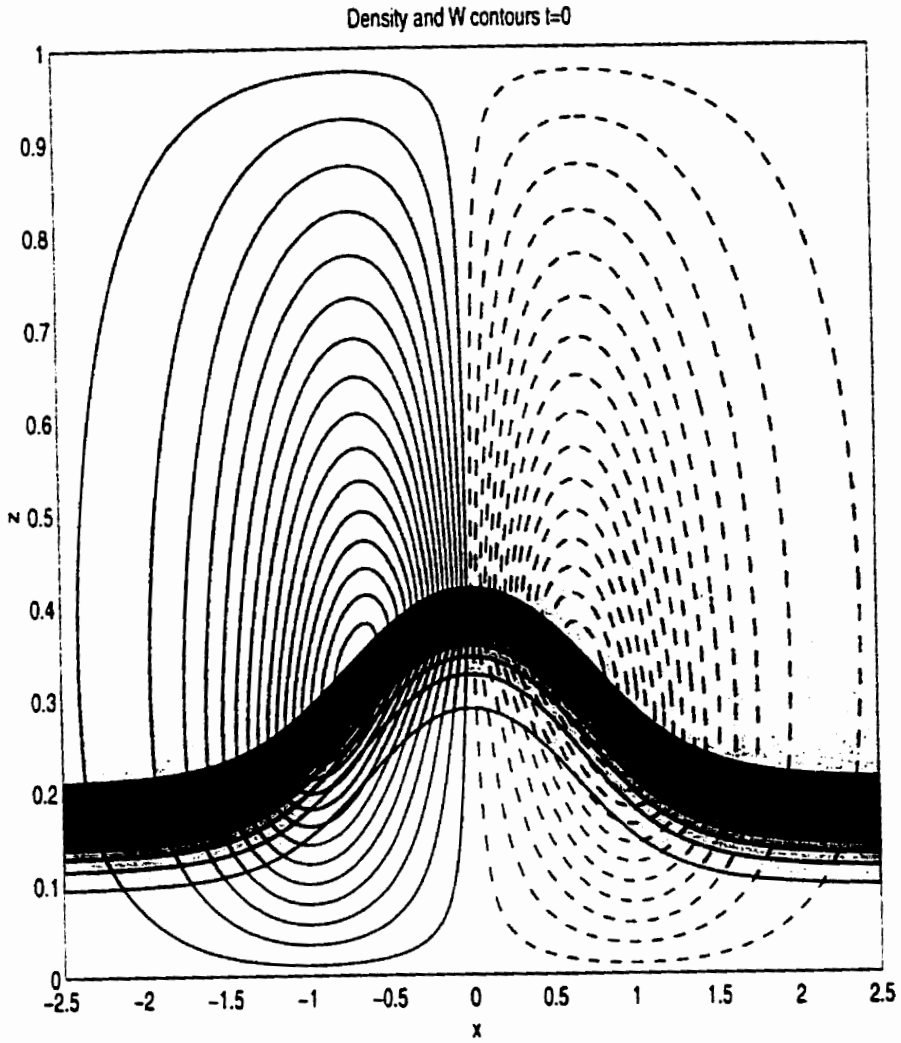

Figure 5.40: Density and vertical velocity contours for (η_{max} = 0.22 ISW with (z_0, d) = $(0.15, 0.05)$, (U_s, Re) = $(0.626, 6.45 \times 10^5)$ at t = 0. Positive velocity (solid), negative velocity (dashed).

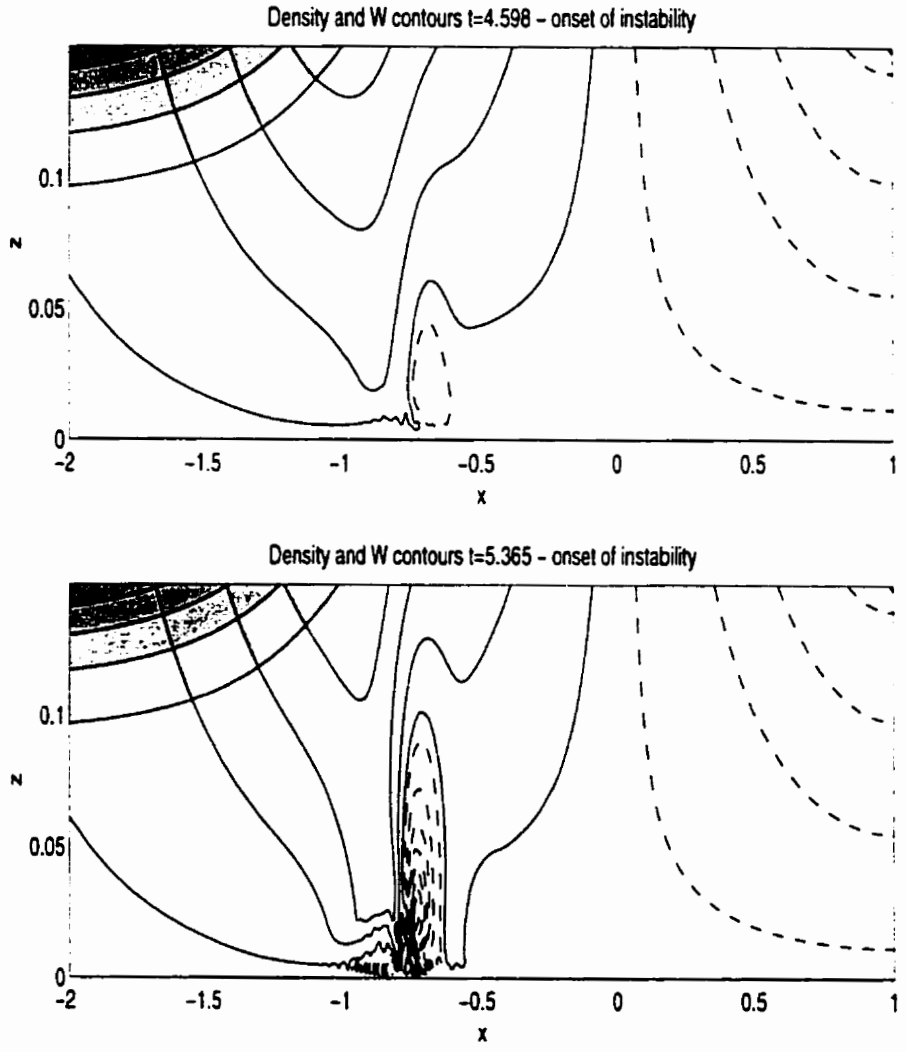

Figure 5.41: Density and vertical velocity contours for ($\eta_{max} = 0.22$ ISW with $(z_0, d) = (0.15, 0.05)$, $(U_s, Re) = (0.626, 6.45 \times 10^5)$ at $t = 4.598$ and $t = 5.365$. Positive velocity (solid), negative velocity (dashed).

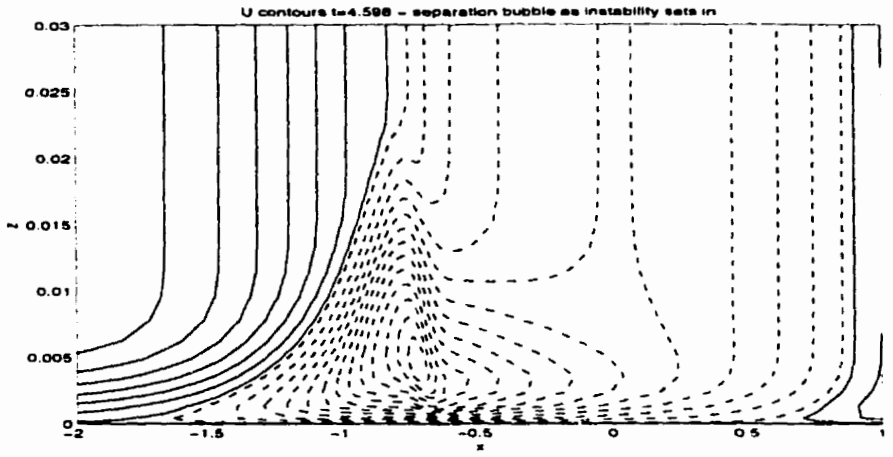

Figure 5.42: As figure 5.41 but for horizontal velocity at $t = 4.598$ only.

5.2.6 Sediment Resuspension

We have stated in the introduction to this chapter that the primary motivation for studying the interaction of ISWs with the bottom BL was provided by the measurements of BDR which showed abnormally high sediment concentration in the water column when a packet of ISWs of elevation passed by. Our results regarding the global instability of ISWs suggest two implications for sediment measurements in the water column. The first is the transport of sediment already suspended in the bottom BL by the anomalous regions of positive vertical velocity which we have shown to be associated with a global instability (for example figure 5.10). The second is the resuspension of sediment by increased bottom stress.

We will consider transport first. To keep the number of figures reasonable we will focus on the $(z_0, d) = (0.1, 0.05)$, larger wave case. In figure 5.50 we consider the case of no upstream vorticity ($U_s = 0.0$) with $Re = 6.8 \times 10^5$. We show the horizontal profiles of the vertical velocity at the same height used for the global instability criterion ($z = 0.0083$ or $z = 0.5$ m in dimensional variables). As the BL grows the vertical velocity at this height is reduced, reaching a steady state whose maximum vertical velocity is about one third of the original, inviscid value. In figure 5.51 we show the corresponding case for $(U_s, Re) = (0.76, 6.8 \times 10^5)$. As the instability develops (and continuing to later times) there are large variations in the vertical velocity, with the largest vertical

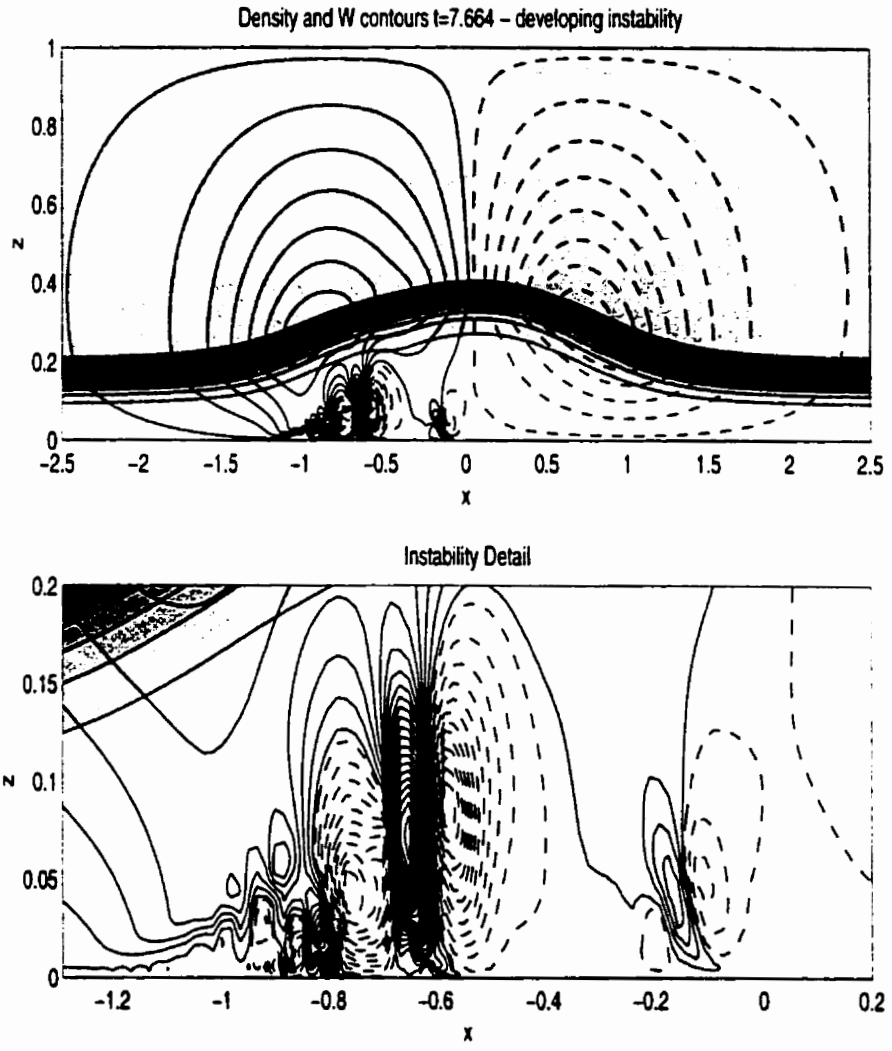

Figure 5.43: As figure 5.41 at later time, $t = 7.664$

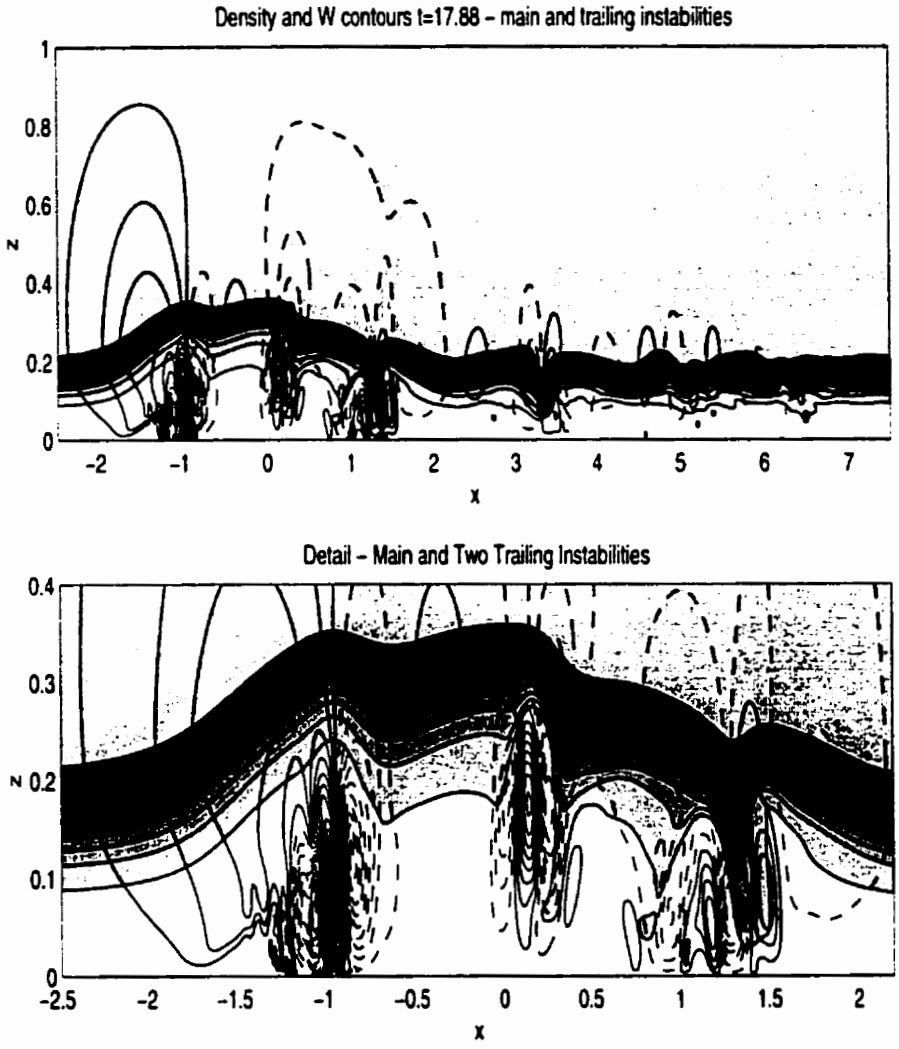

Figure 5.44: As figure 5.41 at later time, $t = 17.88$

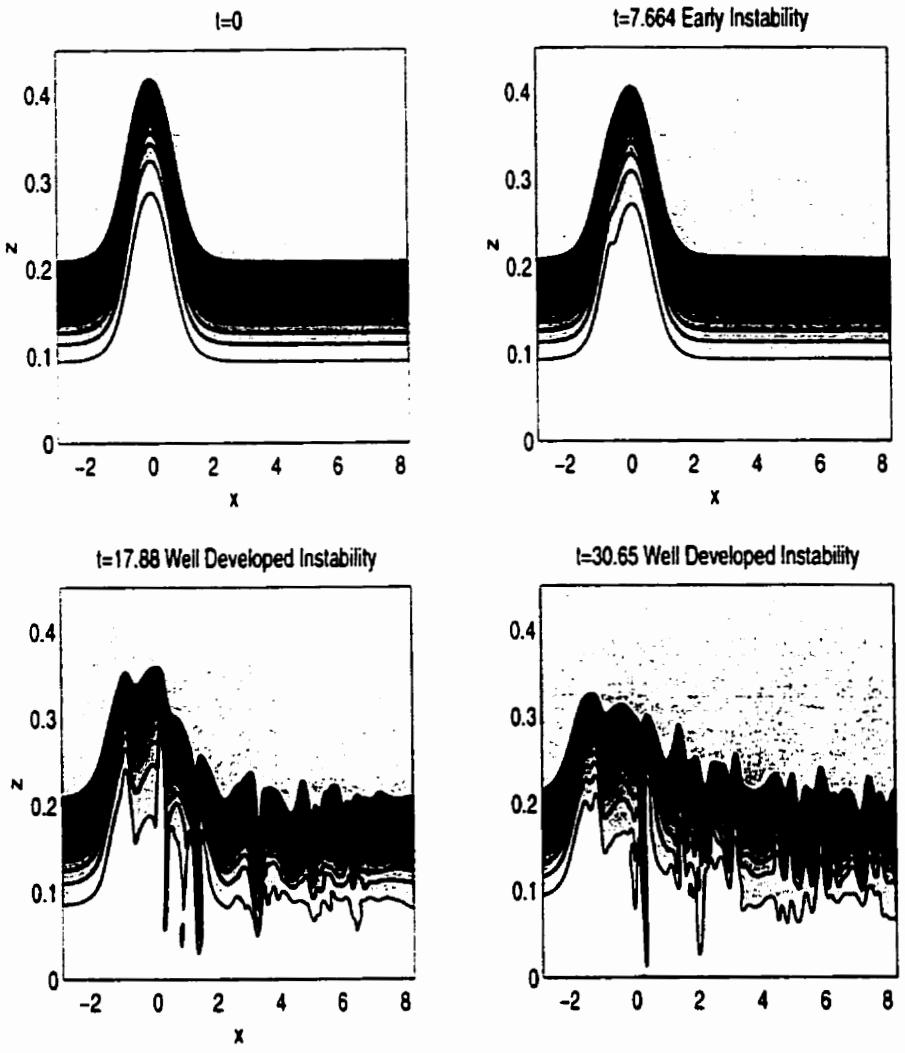

Figure 5.45: Density contours for ($\eta_{max} = 0.22$) ISW with $(z_0, d) = (0.15, 0.05)$, $(U_s, Re) = (0.626, 6.45 \times 10^5)$ showing evolution of instability.

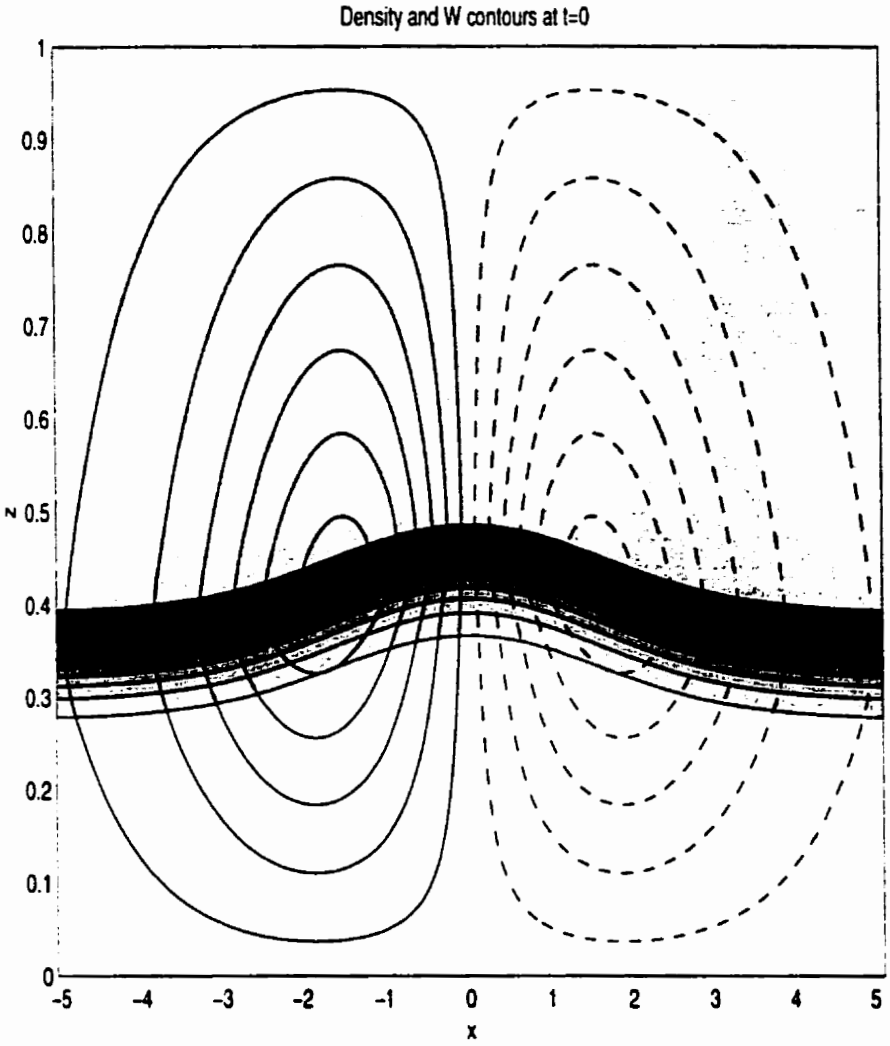

Figure 5.46: Density and vertical velocity contours for (η_{max} = 0.099 ISW with (z_0, d) = $(0.3333, 0.05)$, (U_s, Re) = $(0.85, 2.4 \times 10^5)$ at t = 0. Positive velocity (solid), negative velocity (dashed).

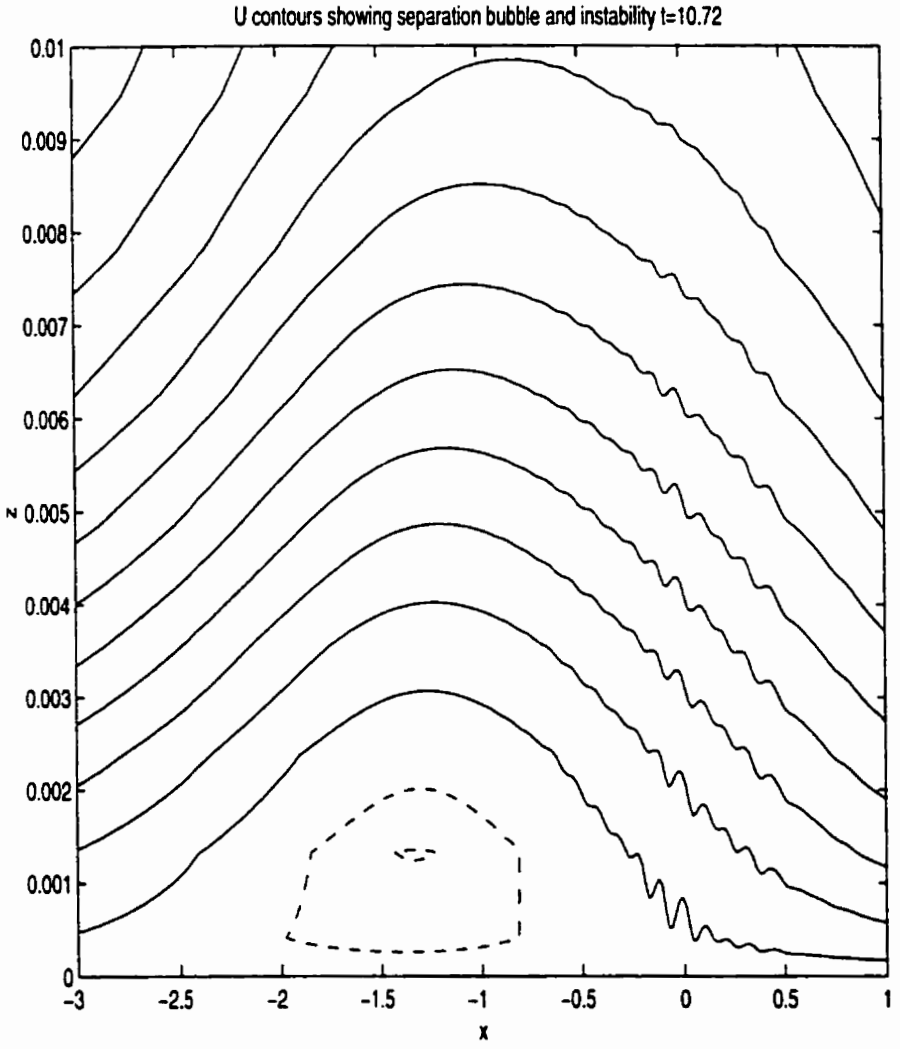

Figure 5.47: Horizontal velocity contours for ($\eta_{max} = 0.099$ ISW with $(z_0, d) = (0.3333, 0.05)$, $(U_s, Re) = (0.85, 2.4 \times 10^5)$ at $t = 10.72$. Positive velocity (solid), negative velocity (dashed).

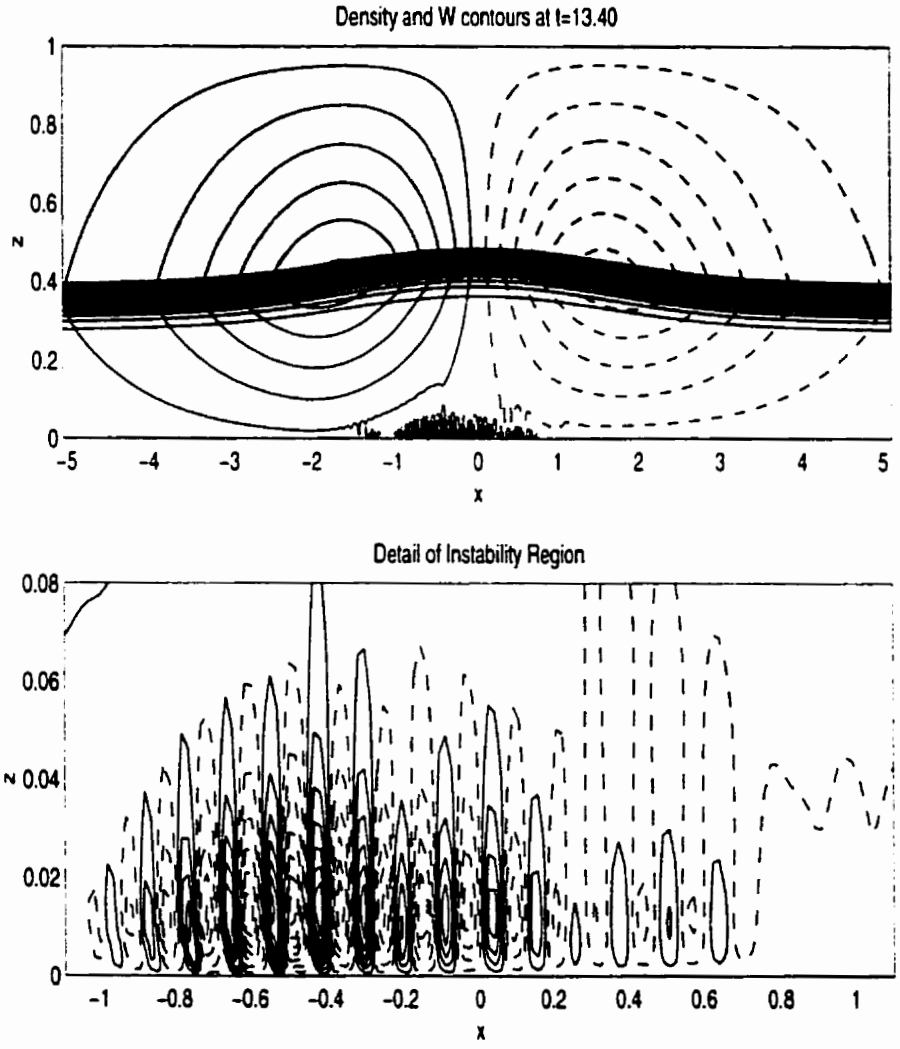

Figure 5.48: Instability development. As figure 5.46 for later time, $t = 13.40$.

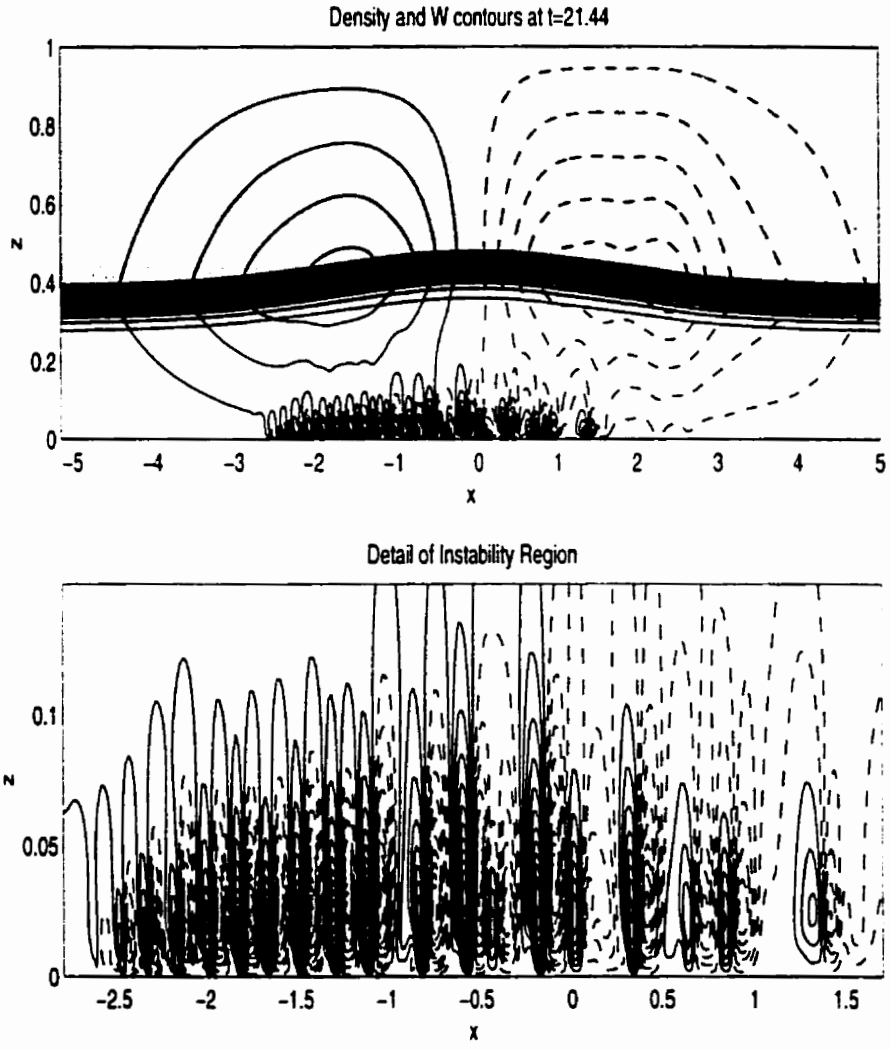

Figure 5.49: Instability development. As figure 5.46 for later time, $t = 21.44$.

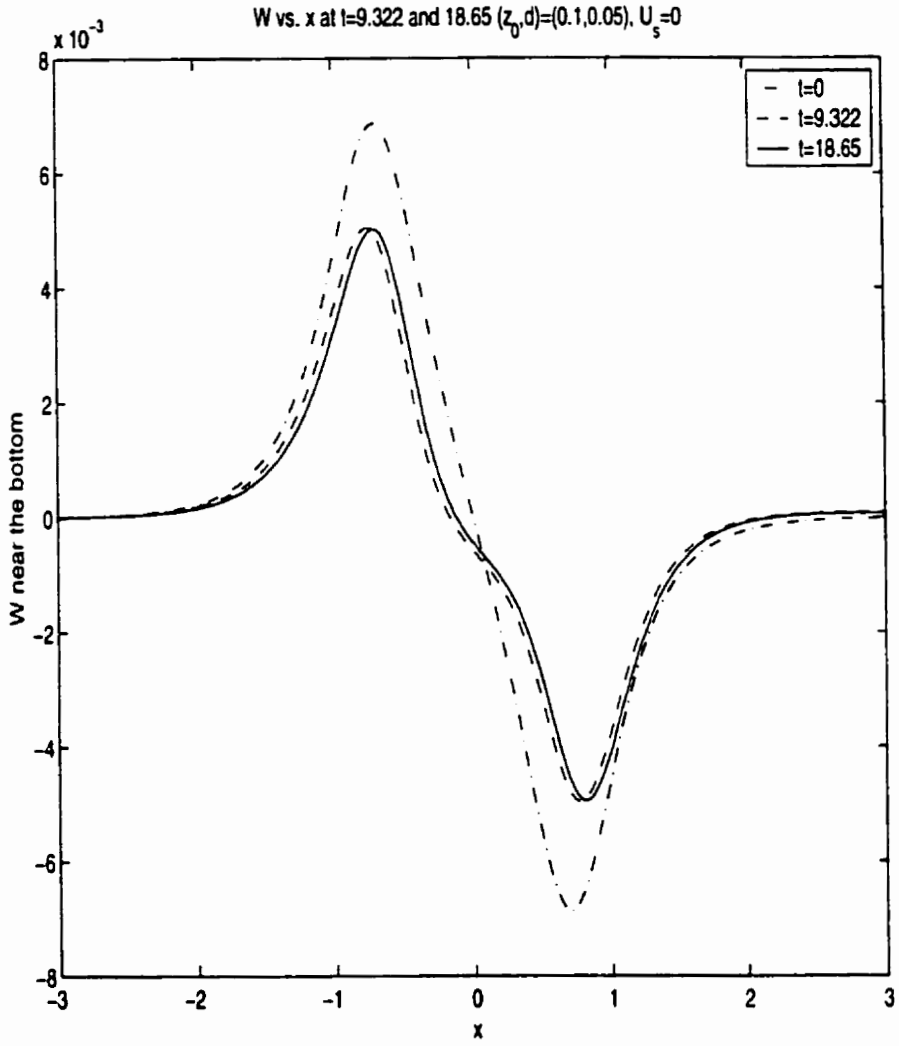

Figure 5.50: Vertical velocity vs. x at a fixed height $z = 0.0083$ for the case $\eta_{max} = 0.19$ ISW with $(z_0, d) = (0.1, 0.05)$, $(U_s, Re) = (0.0, 6.8 \times 10^5)$.

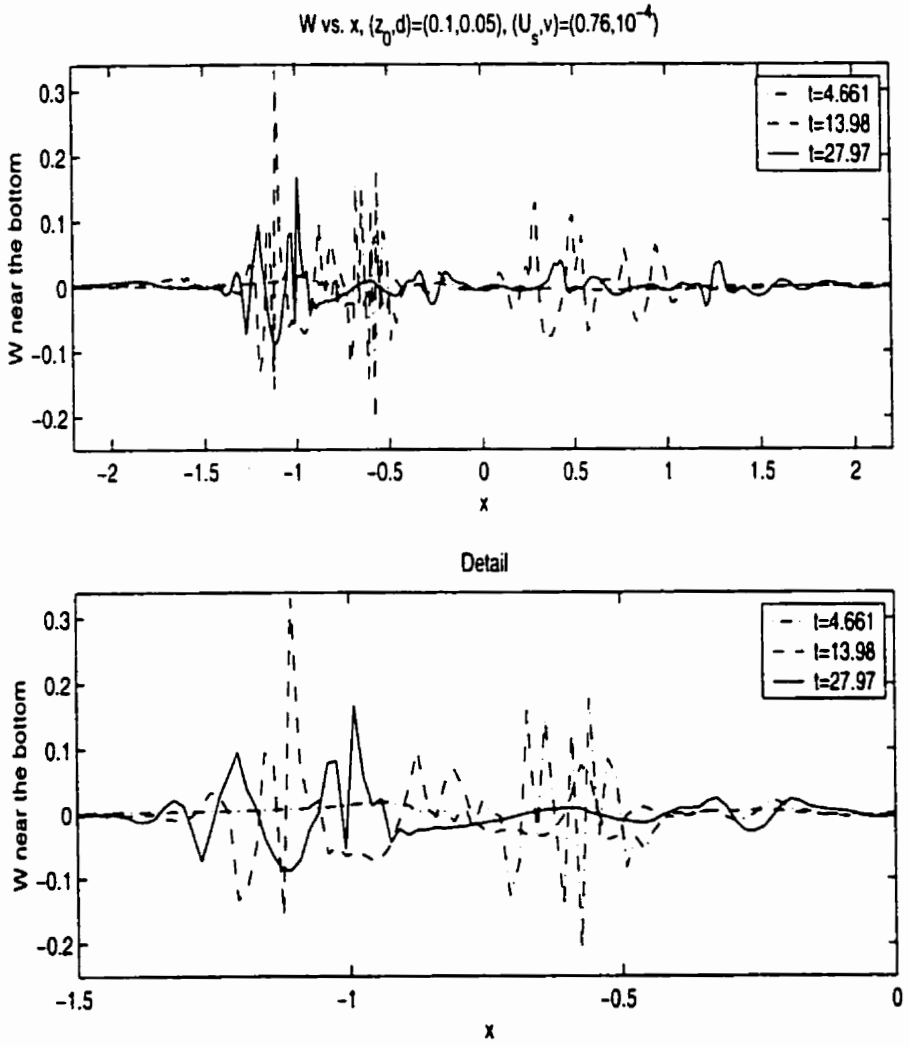

Figure 5.51: Vertical velocity vs. x at a fixed height $z = 0.0083$ for the case $\eta_{max} = 0.19$ ISW with $(z_0, d) = (0.1, 0.05)$, $(U_s, Re) = (0.76, 6.8 \times 10^5)$.

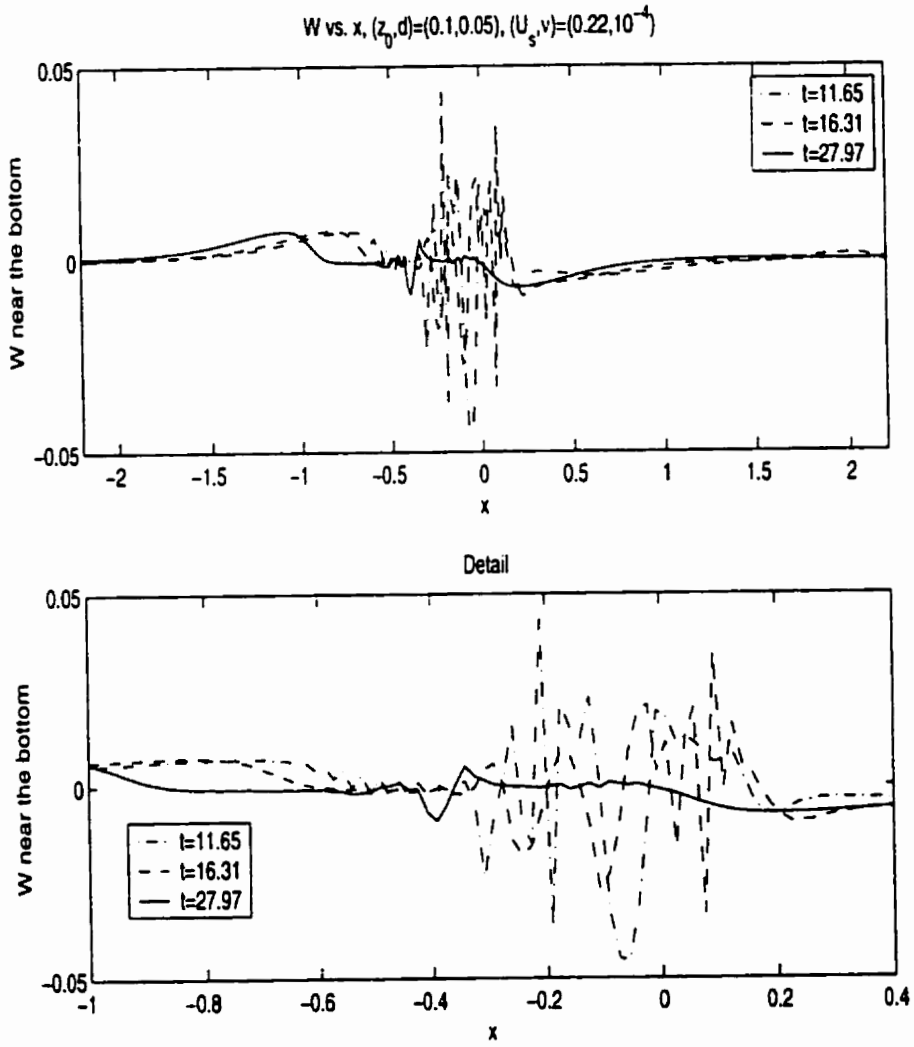

Figure 5.52: Vertical velocity vs. x at a fixed height $z = 0.0083$ for the case $\eta_{max} = 0.19$ ISW with $(z_0, d) = (0.1, 0.05)$, $(U_s, Re) = (0.22, 6.8 \times 10^5)$.

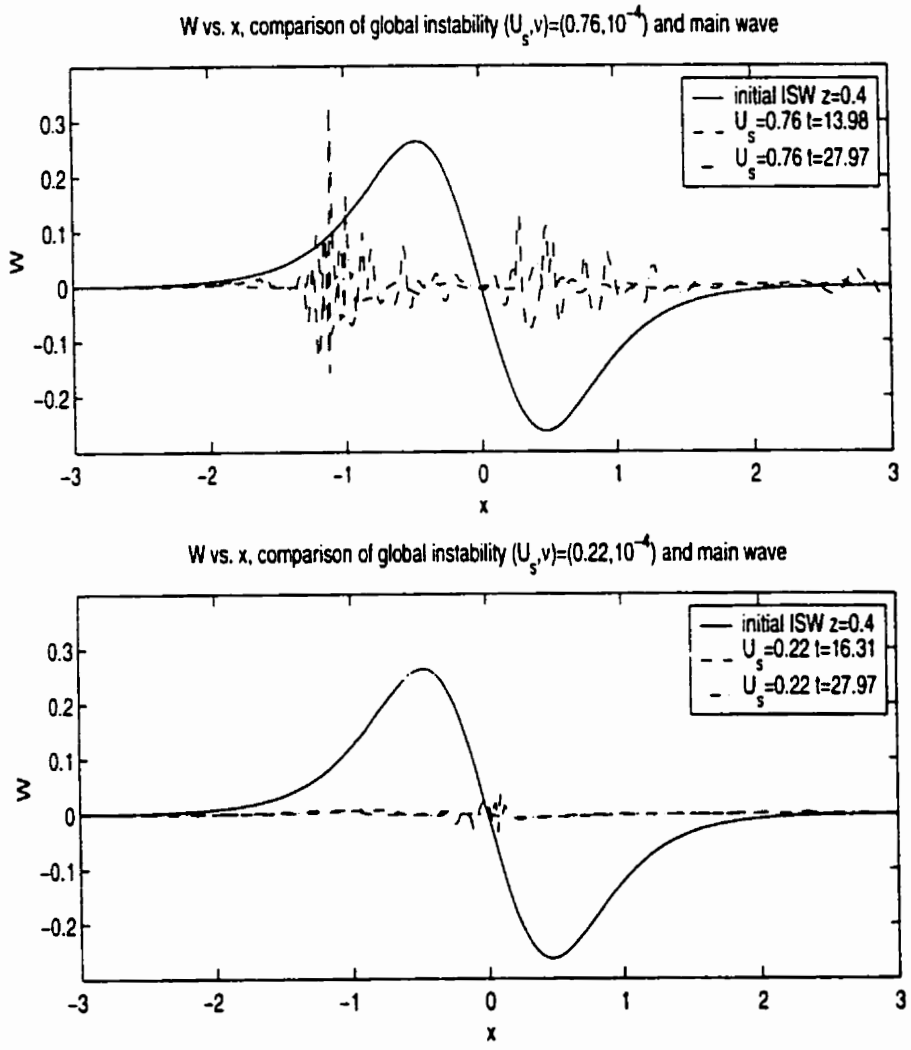

Figure 5.53: Vertical velocity vs. x at two fixed heights, $z = 0.4$ at $t = 0$ (showing wave-induced vertical currents) and $z = 0.0083$ for later times (showing instability induced vertical currents). $\eta_{max} = 0.19$, $(z_0, d) = (0.1, 0.05)$, $(U_s, Re) = (0.76, 6.8 \times 10^5)$ and $(U_s, Re) = (0.22, 6.8 \times 10^5)$.

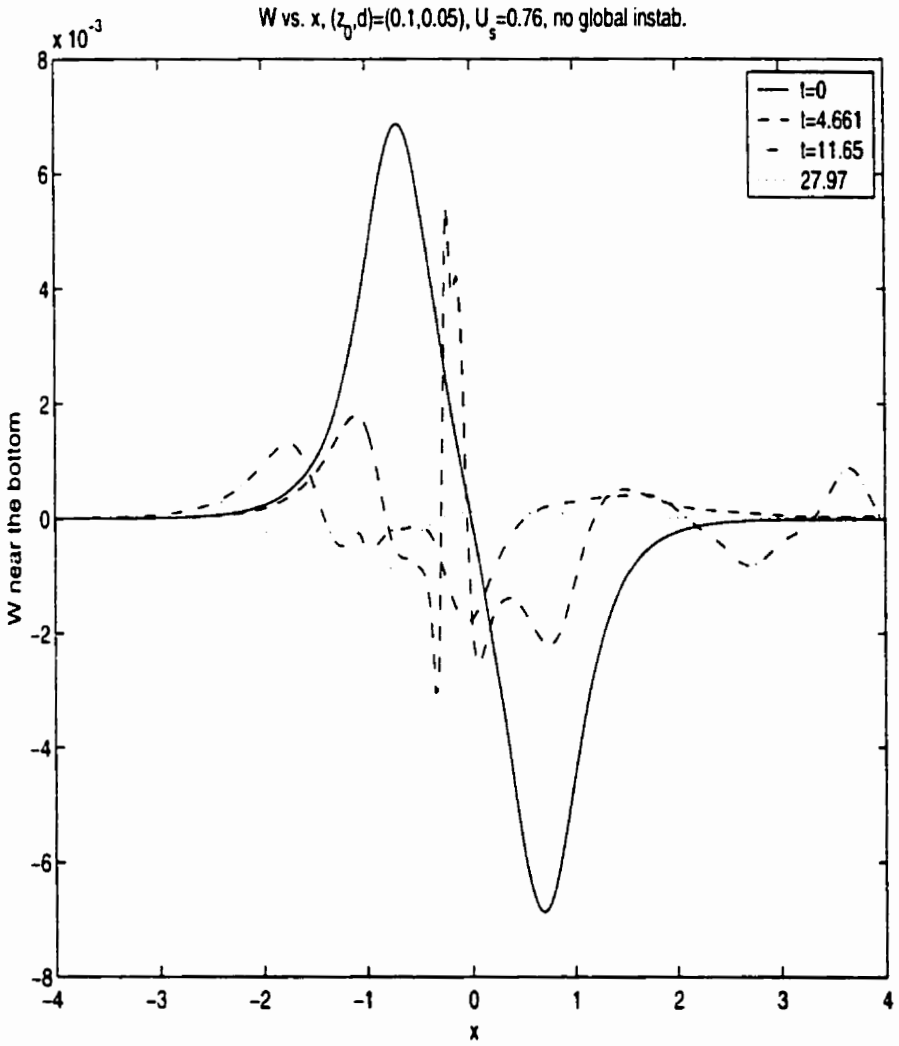

Figure 5.54: Vertical velocity vs. x at a fixed height, $z = 0.0083$ (showing that cases of no global instability do not induce persistently large vertical currents in the bottom BL). $\eta_{max} = 0.19$, $(z_0, d) = (0.1, 0.05)$, $(U_s, Re) = (0.76, 1.13 \times 10^4)$.

currents more than 20 times larger than the inviscid (or the $U_s = 0$) value.

Figure 5.52 shows similar results for the $(U_s, Re) = (0.22, 6.8 \times 10^5)$ case. Note however that the increase in maximum vertical velocity over the inviscid value is now only about 5 times and that by $t = 27.97$ the vertical currents are only of comparable magnitude to the $U_s = 0$ case and as such not likely to make an impact on sediment transport.

As we can see from figure 5.4 the largest wave-induced vertical currents occur well above the bottom. It is thus interesting to compare the vertical currents due to the instability with those due to the wave. This is what figure 5.53 shows. We choose to plot the vertical currents due to the ISW at a fixed height $z = 0.4$, giving a typical horizontal profile of the largest vertical currents due to the wave. We can see that the instability in the $(U_s, Re) = (0.76, 6.8 \times 10^5)$ case induces vertical currents as large as the largest induced by the ISW, while the $(U_s, Re) = (0.22, 6.8 \times 10^5)$ case does not. Thus more upstream vorticity at fixed ν implies more sediment transport out of the bottom BL.

In figure 5.54 we show the vertical velocity profiles for the $(U_s, Re) = (0.76, 1.13 \times 10^4)$ which, according to our criterion, did not undergo a global instability. It can be seen that while the interaction of the upstream vorticity with the ISW does lead to closely spaced regions of updraft and downdraft the maximum vertical current never surpasses the original inviscid value (in sharp contrast with the cases presented above). In addition, the large values of vertical currents are short lived, being associated with the shedding of small ISWs behind the original wave.

To summarize, in all cases where our global instability criterion is satisfied, we find vertical currents capable of pumping previously suspended sediment out of the BL and into the main water column. As the value of U_s is increased (with fixed Re), the vertical currents in the bottom BL increase to be as large as the maximum wave-induced vertical current for inviscid waves. Since ISWs generally have the largest wave-induced vertical currents well away from the bottom this marks a significant difference between inviscid ISWs and ISWs with a viscous BL and an upstream source of vorticity. For the latter waves a great deal of sediment can be transported into the water column (as evidenced by the intrusions of heavy fluid into the pycnocline in figure 5.3).

The second issue is the actual resuspension of sediment. The initiation of sediment motion is

an extremely complex problem involving complex fluid-solid and solid-solid interactions. Much of the complex physical issues (grain size, grain shape, grain cohesion, etc.) will be ignored in our simplistic presentation (see for example the book by Nielsen [47] some of whose presentation we follow, or the book by Sleath [57]). The models available in the literature (including the two books mentioned above) generally deal with surface wave effects, only. This focus on surface waves is quite understandable as surface waves are important in the coastal zone where man-made structures most often interact with the ocean. Thus the state of research on the onset of sediment motion in deeper water where surface wave effects are not important is rather incomplete (though the author can hardly claim to have a great deal of knowledge in this field).

Sediment resuspension can be modeled according to a conservation law which states that the rate of sediment transport from the ocean bottom to the fluid just above the bottom per unit of time is equal to the rate of pickup minus the rate of deposition. The rate of pickup is specified by empirical pickup functions (see for example [47] page 223) which differ according to the type of flow (steady flow, oscillatory flow due to surface waves, etc.). In general the pickup functions depend on various physical properties of the sediment. In the case of sinusoidal surface waves (and surface waves superimposed on a steady current) the role of the flow is represented by the Shields parameter. The Shields parameter is shear stress at the bottom, nondimensionalized by a combination of parameters based on the physics of the sediment (i.e. grain density, grain diameter, etc.). Furthermore, in order to fit experimental data, the Shields parameter is modified for more complex situations such as wave-current interactions. We do not wish to address these issues here, hence we will focus our attention on the shear stress at the bottom. The idea is that once the shear stress on the bottom due to the instability crosses some threshold, sediment begins to move and is resuspended in the water column. It is likely that the threshold of motion will have to be determined by observation or experiment, and as such we will not discuss the threshold stress value in this thesis.

The bottom stress is important for the issue of ISW-induced sediment motion. For this brief

discussion we take the nondimensional shear stress to be given by

$$\tau = \frac{1}{Re} u_z. \tag{5.2}$$

In figure 5.55 we show the shear stress for the $(z_0, d, U_s, Re) = (0.1, 0.05, 0.76, 6.8 \times 10^5)$ case compared with the $(U_s, Re) = (0.76, 1.13 \times 10^4)$ and $(U_s, Re) = (0.0, 6.8 \times 10^5)$ cases. We can see that the global instability is responsible for a large increase in τ over both the no upstream vorticity and upstream vorticity with no global instability cases.

We found that, consistent with the results on vertical velocity, the $(U_s, Re) = (0.22, 6.8 \times 10^5)$ case is responsible for much smaller values of τ when compared with the $(U_s, Re) = (0.76, 6.8 \times 10^5)$ case. In fact the oscillations in the bottom stress due to the global instability for $(U_s, Re) = (0.22, 6.8 \times 10^5)$ have an amplitude of about one third the maximum bottom stress magnitude in the $(U_s, Re) = (0.0, 6.8 \times 10^5)$ case. However both the $U_s = 0.76$ and $U_s = 0.22$ cases (with $Re = 6.8 \times 10^5$)) show a great deal of variation of the nondimensional bottom stress with x. This is in contrast to the slowly varying nondimensional bottom stress found when $U_s = 0.0$. The fast spatial variation of the nondimensional bottom stress (that persists in time) for cases in which a global instability occurs may provide a mechanism for setting sediment into motion. This conjecture, as well as the issue of what is a correct estimate of the bottom stress, merit further investigation in the future.

We should note that surface wave-induced sediment motion models usually take the bottom BL to be turbulent, and hence define the dimensional bottom stress, τ_b as

$$\tau_b = \frac{1}{2} \rho u_*^2, \tag{5.3}$$

for an appropriately defined u_*. For the present results there is no unambiguous way to define u_*, though if we were to consider τ_b to be based on u at $z = 0.008333$ (or $z = 0.5$ m in dimensional variables) the global instability would again be responsible for an increase in τ_b.

In summary, we have shown that the global instability leads to an increase in bottom stress when compared to cases of no global instability. Since the bottom stress is used in phenomenolog-

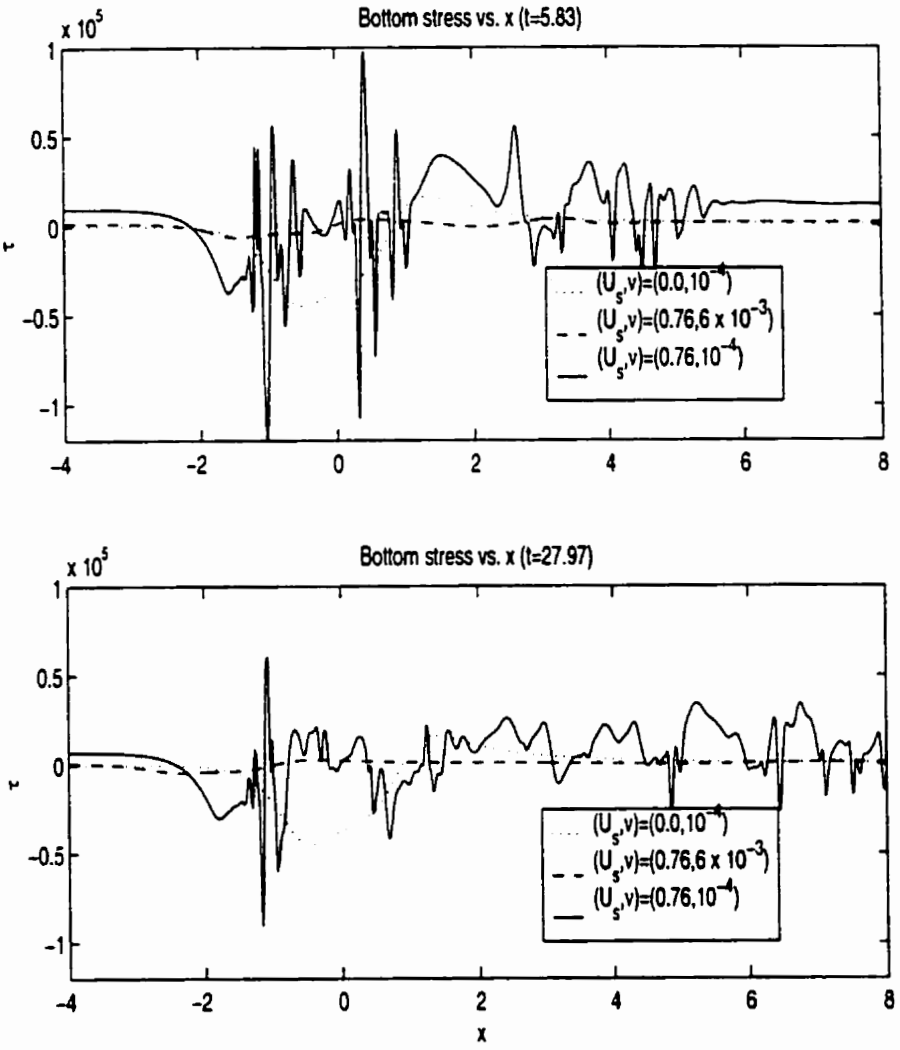

Figure 5.55: Nondimensional bottom stress vs. x.

ical pickup function models to increase the concentration of sediment in the BL our results show that ISW interaction with upstream vorticity can serve as a mechanism for sediment resuspension. Coupled with the instability induced pumping out of the bottom BL the presented results show that global instability can explain the correlation between ISW passage and an increase in sediment concentration measured well away from the bottom (as in [8]).

5.3 Conclusions and Future Directions

In this chapter we have discussed the interaction between fully nonlinear ISWs and the bottom, viscous BL using a numerical model with a constant eddy viscosity and diffusivity. The Prandtl number was set to one for all simulations. We found that when there is no background current the adjustment of an inviscid ISW to no-slip bottom BCs was very small. The only change from an inviscid ISW was to set up a laminar bottom BL. However when a background current with non-zero bottom velocity was included in the computation of the inviscid ISW the adjustment was markedly different. For simplicity, we concentrated on constant background currents U_s. The value of U_s controls the amount of vorticity produced upstream of the ISW once the no-slip bottom BCs are switched on. We found that for all non-zero values of U_s and all eddy viscosities used there was a complex interaction between the upstream vorticity and the ISW as the upstream vorticity was advected into the wave.

For larger values of the eddy viscosity it was found that the interaction leads to the shedding of smaller ISWs behind the main wave. For smaller values of eddy viscosity the interaction was much more violent, with vortex shedding and ejection of material from the bottom BL into the main water column. This type of interaction was referred to as a global instability (consistent with [10]). A criterion for the onset of the instability was defined based on the vertical current at a fixed height above (but close to) the bottom. Through extensive numerical experimentation it was found that this criterion was very good at discriminating between cases of ISW shedding and vortex shedding. From a practical point of view, the instability criterion is useful since the vertical velocity near the bottom will give some information on how much sediment suspended in the bottom BL will be pumped up into the water column.

We used the instability criterion to explore the parameter space (U_s, ν) (or alternatively (U_s, Re)) for several different ISWs and stratifications to get bounds on when a global instability will and will not occur. It was found that bounds depended on the wave amplitude, with larger waves exhibiting a global instability for smaller values of U_s (with ν fixed), as expected. Furthermore, larger values of U_s (i.e. more upstream vorticity production) exhibit global instability for larger ranges of ν (Re). If the value of the eddy viscosity is too large no global instability

will occur, regardless of the size of the ISW or U_s, and the initial ISW will break down via breakdown of the initial ISW into a train of smaller ISWs (we termed this 'laminar' breakdown).

We discussed several examples of the global instability onset and evolution in detail to show the similarities and differences between different stratifications and ISW amplitudes. As discussed in the chapter on steady waves, three different possibilities bound the ISW amplitude. We found that the global instability did not change qualitatively when a stratification did, or did not have a conjugate flow solution provided that the maximum amplitude (η_b) was not given by the conjugate flow amplitude (i.e. given by wave-breaking or shear instability of the variational algorithm). For the case when the conjugate flow amplitude did give the upper bound on a_{max} the ISWs were very broad and the instability set in as a shear instability (as opposed to vortex shedding).

In order to get some idea of how the present results relate to observations of sediment in the main water column we presented horizontal profiles of the vertical velocity at a fixed height above (but close to) the bottom ($z = 0.5$ m in all cases). We found that the global instability, and vortex shedding in particular, causes a large increase in w at this height. In some cases we found that it was possible to increase w near the bottom to be larger than the largest ISW-induced vertical velocity (which occurs well away from the bottom). Thus the global instability provides a strong pumping mechanism to move sediment from the bottom BL to the main water column.

The onset of sediment motion was also discussed. The treatment was brief due to the inherent physical complexity of the problem. We looked at the effect of the global instability on the bottom shear stress. The bottom stress in cases of global instability was found to greatly exceed the bottom stress in cases of no global instability. However this result depended on a particular nondimensionalization for the bottom stress (to account for the large changes in eddy viscosity). For this reason the results relating to ISW induced sediment motion are open to question and deserving of more extensive future study. We should note that sediment motion in the BL is likely much more complex than our naive model. In particular, experiments ([48]) have shown that the coherent structures in a turbulent BL have a profound influence on how sediment motion begins, and where the moving sediment gathers. Of course, eddy viscosity-type models cannot model this behaviour and the dynamics once the BL is turbulent remains largely unexplored. Nevertheless,

the global instability provides a mechanism for getting sediment high into the water column.

A quadratic stress boundary condition is often used in large scale ocean models as a simple means to incorporate a turbulent bottom boundary layer. Preliminary investigations with a quadratic bottom stress BC

$$u_z(x,0,t) = Ku|u|, \tag{5.4}$$

where K is an empirical constant, indicate that a global instability sets in at times comparable to, and in a qualitatively identical manner to, the no slip BC cases.

The treatment in this chapter is far from complete. The parameter space involved is very large and as such only certain regions were explored. Furthermore the actual onset of the instability should be explored further. While vorticity dynamics provides a simplistic explanation for the dynamics of the interaction between the upstream vorticity and the ISW, a much more detailed treatment would prove useful. This would require a numerical model that allows the resolution of the region of interaction to a much higher degree, with a smaller aspect ratio between the grid height and width. The difficulty lies in how to incorporate the spatially large ISW into such a model (in a clearer manner than [10]).

Issues relating to the dynamics after instability onset would likely require a 3D model to investigate properly. The same challenges as the 2D model described above would have to be addressed, along with issues relating to memory and computation time. Due to the high cost of such simulations it may be that an entirely different approach, based on Reynolds averaged equations and turbulence modeling, may be needed.

In ([11]) the issue of resuspension by waves of depression is brought up. While this appears to be possible given our results, a detailed investigation remains to be carried out. In the author's opinion the gap between the present simulations and specific oceanic measurements is quite large and a very obvious line of research would seek to redress this problem.

Finally, as mentioned in the previous chapter, realistic bottom topography would greatly complicate the dynamics. In ([8]) it is mentioned that the ISWs responsible for the measured sediment resuspension are likely generated by topographic resonance. Numerical simulations that tested this hypothesis would provide one means of including bottom topography while still

maintaining a connection with the present work.

In conclusion, throughout this work we have shown a variety of fascinating physical phenomena relating to fully nonlinear ISWs. In general, the starting point for all our investigations was the variational algorithm that allowed the calculation of fully nonlinear ISWs. As many questions remain unanswered, it is the author's hope for the future that fully nonlinear ISWs, and the host of interesting behaviours they exhibit, will merit the same sort of attention paid to WNL in the past.

Bibliography

[1] Ablowitz, M.J., Segur, H. (1981) *Solitons and the inverse scattering transform*, SIAM Studies in Applied Math, Vol.4, SIAM, Philadelphia.

[2] Akylas, T.R., Grimshaw, R.H. (1992) Solitary internal waves with oscillatory tails, *Journal of Fluid Mechanics*, **242**, 279-298.

[3] Apel, J.R., Byrne, H.M., Proni, J.R., Charnell, R.L. (1975) Observations of oceanic internal and surface waves from the Earth Resources Technology Satellite, *Journal of Geophysical Research*, **80**, 865.

[4] Benjamin, T.B., (1966) Internal waves of finite amplitude and permanent form, *Journal of Fluid Mechanics*, **25**, 241.

[5] Benjamin, T.B., (1967) Internal waves of permanent form in fluids of great depth *Journal of Fluid Mechanics*, **29**, 559-592.

[6] Benjamin, T.B., (1986) On the Boussinesq model for two-dimensional wave motions in heterogeneous fluids, *Journal of Fluid Mechanics*, **165**, 445.

[7] Benney, D.J., (1966) Long nonlinear waves in fluid flows, *Journal of Mathematics and Physics*, **45**, 52.

[8] Bogucki, D., Dickey, T., Redekopp, L.G. (1997) Sediment resuspension and mixing by resonantly generated internal solitary waves, *Journal of Physical Oceanography*, **27**, 1181.

[9] Bogucki, D., Garret, C. (1993) A simple model for the shear-induced decay of an internal solitary wave, *Journal of Physical Oceanography*, **23**, 1767.

[10] Bogucki, D.J., Redekopp, L.G. (1999) A mechanism for sediment resuspension by internal solitary waves, *Geophysical Review Letters*, **26**, 1317

[11] Bogucki, D.J., Redekopp, L.G. (2000) Resuspension and boundary mixing stimulated by long internal waves, *Proceedings of the Fifth International Symposium on Stratified Flows*, ed. Lawrence, G.A., Pieters, R., Yonemitsu, N., 283.

[12] Brown, D.J., Christie, D.R. (1998) Fully nonlinear solitary waves in continuously stratified incompressible Boussinesq fluids, *Physics of Fluids*, **10**, 2569-2586.

[13] Caulfield, C.P., Peltier, W.R. (2000) The anatomy of the mixing transition in homogeneous and stratified free shear layers, *Journal of Fluid Mechanics*, **413**, 1.

[14] Davis, R.E., Acrivos, A. (1967) Solitary waves in deep water, *Journal of Fluid Mechanics*, **29**, 593-607.

[15] Derzho, O., G., Grimshaw, R. (1997) Solitary waves with a vortex core in a shallow layer of stratified fluid, *Physics of Fluids*, **9**, 3378.

[16] Drazin, P.G., Johnson, R.S., (1989) *Solitons: An Introduction*, Cambridge University Press, Cambridge.

[17] Gardner, C.S., Greene, J.M., Kruskal, M.D., Miura, R.M. (1967) Method for solving the KdV equation, *Physical Review Letters*, **19**, 1095.

[18] Gardner, C.S., Greene, J.M., Kruskal, M.D., Miura, R.M. (1974) Korteweg-deVries equations and generalizations. VI. Methods for exact solution, *Communications in Pure and Applied Math*, **27**, 97.

[19] Garret, C., Munk, W. (1979) Internal waves in the ocean, *Annual Review of Fluid Mechanics*, **11**, 339.

[20] Gear, J., Grimshaw, R., (1983) A second-order theory for solitary waves in shallow fluids, *Physics of Fluids*, **26**, 14.

[21] Gill, A.E., (1982) *Atmosphere-Ocean Dynamics*, Academic Press, NY.

[22] Grimshaw, R. (1997) Internal Solitary Waves in *Advances in Coastal and Ocean Engineering*, ed. P. L-F. Liu, World Scientific Publishing, Vol. 3, 1.

[23] Grue, J., Jensen, A., Rusas, P.O., Sveen, J.K. (2000) *Journal of Fluid Mechanics*, **413**, 181-217.

[24] Hanazaki, H. (1994) On the three-dimensional internal waves excited by topography in the flow of a stratified fluid, *Journal of Fluid Mechanics*, **263**, 293.

[25] Holloway, P.E., Pelinovsky, E., Talipova, T., Barnes, B. (1997) A nonlinear model of internal tide transformation on the Australian north-west shelf, *Journal of Physical Oceanography*, **27**, 871.

[26] Howard, L.N. (1961) Note on a paper of John W. Miles, *Journal of Fluid Mechanics*, **13**, 158.

[27] Huthnance, J.M. (1989) Internal tides and waves near the continental shelf edge, *Geophysical Fluid Dynamics*, **48**, 81.

[28] Johnson, R.S. (1997) *A Modern Introduction to the Mathematical Theory of Water Waves*, Cambridge University Press, Cambridge.

[29] Kundu, P.K. (1990) *Fluid Mechanics*, Academic Press, San Diego.

[30] Lamb, K.G. (1994) Numerical simulations of stratified inviscid flow over a smooth obstacle, *Journal of Fluid Mechanics*, **260**,1.

[31] Lamb, K.G. (1994) Numerical experiments of internal wave generation by strong tidal flow across a finite amplitude bank edge, *Journal of Geophysical Research*, **99**, 843.

[32] Lamb, K.G. (1997) Particle transport by nonbreaking, solitary waves, *Journal of Geophysical Research*, **102**, 18,641.

[33] Lamb, K.G. (1997) Are internal waves solitons?, *Studies in Applied Math*, **101**, 289.

[34] Lamb, K.G., Theoretical descriptions of shallow-water solitary internal waves: Comparisons with fully-nonlinear waves, submitted to Eur. J. Mech./B., 1999.

[35] Lamb, K.G. (1999) A numerical investigation of solitary internal waves with trapped cores formed via shoaling, submitted to *Journal of Fluid Mechanics*.

[36] Lamb, K.G. (2000) Conjugate flows for a three-layer fluid, *Physics of Fluids*, **12**, 2169.

[37] Lamb, K.G., Wan, B. (1998) Conjugate flows and flat solitary waves for a continuously stratified fluid, *Physics of Fluids*, **10**, 2061.

[38] Lamb, K.G., Yan, L. (1996) The evolution of internal wave undular bores: Comparisons of a fully nonlinear numerical model with weakly nonlinear theory, *Journal of Physical Oceanography*, **26**, 2712.

[39] Leibovich, S., Seebass, A.R., eds. (1974) *Nonlinear Waves*, Cornell University Press, Ithaca.

[40] LeBlond, P.H., Mysak, L.A. (1977) *Waves in the Ocean*, Elsevier, Amsterdam.

[41] Long, R.R. (1953) Some aspects of the flow of stratified fluids I: A theoretical investigation, *Tellus*, 42.

[42] Lorenz, E.N. (1955) Available potential energy and the maintenance of the general circulation, *Tellus*, **7**, 157.

[43] Majda, A.J., Schefter, M.G. (2000) Elementary stratified flows with instability at large Richardson number, *Journal of Fluid Mechanics*, **376**, 319.

[44] Maslowe, S.A., Redekopp, L.G. (1980) Long nonlinear waves in stratified shear flows, *Journal of Fluid Mechanics*, **101**, 321.

[45] Miles, J.W. (1961) On the stability of heterogeneous flows, *Journal of Fluid Mechanics*, **10**, 496.

[46] Miles, J.W. (1980) Solitary Waves, *Annual Review of Fluid Mechanics*, **12**, 11.

[47] Nielsen, P. (1992) *Coastal bottom boundary layers and sediment transport*, World Scientific, Singapore.

[48] Nino, Y, Garcia, M.H. (1996) Experiments on particle-turbulence interactions in the near wall region of a channel flow: implications for sediment transport, *Journal of Fluid Mechanics*, **326**, 285.

[49] Osborn, A.R., Burch, T.L. (1980) Internal solitons in the Andaman sea, *Science*, **208**, 451.

[50] Ostrovsky, L.A., Stepanyants, Yu.A. (1989) Do internal solitons exist in the ocean?, *Reviews of Geophysics*, **27**, 293.

[51] Pauley, L.L., Moin, P., Reynolds, W.C. (1993) The unsteady structure of two-dimensional separation, *Journal of Fluid Mechanics*, **220**, 397.

[52] Ripley, M., Pauley, L.L. (1993) The unsteady structure of two-dimensional steady laminar separation, *Physics of Fluids A*, **5**, 3099.

[53] Pelinovsky, D.E., Grimshaw, R.H.J. (1997) Structural transformation of eigenvalues for a perturbed algebraic soliton potential, *Physical Letters A*, **229**, 165-172.

[54] Redekopp, L.G. (1999) Long internal waves in shear flows: topographic resonance and a mechanism for sediment resuspension, submitted to Dynamics of Atmospheres and Oceans.

[55] Sandstrom, H., Elliot, J.A. (1984) Internal tide and solitons on the Scotian Shelf: a nutrient pump at work, *Journal of Geophysical Research*, **89(C4)**, 6415.

[56] Serebryany, A.N., Shapiro, G.I. (2000) Overturning of soliton-like internal waves on the Pechora sea shelf, *Proceedings of the Fifth International Symposium on Stratified Flows*, ed. Lawrence, G.A., Pieters, R., Yonemitsu, N., 1029.

[57] Sleath, J.F.A. (1984) *Sea Bed Mechanics*, Wiley Interscience, NY.

[58] Stamp, A.P., Jacka, M. (1995) Deep-water internal solitary waves, *Journal of Fluid Mechanics*, **305**, 347-371.

[59] Stastna, M., Lamb, K.G. (2001) Large shallow-water internal solitary waves: fully nonlinear waves and comparisons with weakly nonlinear theory, *unpublished manuscript*.

[60] Terez, D.E., Knio, O.M. (1998) Numerical simulations of large-amplitude internal solitary waves, *Journal of Fluid Mechanics*, **362**, 53-82.

[61] Trevorrow, M.V. (1998) Observations of internal solitary waves near the Oregon coast with an inverted echo sounder, *Journal of Geophysical Research*, **103(C4)**, 7671.

[62] Tung, K.K., Ko, D.R.S., Chang, J.J. (1981) Weakly nonlinear internal waves in shear, *Studies in Applied Mathematics*, **65**, 189-221.

[63] Tung, K.K., Chan, T.F., Kubota, T. (1982) Large amplitude internal waves of permanent form, *Studies in Applied Mathematics*, **66**, 1.

[64] Turkington, B., Eydeland, A., Wang, S. (1991) A computational method for solitary internal waves in a continuously stratified fluid, *Studies in Applied Mathematics*, **85**, 93.

[65] Wang, S., Internal cnoidal waves in continuously stratified fluids, *PhD. thesis*, University of Massachussets,1991.

[66] Whitham, G.B. (1974) *Linear and Nonlinear Waves*, Wiley, New York.

[67] Yih, C. (1965) *Dynamics of Nonhomegeneous Fluids*, MacMillan, NY.

[68] Zabusky, N.J., Kruskal, M.D. (1965) Interactions of "solitons" in a collisionless plasma and the recurrence of initial states, *Physical review Letters*, **15**, 240.

[69] Zhou, X., Grimshaw, R. (1989) The effect of variable currents on internal solitary waves. *Dynamics of Atmospheres and Oceans*, **14**, 17.